

UC Santa Barbara

UC Santa Barbara Electronic Theses and Dissertations

Title

High Performance Organic Electronics Processing with Green Solvents

Permalink

<https://escholarship.org/uc/item/96x1k1c1>

Author

Du, Zhifang

Publication Date

2023

Peer reviewed|Thesis/dissertation

UNIVERSITY OF CALIFORNIA

Santa Barbara

High Performance Organic Electronics Processing with Green Solvents

A dissertation submitted in partial satisfaction of the
requirements for the degree Doctor of Philosophy

in Chemistry

by

Zhifang Du

Committee in charge:

Professor Thuc-Quyen Nguyen, Chair

Professor Christopher Bates

Professor Mattanjah de Vries

Professor Mahdi Abu-Omar

March 2023

The dissertation of Zhifang Du is approved.

Professor Mattanjah de Vries

Professor Christopher Bates

Professor Mahdi Abu-Omar

Professor Thuc-Quyen Nguyen, Committee Chair

March 2023

High Performance Organic Electronics Processing with Green Solvents

Copyright © 2023

by

Zhifang Du

iii

ACKNOWLEDGEMENTS

I often find myself writing down important things to remember, as I may not recall them later, and that's what I believe acknowledgement is supposed to be. Pursuing a Ph.D. has been a long journey, and I wouldn't have made it this far without the support of the people around me. The past five years have been a struggle, and there were times when I even doubted if it was worth continuing. Fortunately, I was never alone. Despite living over 7,000 miles away across the ocean, my parents have been a constant source of encouragement and support, even through the COVID-19 pandemic that has kept us apart since 2019 till now. Our weekly chats on Saturday nights, which were early Sunday mornings for them and after work hours for me, have helped me stay connected with them despite the distance. The words I typed on WeChat could never express the depth of my missing for them, and the complexity of my feelings that only the moon might understand. I am immensely grateful to my parents, and one of my biggest wishes is to have more time to spend with them after this long Ph.D. marathon.

I am also deeply grateful to my significant other, zzhu, for all the wonderful moments we have shared and for her unconditional love and endless support. Even as she pursued her own Ph.D. studies, she always made time to listen to me when I needed someone to share my feelings with, and comforted me with hugs. Life is brighter and warmer with her around, and she is the sun that I have always been searching for, and want to spend my life with.

On campus, my Ph.D. journey would not have been possible without the support of my supervisor, Prof. Thuc-Quyen Nguyen. I am grateful to her for letting me do a rotation and for taking me into her lab at the beginning of my Ph.D., and for all the guidance and support that she has provided over the past five years. As an organic chemistry major during my undergraduate studies, the field of organic electronics was entirely new and challenging to me at the beginning. And I still can't believe how much I have learned from Quyen during my Ph.D., both in scientific research and in daily life. From lab rotations to committee selection, candidacy exams, project leadership, scholarship applications, conference attendance, job searching, interview skills, freshman training, and lab collaboration, she has been a constant source of guidance and patience, helping me grow strong enough to face the real world. I am also grateful to Prof. Mahdi Abo Omar, Prof. Martin Moskovits, Prof. Chris Bates, and Prof. Mattanjah de Vries, who have supported me as my committee members during my fellowship application and career training.

In the lab, I have had the privilege of being mentored by many former graduate students and postdocs in Quyen's group, including Dr. Hung Phan, Dr. Joachim Vollbrecht, Dr. Viktor Brus, Dr. Seojin Ko, Dr. Jianfei Huang, Dr. Jaewon Lee, Dr. David Cao, Dr. Akchheta Karki, Dr. Alex Lill, Dr. Brett Yurash, and Dr. Lijiao Ren. Their wealth of technical knowledge and valuable suggestions have been invaluable to me during my time here. Dr. Hung Phan, in particular, guided me into the world of organic electronics with great patience. I still remember the day when we had properly changed for entering the cleanroom, then he realized that he

had left his samples in the middle lab. Despite my busy first-year schedule, Hung still made time for us to hang out late at night after lab work, and we would often stay up drinking until midnight. I learned a great deal from him about the duties and responsibilities of a graduate student, and I am very grateful for all of his help at the beginning of my graduate school journey. Dr. Joachim Vollbrecht, Dr. Viktor Brus, and Dr. Seojin Ko shared an office with me that had a beautiful mountain view, and we sat close to each other. There were always moments when Joachim would start a discussion about device physics with Viktor or complain about Seojin's device quality and then suggest that he should go home and find a girl to marry. Just sitting next to them, I learned essential skills such as device fabrication, sample testing, optimization, physics behind the devices, and most importantly, communication with people. They kindly guided me and gave me directions when I was confused during my first two years, and I miss those old days sitting in the same room next to them with gratitude. Dr. Jianfei Huang moved to the desk next to mine after Joachim left, and he helped me move out of my comfort zone from organic solar cells to photodetectors. I will never forget the night before he left when he explained all the experimental details of a heart-rate sensor using organic photodetectors and allowed me to film it for future reference. Jianfei is a real scientist who conducts research with detailed plans and experimental procedures. It was an honor for me to learn from him and work with him. Dr. Jaewon Lee is an expert in organic synthesis and was even willing to provide materials in gram scale. We had many discussions downstairs next to the no-smoking sign, including novel materials design, synthesis, and characterization. He worked hard and spent less time with his family due to his

busy schedule, and I appreciate all the materials he allowed me to handle and all the suggestions he provided. Dr. David Cao, Dr. Akchheta Karki, and Dr. Alex Lill were in their third year when I joined the group. They showed me all the techniques of the lab and shared all the tips they had learned about the spin coater, evaporator, AFM, glovebox, pump oil change, catalyst regeneration, etc. These tricks made me feel comfortable using the equipment in Quyen's lab throughout my Ph.D. journey. We also became good friends and would hang out together, playing basketball and doing heavy exercise at the rec center after a workday. It was a great pleasure to meet them during my graduate school. Dr. Brett Yurash and Dr. Lijiao Ren helped me with the big nitrogen tank that every new member of Quyen's group finds confusing. They also gave me suggestions on my daily life when I first entered UCSB. I feel fortunate to have met all of these former graduate students and postdocs in Quyen's group who have helped and guided me throughout my Ph.D. journey. I will always remember the valuable knowledge and skills learnt from them.

It's also been a joy to work alongside my past and current lab mates — Nora Schopp, Dr. Hoang Luong, Dr. Tung Nguyen, Sangcheol Yoon, Sangmin Chae, Hiba Wakidi, Dr. Ahra Yi, Jirat Chatsirisupachai, Patchareeporn Panoy, Alana Dixon, Jingcong Chen, Chokchai Kaiyasuan, Brian Kim, Jae Young Kim, Emmanuel Lanuza, George (Kunyu) Li, Sam Mugiraneza, Francesca Pallini, Zhongze (Jason) Qu, Thanh Vuong, Yuxiang Wan. Nora's enthusiasm and dedication to the project were inspiring. She was always willing to lend a hand in the lab, manage lab safety and equipment, and provide suggestions on my research. Her

hard work and positive attitude always inspired me during graduate school. Hoang expertise in OPD device characterization and testing was a tremendous asset to my projects. His attention to detail and technical proficiency ensured that the devices were characterized with the highest quality. It was my great pleasure working with him and I really enjoyed learning new ideas and techniques from him. Together with my lab mates, we have tackled challenging projects and supported each other through the ups and downs of research. I am grateful for their friendship and collaboration, and I know that our experiences in the lab will stay with me for years to come.

My Ph.D. would not have been possible without the expertise and collaborative efforts of Prof. G. N. Manjunatha Reddy, Prof. Harald Ade, Prof. John Reynolds, Prof. Mario Leclerc, Prof. Seth Marder, Prof. Jean-Luc Bredas, Prof. Michael Toney, Dr. Ziyue Zhu, Dr. Mathieu Mainville, Dr. Sina Sabury, Dr. Austin L. Jones, Dr. Junxiang Zhang, Dr. Pattarawadee Therdkatanyuphong, Dr. Zhengxing Peng, Dr. Yunpeng Qin, and Dr. Steven Xiao, thanks to their guidance, support, and close collaboration throughout my research journey. I would like to express my deepest gratitude to all of them. Their contributions to my Ph.D. research were important and their insights and suggestions were invaluable in the design, synthesis and characterization of the materials and electronic devices. Without their help and valuable suggestions, my work wouldn't be possible.

Last but definitely not least, I am grateful to the academic community and technicians in UCSB, who provided a rich intellectual environment for me to grow and learn. Great thanks

to Dr. Tom Mates, Dr. Guang Wu, Dr. Oleksandr Polonskyi, and Wan Ying Ho. Their dedication to advancing knowledge in modern techniques inspired me to continue to explore new ideas and perspectives.

Curriculum Vitae

of

Zhifang Du

EDUCATION

09/2017 – 03/2023

Ph.D. Candidacy in Material Chemistry

University of California, Santa Barbara

Advisor: Prof. Thuc-Quyen Nguyen

07/2016 – 09/2016

International Research Intern

University of California, Los Angeles

Advisor: Prof. Michael E. Jung

09/2013 - 06/2017

B.S. in Chemistry

Shandong University

HONORS & AWARDS

2017-2023, UCSB:

- Graduate Division Dissertation Fellowship
- Chair's Fellowship from the Department of Chemistry & Biochemistry
- Outstanding Service to the Department Award
- Academic Senate Doctoral Student Travel Grant

2013-2017, Shandong University and UCLA:

- Merit Student
- First Class Undergraduate Student Scholarship
- Second Class Outstanding Scholarship
- UCLA CSST Scholarship

PUBLICATIONS

1. **Z. Du**, H.M. Luong, S. Sabury, A. L. Jones, Z. Zhu, P. Panoy, S. Chae, A. Yi, H. Jung Kim, S. Xiao, V.V. Brus, G. N. M. Reddy, J. R. Reynolds, T.-Q. Nguyen, High-Detectivity Wearable Organic Photodetectors Processed from Green Solvent for Self-Powered Pulse Rate and Oximetry Measurements. (*Submitted to Advanced Materials*, 2023)
2. **Z. Du**, S. Sabury, A. L. Jones, J. Zhang, P. Therdkatanyuphong, Z. Peng, Z. Zhu, D. Choi, S. Chae, S. Xiao, A. Yi, H. Jung Kim, H. Ade, G. N. M. Reddy, S. R. Marder, J. R. Reynolds, T.-Q. Nguyen, 2-MeTHF Casting Organic Solar Cells Achieving 15% PCE. (*To be submitted soon*)
3. B. R. Luginbuhl, P. Raval, T. Pawlak, **Z. Du**, T. Wang, G. Kupgan, N. Schopp, S. Chae, S. Yoon, A. Yi, H. Jung Kim, V. Coropceanu, J.-L. Brédas, T.-Q. Nguyen and G. N. M. Reddy, Resolving Atomic-Scale Interactions in Nonfullerene Acceptor Organic Solar Cells with Solid-State NMR Spectroscopy, Crystallographic Modelling, and Molecular Dynamics Simulations, *Advanced Materials*, 2022, **34**, 2105943.
4. **Z. Du**, M. Mainville, J. Vollbrecht, A. L. Dixon, N. Schopp, M. Schrock, Z. Peng, J. Huang, S. Chae, H. Ade, M. Leclerc, G. N. M. Reddy and T.-Q. Nguyen, Insights into Bulk-Heterojunction Organic Solar Cells Processed from Green Solvent, *Solar RRL*, 2021, **5**, 2100213.
5. J. Lee, S. Song, J. Huang, **Z. Du**, H. Lee, Z. Zhu, S.-J. Ko, T.-Q. Nguyen, J. Y. Kim, K. Cho and G. C. Bazan, Bandgap Tailored Nonfullerene Acceptors for Low-Energy-Loss Near-Infrared Organic Photovoltaics, *ACS Materials Lett.*, 2020, **2**, 395–402.
6. J. Huang, J. Lee, J. Vollbrecht, V. V. Brus, A. L. Dixon, D. X. Cao, Z. Zhu, **Z. Du**, H. Wang, K. Cho, G. C. Bazan and T.-Q. Nguyen, A High-Performance Solution-Processed Organic Photodetector for Near-Infrared Sensing, *Advanced Materials*, 2020, **32**, 1906027.
7. X. Dai, Z.-Y. Wang, **Z. Du**, J.-Y. Miao and B.-X. Zhao, A simple but effective near-infrared ratiometric fluorescent probe for hydrazine and its application in bioimaging, *Sensors and Actuators B: Chemical*, 2016, **232**, 369–374.
8. X. Dai, **Z. Du**, L.-H. Wang, J.-Y. Miao and B.-X. Zhao, A quick response fluorescent probe based on coumarin and quinone for glutathione and its application in living cells, *Analytica Chimica Acta*, 2016, **922**, 64–70.
9. X. Dai, Z.-Y. Wang, **Z. Du**, J. Cui, J.-Y. Miao and B.-X. Zhao, A colorimetric, ratiometric and water-soluble fluorescent probe for simultaneously sensing glutathione and cysteine/homocysteine, *Analytica Chimica Acta*, 2015, **900**, 103–110.
10. X. Dai, T. Zhang, **Z. Du**, X.-J. Cao, M.-Y. Chen, S.-W. Hu, J.-Y. Miao and B.-X. Zhao, An effective colorimetric and ratiometric fluorescent probe for bisulfite in aqueous solution, *Analytica Chimica Acta*, 2015, **888**, 138–145.

RESEARCH EXPERIENCES

Graduate Researcher, UCSB

09/2017 – Present

- Design, optimize and develop state-of-the-art OPV and OPD systems processing with green solvent in over 20,000 real devices.
- Develop optical and physical modeling of organic electronic devices, in-depth characterization of thin-film morphology and material property with advanced techniques.
- Developed a strategy for using green-solvent casting to improve the device performance of organic solar cells.
- Designed and optimized an organic solar cell system cast from 2-MeTHF with a state-of-the-art power conversion efficiency of 15%.
- Developed wearable organic photodetectors with recorded detectivity processed from green solvents for self-powered pulse rate and oximetry measurements.
- Led the Office of Naval Research (ONR) and Air Force Grant.

International Research Intern, UCLA

07/2016 – 09/2016

- Designed, synthesized, and scaled-up organic small molecules for drugs used as radiation mitigators

Undergraduate Researcher, Shandong University

09/2013 - 06/2017

- Developed effective novel organic molecules as functional fluorescent probes for bioimaging

TECHNICAL SKILLS

- **Device Fabrication and Characterization:**

Design and Fabrication of Organic Photovoltaics, Photodetector and Electrochemical Transistors | Thin-Film Processing | Vapor Deposition | Encapsulation | Current-Voltage Characteristics | Quantum Efficiency | Capacitance Spectroscopy | Modeling Device Physics

- **Material and Thin Film Characterization:**

Film Optical Modeling | Atomic Force Microscopy (AFM) | Photoconductive AFM | Profilometry | X-ray Photoelectron Spectroscopy | Ultraviolet Photoelectron Spectroscopy | NMR | Cyclic Voltammetry | Differential Pulse Voltammetry | Solubility Assessment | Differential Scanning Calorimetry

TEACHING AND MENTORING EXPERIENCES

- Experienced teaching assistant for general chemistry, organic chemistry, advanced analytical techniques, and advanced physics chemistry labs
- Mentoring new graduate students in the research labs

VOLUNTEER EXPERIENCES

Teaching Volunteer for Scientific Outreach, UCSB	2021-2023
DSP Student Teaching Note-Taker Volunteer for labs, UCSB	2017-2020
Volunteer for Academic Communities for Excellence Program, UCSB	2021

ABSTRACT

High Performance Organic Electronics Processing with Green Solvents

by

Zhifang Du

Organic semiconductors have been widely applied to electronic devices including organic solar cells (OSCs), and organic photodetectors (OPDs) in the last decades for their lightweight, flexibility, and great industry potential for high throughput solution processing and roll-to-roll printing technologies. However, traditional solvents used for these organic photovoltaics processing conditions are commonly highly toxic halogenated organic solvents like chlorobenzene (CB), *o*-dichlorobenzene (*o*-DCB), and chloroform (CF) which are not only harmful to human health upon exposure but can also cause long-term effects on the ecosystem. Consequently, research on halogen-free/ “green solvents” (such as xylene, 2-methyltetrahydrofuran (2-MeTHF), methanol, water, etc.) processable organic semiconductors are essential to moving organic photovoltaics from bench chemistry towards real-life applications. In this thesis, three studies are carried out to enhance the sensing performance, as well as to better understand the device physics of bulk heterojunction (BHJ) OPVs and OPDs. The design, fabrication, optimization, as well as characterization of green-solvent processing organic semiconductors, have been discussed in detail including OPV and OPD systems. The characterization of the solid-state properties of the optimized active layers

in these organic electronic devices is further included. The bulk-heterojunction (BHJ) thin films processed from green solvents were characterized with different techniques at different length scales, including atomic force microscopy (AFM), transmission electron microscopy (TEM), grazing-incidence wide-angle X-ray scattering (GIWAXS) and solid-state nuclear magnetic resonance (ssNMR) spectroscopy. The first study gains insights into the structure–processing–property correlation of a PPDT2FBT:PC₆₁BM bulk-heterojunction (BHJ) system processed from a green solvent, ortho-xylene (o-XY). This system is investigated in comparison with the same blend processed from a traditional halogenated solvent, chlorobenzene (CB). The optimized PPDT2FBT:PC₆₁BM devices processed from o-XY can achieve a noteworthy higher power conversion efficiency (PCE) owing to a higher short-circuit current density and fill factor. The second study develop a series of 2-MeTHF processing OPV systems based on newly designed bulk heterojunction (BHJ) consisting of PM7-D3/D5 donors and Y-series non-fullerene acceptors with systematically changing in their side chain length and positions. The optimized 2-MeTHF casting device based on PM7-D3:PTI04 exhibits the best PCE of approaching 15%, which is comparable with the well-known PM6:Y6 system processing from traditional halogenated solvents. The third study reports a designed bulk heterojunction (BHJ) consisting of PM7-D5 donor and Y12 non-fullerene acceptor processed from 2-methyltetrahydrofuran (2-MeTHF) sets a record in light detectivity, which is also comparable with commercially available silicon-based photodiodes. Newly designed PM7-D5:Y12 OPD can be employed in wearable self-powered devices to monitor heart rate and blood oxygen saturation. This development of a framework for a

detailed understanding of the structure-processing-property relationship provides insight into the mechanisms that lead to the improved performance of green-solvent-processed organic electronics.

TABLE OF CONTENTS

Contents

Chapter 1: Introduction	1
1.1 Green solvent processing organic electronic devices.....	1
1.2 Characterization of organic electronic devices	8
1.3 Tips for design, optimization, and characterization of organic electronic devices	13
Chapter 2: Insights into BHJ Organic Solar Cells Processed from Green Solvent	19
2.1 Introduction.....	19
2.2 Characterization of o-xylene processing PPDT2FBT:PCBM BHJ layer.....	21
2.3 Design, optimization, and characterization of PPDT2FBT:PCBM devices.....	29
2.4 Charge dynamic and physical modeling of PPDT2FBT:PCBM devices.....	31
2.5 Conclusions	38
2.6 Experimental methods.....	39
Chapter 3: Organic Solar Cells Processed from 2-MeTHF Approaching 15% Efficiency	43
3.1 Introduction.....	43
3.2 Design, optimization, and characterization of PM7-Dx:Y-series NFAs devices.....	45
3.3 Charge dynamic and physical modeling of PM7-Dx:Y-series NFAs devices	50
3.4 Characterization of 2-MeTHF processing BHJ active layers.....	53

3.5	Conclusions.....	57
3.6	Experimental methods.....	58
Chapter 4: 2-MeTHF Casting High-Performance Wearable Organic Photodetectors for Self-Powered Pulse Oximetry and Photoplethysmography		63
4.1	Introduction.....	63
4.2	Molecular design, green-solvent processing, optical absorption, and energy levels.....	65
4.3	Characterization of 2-MeTHF processing PM7-D5:Y12 active layers.....	69
4.4	Characterization of PM7-D5:Y12 OPD devices	77
4.5	Wearable PM7:D5 based OPDs for photoplethysmography and pulse oximetry	86
4.6	Conclusions	91
4.7	Experimental methods.....	92
Chapter 5: Conclusions		100
Chapter 6: References		103
Chapter 7: Appendix		115

LIST OF FIGURES

Figure 1-1. A typical structure of organic photovoltaic devices	2
Figure 1-2. Photodiode-based organic photodetectors	4
Figure 1-3. Common halogenated host solvents and additives used in organic electronic devices fabrication	5
Figure 1-4. Halogen-free and green solvents used in organic electronic devices fabrication	6
Figure 1-5. Some advanced techniques for probing film morphology at different length scales	8
Figure 1-6. A standard J - V curve of a solar cell, focused on the power-generating quadrant. The key parameters that determine the efficiency of the solar cell (J_{SC} , V_{OC} , and FF) are highlighted in the image.....	10
Figure 1-7. The operational mechanism of a photoplethysmography (PPG)-based wearable setup for real-time heart rate monitoring using flexible OPDs is depicted. A snapshot of the wearable OPD fabricated on a flexible substrate is shown on the bottom right, worn by a volunteer on their finger without any wires connected	11
Figure 2-1. (a) Molecular structures and (b) energy level diagram of PPDT2FBT and PC ₆₁ BM.....	21
Figure 2-2. 1 μ m * 1 μ m AFM topography images of PPDT2FBT:PC ₆₁ BM films cast from (a) CB and (b) o-XY. 2D GIWAXS images of the PPDT2FBT:PC ₆₁ BM films cast from (c) CB and (d) o-XY onto ZnO/ITO substrates	23
Figure 2-3. Solid-state ¹ H-detected 2D ¹³ C- ¹ H heteronuclear correlation NMR spectra of PPDT2FBT:PC ₆₁ BM blends processed from (a) CB and (b) o-XY solvents, accompanied by 1D ¹ H MAS of blends in the top horizontal dimension and 1D ¹³ C{ ¹ H} CP MAS spectra of neat D and A compounds and blends in the vertical dimensions. 2D ¹ H- ¹³ C correlation peaks are color coded as depicted in the molecular structure. All spectra are acquired at 18.8 T (¹ H, 800.1 MHz and ¹³ C, 201.2 MHz) with 50 kHz MAS at room temperature	28
Figure 2-4. (a) J - V curves of the PPDT2FBT:PC ₆₁ BM solar cells processed from o-XY and CB under AM 1.5 G illumination at 100 mW cm ⁻² and (b) V_{OC} vs. light intensity.....	30
Figure 2-5. The voltage-dependent charge carrier density of PPDT2FBT:PC ₆₁ BM devices processed from (a) o-XY and (b) CB under different illumination intensities	35
Figure 2-6. (a) Charge carrier lifetime τ_{rec} and extraction time τ_{ex} , and (b) voltage-dependent competition factor θ of the investigated devices	37
Figure 3-1. Chemical structures of (a) PM7-D3 and PM7-D3, and (b) PTI04, Y12, and DTY6. (c) Normalized absorption of pristine films processed from 2-MeTHF. (d) Energy level diagram. (e) DFT simulation of PM7-D3 and PM7-D3.....	45

Figure 3-2. (a) J - V characteristics, (b) EQE spectra, (c) charge collection probability, (d) voltage-dependent charge carrier density, (e) voltage-dependent effectivity mobility, and (f) the fitting of recombination current density of 2-MeTHF processed OPVs composed of PM7-D3:PTI04, PM7-D3:Y12, PM7-D3:DTY6, and PM7-D3:PTI04 under AM 1.5G illumination at 100 mW cm^{-2} 49

Figure 3-3. (a) $5 \mu\text{m} * 5 \mu\text{m}$ AFM topography images, (b) 2D GIWAXS patterns, (c) the corresponding in-plane (dash lines) and out-of-plane (solid lines) GIWAXS profiles, and (d) RSoXS profiles for the corresponding BHJ films processed from 2-MeTHF 54

Figure 3-4. (a) D/(A+D) molar ratio of PM7-D3:PTI04, PM7-D3:Y12, PM7-D3:DTY6, and PM7-D3:PTI04 BHJ films calculated from the Cl/F ratio of the XPS depth profiles as a function of etching degree (%), where etching begins at the top air/film interface. Dotted lines represent the ideal D/(D+A) molar ratio calculated from the original D:A ratio of 1:1.2 by weight. (b) Schematic of the PM7-D3:PTI04 with more uniform vertical phase separation, and (c) other three blend films showing vertical phase gradation with an acceptor-rich region near the blend/PEDOT:PSS interface. 55

Figure 3-5. Synthetic procedures of PM7-D3 59

Figure 3-6. Synthetic procedure of PTI04 59

Figure 4-1. (a) Chemical structures of the donor PM7-D5 and the acceptor Y12. (b) Normalized thin-film absorption of PM7-D5 (black), Y12 (red), and BHJ blends (blue). (c) Energy level diagram of PM7-D5 and Y12 68

Figure 4-2. (a) High-resolution $2 \mu\text{m} \times 2 \mu\text{m}$ AFM topography images, (b) TEM images, (c) 2D GIWAXS patterns, and (d) the corresponding in-plane (dash lines) and out-of-plane (solid lines) GIWAXS profiles of PM7-D5:Y12 blend films processed with 2-MeTHF, CB, and o-XY, respectively. 70

Figure 4-3. (a) Solid-state 1D ^{19}F MAS NMR spectra of neat Y12 and PM7-D5:Y12 blend films processed from 2-MeTHF and CB solvents with ^{19}F chemical shifts corresponding to distinct Y12 moieties. (b) 2D ^{19}F - ^{19}F exchange NMR spectra of PM7-D5:Y12 BHJs processed from different solvents. Solid-state 2D ^1H - ^{13}C HETCOR spectra of PM7-D5, Y12, and PM7-D5:Y12 blend processed from (c) 2-MeTHF and (d) CB solvents. All spectra were recorded at 18.8 T (^1H 800 MHz) and at 50 kHz MAS 73

Figure 4-4. (a) J - V curves in the dark, (b) EQE and responsivity at -2 V, (c) EQE under different biases (0 V, -0.1 V, -1 V, and -2 V) and $\text{EQE}_{(0 \text{ V})}/\text{EQE}_{\text{bias}}$, (d) D_{sh}^* of PM7-D5:Y12 OPDs and a commercial Si photodiode (Newport 818-UV) under the self-powered mode (0 V), (e) linear dynamic range under the illumination of 850 nm, and (f) normalized phototransient response under the illumination of 850 nm of PM7-D5:Y12 OPDs processed with o-XY (red), CB (blue), and 2-MeTHF (green) 78

Figure 4-5. (a) Working principle of a PPG-based real-time heart rate setup with wearable OPDs. Bottom right: a photograph of an OPD fabricated on flexible substrates wearing on a volunteer's finger

without wire connections. (b) A model of the light pathway of pulse oximeters using measured cardiac cycles from our designed OPDs as an example. (c) Time series pulse signal obtained from the PPG measurement at after-exercise (upper) condition and relaxing (lower) conditions. Inset: HR determined from the FFT of the PPG signal. (d) Output current signal from wearable OPD with $S_aO_2 = 97\%$. The blue and red shapes represent the signals when illuminated with the 850 nm and 940 nm LEDs, respectively. 87

Figure 4-6. Synthetic procedures of PM7-D5 93

Figure S1. 2-D GIWAXS images of the pristine PPDT2FBT films processed with a) CB and b) *o*-XY solvent and PC₆₁BM films processed with c) CB and d) *o*-XY solvent..... 117

Figure S2. In-plane and out-of-plane GIWAXS profiles for the pristine a,b) PPDT2FBT and c,d) PC₆₁BM films cast from CB and *o*-XY 118

Figure S3. In-plane and out-of-plane GIWAXS profiles for the PPDT2FBT:PC₆₁BM blend films casted from CB and *o*-XY on ZnO/ITO substrates 119

Figure S4. Lorentz corrected and film thickness-normalized RSoXS profiles for the PPDT2FBT:PC₆₁BM blend casted from CB and *o*-XY 120

Figure S5. Normalized UV-vis absorption spectra of a) PPDT2FBT, b) PC₆₁BM and c) PPDT2FBT:PC₆₁BM films 120

Figure S6. Spectra used to calculate solubility. Plot of PPDT2FBT concentration in a) CB and b) *o*-XY vs. absorbance at 643 nm. Plot of PC₆₁BM concentration in c) CB and d) *o*-XY vs. absorbance at 331 nm..... 121

Figure S7. Solid-state 1D ¹H MAS NMR spectra of PPDT2FBT, PC₆₁BM, and PPDT2FBT:PC₆₁BM blends processed from CB and *o*-XY solvents..... 124

Figure S8. Solid-state 1D ¹³C{¹H} CP-MAS NMR spectra of PPDT2FBT, PC₆₁BM, and PPDT2FBT:PC₆₁BM blends processed from chlorobenzene and *o*-xylene solvents 125

Figure S9. Solid-state 2D ¹H-¹³C HETCOR NMR spectra of PPDT2FBT, PC₆₁BM, and PPDT2FBT:PC₆₁BM blends processed from a,b) chlorobenzene and c,d) *o*-xylene solvents 126

Figure S10. Solid-state 2D ¹H-¹H DQ-SQ correlation NMR spectra of PPDT2FBT, PC₆₁BM, and PPDT2FBT:PC₆₁BM blends processed from a) chlorobenzene and b) *o*-xylene solvents. Red arrows indicate the subtle differences in the aromatic ¹H DQ signals, which correspond to the changes in the local chemical environments of acceptor molecules in the BHJ blend processed from a green (*o*-XY) solvent 127

Figure S11. The optical properties of the PPDT2FBT:PC₆₁BM film prepared with CB and *o*-XY: a) refractive index, b) extinction coefficient and c) reflectance..... 128

Figure S12. (a) Calculated generation rates of free charge carriers and (b) simulated J_{sc} in dependence of the active layer thickness of PPDT2FBT:PC ₆₁ BM devices processed from CB and o-XY.....	128
Figure S13. The chemical capacitance spectroscopy of PPDT2FBT:PC ₆₁ BM devices processing from (a) o-XY and (b) CB under different illumination intensities	129
Figure S14. The effective mobility (μ_{eff}) of PPDT2FBT:PC ₆₁ BM devices processed from o-XY and CB under 100 mW cm ⁻² illumination.....	129
Figure S15. Measured and calculated recombination current density of PPDT2FBT:PC ₆₁ BM solar cells processed from a) o-XY and b) CB under different illumination intensities	131
Figure S16. Relationship between saturated photocurrent density $J_{ph,sat}$ and light intensity of PPDT2FBT: PC ₆₁ BM devices from (a) o-XY and (b) CB. The slope of the plot is used as the empirical parameter j	133
Figure S17. S Experimental (symbols) and calculated (solid lines) V_{oc} vs. light intensity plots of the two investigated solar cells	134
Figure S18. EQE spectra of PPDT2FBT:PC ₆₁ BM devices casted from o-XY and CB under illumination of an AM 1.5 G at 100 mW·cm ⁻²	136
Figure S19. The corrected capacitance spectroscopy of PPDT2FBT:PC ₆₁ BM devices processing from o-XY a) in the dark and b) at simulated 100 mW·cm ⁻² AM 1.5 G illumination. The corrected capacitance spectroscopy of PPDT2FBT:PC ₆₁ BM devices processing from CB c) in the dark and d) at simulated 100 mW·cm ⁻² AM 1.5 G illumination.....	137
Figure S20. ¹ H NMR of 2-butyloctyl 2-bromothiophene-3-carboxylate (2).....	139
Figure S21. ¹³ C{ ¹ H} NMR of 2-butyloctyl 2-bromothiophene-3-carboxylate (2).....	140
Figure S22. ¹ H NMR of bis(2-butyloctyl) [2,2':5',2":5",2'''-quaterthiophene]-3,3'''-dicarboxylate (3)	141
Figure S23. ¹³ C{ ¹ H} NMR of bis(2-butyloctyl) [2,2':5',2":5",2'''-quaterthiophene]-3,3'''-dicarboxylate (3).....	142
Figure S24. ¹ H NMR of bis(2-butyloctyl) 5,5'''-dibromo-[2,2':5',2":5",2'''-quaterthiophene]-3,3'''-dicarboxylate (4)	143
Figure S25. ¹³ C{ ¹ H} NMR of bis(2-butyloctyl) 5,5'''-dibromo-[2,2':5',2":5",2'''-quaterthiophene]-3,3'''-dicarboxylate (4)	144
Figure S26. ¹ H NMR spectra of PM7-D3 in o-dichlorobenzene-D4 at 110 °C. δ (ppm): 8.08-7.78 (m, 4H), 7.71-7.53 (m, 4H), 7.32 (s, 2H), 4.46 (m, 4H), 3.09 (m, 4H), 2.03 (m, 4H), 1.78-1.41 (m, 48H), 1.25-1.00 (m, 24H).....	146

Figure S27. High temperature (140 °C) GPC trace of PM7-D3 in 1,2,4-trichlorobenzene. Mn: 64.6 kg/mol, Mw: 148.6 kg/mol, Đ: 2.30 (vs polystyrene).....	147
Figure S28. Chemical structure of intermediates for synthesis of Y-series NFAs.....	148
Figure S29. ¹ H NMR of 5-bromothiophene-3-carboxylic acid (1)	149
Figure S30. ¹³ C{ ¹ H} NMR of 5-bromothiophene-3-carboxylic acid (1)	150
Figure S31. ¹ H NMR of 2-butyloctyl 5-bromothiophene-3-carboxylate (2).....	151
Figure S32. ¹³ C{ ¹ H} NMR of 2-butyloctyl 5-bromothiophene-3-carboxylate (2).....	152
Figure S33. ¹ H NMR of bis(2-butyloctyl) [2,2'-bithiophene]-4,4'-dicarboxylate (3)	144
Figure S34. ¹³ C{ ¹ H} NMR of bis(2-butyloctyl) [2,2'-bithiophene]-4,4'-dicarboxylate (3)	146
Figure S35. ¹ H NMR of bis(2-butyloctyl) 5,5'-dibromo-[2,2'-bithiophene]-4,4'-dicarboxylate	157
Figure S36. ¹³ C{ ¹ H} NMR of bis(2-butyloctyl) 5,5'-dibromo-[2,2'-bithiophene]-4,4'-dicarboxylate (4).....	158
Figure S37. ¹ H NMR of bis(2-butyloctyl) [2,2':5',2'':5'',2'''-quaterthiophene]-3',4''-dicarboxylate ...	159
Figure S38. ¹³ C{ ¹ H} NMR of bis(2-butyloctyl) [2,2':5',2'':5'',2'''-quaterthiophene]-3',4''-dicarboxylate (5).....	161
Figure S39. ¹ H NMR of bis(2-butyloctyl) 5,5'''-dibromo-[2,2':5',2'':5'',2'''-quaterthiophene]-3',4''-dicarboxylate (6)	162
Figure S40. ¹³ C{ ¹ H} NMR of bis(2-butyloctyl) 5,5'''-dibromo-[2,2':5',2'':5'',2'''-quaterthiophene]-3',4''-dicarboxylate (6)	163
Figure S41. ¹ H NMR spectra of PM7-D5 in <i>o</i> -dichlorobenzene-D4 at 110 °C	163
Figure S42. ¹³ C{ ¹ H} NMR of 2-butyloctyl 5-bromothiophene-3-carboxylate (2).....	164
Figure S43. The device structure of designed OPDs. For wearable devices, bottom substrate was PET instead of glass	168
Figure S44. Differential pulse voltammograms of PM7-D5 during (a) electrochemical reduction and (b) oxidation. Differential pulse voltammograms of Y12 during (c) electrochemical reduction and (d) oxidation. The intersections of red lines indicate the extraction of onset potentials of ionization and electron affinity from DPV	170
Figure S45. Enlarged TEM images of PM7-D5:Y12 blend films processed with 2-MeTHF, CB, and <i>o</i> -XY, respectively.	171
Figure S46. In-plane and out-of-plane GIWAXS images for the pristine (a-c) PM7-D5, (d-f) Y12, and (g-i) blend films processed from 2-MeTHF, CB, and <i>o</i> -XY, respectively.....	173

Figure S47. In-plane and out-of-plane GIWAXS profiles for the pristine (a-c) PM7-D5, (d-f) Y12, and (g-i) blend films processed from 2-MeTHF, CB, and o-XY, respectively.....	174
Figure S48. Solid-state 1D ^1H spectra of neat films and PM7-D5:Y12 blend films processed from CB and 2-MeTHF. All spectra were acquired at 18.8 T ($^1\text{H} = 800.1$ MHz) and at 50 kHz MAS.....	175
Figure S49. Solid-state 1D ^{13}C spectra of neat films and PM7-D5:Y12 blend films processed from CB and 2-MeTHF. All spectra were acquired at 18.8 T (Larmor frequencies of ^1H and ^{13}C nuclei are 800.1 MHz and 201.2 MHz, respectively).....	177
Figure S50. D_{sh}^* of OPDs cast from different solvents under an applied bias of (a) -2 V, and (b) -0.1 V.....	179
Figure S51. Noise current spectral density of the OPDs processed with different solvents: (a) 2-MeTHF, (b) CB, and (c) o-XY. These data were also collected at different reverse biases (0 V, -0.1, -1, and -2 V).	181
Figure S52. Specific detectivity (D^*) as a function of frequency and incident light wavelength of OPDs processed with different solvents (2-MeTHF, CB, and o-XY) and under different reverse biases (-0.1 V, -1 V, and -2 V)	182
Figure S53. Specific detectivity of PM7-D5:Y12 OPDs and a commercial Si photodiode (Newport 818-UV) at the frequency of 155 Hz under (a) -2V, and (b) 0 V.....	183
Figure S54. Voltage-dependent charge collection probability (P_c) of 2-METHF OPD under AM 1.5 G illumination at 100 mW cm^{-2}	183
Figure S55. (a) Charge carrier density n and (b) effective mobility μ_{eff} of PM7-D5:Y12 devices under AM 1.5G illumination ($100 \text{ mW}\cdot\text{cm}^{-2}$)	185
Figure S56. Molar extinction coefficients of oxygenated and deoxygenated hemoglobin	186
Figure S57. (a) EQE, (b) responsivity, and (c) shot-noise-limited specific detectivity (D_{sh}^*) of PM7-D5:Y12 OPD processed with 2-MeTHF at -0.1 V with ITO/glass substrate (solid line) and flexible ITO/PET substrate (dash line).....	186
Figure S58. Normalized thin-film absorption of PM7-D5, Y12, and their BHJ blends processed with o-XY, CB and 2-MeTHF, respectively	187

LIST OF TABLES

Table 1. Average photovoltaic performances of 20 OSCs based on PPDT2FBT:PC ₆₁ BM and processed with o-XY and CB under 100 mW·cm ⁻² AM 1.5 G illumination.....	34
Table 2. Photovoltaic parameters of studied PM7-Dx:Y-series OPVs measured under AM1.5 illumination at 100 mW cm ² . Average PCE values are obtained from 10 separate devices.	48
Table 3. Summary of the PM7-Dx:Y-Series NFAs OPV device parameters obtained under simulated AM1.5G illumination.....	51
Table S1. Calculated drying time of the PPDT2FBT:PC ₆₁ BM films under different processing conditions from CB and o-XY	122
Table S2. Photovoltaic performances of PPDT2FBT:PC ₆₁ BM devices processed from o-XY and CB with varied additives and casting temperature under illumination of an AM 1.5G at 100 mW·cm ⁻²	134
Table S3. Results of purity assessment using elemental analysis of PM7-D3.....	146
Table S4. Results of purity assessment using elemental analysis of PM7-D5.....	153

Chapter 1: Introduction

1.1 Green solvent processing organic electronic devices

Organic electronics devices are based on organic molecules including polymers and small molecules with desirable electronic properties, such as processable solubility, high charge carrier mobility, and good mechanical properties.^[1–9] Unlike traditional inorganic semiconductors, organic electronic materials are made from carbon-based molecules or polymers using synthetic strategies developed in organic and polymer chemistry. Followed by material characterization, various functional electronic devices can be further designed, optimized and fabricated, such as organic photovoltaic (OPV),^[4,7,10] photodetector (OPD),^[3,11,12] organic light-emitting diode (OLED),^[13–15] and organic electrochemical transistor (OECT).^[16–18] One of the main advantages of organic electronics is their potential for low-cost industrial scale fabrication compared to traditional electronic devices. Polymeric conductors have attractive properties such as their electrical conductivity and optical properties, which can be controlled by core unit and side chain engineering of the polymer structure, and their relatively high mechanical flexibility. However, there are several challenges that must be overcome before organic electronic materials can be widely implemented, including their thermal instability, high cost of organic active layers, environmentally unfriendly fabrication process, and a relatively short lifetime. One of the most important types of organic electronic devices is organic solar cells, or called as OPVs. Compared with traditional photovoltaic devices based on inorganic materials such as silicon, the key building blocks of the active layer of organic electronic devices are based on novel

designed nontoxic organic materials with high tunability in their physical and chemical properties. According to the U.S. Department of Energy,^[19] the amount of solar energy that reaches the surface of our earth in ninety minutes is more than enough to cover all energy consumption of the whole world for a full year. Solar energy, which is the most environmentally friendly and renewable energy available to human, has shown a great potential to serve as the main source of future energy. To utilize solar energy, people have developed advanced solar technologies named photovoltaics that are able to convert the energy of sunlight into electrical energy, which can be directly used in our daily lives as power sources or can be further stored in batteries for future usage. Recently, OPVs have attracted great attention with considerable rapid development among various photovoltaic technologies, due to their low cost, great mechanical flexibility, and potential for a wide range of low-cost clean energy applications.

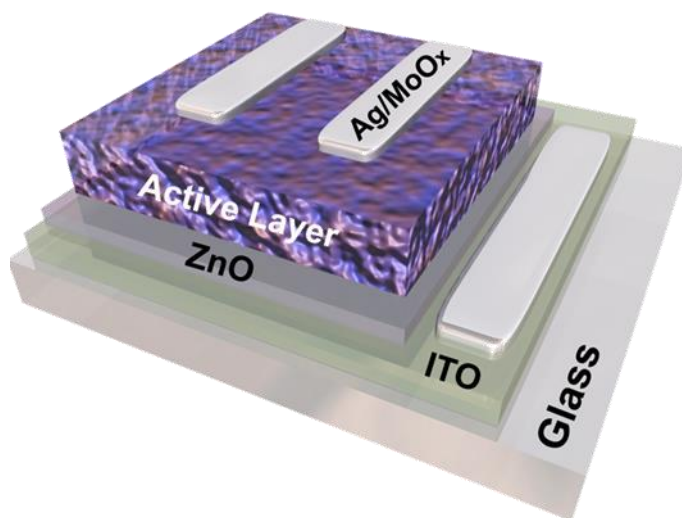


Figure 1-1. A typical structure of organic photovoltaic devices

Most OPV devices are fabricated using the blend of a conjugated polymer donor and a small molecule acceptor as the active layer.^[10,20,21] The donor/acceptor system can generate exciton once exposed to light, generated in either the donor or acceptor layers, to diffuse to a donor/acceptor interface for charge transfer to occur. However, since excitons have a limited diffusion length of around 15 nm, the donor and acceptor layers cannot be thicker than 15 nm each to effectively harvest the energy in the exciton. This limitation on device thickness makes it challenging for the solar cell to absorb sufficient photons. Researchers have attempted to optimize charge transport to the electrodes by designing the best morphology of the donor and acceptor phases. And eventually, it was solved with a concept of a bulk heterojunction (BHJ)^[22] active layer in organic solar cells introduced by Alan Heeger, the former leader of Center for Polymers and Organic Solids (CPOS) in UCSB, who also won the Noble Prize in 2000 as the co-founder of conducting polymers. Based on the structure of BHJ donor and acceptor blend, fullerene acceptors such as PC₆₁BM and its derivatives, were dominantly used as the electron accepting materials when OPV research started in 1995. However, OPV devices reach a barrier of PCE of approximately 10% processing with fullerenes after a few years development.^[23–25] Fullerenes have some limitations as electron acceptors in organic solar cells. For instance, they exhibit weak absorption in the visible region of the solar spectrum, making it challenging to achieve complementary light harvesting with the polymer donors. Additionally, chemical modification of their backbone is not a simple task, leading to low structural flexibility and difficulty in tuning their electronic and optical properties as well as poor solubility in processing solvents. These limitations increase the synthetic complexity and hinder the fullerenes' performance in devices. Furthermore, fullerenes have been reported to have poor photostability in both pristine and blend films in the presence of air due to oxygen

and moisture. Considering all these factors, researchers developed the next generation of acceptors for OPVs using non-fullerene organic small molecules. It is worth noticing that the power conversion efficiencies (PCEs) of single-junction based OPVs has been significantly improved in the past ten years, achieving a recorded PCE of approximately 20%.^[6,9,26,27] The majority of these achievements are enabled by the design of novel polymer donors and NFAs, especially PM6 based polymers and Y-series NFAs. A typical structure of OPV devices is shown in **Figure 1-1**.

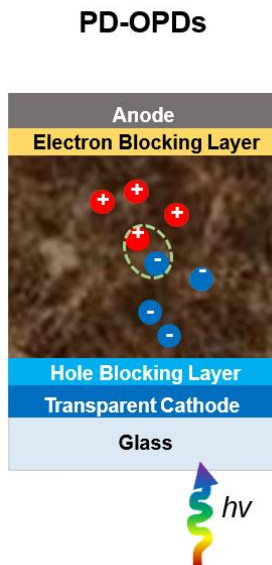


Figure 1-2. Photodiode-based organic photodetectors.

In addition to OPVs, there has been a significant increase in research focusing on organic photodetectors as another type of organic electronic device. **Figure 1-2** shows a device structure of PD-OPDs.^[11] The wide-range and tunable spectral photoresponsivity of OPDs lead them to becoming a promising platform for optical sensing, fast imaging, as well as

optical communication. The advantages of organic photodetectors (OPDs) include tunable detection wavelengths, low-cost manufacturing, and compatibility with lightweight and flexible devices. By optimizing the optical bandgap of organic semiconductors and device architecture, OPDs can detect ultraviolet (UV), visible, and near-infrared (NIR) light without requiring additional optical filters. This simplifies the fabrication process and reduces manufacturing costs. The mechanical flexibility of organic semiconductors also makes them suitable for wearable photodetectors with potential applications in health monitoring.

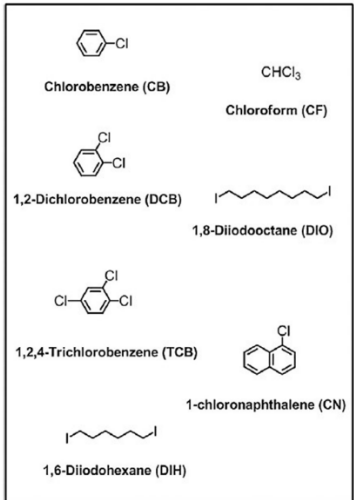
Chemicals	Health Hazard Statements
 <p>Chlorobenzene (CB) CHCl_3 Chloroform (CF)</p> <p>1,2-Dichlorobenzene (DCB) 1,8-Diiodooctane (DIO)</p> <p>1,2,4-Trichlorobenzene (TCB) 1-chloronaphthalene (CN)</p> <p>1,6-Diiodohexane (DIH)</p>	<p>DIO Causes skin irritation, serious eye irritation May cause long lasting harmful effects to aquatic life</p> <p>1-CN Causes skin irritation, serious eye irritation, May cause respiratory irritation, headache, fatigue, vertigo and anorexia</p> <p>CF Harmful if swallowed, Causes skin irritation and serious eye irritation, Toxic if inhaled, Suspected of causing cancer and damaging the unborn child, Causes damage to organs through prolonged or repeated exposure, is a central nervous system depressant and a gastrointestinal irritant. It has caused rapid death attributable to cardiac arrest and delayed death from liver and kidney damage.</p> <p>CB, DCB, TCB Causes skin irritation, Harmful if inhaled or swallowed, Chronic inhalation of vapors or mist may result in damage to lungs, liver, and kidneys. Very toxic to aquatic life with long lasting effects</p>

Figure 1-3. Common halogenated host solvents and additives used in organic electronic devices fabrication.

Despite the potential of organic electronic devices to revolutionize our daily lives, only OLEDs have been commercialized while most other types of organic electronic devices remain in the research phase due to some technical limitations. The primary limitation of commercializing organic electronic devices is their processability. These materials are typically processed from highly toxic halogenated solvents, such as chlorobenzene and

chloroform in research labs, which are detrimental to both the environment and human health (Figure 1-3).^[28] Despite the high-performance and low-cost benefits of OPV/OPD devices, the use of halogenated solvents severely limits large-scale device fabrication and commercialization. In addition to the host solvent, to achieve optimal bulk heterojunction morphology in the thin-film active layer, various halogenated solvent additives have been widely used during device fabrication, including 1-chloronaphthalene and 1,8-diiodooctane. However, these additives have high boiling points, causing residue problems that are less favorable for industrial scale fabrication. Therefore, the development of green solvent processing organic electronics is critical for industrial scale implementation and further real applications.

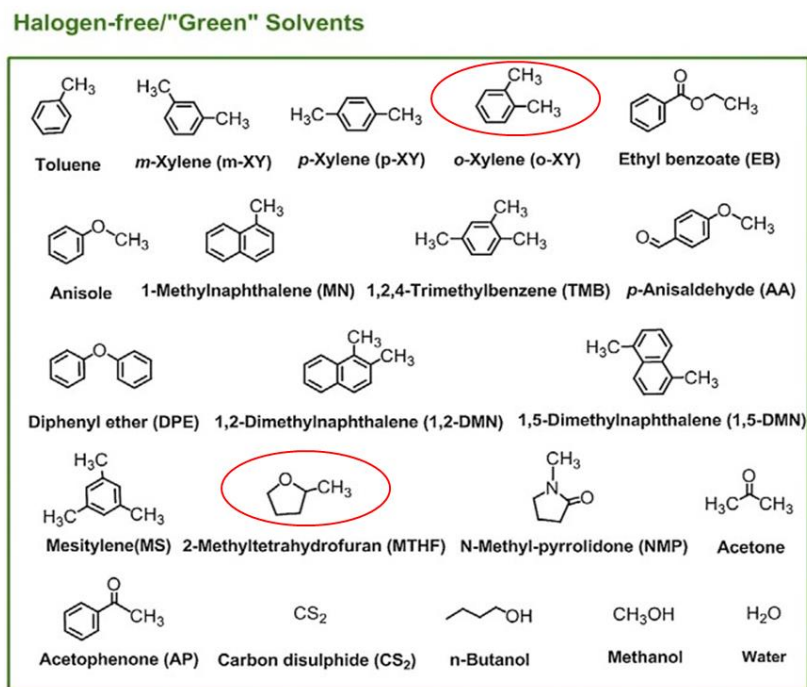


Figure 1-4. Halogen-free and green solvents used in organic electronic devices fabrication.^[28]

As shown in **Figure 1-4**, non-halogenated solvents such as ortho-xylene (o-XY) and trimethylbenzene have shown promise as environmentally friendly solvent candidates for device processing. In particular, 2-MeTHF is a biomass-derived and environmentally friendly solvent that is widely used in organic synthesis in industry. It can be produced from low-cost and renewable agricultural feedstock. Additionally, 2-MeTHF has a lower toxicity compared to halogenated and aromatic solvents, making it a more attractive option for green solvent substitution in the process of organic electronic devices. The chemical structures of o-XY and 2-MeTHF are highlighted in **Figure 1-4**. Currently, there are limited research on green solvent processable organic electronic devices. Some studies have introduced solvation sidechains to enhance solubility in polar processing solvents and designed new light-harvesting materials. However, high-performance OPVs or OPDs that can be processed by green solvents such as 2-MeTHF are still lacking, and fundamental studies on film morphology, optical and charge transport properties, device performance, and applications of organic electronic devices processed by green solvents are still needed. By implementing green processing options for organic electronics, we can accelerate mass production and minimize health hazards and environmental impact during device fabrication, which is crucial for industry-scale implementation. Although some studies have explored the morphology and device performance of organic electronic devices processed from green solvents, a deeper understanding of film morphology at different length scales, as well as charge recombination and extraction, is also necessary to better understand and further enhance the device performance.

1.2 Characterization of organic electronic devices

Morphology characterization

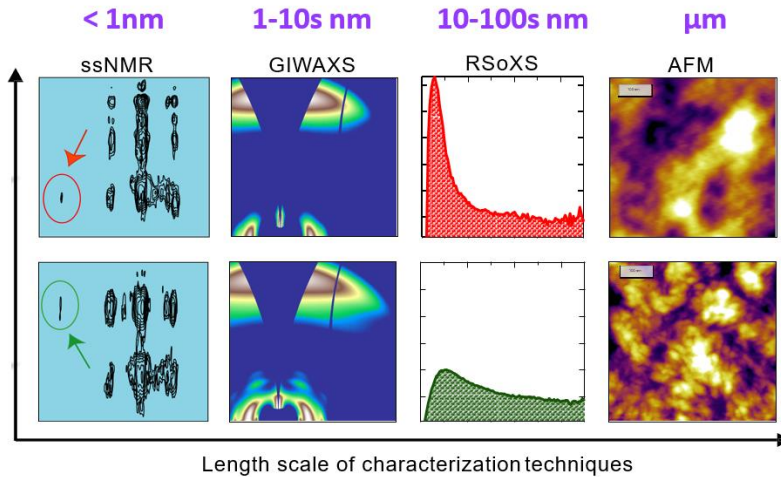


Figure 1-5. Some advanced techniques for probing film morphology at different length scales.

Achieving an optimal BHJ morphology is critical for achieving high device performance in any donor and acceptor blend based organic electronic devices.^{8,20,50} Therefore to gain a multi-dimensional picture of the BHJ morphology down to atomic-level resolution, several advanced morphology techniques have been employed, including photo-conductive AFM (pc-AFM), grazing incidence wide angle X-ray scattering (GIWAXS), resonant soft X-ray scattering (RSoXS), depth-profiled X-ray photoelectron spectroscopy (XPS), and 1-D and 2-D magic-angle spinning (MAS) solid state-NMR (ssNMR).^[8,31-35] **Figure 1-5** further shows some examples of those techniques under different length scale. Specifically, pc-AFM will be used to selectively probe hole- and electron-rich domains, which can be attributed to donor-

or acceptor-rich regions and further used to estimate the domain size in a film.⁵⁰⁻⁵² GIWAXS can be used to study intramolecular ordering and molecule packing in organic thin film devices, such as the orientation of the π -conjugated backbone with the substrate, relative degrees of crystallinity, as well as the amount of mixing between donor and acceptor phases.^{4,32,53-55} RSoXS can provide additional valuable information about the BHJ morphology, such as the domain spacing, relative degrees of phase purity, and molecular orientation.^{56,57} The depth-profiled XPS scanning can be utilized to investigate the distribution and composition of donors and acceptors in the vertical direction of the active layers. By analyzing the signal of specific elements present only in either the polymer donors or NFAs in the BHJ film, the distribution of these materials can be tracked, and the uniformity of the film can be evaluated. Furthermore, the selected high-performing blend systems will also undergo 1-D and 1-2D solid-state MAS NMR analyses to provide insights into inter- and intramolecular D:A interactions. This analysis can determine internuclear distances in the absence of long-range structural order by analyzing heteronuclear dipolar couplings in heterogeneous soft matter materials.^{33,58} In addition, by combining solid-state NMR analyses with X-ray scattering, quantitative information about the ordered and disordered regions in organic semiconductors and interfacial contacts in BHJs can be further obtained.^{36,59-62}

Device characterization

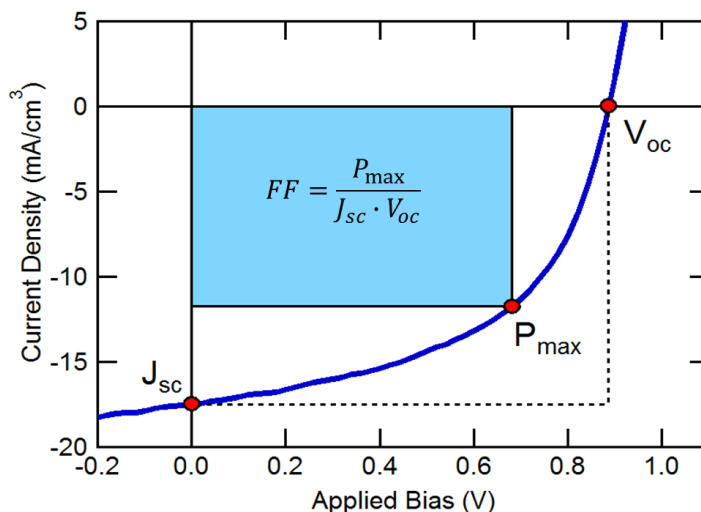


Figure 1-6. A standard J - V curve of a solar cell, focused on the power-generating quadrant. The key parameters that determine the efficiency of the solar cell (J_{sc} , V_{oc} , and FF) are highlighted in the image.

To characterize a photovoltaic device, a white light with a filter that mimics the sun's emission spectrum is used to illuminate the device. Various voltages are then applied to the solar cell under illumination, and the resulting current is recorded to create a current-voltage (J - V) curve as shown in **Figure 1-6**.^[50,51] The J - V curve provides information about the short-circuit current (J_{sc}), which is the current generated by the solar cell when the potential between the cathode and anode is 0 V, the open-circuit voltage (V_{oc}), which is the voltage at which current generation and recombination in the solar cell are equal and no current flows through the circuit, and the fill factor (FF), a parameter that indicates the ratio between the maximum power in the J - V curve ($P_{max} = J \times V$) and the ideal maximum power ($P_{ideal} = J_{sc} \times V_{oc}$), given by $FF = P_{max}/P_{ideal}$. The product of these three parameters determines the power

conversion efficiency (PCE) of the solar cell, given by $PCE (\%) = V_{OC} \times J_{SC} \times FF \times 100\%$.

This method is the basis for all OPV device characterization.

Another powerful tool to exam organic BHJ solar cells is impedance spectroscopy. Voltage-dependent impedance spectrum combined with basic dark and illuminated $J-V$ curves can be further used to gain valuable information, such as bias-dependent charge carrier density, recombination dynamics, effective mobility of OPV devices under working condition.^[2,52–54] Advanced recombination fitting can be performed using the impedance data collected at various light intensities from 1 sun to 0.1 sun. Detailed analysis and device modeling will be discussed in chapter 2, 3, and 4 based on optimized high-performance OPV or OPD systems.

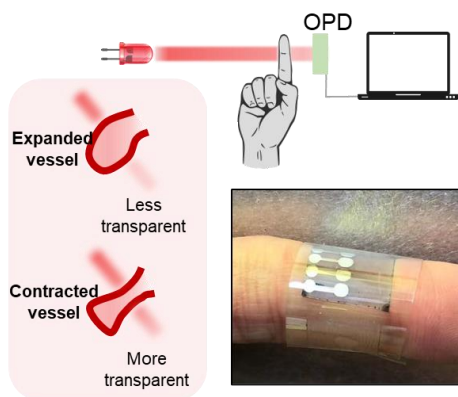


Figure 1-7. The operational mechanism of a photoplethysmography (PPG)-based wearable setup for real-time heart rate monitoring using flexible OPDs is depicted. A snapshot of the wearable OPD fabricated on a flexible substrate is shown on the bottom right, worn by a volunteer on their finger without any wires connected.

For OPD devices, one of the most important photosensing metrics is a high sensitivity toward weak light signals, which requires a low noise level originating from the low dark current. Thus, the overall performance of OPDs depends on key factors including external quantum efficiency (EQE), responsivity (R), specific detectivity (D^*), rise and fall time (T_r and T_f), and linear dynamics range (LDR), each of them will be thoroughly discussed in the following.^[3,12,55,56] The EQE refers to the measurement of the ratio between the number of charge carriers collected by the device and the number of incident photons from the light source, which directly determines the photodetection performance and the R of OPD devices. The sensitivity of a photodetector to weak optical signals can be described by D^* , which together considered the noise level and R of OPDs and can be further expressed in units of Jones. The rise time of OPDs refers to the duration required for a signal to transition from a predetermined low level (10%) to a predetermined high level (90%), while T_f describes the time required for the reverse process. LDR refers to the range of input signals over which the output of the detector scales linearly, which can be generated from the corresponding photocurrent measured under the maximum and minimum irradiance. For OPDs, this range is normally set in between 80 to 160 dB. Furthermore, OPD devices have the potential to be used in real-life applications as wearable health monitoring devices.^[3,57,58] With their high sensitivity and fast response time, OPDs can be used in daily life to detect and convert light signals into electrical signals, which can be processed into useful digital information. As shown in **Figure 1-7**, wearable OPD devices based on flexible substrates can monitor the volume change of blood vessels during the cardiac cycle in the human body, which can be further designed for monitoring pulse, heart rate, and blood oxygen levels.

For the readers, the thesis chapter is stand-alone, and it doesn't rely on work done in other chapters to make sense of the context.

1.3 Tips for design, optimization, and characterization of organic electronic devices

Device design

Based on the author's experience in green solvent processing organic electronic devices, there are three key factors that affect the organic electronic devices processing with green solvents including the solubility of the polymer donor and the NFA, the processibility of the solution into a high quality BHJ film with continuous D:A network, and the intermixing of the donor and the acceptor to generate suitable sized domains.

The solubility of the materials are determined when the molecules are designed (also consider its Mw and D if it's a polymer), which can be also predicted by Hansen Solubility Parameter (HSP).^[59-62] A commercialize software named HSPiP is available for this calculation and the group contribution method described in the handbook is a powerful method to DIY molecules and get their solubility information. Limited by the size of the molecule that can be edited in the HSPiP software, I would suggest using the group contribution and try different combinations based on the donor or the NFA unit, for example, five parts for Y6 including the pi bridge, the donor part, the acceptor part and the side chains on the edge and in the middle. HSP calculations can help people to find a suitable solvent based on the molecule structure, thus, saving time for both material synthesis and solvent

optimization. Accurate solubility can be measured by UV-vis absorption spectrum based on a certain distribution of solutions with different concentrations, and more details are described in the next project using PPDT2FBT as an example.

Materials have to show good processability to generate a favorable BHJ layer with good network for efficient charge transport and collection. To make the active layer processing under good control, an ideal D:A materials should have a total solubility of their mixture of above 15 mg/mL in the selected green solvent. If the synthesized material couldn't reach this certain level of solubility, a hot casting procedure may be helpful to improve the quality of the solvent before spin coating. Both the stocked solution and the substrates should be heated up in order to generate a high-quality film.^[63,64] Statics spin coating method and dynamic spin coating method should be carefully selected under this condition. A hot casting temperature close to the boiling point of the host solvent will make the drying process for the active layer fabrication happen in less than a second. However, such a fast-drying process could lead to unevenly distributed films when the solvent is dropped before the spinning starts, especially on the edge of the substrates. Thus, dynamic spin coating might be a better choice if the drying process is fast during the fabrication process, even if it may cause some sputtering issues on the surface of the substrates. The author suggests that the solution should be added as soon as possible once the spinning starts in order to keep the solution temperature the same as the substrates and shorten the possibility of sputtering of the solution on top of the fast-spinning substrates. A detailed example can be found in the 15% OPV chapter and 2-MeTHF based OPVs during hot casting require to do dynamic casting to form the even BHJ film to reach a high FF close to 70%.

For the intermixing of the donor and acceptor, there is no straightforward strategy. Valuable information can be obtained by Contact Angle Measurement (CAM), drying dynamics simulation, and in-depth analysis of XPS profile of the active layer. The CAM and XPS measurement will be introduced in the characterization section below. For the drying process of the active layer during spin casting, the drying time can be estimated using the HSPiP software.^[59,65] The spinning of the substrates can be transferred using its average linear velocity as the absolute evaporation rate of the solutions. It is worth mentioning that the drying speed of the solvent additives would be more pronouncing during this process due to their relatively high boiling points above 200 °C, which helps to slow down the drying of films during spin coating to get a better mixing of donor and acceptor. On the other hand, the residential solvent additive is the hard to fully evaporated and could the remaining additive in the BHJ film could also lead to further casting problems.

Device optimization

The key rule for device optimization should be variable control. BHJ organic electronic devices are complicated systems, and a minimum change could lead to a big difference in the device performance. The author suggests that the optimization should be carried out with carefully designed procedures. Before you start, the quality of all used materials for device optimization should have a good quality and passed check using ¹H-NMR and UV-Vis absorption spectrum. Bottom substrates of the devices should also maintain the same quality as pervious devices, and the color, the absorption spectrum as well as the sheet resistance of the ITO/glass substrates should all be pre-checked. And most importantly, the experiments should be designed based on the amount of available materials, and the number of batches

should be estimated before starting the experiment. Based on the typically cost of materials during optimization, the author strongly suggests that materials required for at least four batches of devices in addition to the amount for morphology study should be checked and stored in the glovebox before the optimization starts. Check the old receipts for BHJ systems with similar structure for some guidance of new systems, for example, PCE10 based donor series, Y-series acceptors, and PCBM based fullerenes, etc. An ideal optimization should change only one parameter during one batch to get an average device performance, and the limiting factor during the process of the OPV/OPD device should be addressed. Once confirmed, the limiting factor could be further solved with few more batches with all other steps maintaining the same.

There's always a good question for device engineers to think about, that is how you determine that if the device processing conditions is being optimized or not. To answer that question, the engineers should have a general understanding of the material property, device performance and device physics. When a new D:A system based on novel designed polymers and NFAs needs to be optimized, the engineer should try to set a target at the beginning based on pervious system. For example, PM6:Y-series derivatives (new NFAs), a PCE of above 15% should be a promising result for optimized devices. And the studied system can always compare with PM6:Y6 system to get an idea about the limitations of parameters, such as V_{oc} , J_{sc} or FF . The author would like to encourage people to set a goal for the device performance 10 to 15% higher than the reference system. Even if it turns out to be not achievable, the device optimization should still be promising during the experiment part. Meanwhile, some simulation work can also help to get an idea about the V_{oc} and J_{sc} values of the device under

ideal condition without any loss. When the device performance is reaching the goal after several batches of optimization, then it is already a good sign for a good optimization. Another indication of good optimization is a good repeatability of the devices with no batch-to-batch differences. Other people should be able to follow the documented fabrication procedures to reach the same device performance compared to your results. Last but not least, there is always a barrier that people will reach during device optimization, which refers to minimum increasement (less than 5%) of device performance while changing the critical processing parameters. The device performance is raising up fast in the first few batches, then slowing down till this barrier. If so, it may also give you the information that you already optimize the device well.

Device characterization

Organic electronic is a complicated system which requires advanced techniques for in-depth characterization for both the device physics and the BHJ active layer. Detailed characterization with procedures can be found with examples in the following project and here are some suggestions that the author would like to share. For charge dynamics including generation, transport, and collection, impedance measurement would be a great choice considering that it's a bias-dependent measurement for real devices under operational conditions with certain illuminations.^[52-54,63,66] Valuable information can be further generated from the data analysis such as charge carrier density, effective mobility, recombination dynamics, charge generation rate, diffusion length and drift length for free charge carriers, and the charge carrier lifetime, etc. Device modeling can be further set up based on those parameters and give guidance for achieving higher performance. CAM measurement is a good

choice for studying the mixing of the donor and acceptor materials, which can be further utilized to calculate the Flory-Huggins interaction parameters.^[67] The polymer-NFA interaction parameter χ can be used to predict the similarity of their properties and further the mixing of the donor and acceptor. The smaller this value is, the better tendency for the D:A to mix and increase the D:A interface area for efficient charge generation and dissociation. In-depth XPS could also be a powerful tool to study the D:A distribution in the vertical direction of the active layer. X-ray photoelectron spectroscopy is a technique used to determine the elemental composition, chemical state, and electronic state of atoms within a material. XPS spectra are acquired by exposing a solid surface to a beam of X-rays and measuring the kinetic energy of electrons that are ejected from the top 1-10 nm of the material. Thus, when combined with an ion gun that can etch the surface of the film, an in-depth profile can be measured with repeated scanning and etching. The distribution of donor and acceptor can be determined by analyzing the specific atoms that are unique to either the donor or acceptor molecules and generate a map of D:A ratio in the vertical direction. This could give us a direct guidance on the bulk and surface trap existing in the active layer or at the interface between the active layer and the ETL or HTL.

To summarize, achieving optimal device design and performance requires both scientific expertise and a lot of patience. However, the author believes that there is no substitute for scientist effort and perseverance, and no mountain too high for a determined climber to conquer.^[22,68] Here, the author would like to extend sincere wishes to all aspiring engineers who are working towards optimizing organic electronic systems, hoping that their hard work leads to successful outcomes.

Chapter 2: Molecular Engineering for Non-Fullerene Acceptors

2.1 Introduction Characterization of o-xylene processing PPDT2FBT:PCBM BHJ layer

The past five years have witnessed considerable research attention and rapid development of solution-processed bulk heterojunction (BHJ) organic solar cells (OSCs), owing to their low cost, mechanical flexibility and potential for a wide range of clean energy applications.^[7,51] In particular, significant improvement in power conversion efficiencies (PCEs) of over 18% is recently achieved, with this trend expected to continue.^[69,70] High performance OSCs are commonly processed with halogenated solvents such as chlorobenzene (CB), o-dichlorobenzene and chloroform despite being considered highly hazardous to human health and the environment.^[71] Recently, fabrication of OSCs with environmental friendly solvents, such as *ortho*-xylene (o-XY), trimethylbenzene, tetrahydrofuran (THF), 2-methyltetrahydrofuran, and (R)-(+)-limonene, becomes an emergent trend with exciting prospects.^[6,28,64,72–79] Enabling green processing options will accelerate the mass fabrication of OSCs that minimize health hazards and negative impacts on the environment, which is pivotal for industry-scale implementation. While there are some studies that focus on the understanding of morphology and device physics of OSCs processed from green solvents reported, in-depth understanding of film morphology at various length-scales and charge recombination and extraction is needed to further improve the device performance.^{[64,72,74], [80–83]} Ma and Yan's group shows that a series of PffBT4T:PC₇₁BM blends processed from a 1,2,4-trimethylbenzene yields PCEs of up to 11.7%.^[72] Ye et al. achieve a PCE of 12.5% for a polymer donor:IT-M blend processed from (R)-(+)-limonene using sequential deposition

method.^[77] In addition, the study by Hou et al. have illustrated T1:Y12 based systems processed from various green solvents such as THF and *o*-XY, yielding a high PCE of 16.4%.^[6]

A systematic understanding of green-solvent-processed OSCs is urgently needed and requires the characterization of morphologies at different length scales.^[84] Therefore, we carry out a comprehensive study of BHJ morphology at sub-nanometer to sub-micrometer scales, as well as optical and electrical properties of the devices. Herein, we focus on a blend system based on poly[(2,5-bis(2-hexyldecyloxy)phenylene)-alt-(5,6-difluoro-4,7-di(thiophen-2-yl)benzo[c]-[1,2,5]thiadiazole)] (PPDT2FBT) and [6,6]-Phenyl-C61-butyric acid methyl ester (PC₆₁BM), which are processed with a traditional solvent (CB) and a green solvent (*o*-XY). Emphasis is placed on understanding the factors that contribute to more favorable BHJ morphologies in green-solvent-processed OSCs with relatively high PCEs compared to the those processed with the conventional chlorinated solvent. Other green solvents such as 2-Methyl THF and (*R*)-(+)-limonene could certainly be a possible focus for our future study.^[77,85,86]

The chemical structures and energy diagram of PPDT2FBT and PC₆₁BM are shown in **Figure 2-1**. The efficient and cost-effective conjugated polymer, PPDT2FBT ($M_w=82 \text{ kg mol}^{-1}$), is synthesized by a water-based method of direct (hetero)arylation polymerization (DHAP) with few steps, which can potentially facilitate the scaled-up production of organic solar cells.^[87] The optimized PPDT2FBT:PC₆₁BM devices show an increase of PCE from $7.0 \pm 0.1\%$ when processed from CB to $9.1 \pm 0.1\%$ when processed with *o*-XY. This is quite noteworthy, since in most cases either a similar or a reduced PCE are observed when solar

cells are fabricated with green solvents compared to their counterparts processed with halogenated solvents.^[6,64,88–90] Analysis of photovoltaic properties and charge dynamics reveals that the high-performance system processed from o-XY benefits from more efficient charge transport and smaller recombination losses. This work provides insight into the mechanisms that lead to the improved performance of green-solvent-processed devices.

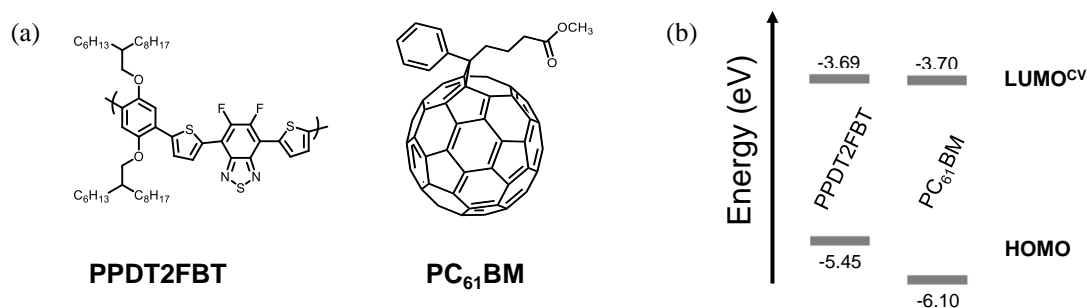


Figure 2-1. (a) Molecular structures and (b) energy level diagram of PPDT2FBT and PC₆₁BM.

2.2 Characterization of o-xylene processing PPDT2FBT:PCBM BHJ layer

The optoelectronic properties of organic solar cells are intimately related to the BHJ morphology and solid-state organization of donor-acceptor moieties, determining charge carrier dynamics including generation, recombination, and extraction processes.^[54] By analyzing BHJ morphologies at different length scales, we can evaluate the impact of solid-state organization on the charge transport and device properties. First, we employ Atomic Force Microscopy (AFM) to study the surface morphology of the PPDT2FBT:PC₆₁BM films

cast from CB at room temperature and o-XY under hot processing conditions at 110 °C (**Figure 2-2a, 2b**).^[91] Both blend films show relatively smooth surface with similar root-mean-square (RMS) values of 1.58 nm for CB and 2.13 nm for o-XY. With high-resolution scans (1 μm * 1 μm), the height profile shows that the film cast from o-XY exhibits smaller topographic features. Next, we examine the molecular orientation and long-range molecular ordering in the BHJ films using Grazing-Incidence Wide-Angle X-ray Scattering (GIWAXS). A detailed analysis of the pristine films can be found in the Appendix (Figure S1, S2). The 2D GIWAXS images of the blend films are shown in **Figure 2-2c** and **2d**, and the corresponding linecuts are shown in Figure S3. Both blend films cast from CB and o-XY display considerably similar molecular ordering characteristics based on the GIWAXS results. Each film contains the isotropic PC₆₁BM producing a scattering halo near 1.3 \AA^{-1} (d-spacing of 0.5 nm) with coherence lengths values of $L_c \approx 2$ nm. In both BHJ films, the dominant features corresponding to the π - π stacking motif with face-on orientation are identified with scattered intensities at 1.64 \AA^{-1} (d-spacing of 0.38 nm) in each direction with no significant difference in the π - π stacking L_c values between them. This result suggests that charge transport can occur both in the in-plane and out-of-plane directions in the photoactive layers, which signifies that the utilization of a green solvent does not detrimentally affect the BHJ molecular packing.^[66] The main differences between the two BHJ films are in the lamellar L_c values. Lamellar stacking peaks are present near 0.3 \AA^{-1} in both directions with a higher order reflection near 0.6 \AA^{-1} . The lamellar L_c values of the film vary from 6.9 nm (CB) to 3.7 nm (o-XY). The L_c for in-plane lamellar stacking decreases by 3.1 nm and that of the higher order reflection for out-of-plane lamellar stacking decreases by 2.1 nm. However, the same peaks are present in both BHJ films, showing that molecular ordering is largely maintained

regardless of the processing solvents. Thus, we employ more advanced techniques for insights on more nuanced morphological traits, such as the D:A interfacial area, the domain sizes, and the composition variations, which monotonically relate to the domain purity.

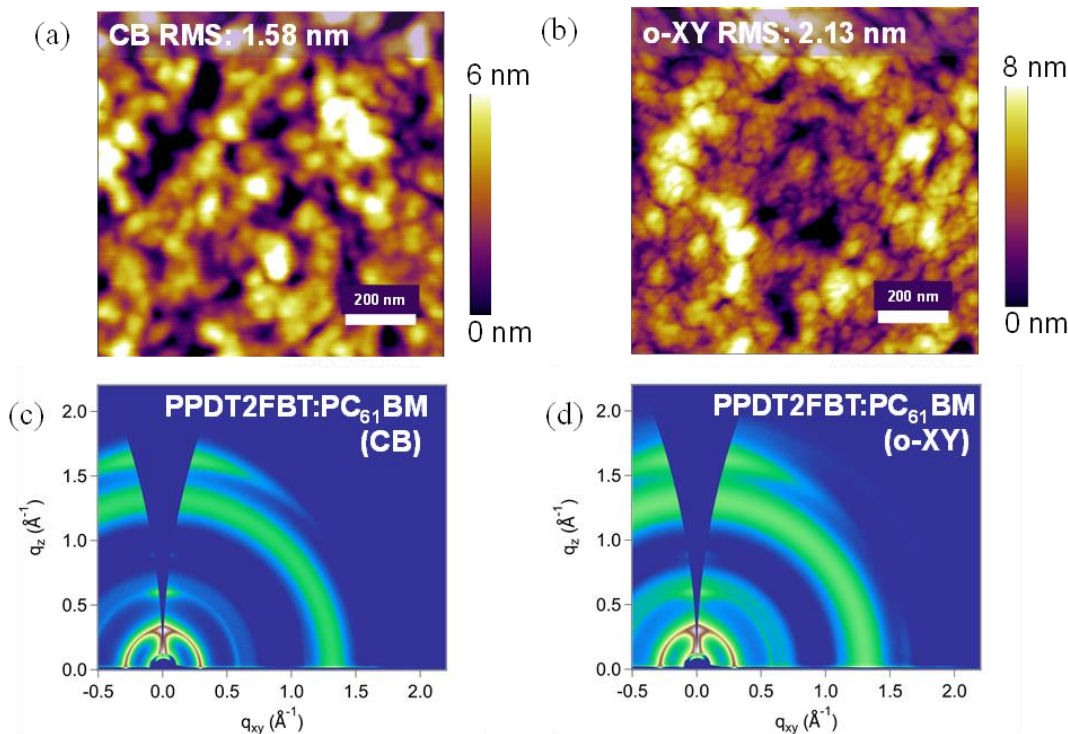


Figure 2-2. $1 \mu\text{m} * 1 \mu\text{m}$ AFM topography images of PPDT2FBT:PC₆₁BM films cast from (a) CB and (b) o-XY. 2D GIWAXS images of the PPDT2FBT:PC₆₁BM films cast from (c) CB and (d) o-XY onto ZnO/ITO substrates.

The Resonant-Soft X-ray Scattering (RSoXS) technique is employed to gain insights into the morphological features including the domain sizes as well as the D:A composition variation of the BHJ blends on a length scale ranging from 10 nm to over 500 nm.^[92–94] The Lorentz-corrected and film thickness-normalized RSoXS profiles of both systems at a photon energy of 283.8 eV are shown in Figure S4 (Appendix), which show apparent differences in

both the position and the intensity of the peak. The peak for the film cast from CB exists at $q \approx 0.069 \text{ nm}^{-1}$, whereas the blend prepared from o-XY shows a peak at $q \approx 0.138 \text{ nm}^{-1}$ with a significantly smaller intensity. The corresponding long period of the o-XY cast film ($\sim 46 \text{ nm}$) is about half of the value of the CB processing film ($\sim 91 \text{ nm}$). Since the domain size can be roughly estimated as half of the long period, the green-solvent-processed films show smaller domains ($\sim 23 \text{ nm}$) than the CB processed films ($\sim 45.5 \text{ nm}$), which is consistent with the surface topography observed in AFM measurement. The average smaller domains predominantly existing in the o-XY processed devices could result in better charge generation due to larger D:A interfacial areas than those of CB processed devices. To further investigate the relative average purity of the domains, the RMS composition variation is obtained from the integration of the scattering intensities. The relatively lower value for the RMS composition variation (0.66) in the o-XY processed BHJ films indicates a lower average domain purity and a higher degree of molecular intermixing of the donor and acceptor, which would enable efficient charge generation in the BHJ layer.^[95] Such differences in the average domain purity are likely resulted from kinetic factors during the film formation, such as the different time of solidification due to the differences in solubility of PPDT2FBT and PC₆₁BM in CB and o-XY, as well as their different drying kinetics. The solubility is measured using the correlation between the solution concentrations and the corresponding absorption curves (Figure S6, Appendix).^[95] PC₆₁BM has a markedly higher solubility (42.1 mg/mL) compared to PPDT2FBT (21.1 mg/mL) in CB, while their solubility parameters are comparable in o-XY (25.9 mg/mL for PC₆₁BM and 18.3 mg/mL for PPDT2FBT). The comparable solubility of PPDT2FBT and low solubility of PC₆₁BM in o-XY lead to an decrease of the distribution of PC₆₁BM in the donor-rich phase during the film formation and reduced phase separation

relative to the smaller domains for o-XY, which is consistent with the RSoXS results and imply a larger D:A interfacial area in the o-XY processed films.^[92,93,96] Next, the drying times of the films are calculated based on the boiling point of the solvent, the average linear velocity of spin coating, and the casting temperature. More details can be found in the Appendix. Although o-XY has a slightly higher boiling point (145 °C) compared to CB (131 °C), films processed from o-XY with a hot solution (110 °C) has a significantly shorter drying time (~0.31 s) compared to CB (~7.14 s) under room temperature. Additionally, the use of additive (DIO) with the boiling point of 169 °C in the CB solution would further slowdown the film drying process (up to 90 s for molecular donor:PC₇₁BM).^[97] The comparable solubility of D:A in o-XY and the faster drying time of the film casting with o-XY could together result in a smaller domain size, a well-mixed phase morphology (kinetically trapped morphology) and a higher D:A interfacial area, which could subsequently improve the charge generation and therefore the device performance.

The bulk and surface characterizations to this point show differences in the morphological features and domain sizes of OPV blends processed from CB and o-XY solvents, and the GIWAXS results indicate preferential face-on orientation of the photoactive layers. However, it is still unclear whether the D:A interactions at molecular level would be different in the CB and o-XY processed films. Thus, we employ solid-state NMR (ssNMR) to probe local structures and interactions within organic semiconductors and their blends.^[4,21,98–105] NMR parameters are sensitive to local bonding environments and intermolecular interactions at sub-nm to nm scale. Information on the local structures and nanoscale interactions in neat donor and acceptor materials can be obtained by examining ¹H and ¹³C sites and their proximities.

We analyze and compare 1D ^1H , ^{13}C and 2D ^1H - ^{13}C and ^1H - ^1H correlation ssNMR spectra of neat PPDT2FBT, PC₆₁BM and PPDT2FBT:PC₆₁BM blends acquired at a high field (18.8 T) NMR spectrometer to unravel the molecular-level interactions in BHJs processed from CB and o-XY solvents. **Figure 2-3** compares ^1H -detected 2D ^1H - ^{13}C HETCOR spectra of PPDT2FBT:PC₆₁BM blends processed from CB and o-XY, whereby 1D ^1H spectra of the blends are shown on the top horizontal axes, and the 1D ^{13}C spectra of the neat compounds and blends are shown in the vertical axes. In particular, 2D ^{13}C - ^1H HETCOR spectra provide an advantage of spreading ^1H and ^{13}C signals into two frequency dimensions, facilitating enhanced resolution that allows the intermolecular interactions between donor and acceptor molecules to be identified. *A priori*, information on the local environments, and inter and intramolecular ^{13}C - ^1H proximities in donor molecules and acceptor molecules themselves can be obtained by analyzing 1D and 2D ssNMR spectra of the neat materials. A detailed analysis of 1D ^1H , ^{13}C and 2D ^{13}C - ^1H spectra of neat materials processed from CB and o-XY solvents is given in **Figures S7-S9** of the Appendix.

To understand the donor-acceptor intermolecular interactions in PPDT2FBT:PC₆₁BM blends processed from the different solvents, we first focus on identifying and distinguishing the 2D correlation intensities originating from the D-D, A-A and D-A moieties. In the HETCOR spectrum of BHJ blend processed from CB (**Figure 2-3a**), the ^{13}C signal at (142 ppm) and ^1H (6.8 ppm) is attributed to the intermolecular ^{13}C - ^1H proximities between quaternary carbon atoms of PC₆₁BM and aromatic protons of the donor polymer (red arrow), indicating the interactions between donor and acceptor molecules. Intercalation of PC₆₁BM molecules into the sidechain regions of PPDT2FBT is best consolidated by the intermolecular

^{13}C - ^1H proximities between carbonyl ^{13}C signals (176 ppm) of PC₆₁BM and sidechain ^1H (~2 ppm) signals of donor polymer.^[4,21,101] By comparison, the 2D ^1H - ^{13}C HETCOR spectrum of PPDT2FBT:PC₆₁BM blends processed from o-XY shows additional 2D signal intensities (solid ovals) corresponding to the donor-acceptor intermolecular interactions, indicating the subtle differences in the relative orientations of intercalated acceptor molecules with respect to the donor polymer. In addition to the well-resolved correlation peak between ^{13}C signals at (142 ppm) and ^1H (6.8 ppm) and between ^{13}C signals (176 ppm) of PC₆₁BM and sidechain ^1H (~2 ppm) signals that corresponds to the proximities between C₆₀ cage of the acceptor and aromatic groups of the donor polymer, the 2D correlation intensity between ^{13}C signals (138 ppm) and ^1H signals (~2.5 ppm) further corroborate the through-space interactions between phenyl rings of PC₆₁BM and sidechains of PPDT2FBT. These 2D ssNMR experiments indicate the close proximities and intermolecular interactions between donor-acceptor molecules, yet differences in molecular-level orientation of acceptor molecules with respect to the aromatic core of the donor polymer, in the BHJ blends processed from CB and o-XY solvents.

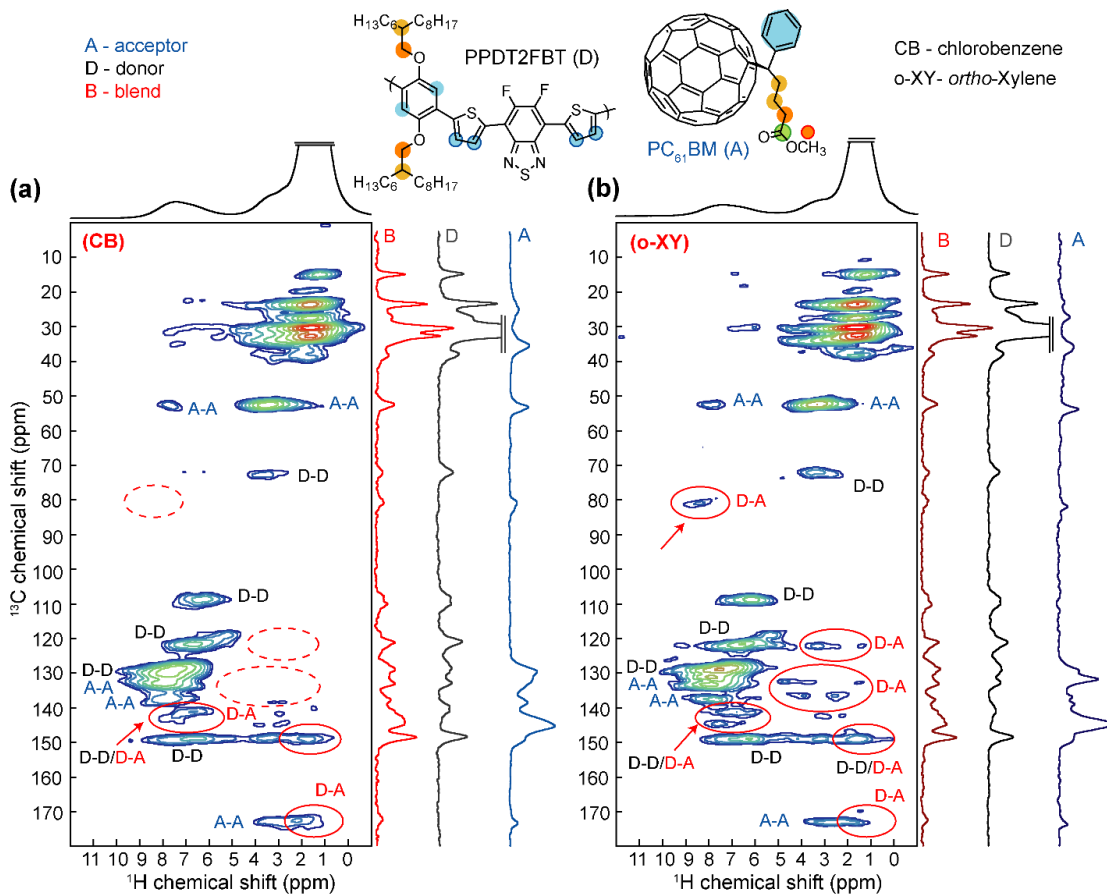


Figure 2-3. Solid-state ^1H -detected 2D ^{13}C - ^1H heteronuclear correlation NMR spectra of PPDT2FBT:PC₆₁BM blends processed from (a) CB and (b) o-XY solvents, accompanied by 1D ^1H MAS of blends in the top horizontal dimension and 1D $^{13}\text{C}\{^1\text{H}\}$ CP MAS spectra of neat D and A compounds and blends in the vertical dimensions. 2D ^1H - ^{13}C correlation peaks are color coded as depicted in the molecular structure. All spectra are acquired at 18.8 T (^1H , 800.1 MHz and ^{13}C , 201.2 MHz) with 50 kHz MAS at room temperature.

Having characterized the inter and intramolecular $\text{H}\cdots\text{C}$ proximities at the donor-acceptor interface, we extend our analysis to characterize the local structures and $\text{H}\cdots\text{H}$ proximities in neat compounds and blends using 2D ^1H - ^1H Double-Quantum–Single-Quantum (DQ-SQ)

correlation NMR spectroscopy. ^1H DQ signals can be excited for dipolar coupled ^1H - ^1H pairs at the sub-nm (<0.5 nm) distances. In a 2D DQ-SQ spectrum, on-diagonal and off-diagonal signals correspond to the through-space dipole-dipole interactions between chemically equivalent and non-equivalent protons, respectively. The analysis of ^1H DQ-SQ spectra of neat donor and acceptor materials, and their blends is given in Figure S10 of the Appendix. Although ^1H DQ-SQ spectra of blends contain overlapped ^1H signals from donor and acceptor molecules, subtle differences in the off-diagonal intensities, which originate from H-H proximities between aliphatic-and aromatic groups of donor and acceptor molecules, further corroborate the different donor-acceptor molecular orientations at the BHJ interfaces of OPV blends processed from CB and o-XY solvents. These differences in molecular orientations and intermolecular interactions at D:A interfaces are expected to influence the charge transport in BHJ blends, leading to different PCE values in their OSCs.

2.3 Design, optimization, and characterization of PPDT2FBT:PCBM devices

To further understand the role of green solvent processing on the BHJ morphology and therefore the device performance, photophysical properties of solar cells fabricated with the inverted device architecture of ITO/ZnO/PPDT2FBT:PC₆₁BM/MoO_x/Ag are analyzed and compared. Under the background of solar cell study, we optimize the additive and the casting temperature for each solvent to compare the difference between green solvent-casted and CB-casted OSCs with best performance for each case. Details of the optimization can be found in **Table S2**. It is worth mentioning that an eco-compatible additive, p-anisaldehyde (AA), has been chosen as the green solvent additive regarding the health and environmental hazards of

common chlorinated additives such as DIO and 1-chloronaphthalene (1-CN).^[86] The current density-voltage (J - V) characteristics of the PPDT2FBT:PC₆₁BM solar cells processed from CB and o-XY in **Figure 2-4a** indicate an increase of the short-circuit current from 12.5 ± 0.3 mA cm⁻² to 15.6 ± 0.2 mA cm⁻² and an increased PCE from $7.0 \pm 0.1\%$ to $9.1 \pm 0.1\%$ using green solvent processing. The average PCE values from 20 devices under the optimized conditions are provided in **Table 1**. The increase in the J_{SC} is in agreement with the morphology results discussed above, in which smaller domain sizes and higher D:A interfacial areas observed in o-XY processed blends should lead to better charge generation. Furthermore, the active layer of the o-XY processed device is thicker than that of the CB cast device (276 nm vs. 238 nm), thus there may be more photons absorbed, resulting in more photogenerated carriers and higher J_{SC} .

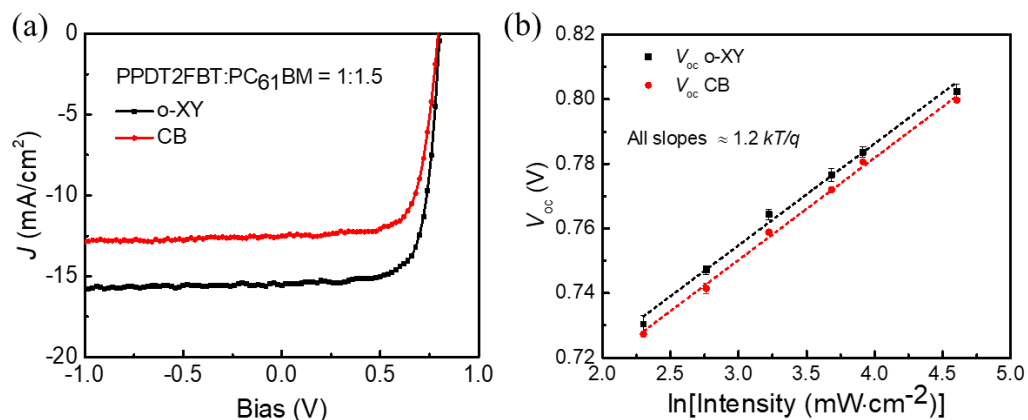


Figure 2-4. (a) J - V curves of the PPDT2FBT:PC₆₁BM solar cells processed from o-XY and CB under AM 1.5 G illumination at 100 mW cm⁻² and (b) V_{OC} vs. light intensity.

Table 1. Average photovoltaic performances of 20 OSCs based on PPDT2FBT:PC₆₁BM and processed with o-XY and CB under 100 mW·cm⁻² AM 1.5 G illumination.

Solvent	J_{SC} (mA cm ⁻²)	V_{OC} (V)	FF	PCE (%)
CB	12.5 ± 0.3	0.79 ± 0.002	0.70 ± 0.01	7.0 ± 0.1
o-XY	15.6 ± 0.2	0.80 ± 0.005	0.72 ± 0.01	9.1 ± 0.1

2.4 Charge dynamic and physical modeling of PPDT2FBT:PCBM devices

To further corroborate the above analysis on the increase in the J_{SC} , we calculate charge generation rate from the optical properties of the blend films processed with CB (238 nm) and o-XY (276 nm). First, the reflectance and transmittance spectra are measured (Figure S11 in the Appendix). While the extinction coefficient k remains unaltered, we find a slightly decreased refractive index n for the o-XY processed film ($n = 1.15-1.30$) compared to the CB processed film ($n = 1.19-1.38$) in the range of 300 nm to 700 nm, causing a reduced reflectance of the incident light. Next, the spatially dependent generation rate is simulated based on the device architecture and the optical properties of the CB and the o-XY processed film with an optical transfer-matrix based model.^[2,23,106,107] The comparison shows that processing with o-XY is beneficial for a thick active layer, since at positions ~200 nm from the bottom electrode the generation rate is higher in the o-XY processed film ($G = 2.0-3.9 \times 10^{21} \text{ cm}^{-3}\text{s}^{-1}$) than the CB processed film ($G = 0.8-2.9 \times 10^{21} \text{ cm}^{-3}\text{s}^{-1}$). Next, we

simulate the maximum, theoretical short-circuit current density $J_{SC,theo}$ based on the generation rate (Figure S12, Appendix) and compare it with the experimentally determined saturated photocurrent density $J_{ph,sat}$, to obtain information on geminate recombination losses.^[108–110] A ratio of $J_{ph,sat}/J_{SC,theo} = 0.995-1.018$ is found for both films, which indicates the absence of geminate recombination losses in both films.

Subsequently, we focus on understanding the losses caused by non-geminate recombination in OSCs processed from CB and o-XY. The dominant non-geminate recombination mechanism in the solar cells is qualitatively determined by analyzing the open-circuit voltage (V_{OC}) dependence on the light intensity (I). Generally, if the $V_{OC}-\ln I$ plot shows a linear relationship with a slope of $s = kT/q$ (k is the Boltzmann-constant, T is the absolute temperature, and q is the elementary charge), the dominant loss mechanism is bimolecular recombination.^[84,111] Deviations of the slope may indicate the presence of trap states (bulk traps: $s > kT/q$; surface traps: $s < kT/q$). In both systems, the slope of the V_{OC} vs. light intensity is equal to $s = 1.2 kT/q$ (**Figure 2-4b**), which is a sign for the presence of trap-assisted Shockley-Read-Hall (SRH) recombination via deep traps in the bulk. A more advanced approach based on capacitance spectroscopy is required to complement the qualitative results obtained from the V_{OC} vs. light intensity plots. Thus, we use a comprehensive analytical model based on a combination of Langevin and Shockley-Read-Hall theory to quantify the total non-geminate recombination losses, including bimolecular recombination as well as bulk and

surface trap-assisted recombination, which can provide valuable information on the charge recombination and extraction dynamics.^[4,101,111–116]

To get quantitative insights into the non-geminate recombination dynamics, capacitance spectroscopy is applied to determine the charge carrier density in the active layer under different operational biases and light intensities.^[52,117] A small AC signal (40 mV) is applied to prevent its effect on the impedance and maintain the steady state properties of the system during the measurement under different illumination as well as DC bias and frequency. Considering the effect of the series resistance of the device as well as the parasitic inductance of the connecting cables,^[118] the measured capacitance of the BHJ layer is corrected and can be described by the following Equation 2-1.

$$C_{\text{cor}} = -\frac{1}{\omega} \left[\frac{Z'' - \omega L'}{(Z' - R_s)^2 + (Z'' - \omega L')^2} \right], \quad (2-1)$$

Here, L' is the inductance of the connecting cables, $\omega = 2\pi\nu$ is the angular frequency of the AC signal, and Z' as well as Z'' are the real and imaginary components of impedance, respectively. In the dark, the corrected capacitance measured under a large reverse bias (-3 V) shows a horizontal line, which is equivalent to a frequency independent capacitance. From this, we can determine the geometrical capacitance (C_g) of the active layer. Voltage-dependent impedance spectroscopy is performed to yield the charge carrier density n (**Figure 2-5**), via integration of the chemical capacitance C_{chem} using the following equations.

$$n(V_{\text{cor}}) = n_{\text{sat}} + \frac{1}{qAL} \int_{V_{\text{sat}}}^{V_{\text{cor}}} C_{\text{chem}} dV_{\text{cor}}, \quad (2-2)$$

$$n_{\text{sat}} = \frac{1}{qAL} C_{\text{sat}}(V_0 - V_{\text{sat}}), \quad (2-3)$$

where V_0 is the forward bias at which the photocurrent is equal to zero, A is the device area (0.094 cm^2), L is the thickness of the active layer, V_{sat} is the reverse bias at which the photocurrent saturates (-3 V), and C_{sat} is the internal capacitance, which is determined by the difference of the corrected capacitance in the dark and under illumination at V_{sat} .^[66,119,120] The obtained charge carrier density at V_{OC} under 100 mW cm^{-2} illumination in devices using green solvent processing show a higher value ($n = 5.9 \times 10^{16} \text{ cm}^{-3}$) than that of the corresponding reference devices ($n = 1.2 \times 10^{16} \text{ cm}^{-3}$). To further understand the device performance, the effective mobility μ_{eff} under 100 mW cm^{-2} illumination (Figure S14) is calculated with the following equation.

$$\mu_{\text{eff}}(n, V_{\text{cor}}) = \frac{J(V)L}{2qn(V)[V_{\text{oc}} - V_{\text{cor}}]}, \quad (2-4)$$

where V_{cor} is the corrected voltage considering the voltage drop over the series resistance ($V_{\text{cor}} = V_{\text{applied}} - J(V)R_{\text{series}}$), and $J(V)$ is the current density obtained from the J - V curves. With the effective mobilities, the devices prepared from o-XY have a significantly higher value ($\mu_{\text{eff}} = 2.16 \times 10^{-3} \text{ cm}^2 \text{ V}^{-1} \text{ s}^{-1}$) in comparison to their counterparts prepared from CB ($\mu_{\text{eff}} = 4.45 \times 10^{-4} \text{ cm}^2 \text{ V}^{-1} \text{ s}^{-1}$).

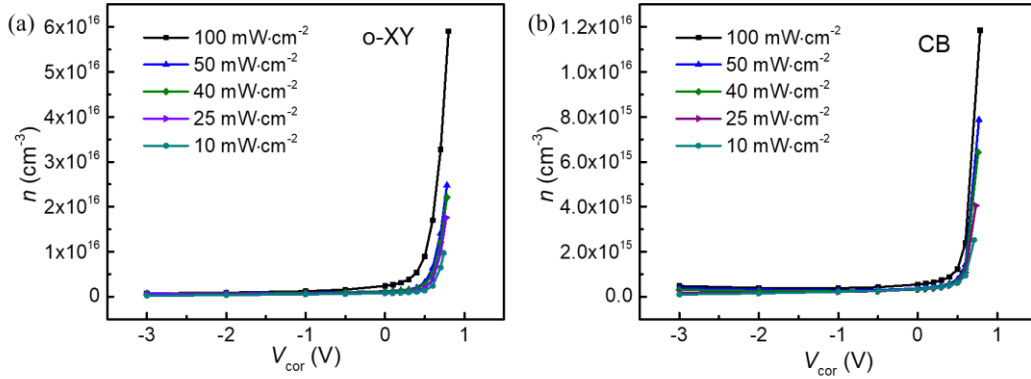


Figure 2-5. The voltage-dependent charge carrier density of PPDT2FBT:PC₆₁BM devices processed from (a) o-XY and (b) CB under different illumination intensities.

To further yield quantitative results for the recombination dynamics, we model the recombination current density J_{rec} using the charge carrier density n and compare the model to the experimental values of the recombination current density J_{rec} obtained from J - V curves.^[4,111,121,122] Details of this modeling can be found in the Appendix.

The Langevin coefficient ζ , the density of deep traps in the bulk $N_{\text{t,b}}$, and the density of surface traps $N_{\text{t,s}}$ are used as fitting parameters to compare the calculated $J_{\text{rec,sum}}$ over five different intensities with the experimental results. The fitted $J_{\text{rec,sum}}$ is in good agreement with the experimental recombination current density J_{rec} for all tested illumination intensities without having to individually adjust the fitting parameters for each intensity (for green solvent cast devices: $\zeta = 0.0278$, $N_{\text{t,b}} = 9.26 \times 10^{12} \text{ cm}^{-3}$; For CB cast devices: $\zeta = 0.0061$, $N_{\text{t,b}} = 2.81 \times 10^{14} \text{ cm}^{-3}$; for both systems, $N_{\text{t,s}}$ is smaller than 10^9 cm^{-2} , which is negligible in the fitting). Moreover, the respective recombination coefficients are further calculated with the fitted trap densities. Both blends show similar bimolecular recombination coefficients ranging

from $k_{bm} = (2.58-6.59) \times 10^{-12} \text{ cm}^3 \text{ s}^{-1}$ and bulk-trap assisted recombination coefficients ranging from $k_{bulk} = (1.10-6.56) \times 10^4 \text{ s}^{-1}$ across the voltage range from -2 V to V_{OC} . Furthermore, the recombination dynamics discussed above can also be verified by fitting the light intensity dependent behavior of the V_{OC} , which is already introduced in the scope of **Figure 2-4b**. In essence, the relevant recombination parameters that have been determined above can be gauged via the experimental V_{OC} at different light intensities and a reasonable correspondence between the experimental and fitted V_{OC} can be observed; a detailed description can be found in the SI (Figure S17). As the recombination coefficients between the blends are quite similar, this alone cannot explain the device performance differences. Therefore, we further quantify the average extraction time of charge carriers (τ_{ex}), as shown in **Figure 2-6a**, to obtain a comprehensive understanding of the charge carrier dynamics using the following equation:

$$\tau_{ex} = \frac{qLn(V)}{J(V)}. \quad (2-5)$$

The o-XY processed devices have a much faster average extraction time $\tau_{ex} = 0.09-0.74 \mu\text{s}$ from -2 V to V_{OC} , compared with the devices processed from CB ($\tau_{ex} = 0.26-5.6 \mu\text{s}$), which is consistent with the higher effective mobility. Meanwhile, the charge recombination lifetime (τ_{rec}) can be further described by the following equation:

$$\tau_{rec} = \tau_{bm} + \tau_{bulk} = \frac{n}{k_{bm}n^2} + \frac{n}{k_{bulk}n} = \frac{1}{k_{bm}n} + \frac{1}{k_{bulk}}. \quad (2-6)$$

The devices prepared from o-XY have a longer charge recombination lifetime ($\tau_{rec} = 32-236 \mu\text{s}$) over the measured voltage range, compared with the devices prepared from CB (τ_{rec}

= 4.2-4.5 μ s), which is another factor contributing to the improved charge carrier collection observed in the o-XY cast device. Furthermore, the voltage-dependent competition factors ($\theta = \frac{\tau_{ex}}{\tau_{rec}}$) are plotted in **Figure 2-6b** to directly compare the relative contributions of the competing non-geminate recombination and extraction processes. In general, smaller competition factors have been shown to indicate reduced non-geminate recombination losses and they correlate with higher FF and J_{SC} values.^[4,123] The devices prepared from o-XY show values of $\theta = 0.023-4.1 \times 10^{-4}$, while the devices prepared from CB show significantly larger values ($\theta = 0.057-1.34$). The small voltage-dependent competition factors in the green-solvent-processed devices are a result of the appropriate combination of long charge carrier lifetimes and fast charge carrier extraction, which ultimately explains the higher PCEs of the studied green-solvent-processed solar cells.^[4,21,124]

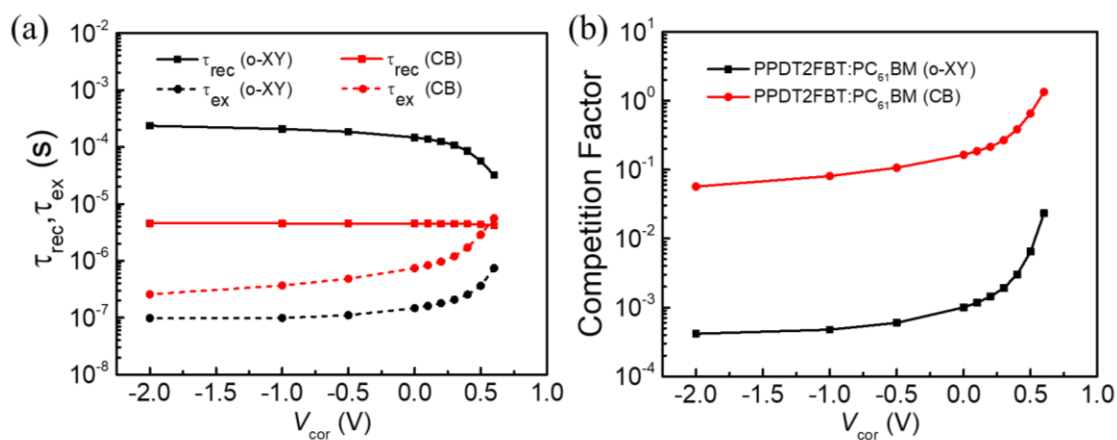


Figure 2-6. (a) Charge carrier lifetime τ_{rec} and extraction time τ_{ex} , and (b) voltage-dependent competition factor θ of the investigated devices.

Based on our study, donors and acceptors with comparable good solubility in green solvent,

and the corresponding film cast from green solvent shows a well-maintained, or even improvement of the favorable BHJ morphology can be suitable for green solvent processing.

2.5 Conclusions

In summary, we investigate differences in the BHJ morphology and the subsequent changes of the optoelectronic properties of PPDT2FBT:PC₆₁BM systems processed from traditional (CB) and green (o-XY) solvents. Comparable good solubility of PPDT2FBT and PC₆₁BM in green solvent, and the corresponding film cast from green solvent with a well-maintained molecular ordering, and even improvement of the favorable BHJ morphology can be suitable for green solvent processing. The characterization of the BHJs at different length scales using AFM, GIWAXS, and RSoXS techniques indicate the presence of a well-mixed phase morphology with increased D:A interfacial areas and smaller domain sizes for the o-XY processed blend. 2D ssNMR spectroscopy results reveal that the PC₆₁BM molecules are intercalated into the sidechain regions of the donor polymers, in particular, the green-solvent-processed BHJ morphology exhibits specific 2D correlations that favor better intermixing and orientation of PC₆₁BM molecules in the vicinity of the PPDT2FBT aromatic core. These features of molecular packing facilitate the charge generation efficiency and transport in the green-solvent-processed devices. Hence, the optimized PPDT2FBT:PC₆₁BM devices processed with o-XY solvent exhibit a higher charge mobility, a faster charge extraction, and a higher PCE ($9.1 \pm 0.1\%$) compared to the CB cast devices ($7.0\% \pm 0.1\%$). Non-geminate recombination and extraction dynamics are determined by employing a quantitative analytical model based on capacitance spectroscopy. A higher charge carrier density and effective mobility are observed in the solar cells prepared from o-XY. As a result, smaller competition

factors stemming from slow non-geminate recombination and fast charge extraction are shown over the studied voltage range (-2 V to V_{OC}) for the green-solvent-processed devices, which correlates well with their higher J_{SC} and FF values. Ultimately, this work demonstrates that it is possible to obtain high PCEs for devices processed from green solvent, which are expected to pave the way towards cleaner commercialization and industrial-scale fabrication of OSCs.

2.6 Experimental methods

Material synthesis. The PPDT2FBT polymer was synthesized by direct (hetero)arylation polymerization (DHAP) according to previously recorded biphasic conditions.^[87,125] In a 20 mL microwave vial, 211.0 mg (0.296 mmol, 1 eq) of 1,4-dibromo-2,5-bis[(2-hexyldecyl)oxy]-benzene, 99.5 mg (0.296 mmol, 1 eq) of 5,6-difluoro-4,7-di-2-thienyl-2,1,3-benzothiadiazole, 2.6 mg (0.0118 mmol, 0.04 eq) of $Pd(OAc)_2$, 16.6 mg (0.0472 mmol, 0.16 eq) of $P(o-OMePh)_3$, 1.635 g (11.8 mmol, 40 eq) of K_2CO_3 and 30.2 mg (0.296 mmol, 1 eq) of pivalic acid are added. The vial is then purged under vacuum and filled with argon. Degassed water (1.5 mL, [0.2]) and degassed toluene (1.5 mL, [0.2]) are then added to the mixture and the vial is sealed. The reaction is stirred for 15 minutes at room temperature, then heated at 100 °C for 20 h with vigorous stirring. The reaction is then cooled down to 70 °C and the resulting polymer is diluted with 10 mL of xylene. The polymer solution mixture is stirred for 10 minutes and precipitated in a 10% HCl:methanol (1:9) solution. The precipitate is filtered through a 0.45 μ m nylon filter and washed on a Soxhlet apparatus with methanol and hexanes, then extracted by chloroform. The polymer solution is reduced to 20–30 mL and poured into methanol prior to filtration with a 0.45 μ m nylon filter. The polymer is solubilized

in toluene and washed at reflux overnight in a sodium diethyldithiocarbamate trihydrate scavenger solution to remove the catalytic residues. The organic phase is washed 5 times with boiling nanopore water to remove the remaining salts. The organic phase is reduced, poured into methanol, and filtered, as previously mentioned. The polymer is vacuum-dried to yield a purple solid. (Yield 79%) $M_n=39 \text{ kg mol}^{-1}$; $M_w=82 \text{ kg mol}^{-1}$; $D=2.1$; λ_{max} absorption=648 nm. Size exclusion chromatography measurements were performed using a Varian Instrument PL120 with a Styrene-DVB gel column. The eluent was 1, 2, 4-trichlorobenzene (TCB), heated at 110°C. The calibration was performed using a monodisperse polystyrene standard.

Fabrication and characterization of organic solar cell devices. All the devices were fabricated in an inverted structure of indium tin oxide (ITO)/zinc oxide (ZnO)/PPDT2FBT:PC₆₁BM/MoO₃/Ag. Photovoltaic devices were fabricated according to the following procedures. ITO substrates (purchased from Thin Film Devices, Inc.) were cleaned by detergent, then sequentially ultrasonicated in DI water, acetone and isopropanol for 30 min. Tetrahydrofuran (THF) and diethyl zinc were mixed in a volume ratio of 5:1 and spin-coated on the clean ITO substrates at 4000 rpm for 30s, followed by 15 min annealing at 150 °C to make the ZnO film. Solutions (total concentration of 40 mg/mL) of PPDT2FBT:PC₆₁BM in a 1:1.5 weight ratio were prepared in either CB with 1 vol% DIO processing additive or o-XY, which was stirred and kept at elevated temperatures (CB at 60 °C, o-XY at 80 °C) over night. Prior to spin casting, 1 vol% p-anisaldehyde (AA, 98%) was added as the solvent additive to the stock o-XY solution and the solution was heated up to 110°C. On the top of the ZnO layer, the hot blend solution was spin-coated (CB: 1100 rpm, o-XY: 1400 rpm, 60 s) to form active layers, of which the thickness was measured by an Ambios XP-100 stylus profilometer. The

MoO₃/Ag (7 nm/120 nm) electrode with an active area of 0.094 cm² was then deposited on top of the active layer by thermal evaporation in high vacuum (<10⁶ torr).

Device measurements. All the photovoltaic and electrical measurements were conducted inside a glovebox under nitrogen atmosphere. Photovoltaic characteristics were measured with a high-quality optical fiber to guide the light from the solar simulator equipped with a Keithley 2635A source measurement unit. *J-V* curves were measured under AM 1.5G illumination (100 mW·cm⁻²). Neutral filters were applied to reach lower light intensities (10, 25, 40, 50 mW·cm⁻²). EQE measurements were conducted with an EQE system, in which the monochromatic light intensity was calibrated using a Si photodiode. The spectral distributions of the real and imaginary components of the impedance of all devices were measured by an impedance analyzer (Solartron SI 1260A) in the dark and under different illumination intensities. To prevent the effect of the AC signal on the impedance during the measurement, a small amplitude AC signal (40 mV) was applied.

Topographic Characterization. All topographic measurements were obtained using an Asylum MFP-3D operating in closed loop mode mounted atop an Olympus inverted optical microscope under an inert atmosphere. Furthermore, n+ diamond coated silicon AFM tips with a resonant frequency of ~20 kHz and a force constant of ~0.5 N m⁻¹ were used (NanoSensors). All images were obtained at a force of 2 nN. First order image flattening was performed on the morphology images and the measured morphology heights were offset to set the scale start point to 0 nm using Asylum Research AFM software version 14, programmed with IGOR Pro.

GIWAXS. All GIWAXS measurements were performed at the Advanced Light Source at Lawrence Berkeley National Lab on the 7.3.3 beamline. The sample was scanned

with an incidence angle of 0.12° and a photon energy of 10 keV ($\lambda = 1.24 \text{ \AA}$), while under a helium environment to minimize beam damage and reduce air scattering. The width of the incident X-ray beam is about 1 mm, and silver behenate was used to calibrate the lengths in the reciprocal space. A 2D detector (PILATUS 2 M from Dectris) with a sample-to-detector distance of 276.9 mm was used to collect the images. The Nika software package for Igor (by Wavemetrics) and the Igor script WAXStools were used to process the figures.^[126,127]

RSoXS. All RSoXS measurements were performed at the Advanced Light Source at Lawrence Berkeley National Lab on the 11.0.1 beamline following the previously established protocols.²⁵ The samples were performed in a transmission geometry with linearly polarized photons under high vacuum (1×10^{-7} torr) and two-dimensional scattering patterns were collected on a cooled ($-45 \text{ }^\circ\text{C}$) CCD with PS300 used for geometry calibration. The Nika software package for Igor (by Wavemetrics) were used for data processing.^[126,127]

Solid-state NMR spectroscopy. Spin-coated PPDT2FBT and PC₆₁BM neat materials and PPDT2FBT:PC₆₁BM blends processed from CB and o-XY solvents were scratched off from the glass substrates and packed into either 1.3 mm (outer diameter) zirconia rotors fitted with Vespel[®] caps. All fast MAS (50 kHz) 1D ¹H, ¹³C, and 2D ¹H-¹³C NMR experiments were carried out on a Bruker Avance Neo (18.8 T, Larmor frequencies of ¹H and ¹³C were 800.1 MHz and 201.2 MHz, respectively) spectrometer with 1.3 mm H-X probehead. Single-pulse ¹H MAS NMR experiments were carried out by co-adding 32 transients. ¹H relaxation delays were of 2 s for the neat PPDT2FBT material and 5 s and PPDT2FBT:PC₆₁BM blends processed from CB and o-XY, respectively. In the case of PC₆₁BM acceptor molecules processed from CB and o-XY, the ¹H relaxation delays were of 6 s and 30 s, as determined from saturation recovery measurements and analyses. All 1D ¹³C{¹H} cross polarization (CP)-

MAS experiments of neat materials and blends were carried out by co-adding 2048 transients. 2D ^1H - ^1H double-quantum – single-quantum (DQ-SQ) spectra of neat compounds and PPDT2FBT:PC₆₁BM blends were acquired using a one rotor period Back-to-Back (BaBa) sequence.^[128,129] 2D ^1H - ^1H DQ-SQ spectra of PPDT2FBT neat materials and PPDT2FBT:PC₆₁BM blends were acquired using 200 t_1 increments, each by co-adding 16 transients, using the States method to achieve sign discrimination in the vertical indirect dimension with a rotor-synchronized t_1 increment of 40 μs corresponds to two rotor periods $2\tau_r$. 2D ^1H - ^1H DQ-SQ spectra of PC₆₁BM materials processed from CB and o-XY were acquired using 80 t_1 increments, each by co-adding 16 transients. The ^1H -detected 2D ^1H - ^{13}C HETCOR spectra were acquired with 160 t_1 increments, each by co-adding 32 transients in PC₆₁BM, 64 transients in PPDT2FBT and 80 transients in the case of blends. The ^1H and ^{13}C experimental shifts were calibrated with respect to neat TMS using adamantane as an external reference (higher ppm ^{13}C resonance, 35.8 ppm, and the ^1H resonance, 1.8 ppm).

Chapter 3: Organic Solar Cells Processed from 2-MeTHF Approaching 15% Efficiency

3.1 Introduction

Solution-processed BHJ organic solar cells (OSCs) has attracted considerable research attention and achieved rapid development benefiting from their highly tunable property of the materials and great potential as a candidate of clean energy resources.^[51,71,121,123,124] Recently, single junction OSC systems with remarkable improvement in their power conversion efficiencies (PCEs) of over 19% has been recently achieved.^[27] However, solvent selection is

becoming an unavoidable problem in the procedure of transferring the optimized lab-scale casting to large-scale industrial device fabrication. High-performance OSCs are commonly processed with traditional solvents with halogenated atoms due to their good solubility of organic semiconductor materials. For example, chloroform and chlorobenzene are widely chosen as casting solvents in lab scale despite being considered highly hazardous to both human health and the environment, which limits the potential large-scale fabrication of OSCs. Therefore, there is a strong need for environmentally friendly solvents casting OSCs with reasonable high PCEs by the community, and eco-friendly solvents generated from renewable agriculture resources could be the best candidates for the processing of the BHJ active layers.^[28] In particular, 2-MeTHF is a green solvent that can be obtained from renewable agricultural feedstock and is widely employed in organic synthesis in industry.^[130,131] Additionally, it has the benefit of being environmentally friendly, with lower toxicity levels compared to halogenated and aromatic solvents such as chlorobenzene and chloroform, making it an appealing choice for replacing these solvents in the fabrication of organic electronic devices.^[6] To achieve comparable high PCE as OSCs cast from traditional solvents such as CF and CB, we designed a series donor and acceptor blends based on PM7-series polymer donors and Y-series NFAs.^[6,132] The optimized PM7-D5:PTI04 device processing with 2-MeTHF as the host solvent shows a high PCE of 14.9%, which is comparable with PM6:Y6 reference system cast from CF. Insight into the BHJ morphology reveals that a favorable sized domain, uniform donor and acceptor distribution, and better intermixing in the active layer of blended PM7-D5:PTI04 system led to relatively high effective mobility for charge carriers and suppress the charge recombination both in the bulk and at the surface between different layers.

3.2 Design, optimization, and characterization of PM7-Dx:Y-series NFAs

device

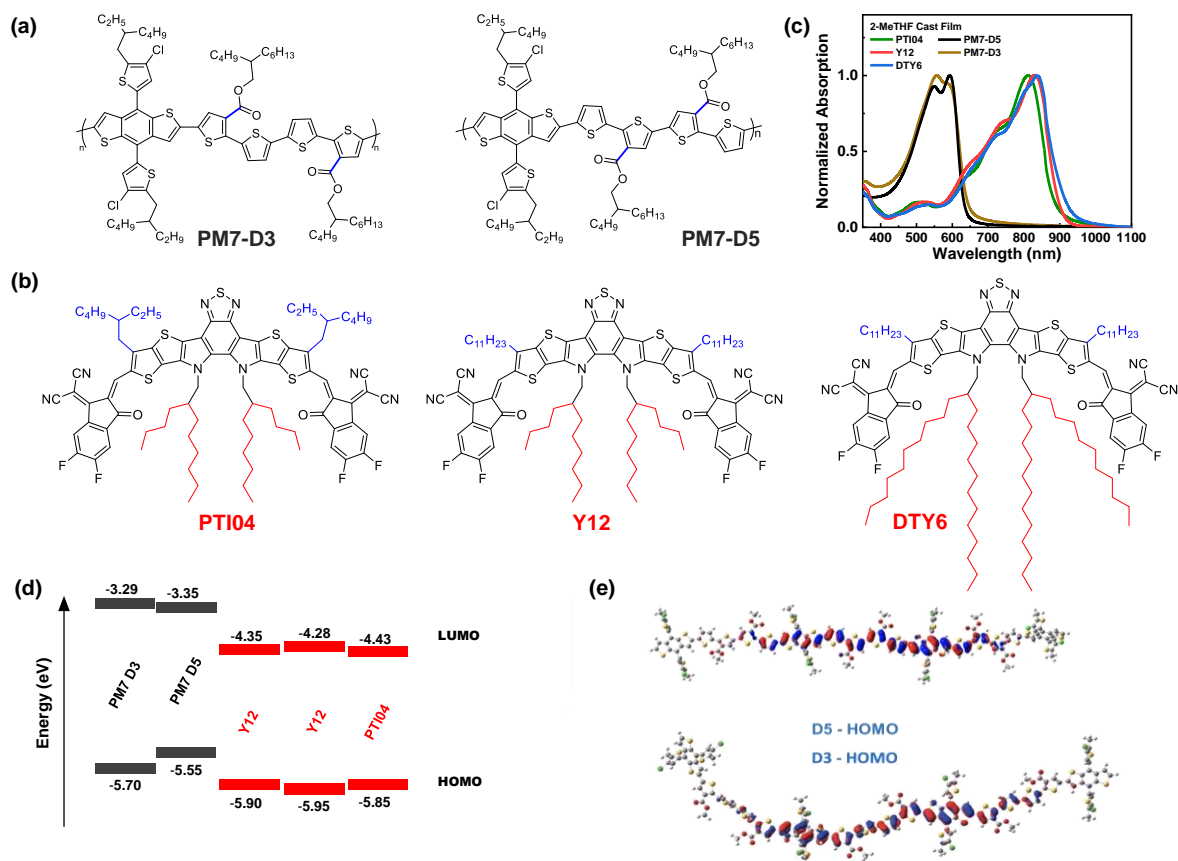


Figure 3-1. Chemical structures of (a) PM7-D3 and PM7-D5, and (b) PTI04, Y12, and DTY6. (c) Normalized absorption of pristine films processed from 2-MeTHF. (d) Energy level diagram. (e) DFT simulation of PM7-D3 and PM7-D5.

The chemical structures of polymer donors (PM7-D3, PM7-D5) and Y-series NFAs (Y12, DTY6, and PTI04) are shown in **Figure 3-1a** and **1b**. The synthetic route to prepare PM7-D3 and PTI04 can be found in the Experiment Methods (**Figure 3-5** and **3-6**), and the NMR spectra for all monomers and molecular precursors can be found in the Appendix (Figure S20-S28). The normalized UV-vis absorption spectrum of pristine films processed from 2-MeTHF

and the energy level diagram are shown in **Figure 3-1c** and **1d**. Considering the only difference between those NFAs occurs on their sidechains, either length difference in the middle or branched structure on the edge, similar energy levels and bandgap are observed. Given the slight variance in the HOMO level of the NFAs, it is possible to enhance the Voc of the OPV device by utilizing PM7-D3 with a lower LUMO level as compared to PM7-D5, presuming equivalent voltage loss. Furthermore, the interchain interactions of PM7-D3 and PM7-D5 can facilitate controlled aggregation properties of the BHJ blend. However, the degree of assembly of the donor polymer or acceptor component can be influenced by the aggregation tendency of the other component in the blend. For instance, when an aggregative polymer is blended with a NFA, the delayed solidification of the donor polymer results in a less favorable final morphology of the blend.^[133] Thus, improving the backbone packing capability is expected to allow a desirable morphology in the BHJ blend. The balance between a fused ring component (benzodithiophene part) and non-fused ring (diester quarterthiophene part) units in the structure of PM7-D3 and PM7-D5, together with branched butyl octyl side chains off of the ester functionalities, enables solubility in a wide range of organic solvents, most importantly non-halogenated solvents such as o-XY and 2-MeTHF. PM7-D5 shows a useful solubility of above 7 mg/mL and PM7-D3 shows above 10 mg/mL in 2-MeTHF. When comparing PM7-D3 with PM7-D5, the position change of the diester quarterthiophene building block to the backbone allows the polymer to have a twisted backbone other than a planarized backbone which is further supported by the DFT calculation based on five monomer units (**Figure 3-1e**). More freedom in the configuration of PM7-D3 benefiting from the twisted backbone can further improve the solubility of the polymer donor in green solvents. It is worth noting that all three NFAs based on Y12 exhibit excellent eco-friendly solvent-

processing capabilities, displaying high solubility in 2-MeTHF (> 10 mg/mL) due to the modified long-length branched chains or branched side chains. Consequently, the combination of PM7-D3 and PM7:D5 blended with Y12, DTY6, and PTI04 as the active layers offers the potential to develop a highly efficient OPV system processed using the environmentally sustainable solvent 2-MeTHF.

To get a deep understanding of green solvent processing on the OPV device performance, photophysical properties of solar cells fabricated with the inverted device architecture of ITO/PEDOT:PSS/PM7-Dx:Y-series NFAs/PNDIT-F3N-Br/Ag are optimized, analyzed and compared. For the purpose of generating a uniform and well-mixed BHJ active layer, we increase the casting temperature to 70 °C for 2-MeTHF as the host solvent to reach a relatively fast drying speed of the thin films during spin coating.^[63] It is worth mentioning that no solvent additive has been further added during the device fabrication to further reduce the health and environmental hazards of common chlorinated additives, such as DIO and 1-chloronaphthalene (1-CN).^[97,134] The current density-voltage (J - V) characteristics of the optimized solar cells processed from 2-MeTHF are shown in **Figure 3-2a** and **Table 2**. Among the four combinations generated from systematically changing of the polymer donors and the NFAs, we observe a best PCE of 14.9% for the PM7-D3:PTI04 device directly processing with 2-MeTHF. On average, a relatively high FF (0.69) and J_{sc} (23.88 mA cm⁻²), which is further confirmed from the integration of EQE signal shown in **Figure 3-2b** together led to the high PCE of this system. To gain a deeper comprehension of the charge collection efficiency in the operational device, the efficiency of exciton dissociation and free charge carrier collection is evaluated by calculating the voltage-dependent charge collection

probability (P_c) using the following equation:

$$P_c = \frac{J_{ph}}{J_{ph,sat}}, \quad (2-7)$$

where photocurrent density (J_{ph}) of the device is the difference between the current density under illumination and in the dark,^[21,135] and $J_{ph,sat}$ is the saturated photocurrent density under -2 V. A high $J_{ph,sat}$ above 20 mA cm^{-2} for all three PM7-D3:NFA blends indicates a fast charge carrier generation rate in all devices. In Figure **3-2c**, the P_c is plotted against the effective voltage ($V_{eff} = V_0 - V_{cor}$), where V_0 is the voltage at which J_{ph} equals to 0, and the corrected voltage ($V_{cor} = V_{app} - JR_s$) is obtained by taking into account the voltage losses due to series resistance (R_s). Under the short-circuit condition, the 2-MeTHF cast PM7-D3:PTI04 device shows $P_c = 0.994$, which is the highest compared with that of other three systems. In other words, PM7-D3:PTI04 device has an efficient charge collection process without the assistance for charge extraction of external electric field.

Table 2. Photovoltaic parameters of studied PM7-Dx:Y-series OPVs measured under AM1.5 illumination at 100 mW cm^{-2} . Average PCE values are obtained from 10 separate devices.

Solvent	D:A	J_{SC} (mA cm ⁻²)	V_{OC} (V)	FF	PCE_{avg} (%)
2-MeTHF	PM7-D3:PTI04	23.88 ± 0.12	0.90 ± 0.01	0.69 ± 0.01	14.91 ± 0.25
	PM7-D3:Y12	23.76 ± 0.61	0.86 ± 0.01	0.54 ± 0.02	11.06 ± 0.49
	PM7-D3:DTY6	20.29 ± 0.37	0.86 ± 0.01	0.65 ± 0.02	11.28 ± 0.35
	PM7-D5:PTI04	17.17 ± 0.51	0.87 ± 0.01	0.64 ± 0.02	9.61 ± 0.45

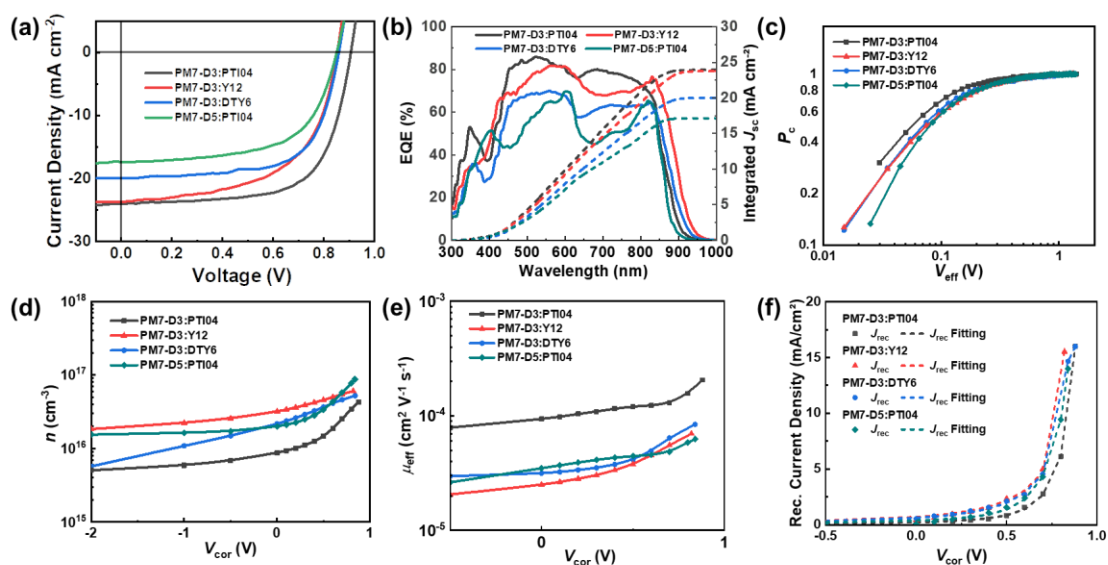


Figure 3-2. (a) J - V characteristics, (b) EQE spectra, (c) charge collection probability, (d) voltage-dependent charge carrier density, (e) voltage-dependent effectivity mobility, and (f) the fitting of recombination current density of 2-MeTHF processed OPVs composed of PM7-D3:PTI04, PM7-D3:Y12, PM7-D3:DTY6, and PM7-D5:PTI04 under AM 1.5G illumination at 100 mW cm⁻².

3.3 Charge dynamic and physical modeling of PM7-Dx:Y-series NFAs devices

In order to gain quantitative insights into the recombination dynamics and charge carrier mobility, voltage-dependent impedance spectroscopy is utilized to determine the charge carrier density in the active layer under varying operational biases and light intensities.^[52,63,66,111] To maintain the steady-state properties of the system during measurement under different illumination, DC bias in a range from -2 V to V_{oc} , and a small AC signal (40 mV) is applied during the scanning. To account for the impact of the device's series resistance and the parasitic inductance of the connecting cables, the measured capacitance of the BHJ layer is corrected and can be represented using the following Equation 3-1.

$$C_{cor} = -\frac{1}{\omega} \left[\frac{Z'' - \omega L'}{(Z' - R_s)^2 + (Z'' - \omega L')^2} \right], \quad (3-1)$$

Here, L' is the inductance of the connecting cables, $\omega = 2\pi\nu$ is the angular frequency of the AC signal, and Z' as well as Z'' are the real and imaginary components of impedance, respectively. In the dark, the corrected capacitance measured under a large reverse bias (-2 V) shows a horizontal line, which is equivalent to a frequency independent capacitance. From this, we can determine the geometrical capacitance (C_g) of the active layer. Voltage-dependent impedance spectroscopy is performed to yield the charge carrier density n (**Figure 5**), via integration of the chemical capacitance C_{chem} using the following equations.

$$n(V_{cor}) = n_{sat} + \frac{1}{qAL} \int_{V_{sat}}^{V_{cor}} C_{chem} dV_{cor}, \quad (3-2)$$

$$n_{sat} = \frac{1}{qAL} C_{sat}(V_0 - V_{sat}), \quad (3-3)$$

where V_0 is the forward bias at which the photocurrent is equal to zero, A is the device area (0.094 cm^2), L is the thickness of the active layer, V_{sat} is the reverse bias at which the photocurrent saturates (-2 V), and C_{sat} is the internal capacitance, which is determined by the difference of the corrected capacitance in the dark and under illumination at V_{sat} .^{31,66,67} The obtained charge carrier density from -2 V to close to V_{oc} range under 100 mW cm^{-2} illumination in PM7-D3:PTI04 devices show an overall lower value ($n < 1.6 \times 10^{16} \text{ cm}^{-3}$) than that other devices ($n > 2.5 \times 10^{16} \text{ cm}^{-3}$), while the effective mobility μ_{eff} ($1.1 \times 10^{-4} \text{ cm}^2 \text{ V}^{-1} \text{ s}^{-1}$) is about one order of magnitude higher than other devices ($< 3.5 \times 10^{-5} \text{ cm}^2 \text{ V}^{-1}$) calculated with the following equation.

$$\mu_{\text{eff}}(n, V_{\text{cor}}) = \frac{J(V)L}{2qn(V)[V_{\text{oc}} - V_{\text{cor}}]}, \quad (3-4)$$

where V_{cor} is the corrected voltage considering the voltage drop over the series resistance, and $J(V)$ is the current density obtained from the J - V curves. Faster charge carrier mobilities in the PM7-D3:PTI04 system benefits the charge transport and collection process, leading to a small remaining of free charge carriers in the BHJ layer, which agrees with the minimum average $n(V)$ in the same system.

Table 3. Summary of the PM7-Dx:Y-Series NFAs OPV device parameters obtained under simulated AM1.5G illumination.

D:A	ξ	$N_{t,bulk}$ (cm ⁻³)	$N_{t,surf}$ (cm ⁻²)	$\tau\mu$ (cm ² V ⁻¹)	L_{dr} (nm)	L_{dr}/d	L_{diff} (nm)	L_{diff}/d
PM7- D3:PTI04	0.035	1.16E+12	6.97E+12	1.17E-09	1044.03	10.44	54.77	0.55
PM7-D3:Y12	0.021	1.56E+13	1.63E+14	8.83E-10	742.37	7.35	47.62	0.47
PM7- D3:DTY6	0.027	7.55E+14	6.68E+13	7.54E-10	661.77	6.75	44.02	0.45
PM7- D3:PTI04	0.028	4.02E+13	1.66E+13	6.64E-10	600.11	6	41.3	0.41

To obtain quantitative insights into the recombination dynamics, we employ a model that relates the recombination current density J_{rec} to the charge carrier density and compare it to experimental values of J_{rec} obtained from J - V curves, which can be achieved by a combination of J - V characteristic (in the dark and under illumination) and voltage-dependent impedance analysis.^[63,111] Detailed model can be found in the Appendix. The density of deep traps in the bulk $N_{t,bulk}$, the density of surface traps $N_{t,surf}$, and the Langevin coefficient ξ are fitting parameters used to calculate and fit the recombination current with the experimental data. A summary of these physical parameters used in the J_{rec} fitting model is shown in **Table 3**. It is worth noticing that the best performance system, PM7-D3:PTI04, has smaller amount of traps existing both in the bulk and at the surface of the OPV device, which could significantly suppress the bulk-trap recombination and the surface trap assisted recombination of charge carriers in the BHJ blend. Meanwhile, benefiting from the fast mobility, the calculated $\tau\mu$ for PM7-D3:PTI04 device exhibits a smallest value, which has been shown to correlate with the high FF in some literature.^[123,136] Next, the drift length (L_{dr}) and diffusion length (L_{diff}) of the BHJ active layers are calculated based on $n(V)$ and μ_{eff} , which are further normalized by the

thickness of the film. Considering the relatively long L_{dr} (all above 600 nm) compared with the average thickness of the active layers (~ 100 nm), longer normalized L_{diff} in PM7-D3:PTI04 system makes a difference when the internal electric field is small. In other words, the drift length at J_{SC} is much greater than the thickness of the active layer. However, the effective diffusion length is smaller than the active layer thickness, which can result in significant losses in carrier extraction when drift is not efficient.^[136] Charge transport and collection process will be mainly controlled by the diffusion process and benefits from the long L_{diff} in the PM7-D3:PTI04 system when getting close to V_{mp} and V_{oc} condition, which ultimately explains the higher PCE of the PM7-D3:PTI04 solar cells among the studied four systems.

3.4 Characterization of 2-MeTHF processing BHJ active layer

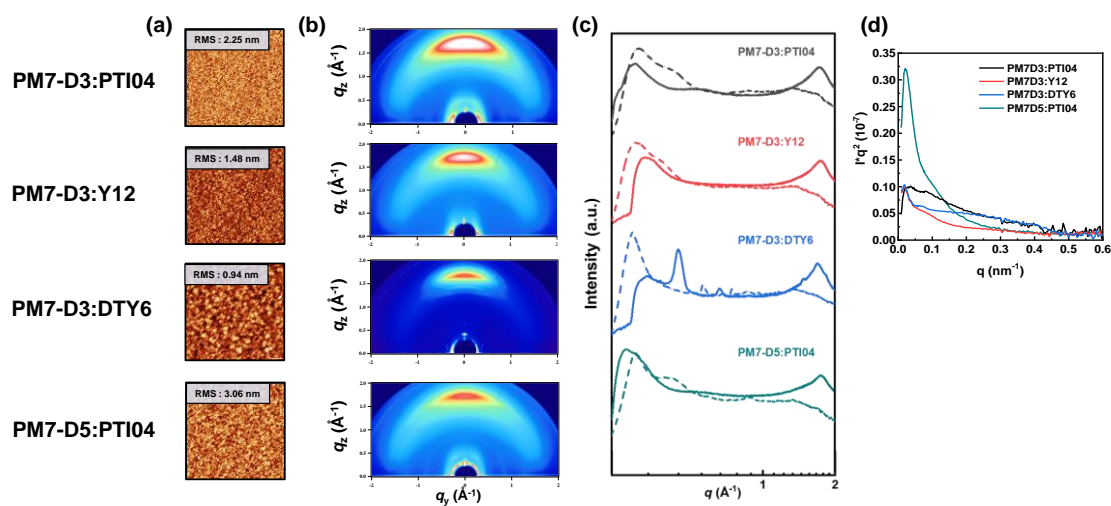


Figure 3-3. (a) 5 μm * 5 μm AFM topography images, (b) 2D GIWAXS patterns, (c) the corresponding in-plane (dash lines) and out-of-plane (solid lines) GIWAXS profiles, and (d) RSoXS profiles for the corresponding BHJ films processed from 2-MeTHF.

The photoelectric properties of OPVs, which govern by the processes of charge generation, transportation, and extraction, are closely linked to the morphology of the active layer and the structural arrangement of the donor-acceptor in the solid-state thin films.^[113,134] To gain detailed insights into the impact of side-chain length and position on the device performance of designed four OPV systems processed from 2-MeTHF, the BHJ morphologies were further characterized with techniques at different length scales (μm to sub-nm).^[4] First, Atomic Force Microscopy (AFM) is employed to analyze the topography of PM7-D3:PTI04, PM7-D3:Y12, PM7-D3:DTY6, and PM7-D3:PTI04 blends under optimized conditions. As shown in **Figure 3a**, under a resolution of 2 μm \times 2 μm , all BHJ blends reveal relatively smooth surfaces with a maximum RMS value of 3.06 nm in nanoscale with continuous networks. GIWAXS analysis indicates that all four systems have a similar pi-pi stacking distance of 0.37 nm in the out-of-planar direction. This result indicates that charge transport can take place in both the in-plane and out-of-plane directions in the photoactive layers, and the side chain engineering of the polymer donor and NFAs does not have an adverse impact on the long-range ordering of molecular packing in the active layer. However, additional peaks are observed for PM7-D3:DTY6 thin film in the in-planar direction located at 0.29, 0.57, and 0.75 nm compared with other systems, which indicates more unpreferred disorder existing in this blend due to the long-branched alkyl chains (2-decyltetradecyl, 2-DT) on the TPBT (dithienothiophen[3.2-b]-pyrrolobenzothiadiazole) central unit of DTY6. To further gain detailed

information in the domain spacing and relative degrees of phase purity, RSoXS measurement was further conducted to all four studied systems.^[74,94] The result indicated that PM7-D3:PTI04 system contains the highest volume fraction (69%) of domains with a preferred average size (26 nm). Considering the exciton diffusion length is ~20 nm in typical organic solar cells, the larger domains above 100 nm in other systems are detrimental for electron transport. The increase in the J_{SC} is in agreement with the morphology results discussed above, in which smaller domain sizes and higher D:A interfacial areas observed in PM7-D3:PTI04 blends could lead to better charge generation and efficient charge collection.

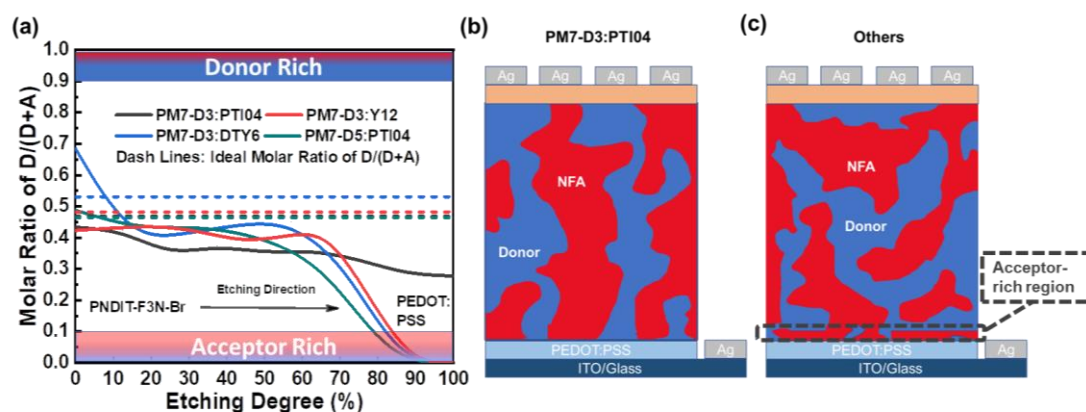


Figure 3-4. (a) D/(A+D) molar ratio of PM7-D3:PTI04, PM7-D3:Y12, PM7-D3:DTY6, and PM7-D3:PTI04 BHJ films calculated from the Cl/F ratio of the XPS depth profiles as a function of etching degree (%), where etching begins at the top air/film interface. Dotted lines represent the ideal D/(D+A) molar ratio calculated from the original D:A ratio of 1:1.2 by weight. (b) Schematic of the PM7-D3:PTI04 with more uniform vertical phase separation, and

(c) other three blend films showing vertical phase gradation with an acceptor-rich region near the blend/PEDOT:PSS interface.

Next, the BHJ films were further characterized using depth-profiled X-ray photoelectron spectroscopic (XPS) to investigate how side-chain length and position affect the donor and acceptor distribution and composition in the vertical direction of the active layers.^[137] The distribution of PM7-series donors and Y-series NFAs can be tracked by the chlorine (Cl) signal and the fluorine (F), respectively, considering the fact that Cl is absent in the donors and F is absent in the NFAs. As a result of the different thicknesses of the active layers, the etching time to reach the bottom of the active layer is slightly different for the blends. The ratio of D/(D+A) for each blend was calculated from the representative element ratio of polymers and NFAs. The detailed calculation can be found in the Appendix. As shown in Figure 4a, the gradually decreasing in the D/(A+D) molar ratio assay the vertical phase gradation in all the blend films. Polymers accumulate more at the top blend/air interface, while a small molecule NFAs enriched region can be observed close to the bottom of the BHJ layer. In particular, the PM7-D3:PTI04 blend tends to be more uniform in the vertical phase arrangement with a gradual reduction of the D/(A+D) ratio from 0.43 to 0.27. In the other three blends, a dramatic drop of the donor component occurs after reaching 70% etching degree, and a region of around 10 nm dominated by small NFA molecules exhibits at the bottom of the active layers. Two different schematic diagrams of the vertical gradation trends in the microstructure of the PM7-D3:PTI04 blend and the other three systems are shown in Figures 4b and 4c. A significant number of acceptors accumulated at the bottom of the BHJ layer can have a significantly negative effect on the device performance of PM7-D3:Y12,

PM7-D3:DTY6, and PM7-D3:PTI04 systems. Serious surface-trap-assisted recombination can occur as a result of the enrichment of NFAs functioned as partial hole-blocking regions at the interface between the PEDOT:PSS layer and the active layer. Compared with these blends, a uniform distribution in the vertical phase of the PM7-D3:PTI04 film implies higher miscibility of PM7-D3 and PTI04, which can contribute to reducing the density of traps and suppressing the recombination of charge carriers in the OPV device, especially surface-trap-assisted recombination, and thus lead to a more efficient charge collection process.^[137] These results are not only consistent with the miscibility of the donors and NFAs investigated by RsoXS, but also with the effective mobility measurements and the recombination current fitting discussed above, which further confirm the origin of the surface trap in the studied system. A favorable uniform BHJ layer increases the probability of excitons reaching and dissociating at the polymer and NFA interfaces, promoting higher effective mobility ($\mu_{\text{eff}} = 10^{-4} \text{ cm}^2 \text{ V}^{-1} \text{ s}^{-1}$) and lower trap density (both in the bulk and at the surface) in the PM7-D3:PTI04 system compared with others, thus leading to a high PCE of 14.9%.

3.5 Conclusions

In summary, we have successfully developed a series of 2-MeTHF processing OPV systems based on newly designed bulk heterojunction (BHJ) consisting of PM7-D3/D5 donors and Y-series non-fullerene acceptors with systematically changing in their side chain length and positions. The optimized 2-MeTHF casting device based on PM7-D3:PTI04 exhibits a best PCE of approaching 15%, which is comparable with the well-known PM6:Y6 system processing from traditional halogenated solvents. The corresponding BHJ thin films processed from 2-MeTHF were characterized at different length scales with advanced techniques

including atomic force microscopy (AFM), grazing-incidence wide-angle X-ray scattering (GIWAXS), Resonant soft X-ray scattering (RSoXS), X-ray photoelectron spectroscopy (XPS), and solid-state nuclear magnetic resonance (ssNMR) spectroscopy. A preferred average domain size of around 25 nm with relatively high domain purity and a more uniform distribution of donor and acceptor inter-mixing is observed in the PM7-D3:PTI04 BHJ film, which facilitates the charge generation and collection process while limits the recombination process in the device, leading to a high effective mobility and remarkable performance. This work can provide further insight into the structure-property-morphology relationship for this field toward environmentally friendly and commercially viable high-performance organic solar cells.

3.6 Experimental methods

Material synthesis and characterizations. All starting materials were purchased from a commercial supplier and were used without further purification. Bis stannyl monomer, compound 5, was purchased from SunaTech. Synthesis information of other intermediate molecules and the dibromo monomer (compound 4) are presented in the following.

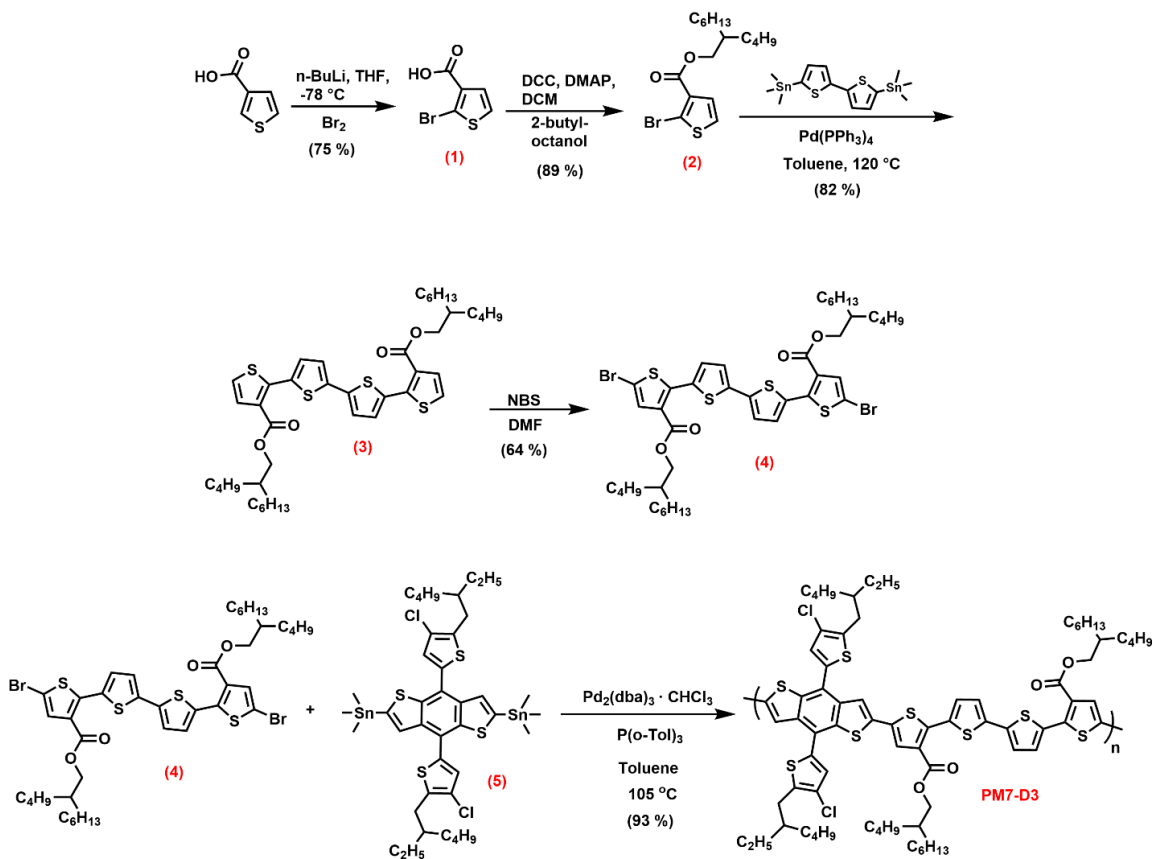


Figure 3-5. Synthetic procedures of PM7-D3.

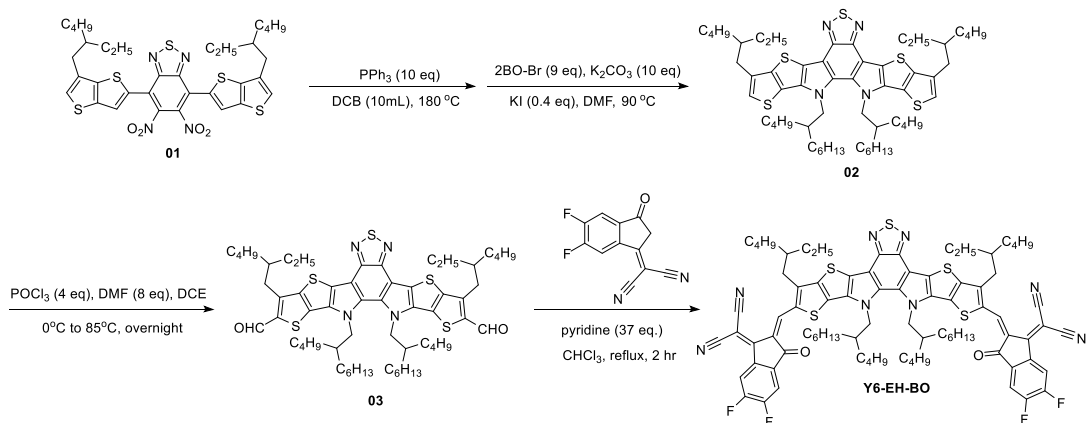


Figure 3-6. Synthetic procedure of Y6-EH-BO (PTI04)

Fabrication and characterization of OPV devices. All the devices were fabricated in a conventional structure of glass/indium tin oxide (ITO)/PEDOT:PSS/active layer/PNDIT-F3N-Br/Ag. OPV devices were fabricated according to the following procedures. ITO substrates (purchased from Thin Film Devices, Inc.) were cleaned by detergent, then sequentially ultrasonicated in DI water, acetone, and isopropanol for 30 min. The substrates were dried using compressed nitrogen and placed in an oven overnight at 100 °C. After cooling down to room temperature, the ITO substrates were treated with UVozone for 15 minutes and a layer of poly(3,4-ethylenedioxythiophene): poly(styrenesulfonate) (PEDOT:PSS, Clevios P VP Al 8043) was spin-coated at 3000 rpm for 60 s onto the ITO substrates. The substrates were then annealed in air at 150 °C for 20 minutes. Solutions (total concentration of 10 mg/mL) of D:A in a 1:1.2 weight ratio were prepared in 2-MeTHF, which was stirred and kept at 40 °C overnight inside a glovebox. Prior to spin casting, the stock solutions and the corresponding substrates were all heated up to 70 °C. On the top of the PEDOT:PSS layer, the hot solution was spin-coated at 1300 rpm to form active layers of approximately 100 nm, of which the thickness was measured by an Ambios XP-100 stylus profilometer. All the films were thermally annealed at 110 °C for 10 minutes. After settling the films to cool to room temperature, 0.5 mg/mL PNDIT-F3N-Br solution dissolved in methanol was spin-coated on top of the active layer as a 5 nm interface layer. The Ag (100 nm) electrode with an active area of 0.05 cm² was then deposited on top of the active layer by thermal evaporation in a high vacuum (<10⁻⁶ torr).

Device measurement. All the photoresponse and electrical measurements were conducted inside a glovebox under a nitrogen atmosphere. *J-V* characteristics were measured with a high-

quality optical fiber to guide the light from the solar simulator equipped with a Keithley 2635A source measurement unit. Illuminated J - V curves were measured under AM 1.5G illumination (100 mW cm^{-2}). Neutral filters were applied to reach lower light intensities (10, 25, 40, 50 $\text{mW}\cdot\text{cm}^{-2}$). EQE measurements were conducted with an EQE system, in which the monochromatic light intensity was calibrated using a commercial Si photodiode (Newport 818-UV). The spectral distributions of the real and imaginary components of the impedance of all devices were measured by an impedance analyzer (Solartron SI 1260A) in the dark and under illumination. To prevent the effect of the AC signal on the impedance during the measurement, a small amplitude AC signal (40 mV) was applied.

Contact Angle Measurement. The static contact angle was measured using the sessile droplet method in a Ramé-Hart goniometer with 0.5 mL drops ($\sim 1 \text{ mm}$) of water or glycerol, dispensed using a syringe pump. The corresponding images were captured with a ThorLabs Zelux camera.

Topographic Characterization. Atomic force images were obtained with an Asylum Research MFP-3D setup with conductive Pt-Ir-coated probes with a resonant frequency of 13 kHz and a force constant of 0.2 N m^{-1} , purchased from Nanoworld. All measurements were carried out under nitrogen in a glove box. AFM images of the electrodes were collected with an Innova AFM setup in tapping mode.

GIWAXS. PLS-II 3C beamline of the Pohang Accelerator Laboratory (PAL) in the Republic of Korea was used to perform the two-dimensional (2D) GIWAXS measurements. 2D-GIWAXS images were collected at 11.57 keV ($\lambda = 1.07156 \text{ \AA}$) with an Eiger 4M detector

(sample-to-detector distance: 414.58 mm). The incidence angle (α_i) of the X-ray beam was set between the critical angles of the thin film and substrate.

RSOXS. All RSoXS measurements were performed at the Advanced Light Source at Lawrence Berkeley National Lab on the 11.0.1 beamline following the previously established protocols.²⁵ The samples were performed in a transmission geometry with linearly polarized photons under high vacuum ($<10^{-7}$ torr) and two-dimensional scattering patterns were collected on a cooled (-45 °C) CCD with PS300 used for geometry calibration. The Nika software package for Igor (by Wavemetrics) were used for data processing.^{73,74}

XPS. All X-ray photoelectron spectroscopy measurements were obtained on using a Kratos Axis Ultra DLD XPS under high vacuum ($<10^{-8}$ Torr) using monochromated X-rays produced using an aluminum source running at a potential of 14 kV. A pass energy of 20 was used for all high-resolution element sweeps. The BHJ samples were prepared with the same procedure as the device fabrication. The films were mounted onto a sample bar using double-sided tape, and electrically grounded to the sample bar using nickel impregnated tape. Data analysis was performed using CasaXPS software licensed to UCSB, and atomic sensitivity factors for each element were taken into account by CasaXPS during the peak integrations.

Chapter 4: 2-MeTHF Casting High-Performance Wearable Organic Photodetectors for Self-Powered Pulse Oximetry and Photoplethysmography

4.1 Introduction

An impressive web of optoelectronic devices is currently utilizing organic photodetectors (OPDs), due to their intriguing photoresponsivity and advantageous characteristics such as lightweight, semi-transparency, flexibility, and bio-compatibility.^[11,138–141] While recent advancements in photo-sensing capabilities of OPDs pave the way towards their integration into flexible electronics as the identification core for autonomous vehicles and wearable medical devices,^[3,12,57,135,142–148] scalability of this technology and large-scale industrial fabrication depends on the ability to process these devices from low-cost and eco-friendly solvents. Therefore, molecular design principles in combination with green solvent processing, advanced characterization and device physics, and understanding interrelationship between them, is expected to be the path forward to develop scalable high-performance OPDs.

Donor-acceptor conjugated polymers and small molecule additives are processed from organic solvents, whereby the choice of solvent is crucially important to achieve optimal bulk heterojunction (BHJ) thin film morphology. Specifically, typical halogenated solvents commonly used in OPD fabrication such as chloroform, chlorobenzene (CB), and *o*-dichlorobenzene are less suitable for pilot-scale device fabrication,^[3,12,135,142–148] due to their well-known negative impact on the environment, eco-system and human health.^[149–151] In

addition, various halogenated solvent additives (e.g., 1,8-diiodooctane (DIO) and 1-chloronaphthalene) have also been used during film casting to form a favorable bulk heterojunction (BHJ) morphology.^[55,152,153] The comparatively high boiling points and slow evaporation speed of these additives indeed slow down film drying process, thus improve the morphology of the BHJ layer at the nanoscale which is crucial for high performance to be achieved.^[97,134] While these additives may help to optimize the BHJ morphology, their complete removal is not practical due to their non-volatile character which may adversely affect the BHJ structure in the long-term. Consequently, there is a great interest in developing high-performance OPDs processed from green solvents without any additives. Currently, there are few studies on green solvent processable OPDs, while new photoresponsive materials have been designed towards stronger photoresponse and wider detective scale. Yen *et al.* designed an OPD based on the P3HT:PCBM system showing a dark current density of 2.90×10^{-8} A cm⁻² and an on/off ratio of 2.90×10^4 , which was processed with the non-halogenated solvent *ortho*-xylene (o-XY).^[154] However, there is still a lack of high-performance OPDs that can be processed by green solvents, such as 2-methyltetrahydrofuran (2-MeTHF), methanol, ethanol, etc. In particular, 2-MeTHF is a biomass-derived (furfural or levulinic acid) and environmentally friendly solvent that is widely used in organic synthesis, which can be produced from low-cost and renewable agriculture feedstock.^[130,131,155,156] Fundamental studies such as film morphology, optical and charge transport properties, device

performance as well as applications of OPDs processed by green solvents remain to be further explored.

In this work, we present high-performing OPDs based PM7-D5 and Y12^[6] processed from 2-MeTHF. PM7-D5 is specifically designed to possess a planar structure and satisfactory solubility in 2-MeTHF as desired for active layer fabrication. The BHJ film morphology is characterized at different length scales from sub-micrometer to sub-nanometers distances using microscopy, X-ray scattering and solid-state NMR spectroscopy techniques. The optimal BHJ morphology can be obtained without solvent additives, yielding high-performance and eco-friendly OPD devices. The PM7-D5:Y12 system processed from 2-MeTHF solvent exhibits optimal BHJ morphology with low dark current density (3.60 nA cm⁻² at -2 V), high external quantum efficiency, and high charge collection probability in comparison to these of the reference devices processed from traditional solvents, CB and o-XY. A combination of these factors leads to a self-powered OPD showing high detectivity over 10¹⁴ Jones and sensitivity of extremely low irradiance below 10⁻¹⁰ W cm⁻² with a fast response (> 80 kHz) over a broad wavelength range (400-900 nm), which demonstrates tremendous potential for practical applications, such as a wearable pulse rate and oximetry sensor, as illustrated in this study.

4.2 Molecular design, green-solvent processing, optical absorption, and energy levels

The chemical structures of PM7-D5 and Y12 are shown in **Figure 4-1a**. The synthetic route to prepare PM7-D5 can be found in the Experiment Methods (**Figure 4-6**), and the NMR

spectra for all monomers and molecular precursors can be found in the Appendix (Figure S29-S41). For PM7-D5, addition of the diester quarterthiophene building block to the backbone allows the polymer to have a planarized backbone while offering rotational freedom due to the non-fused architecture. Ester groups are deliberately designed to point away from each other in the bithiophene core of the quarterthiophene unit, as evidence from the solid-state structures of 2,2'-bithiophenedicarboxylates and dimethyl 2,2'-bithiophene-4,4'-dicarboxylate bearing ester side chains pointed away from each other to minimize the steric hinderance leading to planar structure than its structural isomers dimethyl 2,2'-bithiophene-3,3'-dicarboxylate and dimethyl 2,2'-bithiophene-3,4'-dicarboxylate.^[157] For PM7-D5, the effective interchain interactions can promote controlled aggregation properties of the BHJ blend, though the extent of assembly of one of the components (donor polymer or acceptor) can be altered by the aggregation tendency of the other one in the blend. For instance, in a BHJ blend of an aggregative polymer and a non-fullerene acceptor, a delayed donor polymer solidification was observed and made the final morphology of the blend less favorable.^[133] Thus, improving the backbone packing capability is expected to allow a desirable morphology in the BHJ blend. The balance between a fused ring component (benzodithiophene part) and non-fused ring (diester quarterthiophene part) units in the structure of PM7-D5, together with branched butyl octyl side chains off of the ester functionalities, enables solubility in a wide range of organic solvents, most importantly non-halogenated solvents such as *o*-XY and 2-MeTHF. PM7-D5 shows a useful solubility of above 7 mg/mL in 2-MeTHF, and above 10 mg/mL in *o*-XY and CB. Another factor considered in the design of PM7-D5 is its synthetic scalability. For instance, to compare with a benchmark high-performing donor polymer PM6 in BHJ blends, a chlorinated benzodithiophene unit is used in the PM7-D5, as opposed to

fluorinated homologue used in the synthesis of PM6. Such a strategy reduces the number of synthetic steps needed to prepare the halogenated benzodithiophene unit in PM7-D5 and modified the synthetic pathway using cheaper starting materials, which can further reduce the total cost of PM7-D5 synthesis relative to PM6. Using high-temperature gel permeation chromatography (GPC) analysis, PM7-D5 is measured to have a number-average molecular weight (M_n) of 33.7 kg/mol with a dispersity (\mathcal{D}) of 2.2, as shown in Figure S42. It is worth noting that Y12 shows a good eco-compatible solvent-processed capability with high solubility in green solvents owing to its modified long-length branched chains. Therefore, the combination of PM7-D5:Y12 as the active layer offers an opportunity to design a high-performance OPD system processed with the green solvent 2-MeTHF.

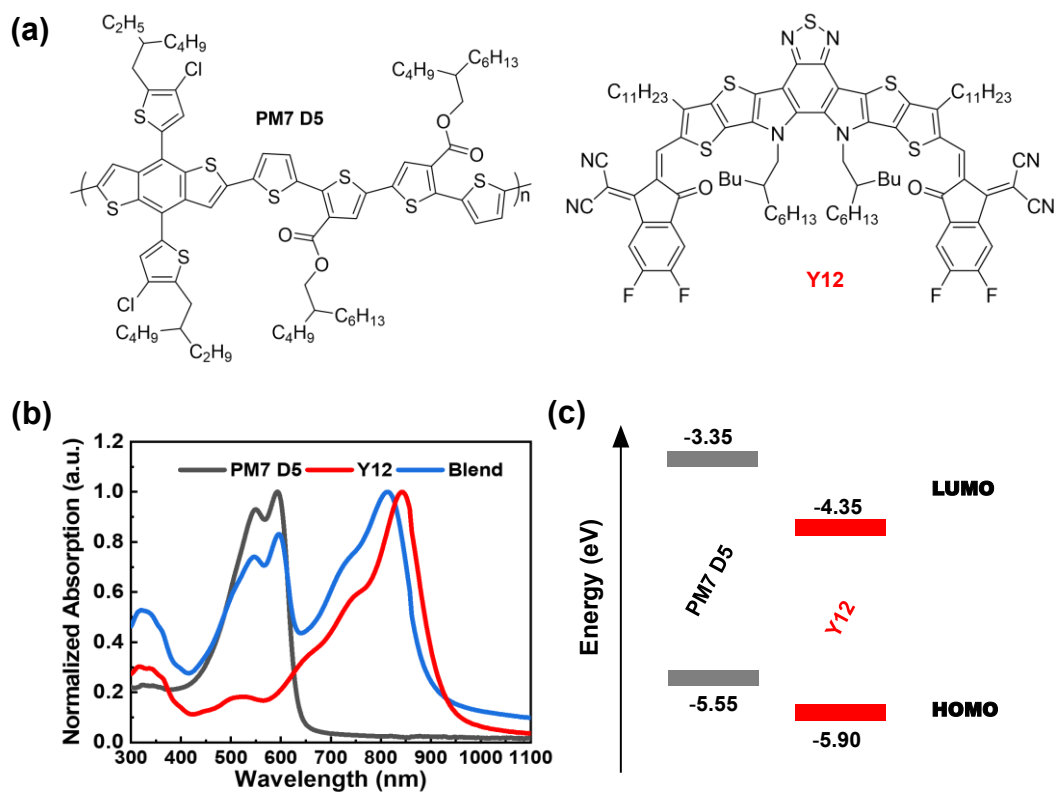


Figure 4-1. (a) Chemical structures of the donor PM7-D5 and the acceptor Y12. (b) Normalized thin-film absorption of PM7-D5 (black), Y12 (red), and BHJ blends (blue). (c) Energy level diagram of PM7-D5 and Y12.

The absorption spectra of pristine P7-D5, pristine Y12 and the blend are shown in **Figure 4-1b**. By combining PM7-D5 with Y12, the PM7-D5:Y12 BHJ possesses a wide photoresponse range with appreciable photoresponse up to 950 nm. The red-shift of the absorption peak of the neat Y12 NFA film in comparison to that of the BHJ film can be ascribed to the different molecular packing and acceptor aggregation.^[158] The designed OPDs adopt an inverted vertical structure shown in Figure S43. The active layer consists of the aforementioned polymer donor PM7-D5, and a non-fullerene acceptor (NFA) abbreviated as Y12, whose highest occupied molecular orbital (HOMO) levels and lowest unoccupied molecular orbital (LUMO) are calculated based on onset potentials of ionization and electron affinity obtained from differential pulse voltammetry (DPV). The onsets were determined on the first DPV scan of the fresh films to minimize contributions from swelling or changes of the morphology in the film (Figure S44). In addition, a fresh film was used for each oxidation or reduction scan to circumvent any electrolyte penetration and chemical changes caused by the opposing electrochemical process. The energy level diagram of PM7-D5 and Y12 is illustrated in **Figure 4-1c**. HOMO levels for PM7-D5 and Y12 are -5.55 and -5.90 eV, and the corresponding LUMO energy levels are -3.35 for PM7-D5 and -4.35 eV for Y12, respectively.

4.3 Characterization of 2-MeTHF processing PM7-D5:Y12 active layers

The BHJ morphology and the solid-state organization of donor-acceptor moieties influence the charge carrier dynamics including generation, transport, and extraction processes, which govern the overall photoresponsivity of OPDs.^[3,54] To reveal the solvent-performance-morphology relationship, we compare the BHJ blend processed from 2-MeTHF with the same BHJ blends processed CB and o-XY that were used as reference systems. The BHJ blend films are characterized at different length scales in the sub-micrometer to sub-nanometer range using different analytical techniques. First, atomic force microscopy (AFM) is employed to study the surface morphology of the PM7-D5:Y12 films cast from CB, o-XY, and 2-MeTHF solvents. As shown in **Figure 2a**, under high-resolution scans of $2\ \mu\text{m} \times 2\ \mu\text{m}$, relatively smooth surfaces are observed in all BHJ blends with comparable root-mean-square (RMS) values (0.97 nm for 2-MeTHF, 1.01 nm for CB, and 0.99 nm for o-XY). Compared with the BHJ blend films cast from CB and o-XY, the height profile of the same film processed from 2-MeTHF exhibits smaller topographic features. Additionally, Transmission electron microscopy (TEM) measurements were carried out to investigate the domain size and aggregation in the blend films processing with different solvents. As shown in **Figure 2b**, a network feature can be only observed in the TEM image of 2-MeTHF cast film indicating a stronger intermolecular packing tendency than the BHJ films obtained from CB and o-XY solvents. Specifically, TEM patterns reveal that the aggregation domains in the 2-MeTHF cast BHJ film are smaller than that of the other films, which can be ascribed to the increased packing density. In other words, the PM7-D5:Y12 system processed with 2-MeTHF reduces the domain sizes of the Y12 molecules in BHJ films and results in close molecular packing in

the in-plane direction, thus benefiting the charge dissociation and transport process and increasing the photoresponsivity of the device, as discussed below *vide infra*.

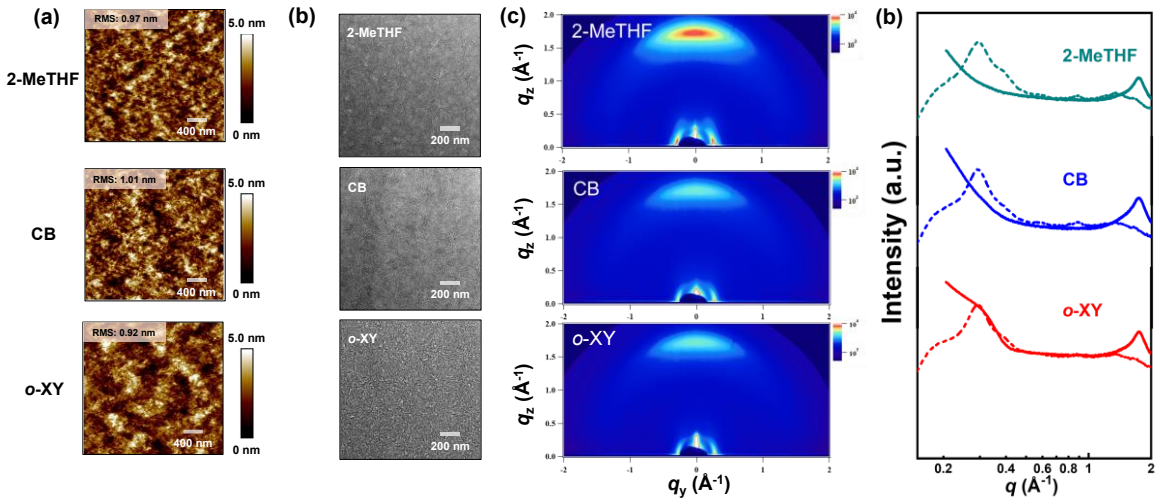


Figure 4-2. (a) High-resolution $2 \mu\text{m} \times 2 \mu\text{m}$ AFM topography images, (b) TEM images (Enlarged TEM images can be found in Figure S45), (c) 2D GIWAXS patterns, and (d) the corresponding in-plane (dash lines) and out-of-plane (solid lines) GIWAXS profiles of PM7-D5:Y12 blend films processed with 2-MeTHF, CB, and o-XY, respectively.

Morphological features and long-range at a few 10's to 100's nm can be resolved by grazing-incidence wide-angle X-ray scattering techniques, which also provide information on molecular orientation of donor and acceptor molecules with respect to the substrates in the BHJ films. The 2D GIWAXS images of the blend films and the corresponding linecuts are shown in **Figure 3c** and **3d**, and the crystal coherence length (L_c) was calculated using the Scherrer equation as follows,

$$L_c = \frac{2\pi K}{\Delta q}, \quad (4-1)$$

where K is the shape factor (typically 0.8-1), and Δq is the full width at half-maximum (FWHM) of a diffraction peak. A detailed analysis of pristine and BHJ films is presented in the Appendix (Figure S46 and S47). As a result, all films display considerably similar face-on molecular orientation with respect to the substrate based on the GIWAXS results. It is worth mentioning that neither the pristine nor blended conditions, casting solvents can barely have any effect on the π - π stacking motif with dominant face-on orientation for the PM7-D5 donor polymer. For PM7-D5:Y12 BHJ films cast from different solvents, the (010) peak corresponding to PM7-D5 is identified near 1.75 \AA^{-1} in the out-of-plane direction with no significant difference in the π - π stacking distance ($d = 0.36 \text{ nm}$) or in the coherence length values (2-MeTHF: $L_c = 3.76 \text{ nm}$, CB: $L_c = 3.44 \text{ nm}$, and o-XY: $L_c = 3.91 \text{ nm}$) of the donor molecule. Regardless of the casting solvents, the d -spacing and L_c values for these BHJ films are also identical for the pristine PM7-D5 films ($d = 0.37 \text{ nm}$, L_c around 3.91 nm). These results show that the PM7-D5 polymer retains its long-range ordering when blended with Y12 processed from different solvents, indicating that the morphology is dominated by the aggregation property of the donor polymer in the film as PM7-D5 has favorable aggregation behavior, which will be further corroborated by solid-state NMR analysis discussed below. Therefore, charge transport can occur in two directions, both in-plane and out-of-plane, in the PM7-D5:Y12 active layers,^[66] which implies the utilization of 2-MeTHF as a green solvent does not detrimentally affect the BHJ molecular packing and ordering.

Within the resolution capabilities of GIWAXS, the observed lamellar stacking peaks of blend films processed from three different solvents only present near 0.3 \AA^{-1} without any higher-order peaks. This indicates the close packing character of Y12 when being co-

deposited with PM7-D5 in the in-plane direction. Noticeably, the lamellar L_c values of the blend films vary from 10.74 nm (2-MeTHF) to 12.29 nm (CB) and 12.61 nm (o-XY). Meanwhile, the 2-MeTHF processed BHJ film maintains a similar lamellar stacking distance around 2.10 nm compared to the same BHJ films processed from CB and o-XY solvents. In other words, only the long-range ordering associated with Y12 molecules is affected by the 2-MeTHF casting process, which leads to smaller L_c in neat films and BHJ films, as compared to the same molecules processed from CB and o-XY solvents. The local chemical environments of end groups and sidechains in acceptor morphology are known to be sensitive to solvent processing, which can be only visualized by gaining access to atomic-level resolution enabled by ssNMR spectroscopy as discussed below.^[159]

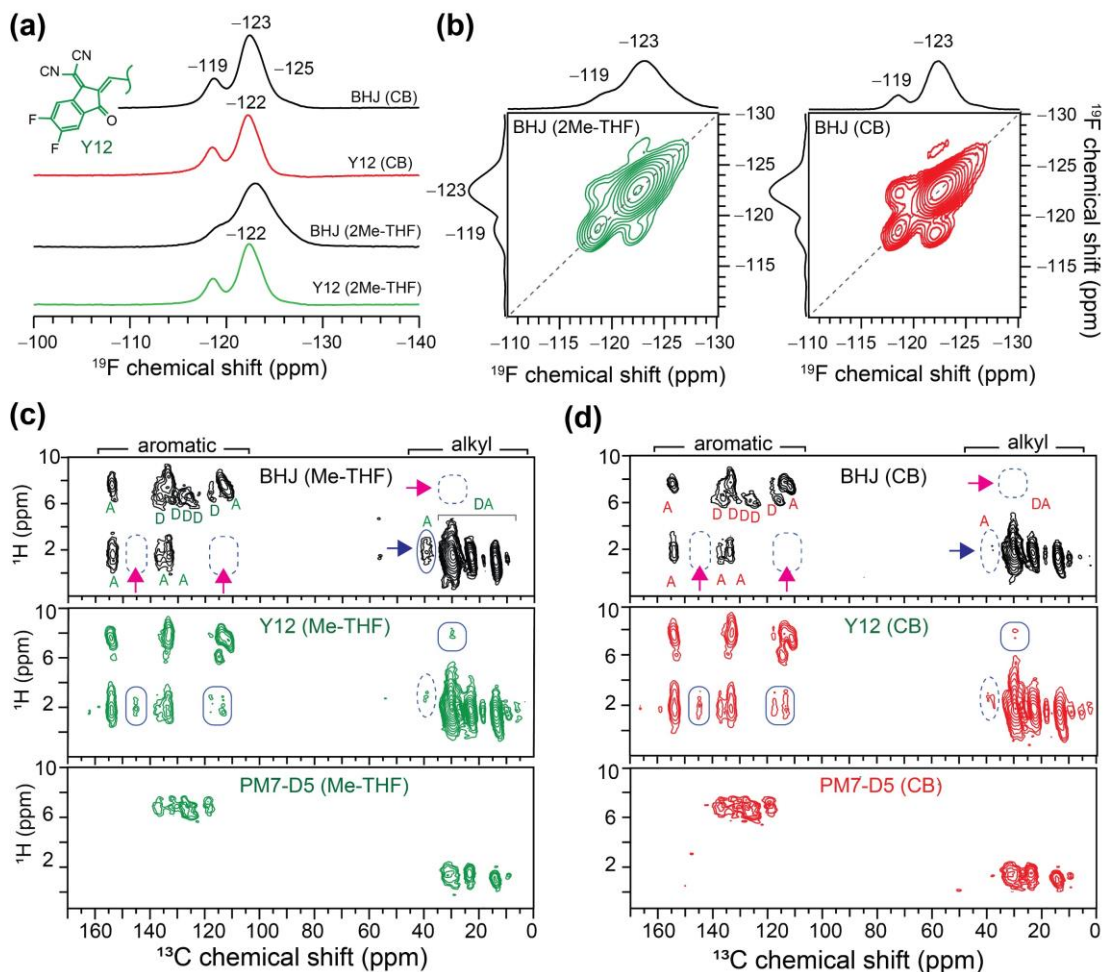


Figure 4-3. (a) Solid-state 1D ^{19}F MAS NMR spectra of neat Y12 and PM7-D5:Y12 blend films processed from 2-MeTHF and CB solvents with ^{19}F chemical shifts corresponding to distinct Y12 moieties. (b) 2D ^{19}F - ^{19}F exchange NMR spectra of PM7-D5:Y12 BHJs processed from different solvents. Solid-state 2D ^1H - ^{13}C HETCOR spectra of PM7-D5, Y12, and PM7-D5:Y12 blend processed from (c) 2-MeTHF and (d) CB solvents. All spectra were recorded at 18.8 T (^1H 800 MHz) and at 50 kHz MAS.

The molecular-level origins of the different packing interactions in neat Y12, PM7 and PM7-D5:Y12 blends can be studied by solid-state NMR spectroscopy. High-field ssNMR

spectroscopy has been increasingly applied to characterize BHJ morphology at sub-nanometer to nanometer distances in organic semiconductors and photovoltaic blends.^[63,102,104,105,159] Specifically, two-dimensional (2D) ^1H - ^{13}C , ^{19}F - ^{19}F and ^1H - ^1H correlation NMR experiments acquired at high fields with fast magic-angle spinning (MAS) are suitable to resolve donor-acceptor inter- and intramolecular interactions.^[21,99,100,159-163] Here, 1D ^1H , ^{13}C , and ^{19}F MAS, and 2D ^1H - ^{13}C , ^1H - ^1H , and ^{19}F - ^{19}F spectra of neat PM7-D5, Y12, and their BHJ blend films cast from 2-MeTHF and CB solvents are analyzed and compared. We examine the local bonding environments of ^1H , ^{13}C , and ^{19}F sites in neat compounds and blend films are investigated by analyzing their chemical shifts. From the analysis of ^{19}F MAS NMR spectra shown in **Figure 4-3a**, neat Y12 processed from 2-MeTHF and CB solvents display distinct ^{19}F peaks at 119 and 122 ppm, whereas the acceptor molecules in BHJ blends processed from the same solvents showed relatively broad peaks at 119 and 123 ppm and an additional small feature at 125 ppm. For nearly chemically equivalent fluorine atoms in the Y12 end groups, a single ^{19}F peak is expected. The different distributions of ^{19}F signals in the ^{19}F NMR spectra of neat compounds and BHJ blends processed from different solvents indicate the presence of different local chemical environments of Y12 end groups, which were not feasible to resolve from electron microscopy and GIWAXS measurements and analyses. In addition, 2D ^{19}F - ^{19}F exchange NMR spectra in **Figure 4-3b** acquired for BHJ films processed from 2-MeTHF and CB solvents show the cross peaks between 119 and 122 ppm, owing to the magnetization exchange between the two adjacent ^{19}F atoms in the same end group but involved in different inter- and intramolecular interactions. This indicates that the local structures of the fluorinated pendant units of Y12 are not substantially influenced by BHJ film formation, however, subtle structural changes in the vicinities of end groups and sidechains are expected, which

corroborates the detailed 2D ^1H - ^{13}C and ^1H - ^1H NMR analysis discussed below.^[159]

Further insight into the different inter- and intramolecular interactions in neat compounds and blends can be obtained by analyzing and comparing the ^1H and ^{13}C spectra of neat compounds and blends. A comparison of 1D ^1H and ^{13}C spectra of neat films and PM7-D5:Y12 blend films processed from 2-MeTHF solvent are shown in the Appendix (Figure S48 and S49). Although the ^1H NMR spectra show differences in the chemical shift distributions in the aromatic regions, the convoluted signals make it difficult to identify the ^1H signals corresponding to specific aromatic sites of donor and acceptor molecules. By comparison, while the $^1\text{H}\rightarrow^{13}\text{C}$ cross-polarization (CP) NMR experiments enable the signals associated with the different alkyl and aromatic ^{13}C sites to be resolved, yet the peak overlapping issue persists. To best consolidate the resolution and local structural information obtained from ^1H and ^{13}C NMR spectra, we acquired and compared the 2D ^1H - ^{13}C heteronuclear correlation (HETCOR) spectra of neat compounds and blends. In experiments of this type, the ^1H - ^{13}C 2D peaks correspond to through-space interactions of dipolar coupled ^1H and ^{13}C sites at sub-nanometer distances. **Figure 4-3c** and **3d** compare the 2D ^1H - ^{13}C HETCOR spectra of neat PM7-D5 and Y12 films and the BHJ blend films cast from 2-MeTHF and CB solvents. For neat PM7-D5 donor polymer processed from 2-MeTHF (**Figure 4-3c**), the 2D correlation peaks at 6-8 ppm (^1H) and 115-130 ppm (^{13}C) corresponding to the directly bonded C-H moieties in the aromatic core (thiophane (T), chlorinated thiophene (CT), and benzodithiophene (BDT) moieties) were identified, and 2D peaks at ~ 1.0 ppm (^1H) and 12-15 ppm (^{13}C), and at 1.5 ppm (^1H) and 20-35 ppm (^{13}C) correspond to the inter- and intramolecular dipolar-coupled C-H moieties in the branched sidechains. For neat Y12 film

obtained from 2-MeTHF, the well-resolved 2D peaks associated at 110-115 ppm (^{13}C) and 6-8 ppm (^1H) correspond to the directly bonded ^{13}C - ^1H moieties in difluorinated indene (end groups), and the peak at 130-135 ppm (^{13}C) and 6-8 ppm (^1H) correspond to the -CH- in bridging position between the fused-ring core and the indene groups. Inter- and intramolecular end-group/sidechain interactions in Y12 are indicated in soft rectangles. In the case of the PM7-D5:Y12 BHJ blend processed from 2-MeTHF, the 2D correlation peaks associated with the PM7-D5 donor polymer appear at identical frequencies and indicated by 'D', which is in line with the small coherence length and domain sizes observed by the GIWAXS and TEM analysis. However, Y12 acceptor morphology changes by means of the local chemical environments of the end groups as well as the branched sidechains (depicted in ovals and soft rectangles), highlighting that the sub-nanometer resolution enabled by the high field solid-state NMR in picking up the morphological changes.^[159] For neat compounds and blend films obtained from CB solvent, a similar analysis of 2D HETCOR spectra is presented in (**Figure 4-3d**), whereby similar 2D peaks were appeared yet the differences in the sidechain morphology is obvious from the peaks depicted in the dashed ovals (blue arrow). The most notable of all is the morphological changes in the Y12 acceptor molecules vicinity of end groups and the lamellar packing interactions in neat compounds and the BHJ blends (magenta arrows). The different lamellar packing interactions (blue arrows) are also evidenced in the BHJ blends processed from 2-MeTHF and CB solvents. This indicates that the subtle changes to the sidechain conformations occur in the local structures of Y12 end groups and branched sidechains in BHJ blends. It is consistent with our GIWAXS and TEM measurements and analysis that showed lamellar packing distance and domain size of D-A moieties in the 2-MeTHF cast BHJ blend become favorably smaller, which benefit the charge generation and

transport process and increase the charge collection probability in OPDs as illustrated in the below sections.

4.4 Characterization of PM7-D5:Y12 OPD devices

One of the most important photosensing metrics of photodetectors is a high sensitivity toward weak light signals, which requires a low noise level originated from the low dark current.^[3,11,164] In addition to BHJ morphology, the overall performance of OPDs depends on several factors such as film thickness, external quantum efficiency (EQE), responsivity (R), specific detectivity (D^*), charge collection probability (P_c), and linear dynamics range (LDR), each of them will be thoroughly discussed in the following. We examined the photodetection performance of OPDs processed from 2-MeTHF, and compared them with the same OPDs processed CB, and o-XY solvents. In particular, for our vertical photodiode-based OPD which operates in the photoconductive mode, a low dark current under reverse bias is required. During the optimization of the PM7-D5:Y12 devices, we have utilized a so-called ‘thick junction’ strategy.^[165] By increasing the thickness of both, the hole-blocking layer ZnO (65 nm), and the active layer (210 nm for 2-MeTHF, 177 nm for o-XY, and 196 nm for CB), the

shunt resistance of the device increases to above $10^9 \Omega \text{ cm}^2$, which significantly reduces the shunt leakage current.

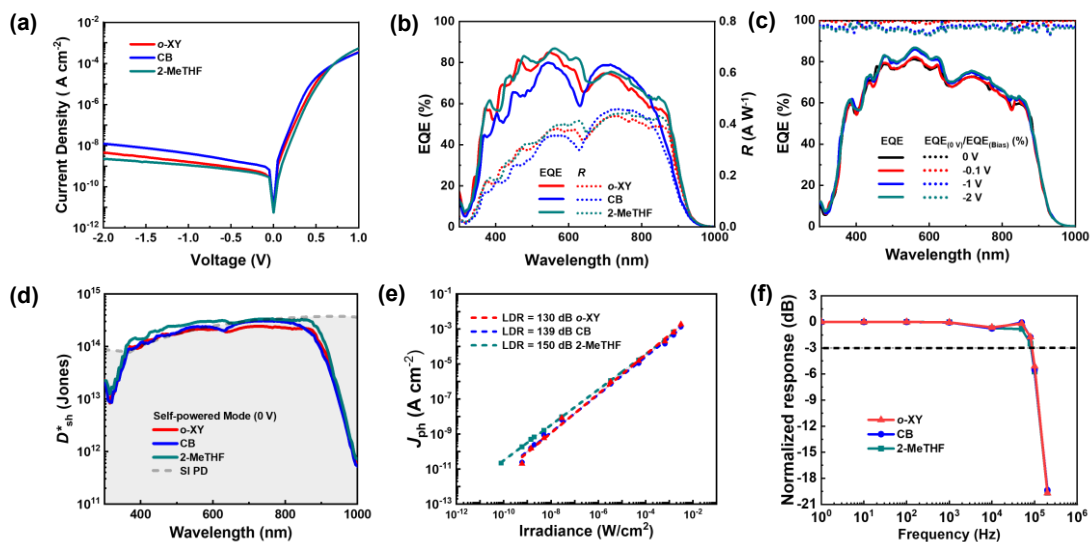


Figure 4-4. (a) J - V curves in the dark, (b) EQE and responsivity at -2 V , (c) EQE under different biases (0 V , -0.1 V , -1 V , and -2 V) and $\text{EQE}_{(0 \text{ V})}/\text{EQE}_{\text{bias}}$, (d) D_{sh}^* of PM7-D5:Y12 OPDs and a commercial Si photodiode (Newport 818-UV) under the self-powered mode (0 V), (e) linear dynamic range under the illumination of 850 nm , and (f) normalized phototransient response under the illumination of 850 nm of PM7-D5:Y12 OPDs processed with o-XY (red), CB (blue), and 2-MeTHF (green).

As shown in the current-density/voltage (J - V) plots in **Figure 4-4a**, the optimized PM7-D5:Y12 device cast from 2-MeTHF shows an extremely low dark current density (J_d) of 3.6 nA cm^{-2} under a reversed bias of -2 V , which is several orders of magnitude lower than many of the OPDs processed with traditional solvents in the literature and, we believe, sets a record for OPDs processed from 2-MeTHF.^[3,12,57,135,142–148] J_d also exhibits a weak dependence on

the applied bias, as can be seen from a relatively flat J - V slope in the reverse bias regime. In particular, J_d only increases by 2.97 nA cm⁻² from 0.63 nA cm⁻² at -0.1 V to 3.60 nA cm⁻² at -2 V for the optimized device processed with 2-MeTHF, which indicates a similar low noise level in the OPD device regardless of applied bias. It further indicates the success of the ‘thick junction’ strategy of the thick ZnO layer and the active layer, which effectively suppresses space charge injection and maintains the low noise level. In addition, good reproducibility and uniformity of the device performance of devices casted by 2-MeTHF are also achieved.

To quantify the photoresponsivity of OPDs, EQE was collected as a function of incident wavelength (**Figure 4-4b**). While all OPDs show promising EQE values under a reverse bias of -2 V from 300 nm to 950 nm, the 2-MeTHF cast device shows the highest EQE values (maximum above 86%) among the measured range in comparison with those of CB and o-XY cast devices (maximum 80% and 84%, respectively). It is worth to note that J_d and EQE of the 2-MeTHF cast device show no significant change after 15 days stored in a glovebox.

An important parameter to evaluate photodetectors is the responsivity (R), which is defined as the ratio of electrical output to optical input and can be calculated using the following equation,

$$R = \frac{\lambda}{1240 \text{ (nm W A}^{-1}\text{)}} \times \frac{\text{EQE}}{100 \%}, \quad (4-2)$$

where λ is the wavelength of the incident light. As shown in **Figure 4-4b**, the optimized PM7-D5 device provides high responsivity over a wide range of 400-900 nm, which includes

maximum responsivity of above 0.40 A W^{-1} in the wavelength region of 500-900 nm, comparable the majority of conventional OPDs.^[3,12,142,143]

Specific detectivity (D^* , given in $\text{cm Hz}^{1/2} \text{ W}^{-1}$ or Jones) describes the sensitivity of a photodetector to a weak irradiance which can be calculated by,

$$D^* = \frac{R\sqrt{AB}}{I_n} = \frac{R\sqrt{A}}{S_n}, \quad (4-3)$$

where A is the device area of the photodetector, B is the corresponding bandwidth, I_n is the noise current and S_n is the noise current spectral density. Assuming that the shot noise dominates the total noise under reverse bias, S_n can be derived from the dark J - V characteristics. Thus, the shot-noise-limited specific detectivity (D_{sh}^*) can be further described by Equation (4),

$$D_{\text{sh}}^* = \frac{R\sqrt{A}}{\sqrt{2qI_d}} = \frac{R}{\sqrt{2qJ_d}}, \quad (4-4)$$

where $q = 1.6 \times 10^{-19}$ (C) is the elementary charge, I_d is the dark current (A) and J_d is the dark current density (A cm^{-2}). Under an applied bias of -2 V , the optimized OPD shows a D_{sh}^* around 5.4×10^{12} to 1.3×10^{13} Jones in a broad wavelength range of 400 to 900 nm (Figure S50a). Intriguingly, the 2-MeTHF OPD still exhibits a comparatively high EQE signal under minimal bias or self-powered condition. As shown in **Figure 4-4c**, the EQE profiles nearly overlap with each other for the 2-MeTHF cast device and are independent of the external bias, which indicates a fast process of charge extraction and collection in the active layer.^[3] Such a

bias-independent EQE response suggests the possibility of operating the OPD under a small reverse bias, *e.g.* $V_{\text{app}} = -0.1$ V, or even self-powered operating OPDs. The ratio between $\text{EQE}_{(0\text{ V})}$ and $\text{EQE}_{(\text{bias})}$ are shown in **Figure 4-4c**, and above 95% of EQE response over the whole detective range of the device at a large reverse bias (-2 V) can be maintained when it is measured at 0 V. In such an operation mode, the OPD can also benefit from a significantly lower level of dark current, which is attributed to a lower level of charge injections from electrodes onto HOMO of donor/ LUMO of acceptor under low/zero reverse bias.^[3,12] As a result, the PM7-D5:Y12 device shows an impressively high D_{sh}^* of around 1.4×10^{13} to 3.2×10^{13} Jones under -0.1 V (Figure S50b) and 1.4×10^{14} to 3.3×10^{14} Jones at 0 V under the self-powered mode (**Figure 4-4d**) over $\lambda = 400$ - 900 nm range. To the best of our knowledge, it also achieves one of the highest D_{sh}^* values over its whole detectivity range in comparison to that for reported OPDs processed with traditional solvents regardless of operating bias.^[6-16] Among the three devices, the 2-MeTHF cast device exhibits the highest D_{sh}^* (2-MeTHF: 3.3×10^{14} Jones, CB: 3.0×10^{14} Jones, o-XY: 2.2×10^{14} Jones) across the entire detective range under the self-powered mode. Furthermore, PM7-D5:Y12 devices exhibit overall high performances even better than a commercial Si photodiode (Newport 818-UV) in **Figure 4-4d**. Such a high D_{sh}^* of the optimized device mainly benefits from the bias-independent EQE signal as well as the minor increase of the dark current due to the applied bias, which will be further discussed below.

The shot noise-limited specific detectivity D_{sh}^* is obtained under a presumption that the shot noise is the main contributor to all noise sources in photodetectors. While reporting the shot noise-limited specific detectivity facilitates the preliminary comparison with literature values,

the assumption that it relies upon does not necessarily hold true in all conditions. This fact can lead to overestimation in specific detectivity D^* by a few orders of magnitude,^[166] and/or the negligence of the frequency dependence nature of photodetector performance.^[167,168] Hence, noise current spectral density (S_n) is further determined by experiment using fast Fourier transform (FFT) of the dark current measured under different reverse biases (0 V, -0.1 V, -1 V, and -2 V) shown in Figure S51. At a glance, regardless of casting solvents, OPDs generally exhibit a higher noise current at a higher applied bias. However, S_n barely increases and stays below 10^{-12} A Hz^{1/2} when the applied bias increases from -0.1 V to -2 V. Such a bias independent phenomenon is mainly due to the relatively thick active layer (~ 200 nm), which delays the onset of the space-charge-limited current and suppresses the noise current under large bias.^[58] We then evaluate the noise equivalent power (NEP), which represents the signal power at a signal-to-noise ratio of one in a 1 Hz output bandwidth, by using the following relation.

$$NEP = \frac{S_n}{R} \quad (4-5)$$

At a frequency of 155 Hz (where EQE and R signals are collected, see Appendix), the 2-MeTHF, CB, and o-XY cast devices give $NEPs$ of 1.4×10^{-13} , 1.4×10^{-13} , and 1.9×10^{-13} W Hz^{1/2} at -0.1 V. They still stay at an appreciable level of sub-picowatt at -2 V ($NEPs$ are 1.6×10^{-13} , 1.8×10^{-13} , and 3.1×10^{-13} W Hz^{1/2} for 2-MeTHF, CB, and o-XY cast devices, respectively), which are state-of-the-art OPD performances.^[169,170] From the measured S_n , we further calculate the specific detectivity (D^*) of devices prepared from different solvents at different voltages (Figure S52). At a low frequency (< 50 Hz) where 1/f noise is the most

significant noise source, the magnitude of D^* over the probed wavelength range (400-900 nm) is still well above the level of 10^{10} Jones. The value of D^* gradually increases to above 10^{11} Jones at higher frequencies and reaches a maximum level of 10^{12} Jones at ~ 1000 Hz, as S_n enters the frequency-independent regime, where the main sources of noise are white noise, including shot noise and thermal noise. In particular, at 155 Hz and 0 V, 2-MeTHF, CB, and o-XY cast devices show the maximum D^* of 1.6×10^{12} , 1.6×10^{12} , and 1.2×10^{12} Jones, respectively. D^* of all devices are favorably better than that of the commercial Si photodiode (Newport 818-UV) in Figure S53b over $\lambda = 400-900$ nm range, which is also comparable to one of the best devices in the OPD field.^[170] The 2-MeTHF processing device shows a higher overall D^* than the other two devices at a higher bias voltage (-2 V), as D^* of the 2-MeTHF cast device stays almost unchanged while those of CB and o-XY cast devices reduce due to the rises of noise currents.

To further understand the charge collection efficiency in the working device, the voltage-dependent charge collection probability (P_c) is calculated with the following equation to evaluate the efficiency of dissociation of exciton and collection of free charge carriers,

$$P_c = \frac{J_{\text{ph}}}{J_{\text{ph,sat}}}, \quad (4-6)$$

where photocurrent density (J_{ph}) of the device is the difference between the current density under illumination and in the dark,^[21,135] and $J_{\text{ph,sat}}$ is the saturated photocurrent density under -2 V (which are 19.21 mA cm^{-2} for 2-MeTHF, 18.91 mA cm^{-2} for CB, and 19.93 mA cm^{-2} for o-XY, respectively). Such a high $J_{\text{ph,sat}}$ indicates a fast charge carrier generation rate in all

devices. In Figure S54, the P_c is plotted against the effective voltage ($V_{eff} = V_0 - V_{cor}$), where V_0 is the voltage at which $J_{ph} = 0$, and the corrected voltage ($V_{cor} = V_{app} - JR_s$) is obtained by taking into account the voltage losses over the series resistance (R_s). Under the short-circuit condition, the 2-MeTHF cast device shows $P_c = 0.985$, which is the highest compared with that of CB ($P_c = 0.962$) and o-XY ($P_c = 0.883$) OPDs. In other words, 2-MeTHF cast device has an efficient charge collection process without the assistance of any applied bias, which is consistent with our observations of the bias-independent EQE and the high D_{sh}^* of the small bias operating OPD. Similar EQE spectra, as discussed before, further consolidates that the charge collection process in the device is barely affected by an increased applied bias, which implies that the PM7-D5:Y12 system has a fairly high charge carrier mobility for both electrons (μ_e) and holes (μ_h). Therefore, we investigated the effective mobility (μ_{eff}) of the working device assuming that $\mu_e = \mu_h$, which can be calculated with the following equation,

$$\mu_{eff}(n, V_{cor}) = \frac{J(V)L}{2qn(V)[V_{oc} - V_{cor}]}, \quad (4-7)$$

where L is the thickness of the active layer, and $n(V)$ is the voltage-dependent charge carrier density determined from impedance analysis in Figure S55a. For the effective mobilities, all

the devices, regardless of casting solvents, show a considerable high effective mobility range ($\mu_{\text{eff}} = 1.1\text{-}3.3 \times 10 \text{ cm}^2 \text{ V}^{-1} \text{ s}^{-1}$) under the whole operating bias in Figure S55b.

The linear dynamic range (LDR) is the next sensing metric to be characterized for the designed photodetectors. LDR depicts the linear range of input signal versus detector output, which can be calculated by,

$$\text{LDR} = 20 \log \frac{I_{\text{upper}}}{I_{\text{lower}}} = 20 \log \frac{J_{\text{upper}}}{J_{\text{lower}}}, \quad (4-8)$$

where I_{upper} and I_{lower} are the maximum and minimum irradiance beyond or below which the device signal-irradiance relation deviates from linearity, respectively, and J_{upper} and J_{lower} are the corresponding photocurrent density. **Figure 4-4e** shows the relation between input irradiance at 850 nm and output photocurrent, confirming that all three types of devices possess a wide LDR of 130 dB or above. Notably, the 2-MeTHF cast device is able to resolve an extremely weak irradiance of $10^{-10} \text{ W cm}^{-2}$ and results in the highest LDR of 150 dB among all three types of devices. In addition, the 3 dB bandwidth ($f_{3\text{dB}}$), defined as the modulating frequency at which the output photocurrent drops to 3 dB (~70.8%) of the original amplitude, is extracted from the photodetector response upon pulses of the 850 nm light source at different frequencies. As shown in **Figure 4-4f**, the $f_{3\text{dB}}$ values for 2-MeTHF, CB, and o-XY cast devices are 82.9, 86.1, and 87.0 kHz, respectively. The values are similar and are all above 80 kHz, implying a comparably fast response speed of PM7-D5:Y12 devices regardless of processing solvents. The 2-MeTHF cast devices also exhibit sub-10- μs response time with

long-term in-operation stability, which makes this platform suitable for applications requiring rapid detector response.

4.5 Wearable PM7:D5 based OPDs for photoplethysmography and pulse oximetry

Having established the detailed morphological characterization vis-à-vis device physics that enable high performance in PM7-D5:Y12 OPDs processed from a green solvent, we next demonstrate the applications of these OPDs for wearable pulse heart rate and oximeter devices. As a light sensor, OPDs with high sensitivity and fast response speed can be widely used in daily applications by real-time detecting and converting light signals to current or voltage output, which can be further translated into useful digital signals.

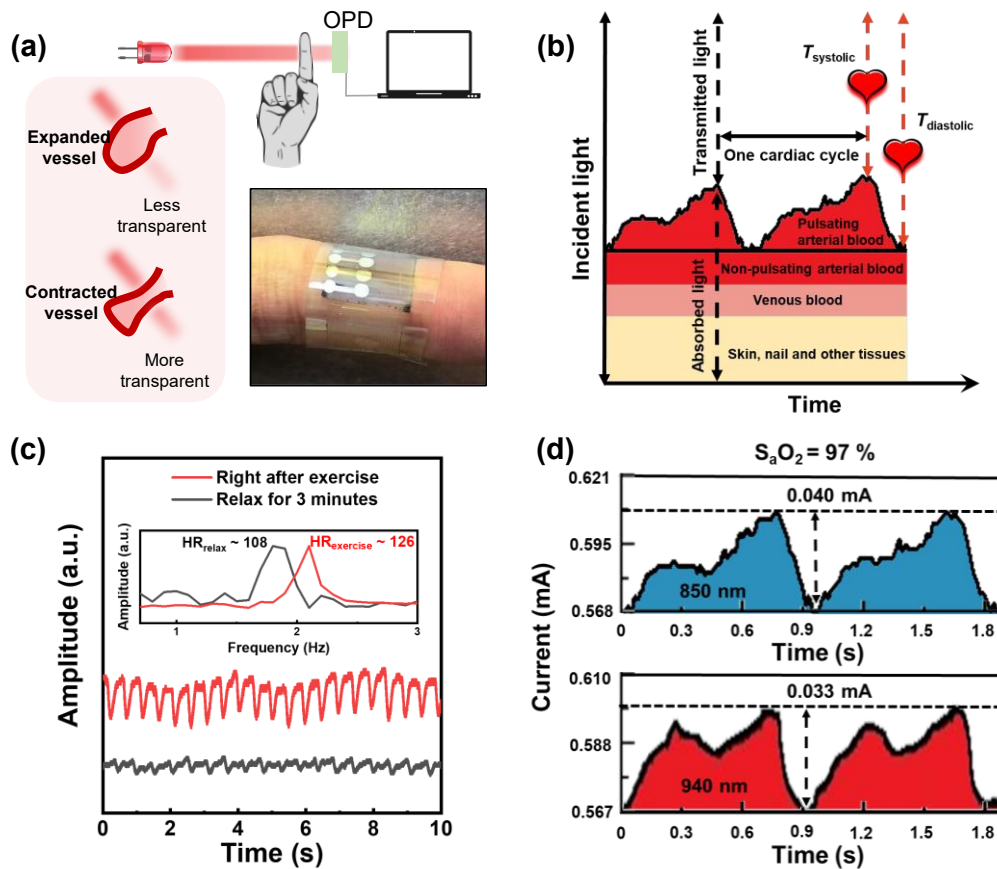


Figure 4-5. (a) Working principle of a PPG-based real-time heart rate setup with wearable OPDs. Bottom right: a photograph of an OPD fabricated on flexible substrates wearing on a volunteer's finger without wire connections. (b) A model of the light pathway of pulse oximeters using measured cardiac cycles from our designed OPDs as an example. (c) Time series pulse signal obtained from the PPG measurement at after-exercise (upper) condition and relaxing (lower) conditions. Inset: HR determined from the FFT of the PPG signal. (d) Output current signal from wearable OPD with $S_aO_2 = 97\%$. The blue and red shapes represent the signals when illuminated with the 850 nm and 940 nm LEDs, respectively.

Figure 4-5a depicts the working principle of a photoplethysmography (PPG)-based heart rate measurement. Due to the volume change of the blood vessels during cardiac cycles, the human body part under test (*e.g.* a pointing finger in this test) becomes more or less transparent under light illumination with LEDs, and the frequency of modulations in transmission (which reflects the heartbeats) can be recorded by a photodetector.^[140,141] Fast Fourier transformation (FFT) of the time-series signal can indicate the frequency of the photoresponse signals, which then can be further translated into heart rate quoted in beats-per-minute.

Another potential application for this OPD platform is oximetry for blood oxygen levels.^[140,141] The oxygen saturation (SO_2) in the blood can be quantified as follows,

$$SO_2 = \frac{C_{HbO_2}}{C_{HbO_2} + C_{Hb}}, \quad (4-9)$$

where C_{HbO_2} and C_{Hb} are the concentration of oxygenated hemoglobin and deoxygenated hemoglobin, respectively. For a pulse oximeter sensor based on OPDs, two light-emitting diodes (LEDs) with different emitting wavelengths are required to combine with an organic photodetector that has high detectivity and sensitivity at the emitting wavelengths of the selected LEDs.^[171] Incident light from the LEDs can be absorbed and reflected by blood and other tissues shown in **Figure 4-5b**. The periodically transmitted light due to systolic and diastolic heartbeats can be converted from the output signal of the highly-sensitive OPD. However, most of the reported pulse oximeters based on the optical property of hemoglobin require additional calibration, since there is a significant difference between the optical path lengths of the two different wavelengths from the used light sources,^[172] and the path length is strongly dependent on the scattering coefficient of hemoglobin under the corresponding

light source.^[173] For example, a commercialized pulse oximeter with green (550 nm) and NIR light (850 nm) will have an unavoidable systematic error due to big differences in the scattering coefficients of hemoglobin ($\mu_{s,550}' = 3.1 \text{ mm}^{-1}$ and $\mu_{s,850}' = 1.8 \text{ mm}^{-1}$) as well as the path lengths of the green and NIR light.^[134] To avoid additional calibration procedures, two NIR LEDs with sufficiently close central wavelengths (850 nm and 940 nm) are selected for our developed OPD system, which have comparable light path lengths as a result of their similar effective scattering coefficient (both μ_s' are around 1.8 mm^{-1} shown in Figure S56) considering the anisotropy factor of red blood cells. We can define the ratio of the absorbed 850 nm (A_{850}) and 940 nm (A_{940}) light as R_{os} ,^[171]

$$R_{os} = \frac{A_1}{A_2} = \frac{\ln(T_{850})}{\ln(T_{940})}, \quad (4-10)$$

which can also be described according to Beer–Lambert’s law with the transmitted 850 nm (T_{850}) and 940 nm (T_{940}) light intensities. The relationship between R_{os} and the oxygen saturation SO_2 then can be derived using the following equation,^[171,172]

$$SO_2 = \frac{\varepsilon_{850, \text{Hb}} - R_{os} \left(\frac{I_{940}}{I_{850}} \right) \varepsilon_{940, \text{Hb}}}{R_{os} \left(\frac{I_{940}}{I_{850}} \right) (\varepsilon_{940, \text{HbO}_2} - \varepsilon_{940, \text{Hb}}) + (\varepsilon_{850, \text{Hb}} - \varepsilon_{850, \text{HbO}_2})}, \quad (4-11)$$

where $\varepsilon_{\lambda, \text{Hb}}$ and $\varepsilon_{\lambda, \text{HbO}_2}$ are the extinction coefficients for oxygenated and deoxygenated hemoglobin at different wavelengths ($\lambda = 850$ or 940 nm, respectively); I_{940} and I_{850} are the path-lengths of 850 nm and 940 nm light, respectively, which have a similar value and lead to the ratio of I_{940}/I_{850} close to 1. Thus, the oxygen saturation of calibration-free oximeter can be rewritten as follows,

$$SO_2 = \frac{\varepsilon_{850, Hb} - R_{os} \varepsilon_{940, Hb}}{R_{os} (\varepsilon_{940, HbO_2} - \varepsilon_{940, Hb}) + (\varepsilon_{850, Hb} - \varepsilon_{850, HbO_2})}, \quad (4-12)$$

By converting the photoresponse of our designed OPD to a transmitted light signal, a relatively accurate blood oxygen level can be further calculated. Such a type of device fabricated on a flexible substrate (bottom right of **Figure 4-5a**) has a great advantage over traditional inorganic pulse oximeters, due to its calibration-free high accuracy, low cost, as well as light-weight and portable design.

To further expand application space for the proposed system, PM7-D5:Y12 OPDs were fabricated using flexible substrates that offer mechanically favorable softness and reduced weight, which makes it more suitable for wearable electronic devices than conventional Si-based photodetectors.^[58] As a preliminary assessment for the wearable electronic application, we conducted a simple photoplethysmography (PPG) test using devices fabricated on flexible ITO-coated polyethylene terephthalate (PET) substrates. As shown in **Figure 4-5a**, such flexible OPDs can be further encapsulated and stuck onto any comfortable human body part with a large curvature. More details of the device fabrication can be found in the Experimental Section. It is also worth mentioning that the photoresponsivity of the photodetector fabricated on the flexible substrate is comparable to that of devices on a traditional ITO/glass substrate, with great device mechanical stability. With the wearable OPD on a finger, the heart rate of a volunteer is collected by a flexible self-powered OPD immediately after running for 1 km and after resting for 5 minutes, as presented in **Figure 4-5c**.[‡] Fast Fourier transformation of the time-series signal (inset of **Figure 4-5c**) indicates a frequency of about 2.1 and 1.8 Hz of the AC signals, which indicates a heart rate of 126 and 108 beat-per-minute, respectively.

Interestingly, the flexible OPD device can be designed as a finger pulse oximeter. This oximeter can measure the transmission of the light through the finger wearing the device to estimate the amount of oxygen-carrying blood cells. Accurate blood oxygen saturation can be examined with the calibration-free pulse oximeter based on PM7-D5:Y12 wearing on a finger with 850 and 940 nm light sources. As shown in **Figure 4-5d**, the output current signal of the self-powered OPD is collected from the same volunteer and can be further converted to a voltage signal, which has a good linear correlation with the irradiance of both 850 nm and 940 nm wavelength light as discussed in the LDR measurement.[‡] By analyzing the light transmission based on the OPD signal, oxygen saturation of 97% is observed in the volunteer's finger without any further calibration of the device, which shows a small error of around 1% compared to the value (98%) measured by commercialized inorganic pulse oximetry.

4.6 Conclusions

In summary, this study proposed a bottom-up approach to develop high-performance PM7-D5:Y12 organic photodetectors for a range of applications. In achieving this, we combined molecular design of donor polymer (PM7-D5) with a biomass-derived environmentally friendly 2-MeTHF solvent. In addition, we provide a detailed framework of understanding PM7-D5:Y12 BHJ morphological features at different length scales and the associated device physics, and the interrelationship between them. Molecularly designed PM7 offers backbone planarity as well as specific inter- and intramolecular interactions to obtain a suitable BHJ morphology. These optimal phase separation and intermolecular interactions in donor and acceptor domains are characterized by AFM, TEM, GIWAXS and ssNMR spectroscopy techniques. The thick film strategy applied in the device optimization effectively blocks the

charge injection, increases the shunt resistance and limits the leakage, leading to a substantially low dark current without a strong correlation with the applied bias (0.63 nA under -0.1 V and 3.60 nA under -2 V). These features enable self-powered OPDs to be fabricated. The presented OPD can retain a considerably high D_{sh}^* around 1.4×10^{13} to 3.2×10^{13} Jones from 400 nm to 900 nm under -0.1 V, which is one of the highest D_{sh}^* in comparison with reported OPDs. The most notable of all is, the green solvent processed can be integrated into flexible PET substrates to develop wearable devices. The self-powered wearable PM7:Y12 OPDs enable heart-rate monitoring (photoplethysmography) and oxygen saturation (pulse oximetry) measurements. Ultimately, the flexible organic photodetector may be directly used for large-scale roll-to-roll fabrication processing with environmentally friendly solvents as an efficient but low-cost real-time monitor for heart rate and blood oxygen level.

4.7 Experimental methods

Material Synthesis. All starting materials were purchased from a commercial supplier and were used without further purification. Compound 7 was purchased directly from SunaTech.

Synthesis information of other intermediate molecules and the dibromo monomer (compound 6) are presented in the following.

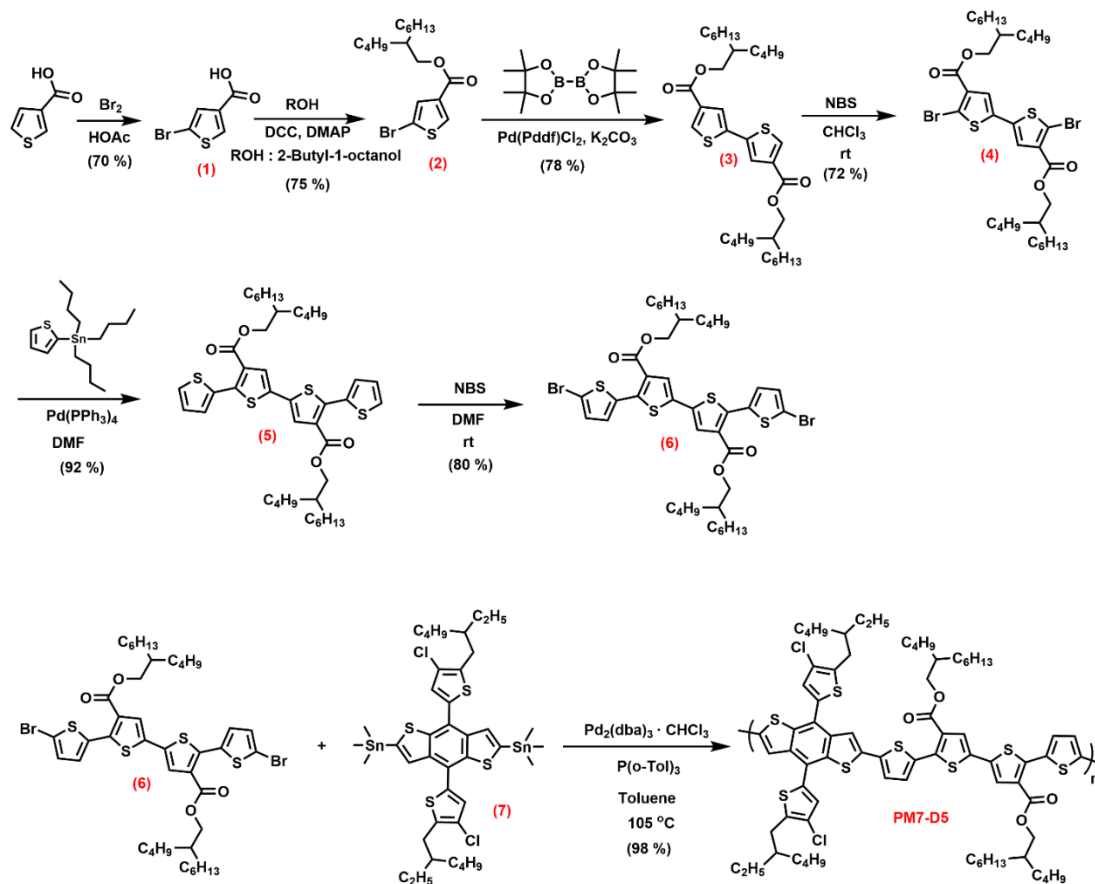


Figure 4-6. Synthetic procedures of PM7-D5.

Synthetic Characterization. ^1H NMR and ^{13}C NMR spectra for all monomers and molecular precursors were acquired on a Bruker Avance IIIHD 500 MHz or Bruker Avance IIIHD 700 MHz instruments using CDCl_3 as solvent; the residual CHCl_3 peak was used as a reference for all reported chemical shifts (^1H : $\delta = 7.26$ ppm, ^{13}C : $\delta = 77.16$ ppm). ^1H NMR for the polymer was acquired on a Bruker Avance IIIHD 400 MHz using *o*-dichlorobenzene- D_4

as the solvent at 110 °C; the residual solvent peak was used as a reference for the polymer chemical shifts (^1H : $\delta = 6.93$ ppm, and $\delta = 7.20$ ppm). Mass spectroscopy of small molecules were obtained by direct infusion atmospheric pressure chemical ionization (APCI) in positive mode using a Thermo Scientific Orbitrap ID-X Tribrid mass spectrometer. Gel permeation chromatography (GPC) was performed using a Tosoh EcoSEC high temperature GPC instrument with RI detector to determine the number average molecular weight (M_n), weight average molecular weight (M_w) and dispersity (\mathcal{D}) for all polymers. Experiments were run using 1,2,4-trichlorobenzene (TCB) as eluent at 140 °C at a flow rate of 1 mL/min on two 7.8 mm x 30 cm, 13 μm TSK-Gel GMHHR-H(S) HT2 columns in series. The instrument was calibrated using polystyrene standards (1,390-1,214,000 g/mol) and the data were analyzed using 8321GPC-WS analysis software. The GPC samples were prepared by dissolving the polymers in TCB at a 1 mg/mL concentration and stirred at 120 °C for at least 3 hours before filtering through a 0.45 mm PTFE filter. Elemental analyses were conducted by Atlantic Microlab Inc.

OPD Device Fabrication. All the devices on an ITO/glass substrate were fabricated in an inverted structure of indium tin oxide (ITO)/zinc oxide (ZnO)/PM7-D5:Y12/MoO_x/Ag. OPD devices were fabricated according to the following procedures. ITO substrates (purchased from Thin Film Devices, Inc.) were cleaned by detergent, then sequentially ultrasonicated in DI water, acetone, and isopropanol for 30 min. Diethyl zinc and tetrahydrofuran (THF) were mixed in a volume ratio of 1.5:1 and spin-coated on the clean ITO substrates at 4000 rpm for 30 s, followed by 15 min annealing at 150 °C to make a thick ZnO film (~65 nm). Solutions (total concentration of 10 mg/mL) of PM7-D5:Y12 in a 1:1.2 weight ratio were prepared in

either CB, o-XY, or 2-MeTHF, which was stirred and kept at elevated temperatures (2-MeTHF at 40 °C, CB at 60 °C, o-XY at 80 °C) overnight. Prior to hot spin casting, the stock solutions and the corresponding substrates were all heated up to a certain temperature (CB: 90 °C, o-XY: 100 °C, and 2-MeTHF: 75 °C), respectively. On the top of the ZnO layer, the hot solution was spin-coated at 650 rpm to form thick active layers (180–210 nm), of which the thickness was measured by an Ambios XP-100 stylus profilometer. All the films were thermally annealed at 110 °C for 10 minutes. After settling the films to cool to room temperature, the MoO_x/Ag (7 nm/120 nm) electrode with an active area of 0.05 cm² was then deposited on top of the active layer by thermal evaporation in a high vacuum (<10⁶ torr). For wearable devices, flexible ITO/PET substrates with a surface resistivity of 100 Ω/sq (purchased from Sigma-Aldrich) were used to replace all the ITO/glass substrates. These flexible devices with wires connected to the electrodes were further encapsulated with another thin PET film on the top using a two-part fast drying epoxy. All the other steps of the fabrication of the flexible devices were the same as the regular devices.

Differential Pulse Voltammetry (DPV) Measurements. Electrochemical differential pulse voltammetry (DPV) measurements were performed using a 2 mV step size, 80 ms step time and 50 mV pulse amplitude. The voltammetry experiments were performed in a glove box using a standard three-electrode cell on a 0.07 cm² glassy carbon button working electrode, an Ag/Ag⁺ (10 mM AgNO₃) reference electrode and a platinum flag counter electrode. Polymer films and NFA films were drop casted from a 1 mg/mL chloroform solution onto the working electrode and allowed to air dry. Electrochemical experiments were performed using dry acetonitrile with a TBAPF₆ supporting electrolyte at a concentration of

0.5 M in an argon filled glovebox. Ferrocene/ferrocenium (-5.12 V vs vacuum) was used as an internal standard calibrated against the Ag/Ag⁺ reference electrode ($E_{1/2} = 85$ mV).

Topographic Characterization. All AFM height images were obtained using a Bruker Multimode 8 atomic force microscopy with tapping mode under nitrogen atmosphere. AFM tips with a force constant of 40 N/m and resonance frequency of c.a. 300 kHz were used in the AFM measurements. First-order image flattening was performed on the morphology images and the measured morphology heights were offset to set the scale start point to 0 nm.

Transmission Electron Microscopy. The morphology of active layers were investigated utilizing transmission electron microscopy Jeol JEM-1400 Plus equipped with a field emission LaB and a high-sensitivity CCD camera Gatan. The analysis of active layers was performed at an accelerating voltage of 120 kV. BHJ films were spin-coated as the active layers in devices on Glass/ITO/PSS substrates. Then, carefully detached from the substrates by dissolving the PSS interlayer in DI water and then transferred on lacey carbon film TEM grids.

GIWAXS Characterization. Two-dimensional (2D)-GIWAXS measurements were performed at the PLS-II 3C beamline of the Pohang Accelerator Laboratory (PAL) in the Republic of Korea. 2D-GIWAXS images were collected at 11 keV ($\lambda_{\text{GIWAXS}} = 1.1271$ Å) with an Eiger 4M detector (sample-to-detector distance: 209.01 mm). The incidence angle (α_i) of the X-ray beam was set between the critical angles of the thin film and substrate.

Solid-state NMR Spectroscopy. For high-field ssNMR experiments, thin-film materials were prepared by dissolving PM7-D5, Y12, and their blends in CB or 2-MeTHF solvents, which were spin coated on glass substrates using the same optimized conditions used for the

device fabrication. The neat and blended thin films were thermal annealed at 110 °C for 10 minutes and allowed to settle to cool to room temperature. All thin films were scratched from the glass substrates using a razor blade to collect these materials (~15 mg each) into glass vials, which were sealed with Parafilm and aluminum foil prior to shipment to the University of Lille for ssNMR studies. The neat Y12 and blend PM7-D5:Y12 materials were separately packed into 1.3 mm (outer diameter) cylindrical zirconia rotors fitted with Vespel[®] caps. All fast magic-angle spinning (MAS, 50 kHz) 1D ¹H, ¹³C, ¹⁹F, and 2D ¹H-¹³C, ¹H-¹H and ¹⁹F-¹⁹F NMR experiments were carried out on a Bruker AVANCE NEO (18.8 T, Larmor frequencies were ¹H = 800.1 MHz, ¹⁹F = 752.9 MHz, ¹³C = 201.2 MHz) spectrometer with a 1.3 mm H-X probehead. The ¹H and ¹³C spectra were calibrated with respect to neat TMS using adamantane as an external reference (¹³C resonance, 35.8 ppm, and the ¹H resonance, 1.85 ppm), and ¹⁹F MAS spectra were calibrated to the ¹⁹F chemical shift of Teflon at -132 ppm, in turn calibrated using neat CFCl₃ (¹⁹F, 0 ppm) as an external reference.

For the next compounds and blends, 1D ¹H MAS NMR experiments were carried out by co-adding 32 transients with a ¹H interscan delay of 3 seconds, and ¹⁹F spectra were acquired with 256 co-added transients, using an interscan delay of 10 seconds. 1D ¹H→¹³C CP-MAS NMR spectra of neat were acquired with 2048 co-added transients and for the blend films, 4096 transients were co-added. The ¹H-detected 2D ¹H-¹³C HETCOR spectra of neat compounds were acquired with 98 *t*₁ increments, each with co-addition of 104 transients, and for the blend film 98 *t*₁ increments were acquired, each with 128 co-added transients, with 4 ms CP contact time. 2D ¹⁹F-¹⁹F spin-diffusion NMR spectra were acquired with a three-pulse

noisy like sequence. For neat Y12 and PM7-D5:Y12, 64 t_1 increments were acquired, 16 co-added transients each, using a 200 ms mixing times.

J–V Curve, EQE and Impedance Measurements. All the photoresponse and electrical measurements were conducted inside a glovebox under a nitrogen atmosphere. PPG and all-pulse oximetry experiments performed on human subjects were carried out with informed consent and under regular conditions. *J–V* characteristics were measured with a high-quality optical fiber to guide the light from the solar simulator equipped with a Keithley 2635A source measurement unit. Illuminated *J–V* curves were measured under AM 1.5G illumination ($100 \text{ mW}\cdot\text{cm}^{-2}$). EQE measurements were conducted with an EQE system, in which the monochromatic light intensity was calibrated using a Si photodiode. The spectral distributions of the real and imaginary components of the impedance of all devices were measured by an impedance analyzer (Solartron SI 1260A) in the dark and under illumination. To prevent the effect of the AC signal on the impedance during the measurement, a small amplitude AC signal (40 mV) was applied.

LDR, Response Speed, and Noise Measurement. In the LDR and response speed measurements, the OPDs were illuminated by LEDs with different center peak wavelengths (850 nm or 940 nm, *Chanzon® LED*). For LDR measurement, the intensity of the LEDs was controlled by using a source measurement unit (Keithley 2602B SMU) and the light intensity was calibrated by using a commercial Si photodetector. The photo-current from OPDs was recorded by using a Keithley 4200-SCS Semiconductor Characterization System. For response speed measurement, a function generator (Stanford Research Systems DS345) was used to modulate the output light source with frequencies from 1 Hz to 200 kHz. The

modulated photocurrent signal from OPDs was amplified (Stanford Research Systems SRS570) and collected by an oscilloscope (Keysight DSOX3022T). The noise measurements of the devices were carried out in the dark using a battery-powered pre-amplifier (Stanford Research Systems SRS570) coupled with an oscilloscope (Keysight DSOX3022T) operated with fast Fourier transform analysis.

PPG and Blood Oxygen Saturation Measurement. The transmission-mode PPG and blood oxygen level measurement setups were illuminated by LEDs at different wavelengths (850 nm or 940 nm, *Chanzon® LED*). The light emitted from LEDs was partially transmitted through a fingertip of a volunteer, which was eventually recorded by our wearable OPD on the volunteer's finger. Considering the fast charge transport and sufficient charge carrier collection in the optimized devices, the OPD was directly operated under short-circuit current mode (*i.e.* without external voltage bias), and the photocurrent was amplified and converted to a voltage signal using a low noise amplifier SR570 (*Stanford Research Systems*). The output voltage signal was then displayed and extracted by using an oscilloscope (Keysight DSOX3022T) operated with fast Fourier transform analysis to get the real-time heart rate. Besides, no further calibration is required for pulse oximetry.

Chapter 5: Conclusions

In the organic electronic research field, replacing halogenated solvents in the processing of OPVs by green solvents is a required step prior to the commercialization of this technology. This dissertation highlights the development of green-solvent-processable OPVs and OPDs in terms of structure design, solvent selection, as well as device optimization and

characterization. By utilizing the material design strategy of side-chain engineering, we can obtain green solvents (*o*-xylene or 2-MeTHF) processable materials and devices, which offer relatively comparable efficiencies as devices cast from traditional halogenated solvents. Specifically, the dissertation outlines three major projects for advancing the development of green solvent processing organic electronic devices, including high-performance OPVs and OPDs. The first project investigates differences in the BHJ morphology and the subsequent changes of the optoelectronic properties of PPDT2FBT:PC₆₁BM systems processed from traditional (CB) and green (*o*-XY) solvents. Comparable good solubility of PPDT2FBT and PC₆₁BM in green solvent, and the corresponding film cast from green solvent with a well-maintained molecular ordering, and even improvement of the favorable BHJ morphology can be suitable for green solvent processing. The characterization of the BHJs at different length scales using AFM, GIWAXS, and RSoXS techniques indicate the presence of a well-mixed phase morphology with increased D:A interfacial areas and smaller domain sizes for the *o*-XY processed blend. 2D ssNMR spectroscopy results reveal that the PC₆₁BM molecules are intercalated into the sidechain regions of the donor polymers, in particular, the green-solvent-processed BHJ morphology exhibits specific 2D correlations that favor better intermixing and orientation of PC₆₁BM molecules in the vicinity of the PPDT2FBT aromatic core. These features of molecular packing facilitate the charge generation efficiency and transport in the green-solvent-processed devices. Hence, the optimized PPDT2FBT:PC₆₁BM devices processed with *o*-XY solvent exhibit a higher charge mobility, a faster charge extraction, and a higher PCE ($9.1 \pm 0.1\%$) compared to the CB cast devices ($7.0\% \pm 0.1\%$). Non-geminate recombination and extraction dynamics are determined by employing a quantitative analytical model based on capacitance spectroscopy. A higher charge carrier density and effective

mobility are observed in the solar cells prepared from o-XY. As a result, smaller competition factors stemming from slow non-geminate recombination and fast charge extraction are shown over the studied voltage range (-2 V to V_{OC}) for the green-solvent-processed devices, which correlates well with their higher J_{SC} and FF values. Ultimately, this work demonstrates that it is possible to obtain high PCEs for devices processed from green solvent, which are expected to pave the way towards cleaner commercialization and industrial-scale fabrication of OSCs. The following second project focuses on a series of 2-MeTHF processing OPV systems based on newly designed bulk heterojunction (BHJ) active layers consisting of PM7-D3/D5 donors and Y-series non-fullerene acceptors with systematic changes in their side chain length and positions. The optimized 2-MeTHF casting device based on PM7-D3:PTI04 exhibits a best PCE of 14.9%, which is also comparable to the well-known PM6:Y6 system processed from traditional halogenated solvents. The corresponding BHJ thin films processed from 2-MeTHF were characterized at different length scales with modern techniques. A preferred average domain size of around 25 nm with relatively high domain purity and a more uniform distribution of donor and acceptor inter-mixing is observed in the PM7-D3:PTI04 BHJ film. This facilitates the charge generation and collection process while limiting the recombination process in the device, leading to high effective mobility of charge carriers and remarkable performance. This work could provide further insight into the structure-property-morphology relationship for this field towards environmentally friendly and commercially viable high-performance organic solar cells. Furthermore, the third project proposed a bottom-up approach to develop high-performance PM7-D5:Y12 organic photodetectors for a range of applications. In achieving this, we combined molecular design of donor polymer (PM7-D5) with a biomass-derived environmentally friendly 2-MeTHF solvent. In addition, we provide

a detailed framework of understanding PM7-D5:Y12 BHJ morphological features at different length scales and the associated device physics, and the interrelationship between them. Molecularly designed PM7 offers backbone planarity as well as specific inter- and intramolecular interactions to obtain a suitable BHJ morphology. These optimal phase separation and intermolecular interactions in donor and acceptor domains are further characterized by advanced techniques in different length scales. The thick film strategy applied in the device optimization effectively blocks the charge injection, increases the shunt resistance and limits the leakage, leading to a substantially low dark current without a strong correlation with the applied bias (0.63 nA under -0.1 V and 3.60 nA under -2 V). These features enable self-powered OPDs to be fabricated. The presented OPD can retain a considerably high D_{sh}^* around 1.4×10^{13} to 3.2×10^{13} Jones from 400 nm to 900 nm under -0.1 V, which is one of the highest D_{sh}^* in comparison with reported OPDs. The most notable of all is, the green solvent processed can be integrated into flexible PET substrates to develop wearable devices. The self-powered wearable PM7:Y12 OPDs enable heart-rate monitoring (photoplethysmography) and oxygen saturation (pulse oximetry) measurements. Ultimately, the flexible organic photodetector may be directly used for large-scale roll-to-roll fabrication processing with environmentally friendly solvents as an efficient but low-cost real-time monitor for heart rate and blood oxygen level. A successful application of the material design and solvent selection strategies could potentially lead to an efficiency breakthrough in green-solvent-processable organic electronic devices.

For organic electronic devices, the selection of processing solvents becomes critical when changing from lab-scale testing to industrial-scale fabrication. Tons of solvents might be

required for one batch of commercialized OPV/OPD modules, and the lack of high-performance green solvent processing organic electronic devices really motivates the author to step into this field and make some small progress. O-xylene and 2-MeTHF are greener solvents compared with CF and CB, but our goal will be eventually real green solvents like ethanol and water. The author hopes that this dissertation could offer rational guidelines for developing greener solvents and active materials for high-performance and environmentally friendly organic photovoltaic and photodetectors, and the author also hope to see this work encourage the scientific community to develop more high-performance systems and eventually commercial products in the near future.

Chapter 6: References

- [1] C. Sun, F. Pan, H. Bin, J. Zhang, L. Xue, B. Qiu, Z. Wei, Z.-G. Zhang, Y. Li, *Nat Commun* **2018**, *9*, 743.
- [2] N. Schopp, V. V. Brus, J. Lee, G. C. Bazan, T.-Q. Nguyen, *Advanced Energy Materials* **2021**, *11*, 2002760.
- [3] J. Huang, J. Lee, J. Vollbrecht, V. V. Brus, A. L. Dixon, D. X. Cao, Z. Zhu, Z. Du, H. Wang, K. Cho, G. C. Bazan, T.-Q. Nguyen, *Advanced Materials* **2020**, *32*, 1906027.
- [4] A. Karki, J. Vollbrecht, A. L. Dixon, N. Schopp, M. Schrock, G. N. M. Reddy, T.-Q. Nguyen, *Advanced Materials* **2019**, *31*, 1903868.
- [5] N. A. Ran, J. A. Love, C. J. Takacs, A. Sadhanala, J. K. Beavers, S. D. Collins, Y. Huang, M. Wang, R. H. Friend, G. C. Bazan, T.-Q. Nguyen, *Advanced Materials* **2016**, *28*, 1482.
- [6] L. Hong, H. Yao, Z. Wu, Y. Cui, T. Zhang, Y. Xu, R. Yu, Q. Liao, B. Gao, K. Xian, H. Y. Woo, Z. Ge, J. Hou, *Advanced Materials* **2019**, *31*, 1903441.
- [7] A. Wadsworth, M. Moser, A. Marks, M. S. Little, N. Gasparini, C. J. Brabec, D. Baran, I. McCulloch, *Chem. Soc. Rev.* **2019**, *48*, 1596.

- [8] M. Seifrid, G. N. M. Reddy, B. F. Chmelka, G. C. Bazan, *Nat Rev Mater* **2020**, *5*, 910.
- [9] Y. Cui, H. Yao, J. Zhang, T. Zhang, Y. Wang, L. Hong, K. Xian, B. Xu, S. Zhang, J. Peng, Z. Wei, F. Gao, J. Hou, *Nat Commun* **2019**, *10*, 2515.
- [10] D. A. Kamkar, M. Wang, F. Wudl, T.-Q. Nguyen, *ACS Nano* **2012**, *6*, 1149.
- [11] H. Ren, J.-D. Chen, Y.-Q. Li, J.-X. Tang, *Advanced Science* **2021**, *8*, 2002418.
- [12] Y. Wei, H. Chen, T. Liu, S. Wang, Y. Jiang, Y. Song, J. Zhang, X. Zhang, G. Lu, F. Huang, Z. Wei, H. Huang, *Advanced Functional Materials* **2021**, *31*, 2106326.
- [13] J. Luo, X.-F. Rong, Y.-Y. Ye, W.-Z. Li, X.-Q. Wang, W. Wang, *Molecules* **2022**, *27*, 1632.
- [14] “Exciplexes in OLEDs: Principles and promises - ScienceDirect,” can be found under <https://www.sciencedirect.com/science/article/pii/S0927796X22000286>, **n.d.**
- [15] “Performance of OLED under mechanical strain: a review | SpringerLink,” can be found under <https://link.springer.com/article/10.1007/s10854-020-04652-5>, **n.d.**
- [16] T. Nguyen-Dang, K. Harrison, A. Lill, A. Dixon, E. Lewis, J. Vollbrecht, T. Hachisu, S. Biswas, Y. Visell, T.-Q. Nguyen, *Advanced Electronic Materials* **2021**, *7*, 2100519.
- [17] A. T. Lill, D. X. Cao, M. Schrock, J. Vollbrecht, J. Huang, T. Nguyen-Dang, V. V. Brus, B. Yurash, D. Leifert, G. C. Bazan, T.-Q. Nguyen, *Advanced Materials* **2020**, *32*, 1908120.
- [18] S. Biswas, Y. Shao, T. Hachisu, T. Nguyen-Dang, Y. Visell, *Advanced Materials Technologies* **2020**, *5*, 2000347.
- [19] “Department of Energy,” can be found under <https://www.energy.gov/>, **n.d.**
- [20] N. P. Holmes, H. Munday, M. G. Barr, L. Thomsen, M. A. Marcus, A. L. D. Kilcoyne, A. Fahy, J. van Stam, P. C. Dastoor, E. Moons, *Green Chem.* **2019**, *21*, 5090.
- [21] A. Karki, J. Vollbrecht, A. J. Gillett, S. Shuyong Xiao, Y. Yang, Z. Peng, N. Schopp, A. L. Dixon, S. Yoon, M. Schrock, H. Ade, G. N. Manjunatha Reddy, R. H. Friend, T.-Q. Nguyen, *Energy & Environmental Science* **2020**, *13*, 3679.
- [22] “Polymer Photovoltaic Cells: Enhanced Efficiencies via a Network of Internal Donor-Acceptor Heterojunctions | Science,” can be found under <https://www.science.org/doi/abs/10.1126/science.270.5243.1789>, **n.d.**
- [23] F. Laquai, D. Andrienko, C. Deibel, D. Neher, in *Elementary Processes in Organic Photovoltaics* (Ed.: K. Leo), Springer International Publishing, Cham, **2017**, pp. 267–291.

- [24] J. Nelson, *Materials Today* **2011**, *14*, 462.
- [25] C.-F. Lin, M. Zhang, S.-W. Liu, T.-L. Chiu, J.-H. Lee, *International Journal of Molecular Sciences* **2011**, *12*, 476.
- [26] Y. Cui, H. Yao, J. Zhang, K. Xian, T. Zhang, L. Hong, Y. Wang, Y. Xu, K. Ma, C. An, C. He, Z. Wei, F. Gao, J. Hou, *Advanced Materials* **2020**, *n/a*, 1908205.
- [27] Y. Cui, Y. Xu, H. Yao, P. Bi, L. Hong, J. Zhang, Y. Zu, T. Zhang, J. Qin, J. Ren, Z. Chen, C. He, X. Hao, Z. Wei, J. Hou, *Advanced Materials* **2021**, *33*, 2102420.
- [28] S. Zhang, L. Ye, H. Zhang, J. Hou, *Materials Today* **2016**, *19*, 533.
- [29] B. Walker, A. B. Tamayo, X.-D. Dang, P. Zalar, J. H. Seo, A. Garcia, M. Tantiwiwat, T.-Q. Nguyen, *Advanced Functional Materials* **2009**, *19*, 3063.
- [30] X.-D. Dang, A. B. Tamayo, J. Seo, C. V. Hoven, B. Walker, T.-Q. Nguyen, *Advanced Functional Materials* **2010**, *20*, 3314.
- [31] M. Corricelli, D. Altamura, M. L. Curri, T. Sibillano, D. Siliqi, A. Mazzone, N. Depalo, E. Fanizza, D. Zanchet, C. Giannini, M. Striccoli, *CrystEngComm* **2014**, *16*, 9482.
- [32] C. D. Liman, S. Choi, D. W. Breiby, J. E. Cochran, M. F. Toney, E. J. Kramer, M. L. Chabinye, *J. Phys. Chem. B* **2013**, *117*, 14557.
- [33] L. Ye, H. Hu, M. Ghasemi, T. Wang, B. A. Collins, J.-H. Kim, K. Jiang, J. H. Carpenter, H. Li, Z. Li, T. McAfee, J. Zhao, X. Chen, J. L. Y. Lai, T. Ma, J.-L. Bredas, H. Yan, H. Ade, *Nature Materials* **2018**, *17*, 253.
- [34] T. Araki, H. Ade, J. M. Stubbs, D. C. Sundberg, G. E. Mitchell, J. B. Kortright, A. L. D. Kilcoyne, *Appl. Phys. Lett.* **2006**, *89*, 124106.
- [35] W. C. Tsoi, P. G. Nicholson, J. S. Kim, D. Roy, T. L. Burnett, C. E. Murphy, J. Nelson, D. D. C. Bradley, J.-S. Kim, F. A. Castro, *Energy Environ. Sci.* **2011**, *4*, 3646.
- [36] D. C. Coffey, O. G. Reid, D. B. Rodovsky, G. P. Bartholomew, D. S. Ginger, *Nano Lett.* **2007**, *7*, 738.
- [37] M. Guide, X.-D. Dang, T.-Q. Nguyen, *Adv. Mater. Weinheim* **2011**, *23*, 2313.
- [38] T.-Y. Huang, H. Yan, M. Abdelsamie, V. Savikhin, S. A. Schneider, N. A. Ran, T.-Q. Nguyen, G. C. Bazan, M. F. Toney, *RSC Adv.* **2019**, *9*, 4106.
- [39] J. Rivnay, S. C. B. Mannsfeld, C. E. Miller, A. Salleo, M. F. Toney, *Chem. Rev.* **2012**, *112*, 5488.
- [40] J. Lee, S.-J. Ko, M. Seifrid, H. Lee, C. McDowell, B. R. Luginbuhl, A. Karki, K. Cho, T.-Q. Nguyen, G. C. Bazan, *Advanced Energy Materials* **n.d.**, *0*, 1801209.

- [41] N. A. Ran, S. Roland, J. A. Love, V. Savikhin, C. J. Takacs, Y.-T. Fu, H. Li, V. Coropceanu, X. Liu, J.-L. Brédas, G. C. Bazan, M. F. Toney, D. Neher, T.-Q. Nguyen, *Nature Communications* **2017**, *8*, 79.
- [42] X. Jiao, L. Ye, H. Ade, *Advanced Energy Materials* **2017**, *7*, 1700084.
- [43] B. P. Rand, D. Cheyons, K. Vasseur, N. C. Giebink, S. Mothy, Y. Yi, V. Coropceanu, D. Beljonne, J. Cornil, J.-L. Brédas, J. Genoe, *Advanced Functional Materials* **2012**, *22*, 2987.
- [44] X.-K. Chen, M. K. Ravva, H. Li, S. M. Ryno, J.-L. Brédas, *Advanced Energy Materials* **2016**, *6*, 1601325.
- [45] A. Karki, G.-J. A. H. Wetzelaer, G. N. M. Reddy, V. Nádaždy, M. Seifrid, F. Schauer, G. C. Bazan, B. F. Chmelka, P. W. M. Blom, T.-Q. Nguyen, *Advanced Functional Materials* **n.d.**, *0*, 1901109.
- [46] A. Melnyk, M. J. N. Junk, M. D. McGehee, B. F. Chmelka, M. R. Hansen, D. Andrienko, *J. Phys. Chem. Lett.* **2017**, *8*, 4155.
- [47] M. T. Seifrid, G. N. M. Reddy, C. Zhou, B. F. Chmelka, G. C. Bazan, *J. Am. Chem. Soc.* **2019**, *141*, 5078.
- [48] K. R. Graham, C. Cabanetos, J. P. Jahnke, M. N. Idso, A. El Labban, G. O. Ngongang Ndjawa, T. Heumueller, K. Vandewal, A. Salleo, B. F. Chmelka, A. Amassian, P. M. Beaujuge, M. D. McGehee, *J. Am. Chem. Soc.* **2014**, *136*, 9608.
- [49] N. C. Miller, E. Cho, M. J. N. Junk, R. Gysel, C. Risko, D. Kim, S. Sweetnam, C. E. Miller, L. J. Richter, R. J. Kline, M. Heeney, I. McCulloch, A. Amassian, D. Acevedo-Feliz, C. Knox, M. R. Hansen, D. Dudenko, B. F. Chmelka, M. F. Toney, J.-L. Brédas, M. D. McGehee, *Advanced Materials* **2012**, *24*, 6071.
- [50] N. Y. Doumon, The Degradation of Organic Solar Cells: From Chemistry to Device Physics through Materials, Thesis fully internal (DIV), University of Groningen, **2019**.
- [51] A. J. Heeger, *Advanced Materials* **2014**, *26*, 10.
- [52] V. V. Brus, *Semicond. Sci. Technol.* **2012**, *27*, 035024.
- [53] V. V. Brus, C. M. Proctor, N. A. Ran, T.-Q. Nguyen, *Advanced Energy Materials* **2016**, *6*, 1502250.
- [54] N. A. Ran, J. A. Love, M. C. Heiber, X. Jiao, M. P. Hughes, A. Karki, M. Wang, V. V. Brus, H. Wang, D. Neher, H. Ade, G. C. Bazan, T.-Q. Nguyen, *Advanced Energy Materials* **2018**, *8*, 1701073.

- [55] J. Huang, J. Lee, H. Nakayama, M. Schrock, D. X. Cao, K. Cho, G. C. Bazan, T.-Q. Nguyen, *ACS Nano* **2021**, *15*, 1753.
- [56] S. Xing, V. C. Nikolis, J. Kublitski, E. Guo, X. Jia, Y. Wang, D. Spoltore, K. Vandewal, H. Kleemann, J. Benduhn, K. Leo, *Advanced Materials* **2021**, *33*, 2102967.
- [57] Y. Wang, J. Kublitski, S. Xing, F. Dollinger, D. Spoltore, J. Benduhn, K. Leo, *Materials Horizons* **2022**, *9*, 220.
- [58] P. C. Y. Chow, T. Someya, *Advanced Materials* **2020**, *32*, 1902045.
- [59] C. M. Hansen, *Hansen Solubility Parameters: A User's Handbook, Second Edition*, CRC Press, Boca Raton, **2007**.
- [60] D. T. Duong, B. Walker, J. Lin, C. Kim, J. Love, B. Purushothaman, J. E. Anthony, T.-Q. Nguyen, *Journal of Polymer Science Part B: Polymer Physics* **2012**, *50*, 1405.
- [61] D. Negera, T. Yohannes, *IJASRE* **2018**, *4*, 119.
- [62] M. Weng, *J. Appl. Polym. Sci.* **2016**, *133*, n/a.
- [63] Z. Du, M. Mainville, J. Vollbrecht, A. L. Dixon, N. Schopp, M. Schrock, Z. Peng, J. Huang, S. Chae, H. Ade, M. Leclerc, G. N. M. Reddy, T.-Q. Nguyen, *Solar RRL* **2021**, *5*, 2100213.
- [64] H. Zhao, H. B. Naveed, B. Lin, X. Zhou, J. Yuan, K. Zhou, H. Wu, R. Guo, M. A. Scheel, A. Chumakov, S. V. Roth, Z. Tang, P. Müller-Buschbaum, W. Ma, *Advanced Materials* **2020**, *32*, 2002302.
- [65] M. D. Tyona, *Advances in materials Research* **2013**, *2*, 195.
- [66] M. C. Heiber, T. Okubo, S.-J. Ko, B. R. Luginbuhl, N. A. Ran, M. Wang, H. Wang, M. Afsar Uddin, H. Young Woo, G. C. Bazan, T.-Q. Nguyen, *Energy & Environmental Science* **2018**, *11*, 3019.
- [67] X. Guo, N. Zhou, S. J. Lou, J. Smith, D. B. Tice, J. W. Hennek, R. P. Ortiz, J. T. L. Navarrete, S. Li, J. Strzalka, L. X. Chen, R. P. H. Chang, A. Facchetti, T. J. Marks, *Nature Photon* **2013**, *7*, 825.
- [68] A. J. Heeger, *Advanced Materials* **2014**, *26*, 10.
- [69] G. Ji, W. Zhao, J. Wei, L. Yan, Y. Han, Q. Luo, S. Yang, J. Hou, C.-Q. Ma, *J. Mater. Chem. A* **2018**, *7*, 212.
- [70] R. Ma, T. Liu, Z. Luo, Q. Guo, Y. Xiao, Y. Chen, X. Li, S. Luo, X. Lu, M. Zhang, Y. Li, H. Yan, *Sci. China Chem.* **2020**, *63*, 325.
- [71] J. Hou, O. Inganäs, R. H. Friend, F. Gao, *Nature Materials* **2018**, *17*, 119.

- [72] J. Zhao, Y. Li, G. Yang, K. Jiang, H. Lin, H. Ade, W. Ma, H. Yan, *Nat Energy* **2016**, *1*, 1.
- [73] L. Ye, Y. Xiong, Q. Zhang, S. Li, C. Wang, Z. Jiang, J. Hou, W. You, H. Ade, *Advanced Materials* **2018**, *30*, 1705485.
- [74] L. Ye, Y. Xiong, S. Li, M. Ghasemi, N. Balar, J. Turner, A. Gadisa, J. Hou, B. T. O'Connor, H. Ade, *Advanced Functional Materials* **2017**, *27*, 1702016.
- [75] L. Ye, Y. Xiong, H. Yao, A. Gadisa, H. Zhang, S. Li, M. Ghasemi, N. Balar, A. Hunt, B. T. O'Connor, J. Hou, H. Ade, *Chem. Mater.* **2016**, *28*, 7451.
- [76] Z. Ma, B. Zhao, Y. Gong, J. Deng, Z. Tan, *Journal of Materials Chemistry A* **2019**, *7*, 22826.
- [77] L. Ye, Y. Xiong, Z. Chen, Q. Zhang, Z. Fei, R. Henry, M. Heeney, B. T. O'Connor, W. You, H. Ade, *Advanced Materials* **2019**, *31*, 1808153.
- [78] T. L. Nguyen, H. Choi, S.-J. Ko, M. A. Uddin, B. Walker, S. Yum, J.-E. Jeong, M. H. Yun, T. J. Shin, S. Hwang, J. Y. Kim, H. Y. Woo, *Energy Environ. Sci.* **2014**, *7*, 3040.
- [79] S. Lee, D. Jeong, C. Kim, C. Lee, H. Kang, H. Y. Woo, B. J. Kim, *ACS Nano* **2020**, *14*, 14493.
- [80] L. Perdigón-Toro, H. Zhang, A. Markina, J. Yuan, S. M. Hosseini, C. M. Wolff, G. Zuo, M. Stolterfoht, Y. Zou, F. Gao, D. Andrienko, S. Shoaee, D. Neher, *Advanced Materials* **2020**, *32*, 1906763.
- [81] N. A. Ran, S. Roland, J. A. Love, V. Savikhin, C. J. Takacs, Y.-T. Fu, H. Li, V. Coropceanu, X. Liu, J.-L. Brédas, G. C. Bazan, M. F. Toney, D. Neher, T.-Q. Nguyen, *Nat Commun* **2017**, *8*, 79.
- [82] F. D. Eisner, M. Azzouzi, Z. Fei, X. Hou, T. D. Anthopoulos, T. J. S. Dennis, M. Heeney, J. Nelson, *J. Am. Chem. Soc.* **2019**, *141*, 6362.
- [83] J. Wu, J. Lee, Y.-C. Chin, H. Yao, H. Cha, J. Luke, J. Hou, J.-S. Kim, J. R. Durrant, *Energy & Environmental Science* **2020**, *13*, 2422.
- [84] X. Song, N. Gasparini, L. Ye, H. Yao, J. Hou, H. Ade, D. Baran, *ACS Energy Lett.* **2018**, *3*, 669.
- [85] Z. Li, L. Ying, P. Zhu, W. Zhong, N. Li, F. Liu, F. Huang, Y. Cao, *Energy Environ. Sci.* **2019**, *12*, 157.
- [86] C. Sprau, F. Buss, M. Wagner, D. Landerer, M. Koppitz, A. Schulz, D. Bahro, W. Schabel, P. Scharfer, A. Colmann, *Energy & Environmental Science* **2015**, *8*, 2744.

- [87] M. Mainville, V. Tremblay, M. Z. Fenniri, A. Laventure, M. E. Farahat, R. Ambrose, G. C. Welch, I. G. Hill, M. Leclerc, *Asian Journal of Organic Chemistry* **2020**, *9*, 1318.
- [88] C. Kim, H. Kang, N. Choi, S. Lee, Y. Kim, J. Kim, Z. Wu, H. Young Woo, B. J. Kim, *Journal of Materials Chemistry C* **2020**, *8*, 15224.
- [89] W. Shen, M. Xiao, J. Tang, X. Wang, W. Chen, R. Yang, X. Bao, Y. Wang, J. Jiao, L. Huang, J. Liu, W. Wang, L. A. Belfiore, *RSC Advances* **2015**, *5*, 47451.
- [90] J. Yang, A. Garcia, T.-Q. Nguyen, *Appl. Phys. Lett.* **2007**, *90*, 103514.
- [91] X.-D. Dang, A. B. Tamayo, J. Seo, C. V. Hoven, B. Walker, T.-Q. Nguyen, *Advanced Functional Materials* **2010**, *20*, 3314.
- [92] B. A. Collins, Z. Li, J. R. Tumbleston, E. Gann, C. R. McNeill, H. Ade, *Advanced Energy Materials* **2013**, *3*, 65.
- [93] L. Ye, S. Li, X. Liu, S. Zhang, M. Ghasemi, Y. Xiong, J. Hou, H. Ade, *Joule* **2019**, *3*, 443.
- [94] E. Gann, A. T. Young, B. A. Collins, H. Yan, J. Nasiatka, H. A. Padmore, H. Ade, A. Hexemer, C. Wang, *Review of Scientific Instruments* **2012**, *83*, 045110.
- [95] C. M. Proctor, C. Kim, D. Neher, T.-Q. Nguyen, *Advanced Functional Materials* **2013**, *23*, 3584.
- [96] K. D. Rosenthal, M. P. Hughes, B. R. Luginbuhl, N. A. Ran, A. Karki, S.-J. Ko, H. Hu, M. Wang, H. Ade, T.-Q. Nguyen, *Advanced Energy Materials* **2019**, *9*, 1901077.
- [97] L. A. Perez, K. W. Chou, J. A. Love, T. S. van der Poll, D.-M. Smilgies, T.-Q. Nguyen, E. J. Kramer, A. Amassian, G. C. Bazan, *Advanced Materials* **2013**, *25*, 6380.
- [98] F. Etzold, I. A. Howard, N. Forler, A. Melnyk, D. Andrienko, M. Ryan Hansen, F. Laquai[‡], *Energy & Environmental Science* **2015**, *8*, 1511.
- [99] B. Yurash, D. Leifert, G. N. M. Reddy, D. X. Cao, S. Biberger, V. V. Brus, M. Seifrid, P. J. Santiago, A. Köhler, B. F. Chmelka, G. C. Bazan, T.-Q. Nguyen, *Chem. Mater.* **2019**, *31*, 6715.
- [100] M. T. Seifrid, G. N. M. Reddy, C. Zhou, B. F. Chmelka, G. C. Bazan, *J. Am. Chem. Soc.* **2019**, *141*, 5078.
- [101] J. Vollbrecht, J. Lee, S.-J. Ko, V. V. Brus, A. Karki, W. Le, M. Seifrid, M. J. Ford, K. Cho, G. C. Bazan, T.-Q. Nguyen, *Journal of Materials Chemistry C* **2020**, *8*, 15175.
- [102] M. R. Hansen, R. Graf, H. W. Spiess, *Chem. Rev.* **2016**, *116*, 1272.

- [103] K. R. Graham, C. Cabanetos, J. P. Jahnke, M. N. Idso, A. El Labban, G. O. Ngongang Ndjawa, T. Heumueller, K. Vandewal, A. Salleo, B. F. Chmelka, A. Amassian, P. M. Beaujuge, M. D. McGehee, *J. Am. Chem. Soc.* **2014**, *136*, 9608.
- [104] N. Cates, E. Cho, R. Gysel, C. Risko, V. Coropceanu, C. E. Miller, S. Sweetnam, A. Sellinger, M. Heeney, I. McCulloch, J.-L. Brédas, M. F. Toney, M. D. McGehee, *Advanced Energy Materials* **2012**, *2*, 1208.
- [105] M. Seifrid, G. N. M. Reddy, B. F. Chmelka, G. C. Bazan, *Nature Reviews Materials* **2020**, *5*, 910.
- [106] D. Credgington, F. C. Jamieson, B. Walker, T.-Q. Nguyen, J. R. Durrant, *Advanced Materials* **2012**, *24*, 2135.
- [107] G. F. A. Dibb, F. C. Jamieson, A. Maurano, J. Nelson, J. R. Durrant, *J. Phys. Chem. Lett.* **2013**, *4*, 803.
- [108] D. Baran, N. Gasparini, A. Wadsworth, C. H. Tan, N. Wehbe, X. Song, Z. Hamid, W. Zhang, M. Neophytou, T. Kirchartz, C. J. Brabec, J. R. Durrant, I. McCulloch, *Nat Commun* **2018**, *9*, 2059.
- [109] C.-H. Tan, J. Gorman, A. Wadsworth, S. Holliday, S. Subramaniyan, S. A. Jenekhe, D. Baran, I. McCulloch, J. R. Durrant, *Chemical Communications* **2018**, *54*, 2966.
- [110] C. M. Proctor, S. Albrecht, M. Kuik, D. Neher, T.-Q. Nguyen, *Advanced Energy Materials* **2014**, *4*, 1400230.
- [111] J. Vollbrecht, V. V. Brus, S.-J. Ko, J. Lee, A. Karki, D. X. Cao, K. Cho, G. C. Bazan, T.-Q. Nguyen, *Advanced Energy Materials* **2019**, *9*, 1901438.
- [112] D. Baran, T. Kirchartz, S. Wheeler, S. Dimitrov, M. Abdelsamie, J. Gorman, R. S. Ashraf, S. Holliday, A. Wadsworth, N. Gasparini, P. Kaienburg, H. Yan, A. Amassian, C. J. Brabec, J. R. Durrant, I. McCulloch, *Energy & Environmental Science* **2016**, *9*, 3783.
- [113] H. Cha, S. Wheeler, S. Holliday, S. D. Dimitrov, A. Wadsworth, H. H. Lee, D. Baran, I. McCulloch, J. R. Durrant, *Advanced Functional Materials* **2018**, *28*, 1704389.
- [114] T. Kirchartz, B. E. Pieters, J. Kirkpatrick, U. Rau, J. Nelson, *Phys. Rev. B* **2011**, *83*, 115209.
- [115] D. Credgington, R. Hamilton, P. Atienzar, J. Nelson, J. R. Durrant, *Advanced Functional Materials* **2011**, *21*, 2744.
- [116] R. Hamilton, C. G. Shuttle, B. O'Regan, T. C. Hammant, J. Nelson, J. R. Durrant, *J. Phys. Chem. Lett.* **2010**, *1*, 1432.

- [117] C. G. Shuttle, R. Hamilton, B. C. O'Regan, J. Nelson, J. R. Durrant, *Proceedings of the National Academy of Sciences* **2010**, *107*, 16448.
- [118] C. M. Proctor, T.-Q. Nguyen, *Appl. Phys. Lett.* **2015**, *106*, 083301.
- [119] S. D. Collins, N. A. Ran, M. C. Heiber, T.-Q. Nguyen, *Advanced Energy Materials* **2017**, *7*, 1602242.
- [120] V. V. Brus, H. K. Lee, C. M. Proctor, M. Ford, X. Liu, M. A. Burgers, J. Lee, G. C. Bazan, T.-Q. Nguyen, *Advanced Energy Materials* **2018**, *8*, 1801807.
- [121] S. Albrecht, J. R. Tumbleston, S. Janietz, I. Dumsch, S. Allard, U. Scherf, H. Ade, D. Neher, *J. Phys. Chem. Lett.* **2014**, *5*, 1131.
- [122] G. F. A. Dibb, T. Kirchartz, D. Credginton, J. R. Durrant, J. Nelson, *J. Phys. Chem. Lett.* **2011**, *2*, 2407.
- [123] D. Bartesaghi, I. del C. Pérez, J. Kniepert, S. Roland, M. Turbiez, D. Neher, L. J. A. Koster, *Nat Commun* **2015**, *6*, 7083.
- [124] A. Karki, J. Vollbrecht, A. J. Gillett, P. Selter, J. Lee, Z. Peng, N. Schopp, A. L. Dixon, M. Schrock, V. Nádaždy, F. Schauer, H. Ade, B. F. Chmelka, G. C. Bazan, R. H. Friend, T.-Q. Nguyen, *Advanced Energy Materials* **2020**, *10*, 2001203.
- [125] F. Grenier, K. Goudreau, M. Leclerc, *J. Am. Chem. Soc.* **2017**, *139*, 2816.
- [126] E. Verploegen, C. E. Miller, K. Schmidt, Z. Bao, M. F. Toney, *Chem. Mater.* **2012**, *24*, 3923.
- [127] J. Ilavsky, *J Appl Cryst* **2012**, *45*, 324.
- [128] G. N. M. Reddy, M. Malon, A. Marsh, Y. Nishiyama, S. P. Brown, *Anal. Chem.* **2016**, *88*, 11412.
- [129] Y. Hong, G. N. Manjunatha Reddy, Y. Nishiyama, *Solid State Nuclear Magnetic Resonance* **2020**, *106*, 101651.
- [130] V. Pace, P. Hoyos, L. Castoldi, P. Domínguez de María, A. R. Alcántara, *ChemSusChem* **2012**, *5*, 1369.
- [131] O. Al Musaimi, Y. E. Jad, A. Kumar, A. El-Faham, J. M. Collins, A. Basso, B. G. de la Torre, F. Albericio, *Org. Process Res. Dev.* **2018**, *22*, 1809.
- [132] J. Yuan, Y. Zhang, L. Zhou, G. Zhang, H.-L. Yip, T.-K. Lau, X. Lu, C. Zhu, H. Peng, P. A. Johnson, M. Leclerc, Y. Cao, J. Ulanski, Y. Li, Y. Zou, *Joule* **2019**, *3*, 1140.
- [133] I. Pelse, A. L. Jones, L. J. Richter, J. R. Reynolds, *Chem. Mater.* **2021**, *33*, 657.

- [134] H.-C. Liao, C.-C. Ho, C.-Y. Chang, M.-H. Jao, S. B. Darling, W.-F. Su, *Materials Today* **2013**, *16*, 326.
- [135] N. Gasparini, A. Gregori, M. Salvador, M. Biele, A. Wadsworth, S. Tedde, D. Baran, I. McCulloch, C. J. Brabec, *Advanced Materials Technologies* **2018**, *3*, 1800104.
- [136] N. Tokmoldin, J. Vollbrecht, S. M. Hosseini, B. Sun, L. Perdigón-Toro, H. Y. Woo, Y. Zou, D. Neher, S. Shoaee, *Adv. Energy Mater.* **2021**, 2100804.
- [137] X. Guo, N. Zhou, S. J. Lou, J. Smith, D. B. Tice, J. W. Hennek, R. P. Ortiz, J. T. L. Navarrete, S. Li, J. Strzalka, L. X. Chen, R. P. H. Chang, A. Facchetti, T. J. Marks, *Nature Photon* **2013**, *7*, 825.
- [138] H. Xu, J. Liu, J. Zhang, G. Zhou, N. Luo, N. Zhao, *Advanced Materials* **2017**, *29*, 1700975.
- [139] R. Weissleder, *Nat Biotechnol* **2001**, *19*, 316.
- [140] C. M. Lochner, Y. Khan, A. Pierre, A. C. Arias, *Nat Commun* **2014**, *5*, 5745.
- [141] T. Yokota, P. Zalar, M. Kaltenbrunner, H. Jinno, N. Matsuhisa, H. Kitanosako, Y. Tachibana, W. Yukita, M. Koizumi, T. Someya, *Science Advances* **2016**, *2*, e1501856.
- [142] Z. Zhong, L. Bu, P. Zhu, T. Xiao, B. Fan, L. Ying, G. Lu, G. Yu, F. Huang, Y. Cao, *ACS Appl. Mater. Interfaces* **2019**, *11*, 8350.
- [143] Y.-L. Wu, K. Fukuda, T. Yokota, T. Someya, *Advanced Materials* **2019**, *31*, 1903687.
- [144] M. S. Jang, S. Yoon, K. M. Sim, J. Cho, D. S. Chung, *J. Phys. Chem. Lett.* **2018**, *9*, 8.
- [145] J. H. Kim, A. Liess, M. Stolte, A.-M. Krause, V. Stepanenko, C. Zhong, D. Bialas, F. Spano, F. Würthner, *Advanced Materials* **2021**, *33*, 2100582.
- [146] W. Li, Y. Xu, X. Meng, Z. Xiao, R. Li, L. Jiang, L. Cui, M. Zheng, C. Liu, L. Ding, Q. Lin, *Advanced Functional Materials* **2019**, *29*, 1808948.
- [147] W. Wang, F. Zhang, M. Du, L. Li, M. Zhang, K. Wang, Y. Wang, B. Hu, Y. Fang, J. Huang, *Nano Lett.* **2017**, *17*, 1995.
- [148] R. Nie, X. Deng, L. Feng, G. Hu, Y. Wang, G. Yu, J. Xu, *Small* **2017**, *13*, 1603260.
- [149] M. E. Meek, R. Beauchamp, G. Long, D. Moir, L. Turner, M. Walker, *J Toxicol Environ Health B Crit Rev* **2002**, *5*, 283.
- [150] B. J. Versonnen, K. Arijs, T. Verslycke, W. Lema, C. R. Janssen, *Environmental Toxicology and Chemistry* **2003**, *22*, 329.

- [151] M. Braechevelt, G. Mirschel, A. Wiessner, M. Rueckert, N. Reiche, C. Vogt, A. Schultz, H. Paschke, P. Kuschke, M. Kaestner, *Ecological Engineering* **2008**, *33*, 45.
- [152] S. Bao, H. Yang, H. Fan, J. Zhang, Z. Wei, C. Cui, Y. Li, *Advanced Materials* **2021**, *33*, 2105301.
- [153] S. Albrecht, W. Schindler, J. Kurpiers, J. Kniepert, J. C. Blakesley, I. Dumsch, S. Allard, K. Fostiropoulos, U. Scherf, D. Neher, *J. Phys. Chem. Lett.* **2012**, *3*, 640.
- [154] C.-T. Yen, Y.-C. Huang, Z.-L. Yu, H.-C. Cha, H.-T. Hsiao, Y.-T. Liang, F. S.-S. Chien, C.-S. Tsao, *ACS Appl. Mater. Interfaces* **2018**, *10*, 33399.
- [155] A. A. Rajkiewicz, K. Skowerski, B. Trzaskowski, A. Kajetanowicz, K. Grela, *ACS Omega* **2019**, *4*, 1831.
- [156] S. Monticelli, L. Castoldi, I. Murgia, R. Senatore, E. Mazzeo, J. Wackerlig, E. Urban, T. Langer, V. Pace, *Monatsh Chem* **2017**, *148*, 37.
- [157] M. Pomerantz, A. S. Amarasekara, H. V. R. Dias, *J. Org. Chem.* **2002**, *67*, 6931.
- [158] J. Fang, Z. Wang, Y. Chen, Q. Zhang, J. Zhang, L. Zhu, M. Zhang, Z. Cui, Z. Wei, H. Ade, C.-Q. Ma, *Cell Reports Physical Science* **2022**, *3*, 100983.
- [159] B. R. Luginbuhl, P. Raval, T. Pawlak, Z. Du, T. Wang, G. Kupgan, N. Schopp, S. Chae, S. Yoon, A. Yi, H. Jung Kim, V. Coropceanu, J.-L. Brédas, T.-Q. Nguyen, G. N. M. Reddy, *Advanced Materials* **2022**, *34*, 2105943.
- [160] H. N. Tsao, D. M. Cho, I. Park, M. R. Hansen, A. Mavrinskiy, D. Y. Yoon, R. Graf, W. Pisula, H. W. Spiess, K. Müllen, *J. Am. Chem. Soc.* **2011**, *133*, 2605.
- [161] D. Dudenko, A. Kiersnowski, J. Shu, W. Pisula, D. Sebastiani, H. W. Spiess, M. R. Hansen, *Angewandte Chemie* **2012**, *124*, 11230.
- [162] S. R. Chaudhari, J. M. Griffin, K. Broch, A. Lesage, V. Lemaure, D. Dudenko, Y. Olivier, H. Sirringhaus, L. Emsley, C. P. Grey, *Chemical Science* **2017**, *8*, 3126.
- [163] Q. Wang, S. Böckmann, F. Günther, M. Streiter, M. Zerson, A. D. Scaccabarozzi, W. L. Tan, H. Komber, C. Deibel, R. Magerle, S. Gemming, C. R. McNeill, M. Caironi, M. R. Hansen, M. Sommer, *Chem. Mater.* **2021**, *33*, 2635.
- [164] D. Yang, D. Ma, *Advanced Optical Materials* **2019**, *7*, 1800522.
- [165] A. Armin, M. Hamsch, I. K. Kim, P. L. Burn, P. Meredith, E. B. Namdas, *Laser & Photonics Reviews* **2014**, *8*, 924.
- [166] I. K. Kim, J. H. Jo, J. (Brian) Lee, Y. J. Choi, *Organic Electronics* **2018**, *57*, 89.
- [167] Z. Wu, Y. Zhai, H. Kim, J. D. Azoulay, T. N. Ng, *Acc. Chem. Res.* **2018**, *51*, 3144.

- [168] Y. Fang, A. Armin, P. Meredith, J. Huang, *Nature Photon* **2019**, *13*, 1.
- [169] J. Liu, M. Gao, J. Kim, Z. Zhou, D. S. Chung, H. Yin, L. Ye, *Materials Today* **2021**, *51*, 475.
- [170] C. Fuentes-Hernandez, W.-F. Chou, T. M. Khan, L. Diniz, J. Lukens, F. A. Larrain, V. A. Rodriguez-Toro, B. Kippelen, *Science* **2020**, *370*, 698.
- [171] J. G. Webster, *Design of Pulse Oximeters*, CRC Press, **1997**.
- [172] M. Nitzan, S. Noach, E. Tobal, Y. Adar, Y. Miller, E. Shalom, S. Engelberg, *Sensors* **2014**, *14*, 7420.
- [173] F. E. Robles, S. Chowdhury, A. Wax, *Biomed. Opt. Express*, *BOE* **2010**, *1*, 310.
- [174] D.-M. Smilgies, *J Appl Cryst* **2009**, *42*, 1030.
- [175] T. Wang, A. J. Pearson, D. G. Lidzey, *J. Mater. Chem. C* **2013**, *1*, 7266.
- [176] “Acceptor Gradient Polymer Donors for Non-Fullerene Organic Solar Cells | Chemistry of Materials,” can be found under <https://pubs.acs.org/doi/10.1021/acs.chemmater.9b03327>, **n.d.**
- [177] Y.-S. Wu, Y.-C. Lin, S.-Y. Hung, C.-K. Chen, Y.-C. Chiang, C.-C. Chueh, W.-C. Chen, *Macromolecules* **2020**, *53*, 4968.
- [178] W. Choi, Y. S. Choi, H. Kim, J. Yoon, Y. Kwon, T. Kim, J.-H. Ryu, J. H. Lee, W. Lee, J. Huh, J. M. Kim, W.-S. Yoon, *Chem. Mater.* **2021**, *33*, 1935.
- [179] A. L. Jones, C. H. Y. Ho, P. R. Riley, I. Angunawela, H. Ade, F. So, J. R. Reynolds, *J. Mater. Chem. C* **2020**, *8*, 15459.
- [180] F. E. Robles, S. Chowdhury, A. Wax, *Biomed Opt Express* **2010**, *1*, 310.

Chapter 7: Appendix

GIWAXS Analysis of the Pristine Film of PPDT2FBT and PC₆₁BM. Grazing incidence wide angle X-ray scattering was performed on the neat films of PPDT2FBT and PC₆₁BM to observe the effect of solvent choice (o-Xy or chlorobenzene) on the molecular ordering within the active layer. The 2D GIWAXS images of the pristine films are shown in Figure S1. The 1D linecuts show the scattered intensity in the q_z plane, perpendicular to the substrate, and the q_{xy} plane, parallel to the substrate (Figure S2). Coherence lengths (L_c) calculated using the Scherrer equation are the distance over which the molecular order producing each scattering feature is maintained within the film.^[174] Both blend components display face-on orientation relative to the substrate indicated by intense scattering at high q_z and low q_{xy} , which has been shown to facilitate the charge transport in the vertical direction of the active layer.^[175]

The fullerene acceptor PC₆₁BM is isotropically oriented as shown by the scattering rings at approximately 0.7 \AA^{-1} (0.9 nm) and 1.3 \AA^{-1} (0.5 nm). These features are maintained within the film for distances of approximately 2 nm as indicated by the calculated L_c values. PC₆₁BM spin cast from chlorobenzene maintain these ordered features over a slightly longer distance. Although the scattering feature at $1.32 q_{xy}$ does not change significantly when either solvent is used, other L_c values differ by 0.36-1.05 nm. The molecular order within the PPDT2FBT polymer differs to a significantly greater degree when casted from chlorobenzene or o-xylene. The polymer spun from chlorobenzene displays π - π stacking both out-of plane (face-on) at $1.66 q_z$ (d: 0.38 nm; L_c : 2.58 nm) and in-plane (edge-on) $1.64 q_{xy}$ (d: 0.38 nm; L_c : 3.24 nm). However, the face-on π - π scattering is more intense leading to a conclusion that although the

edge-on π - π stacks are maintained over a slightly longer distance there is a greater portion of polymer units orienting face-on within this film. Further, in-plane lamellar stacking at $0.29 q_{xy}$ (d: 2.16 nm; L_c : 14.75 nm) corresponding to face-on units is maintained over a longer distance. Scattering features at 0.58 and $1.12 q_{xy}$ also indicate that these lamellar stacks are well maintained as they extend through the film because these are higher order reflections, appearing near integer multiples of the original $0.29 q_{xy}$ peak. In contrast to this, the lamellar stacking from edge-on units $0.30 q_z$ (d: 2.12 nm; L_c : 9.04 nm) is maintained over a shorter L_c and results in only one well defined higher order reflection at $0.60 q_z$. Spin casting from o-xylene instead of chlorobenzene results in a significantly diminished fraction of scattering from the out-of-plane π - π stacking peak $1.66 q_z$ (d: 0.38 nm; L_c : 3.23 nm) in comparison with scattering from lamellar stacking of edge-on units as shown in the 1D linecuts. The xylene-cast film contains lamellar stacking from face-on units at $0.28 q_{xy}$ (d: 2.21 nm; L_c : 18.36 nm) which is maintained over twice the distance of this stacking from edge-on units at $0.28 q_z$ (d: 2.23 nm; L_c : 6.38 nm). Other peaks in the out-of-plane direction for this film can be attributed to higher order reflections of the lamellar stacking peak from edge-on units. Although lamellar stacking contributes to a much greater portion of the scattering profile when the polymer is spin cast from o-xylene, the dominant π - π stacking motif is still face-on.

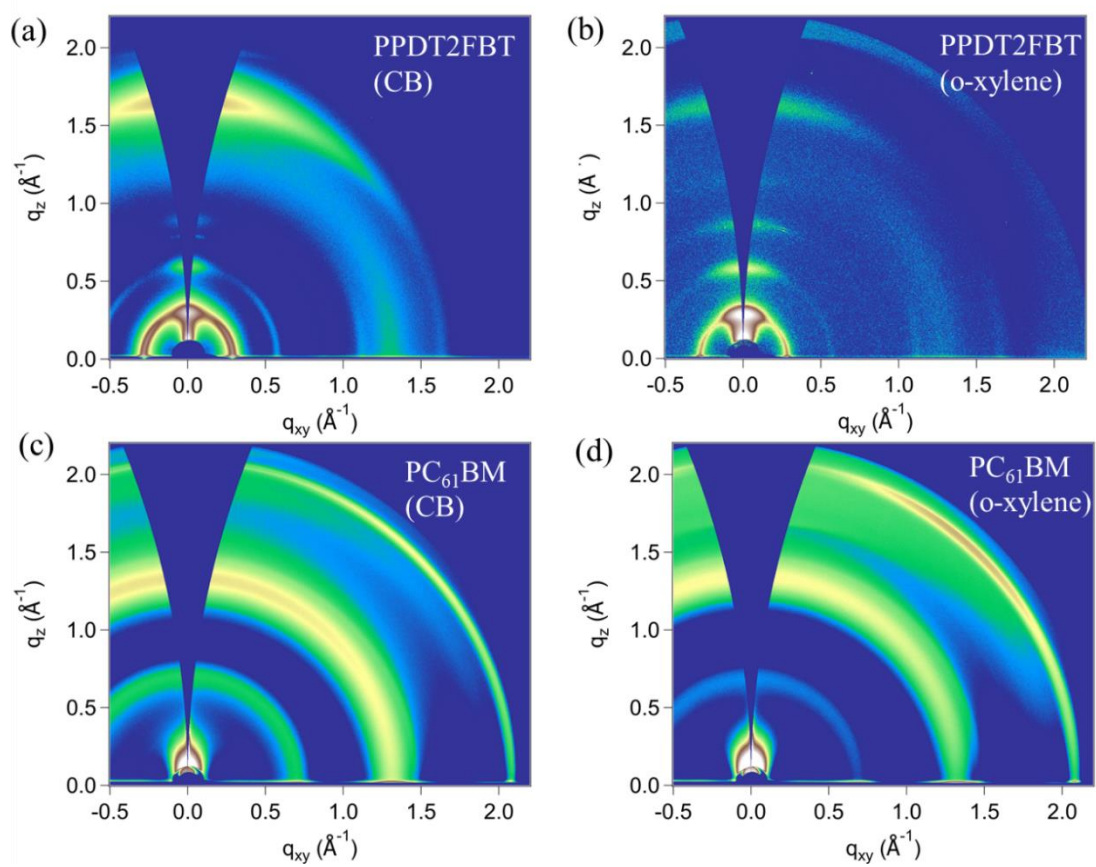
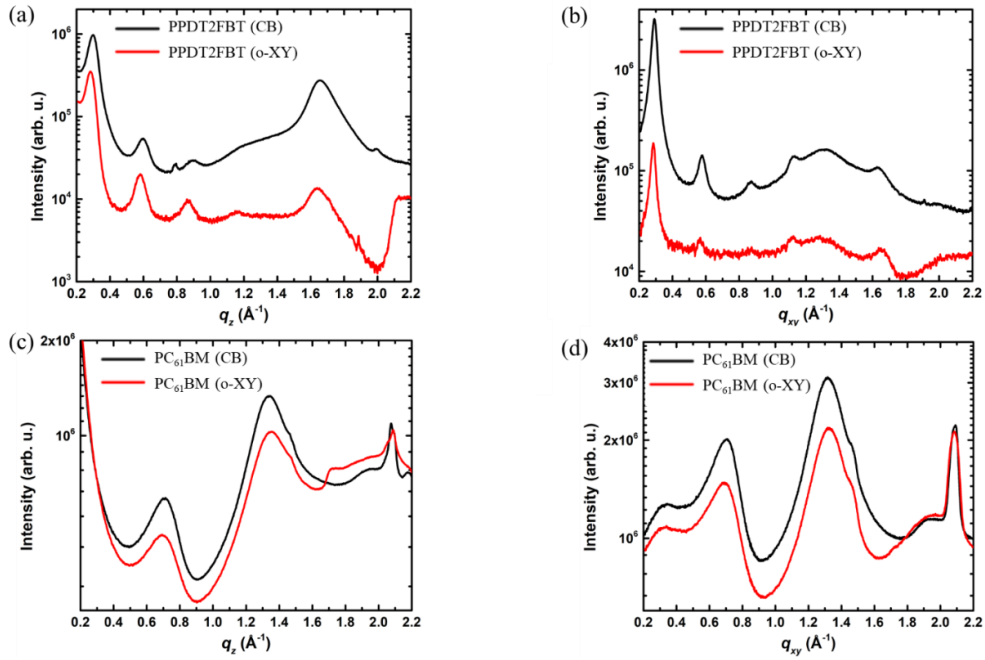


Figure S1. 2-D GIWAXS images of the pristine PPDT2FBT films processed with a) CB and b) o-XY solvent and PC₆₁BM films processed with c) CB and d) o-XY solvent.



PPDT2FBT (CB)					
Qz (Å ⁻¹)	d (nm)	Lc (nm)	Qxy (Å ⁻¹)	d (nm)	Lc (nm)
0.30	2.12	9.04	0.29	2.16	14.75
0.60	1.06	4.87	0.58	1.09	9.68
1.66	0.38	2.58	1.12	0.56	8.27
			1.31	0.48	1.36
			1.64	0.38	3.24

PPDT2FBT (o-XY)					
Qz (Å ⁻¹)	d (nm)	Lc (nm)	Qxy (Å ⁻¹)	d (nm)	Lc (nm)
0.28	2.23	6.38	0.28	2.21	18.36
0.58	1.08	6.59			
0.87	0.73	7.19			
1.64	0.38	3.23			

PC ₆₁ BM (CB)					
Qz (Å ⁻¹)	d (nm)	Lc (nm)	Qxy (Å ⁻¹)	d (nm)	Lc (nm)
0.71	0.89	1.80	0.70	0.89	2.46
1.34	0.47	1.84	1.32	0.48	2.18

PC ₆₁ BM (o-XY)					
Qz (Å ⁻¹)	d (nm)	Lc (nm)	Qxy (Å ⁻¹)	d (nm)	Lc (nm)
0.69	0.91	1.28	0.72	0.87	1.41
1.35	0.46	1.48	1.32	0.47	2.06

Figure S2. In-plane and out-of-plane GIWAXS profiles for the pristine a,b) PPDT2FBT and c,d) PC₆₁BM films cast from CB and o-XY.

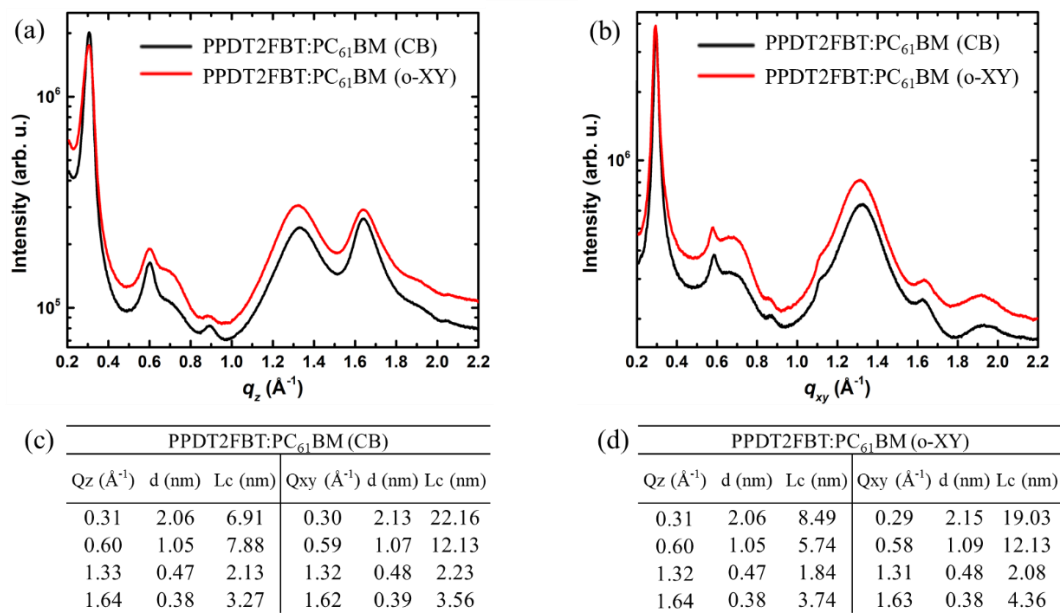


Figure S3. In-plane and out-of-plane GIWAXS profiles for the PPDT2FBT:PC₆₁BM blend films casted from CB and o-XY on ZnO/ITO substrates.

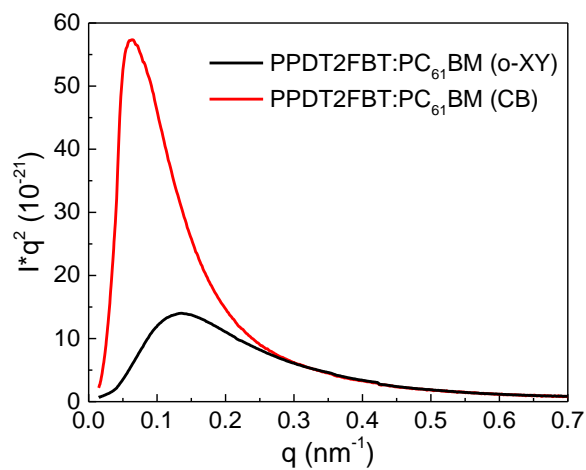


Figure S4. Lorentz corrected and film thickness-normalized RSoXS profiles for the PPDT2FBT:PC₆₁BM blend casted from CB and o-XY.

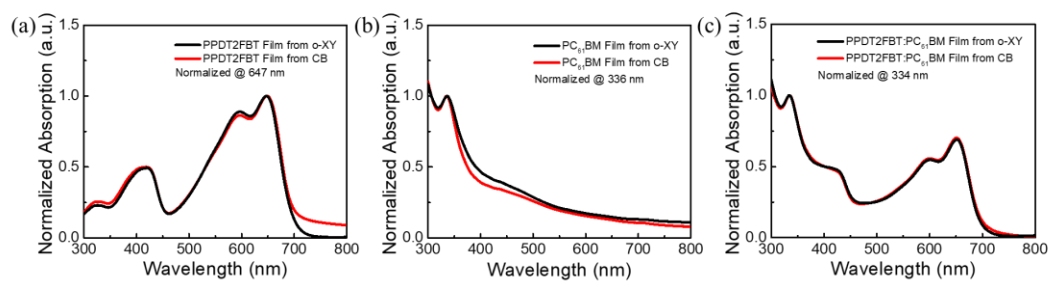


Figure S5. Normalized UV-vis absorption spectra of a) PPDT2FBT, b) PC₆₁BM and c) PPDT2FBT:PC₆₁BM films.

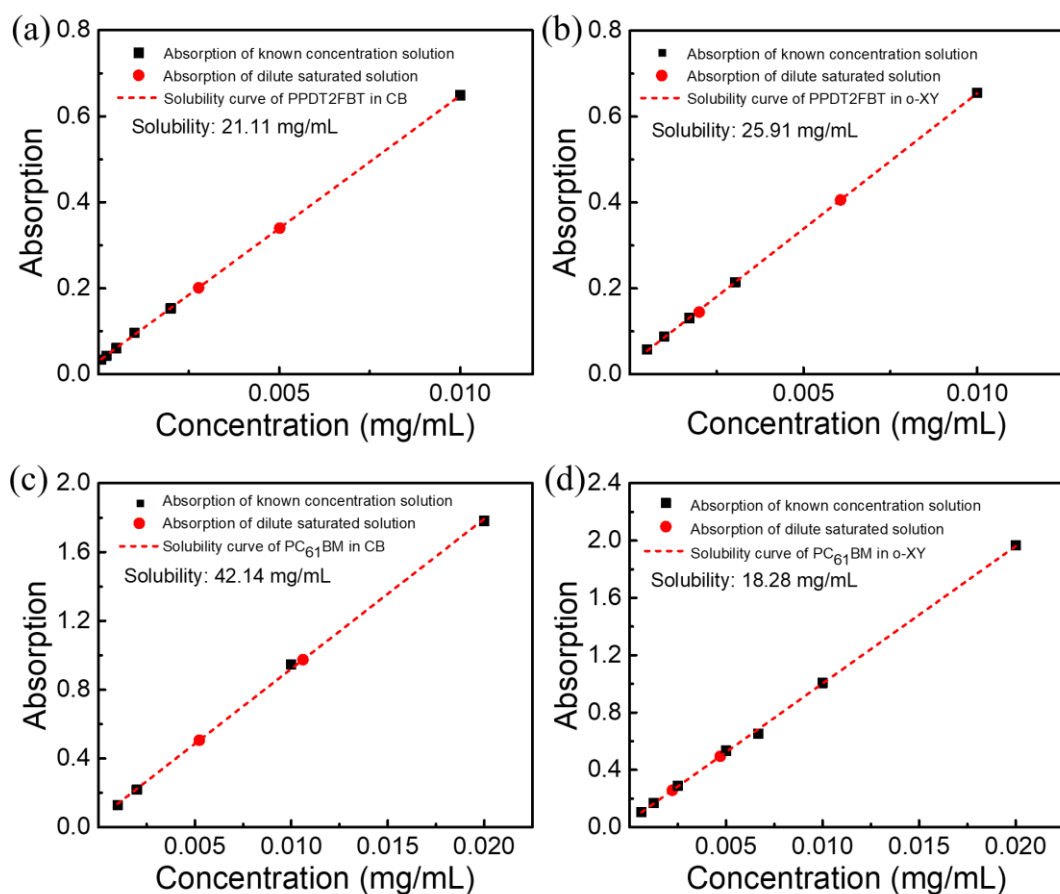


Figure S6. Spectra used to calculate solubility. Plot of PPDT2FBT concentration in a) CB and b) o-XY vs. absorbance at 643 nm. Plot of PC₆₁BM concentration in c) CB and d) o-XY vs. absorbance at 331 nm.

Drying time of the PPDT2FBT:PC₆₁BM films. The drying time of the PPDT2FBT:PC₆₁BM films can be calculated with the HSPIP program (5th Edition 5.2.05). The speed of the air (V_{air}) can be described as the average linear velocity of the spin coating speed, which can be shown as

$$V_{air} = \omega r = 2\pi n r \quad (S1)$$

where r is the average radial distance, ω is the rotational speed, and n is the revolutions per minute during the spin coating. Considering that the size of the glass substrate is 1 cm \times 1cm and the center of the rotation lies in the middle of the substrate, the average radial distance r should be 0.25 cm. And the revolutions per minute are equal to the spin coating speeds, which is 1100 rpm for CB and 1400 rpm for o-XY. The boiling point used for the calculation are 144 °C for o-XY, 131°C for CB, 248 °C for AA and 144 °C for DIO. With all these parameters put in the HSPIP program, the drying time of the PPDT2FBT:PC₆₁BM films under different processing conditions from CB and o-XY are calculated and shown in **Table S1**.

Table S1. Calculated drying time of the PPDT2FBT:PC₆₁BM films under different processing conditions from CB and o-XY.

Casting Temperature (°C)	Solvent	CB(1% DIO)	CB	o-XY (1% AA)	o-XY
	25		3000s	7.14s	22.9s
110		4.895s	0.357s	0.4s	0.31 s

Solid state NMR analysis. **Figure S7** compares the ^1H MAS NMR spectra, whereby the ^1H signals from alkyl sidechains and aromatic groups can be distinguished and identified for the donor and acceptor molecules. However, the ^1H signals correspond to specific aromatic moieties such as phenyl and thiophene protons were not evidently resolved in the spectra of blends, which obscures the accurate spectral assignments. By comparison, intrinsic high-resolution associated with ^{13}C NMR allows the ^{13}C signals correspond to different carbon sites in donor and acceptor molecules to be distinguished, identified and compared. In a $^{13}\text{C}\{^1\text{H}\}$ cross-polarization(CP)-MAS experiment, $^1\text{H}\rightarrow^{13}\text{C}$ polarization transfer is achieved via inter and intramolecular ^{13}C - ^1H dipolar interactions, facilitating the enhancement of ^{13}C signal intensities. For example, signals in $^{13}\text{C}\{^1\text{H}\}$ CP-MAS NMR spectra acquired with a short (<0.1 ms) CP contact time correspond to directly bonded C-H moieties, and a longer CP contact time (>0.5 ms) enhances ^{13}C signals correspond to protonated and quaternary carbon atoms through long-range ^{13}C - ^1H dipolar interactions. **Figure S8** compares the 1D $^{13}\text{C}\{^1\text{H}\}$ CP-MAS NMR spectra of neat donor polymers and acceptors, and their blends processed from CB and o-XY solvents; the aliphatic and aromatic ^{13}C signals originating from the donor and acceptor molecules are distinguished and identified. In addition, consensus on the ^1H - ^{13}C proximities at donor-acceptor interfaces can be rationalized by examining and comparing the 2D ^{13}C - ^1H heteronuclear correlation (HETCOR) spectra of neat PPDT2FBT and PC₆₁BM compounds and PPDT2FBT:PC₆₁BM blends.

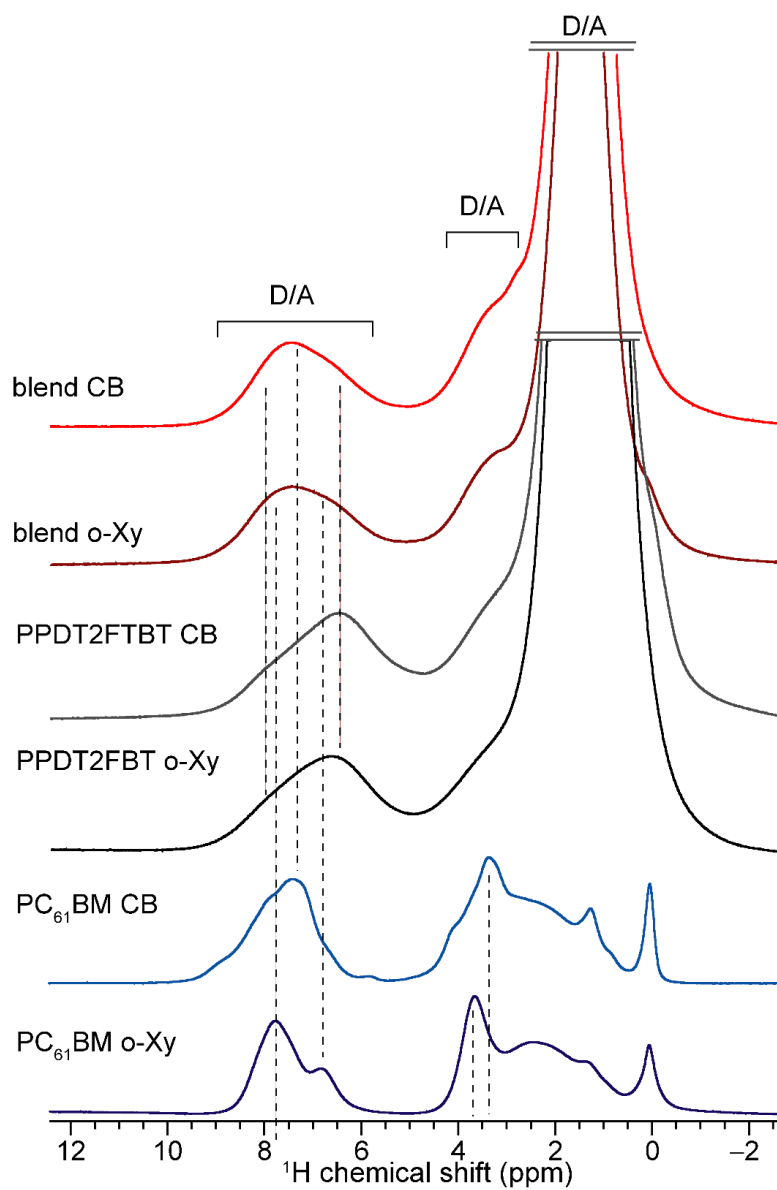


Figure S7. Solid-state 1D ^1H MAS NMR spectra of PPDT2FBT, PC_{61}BM , and PPDT2FBT: PC_{61}BM blends processed from CB and o-XY solvents.

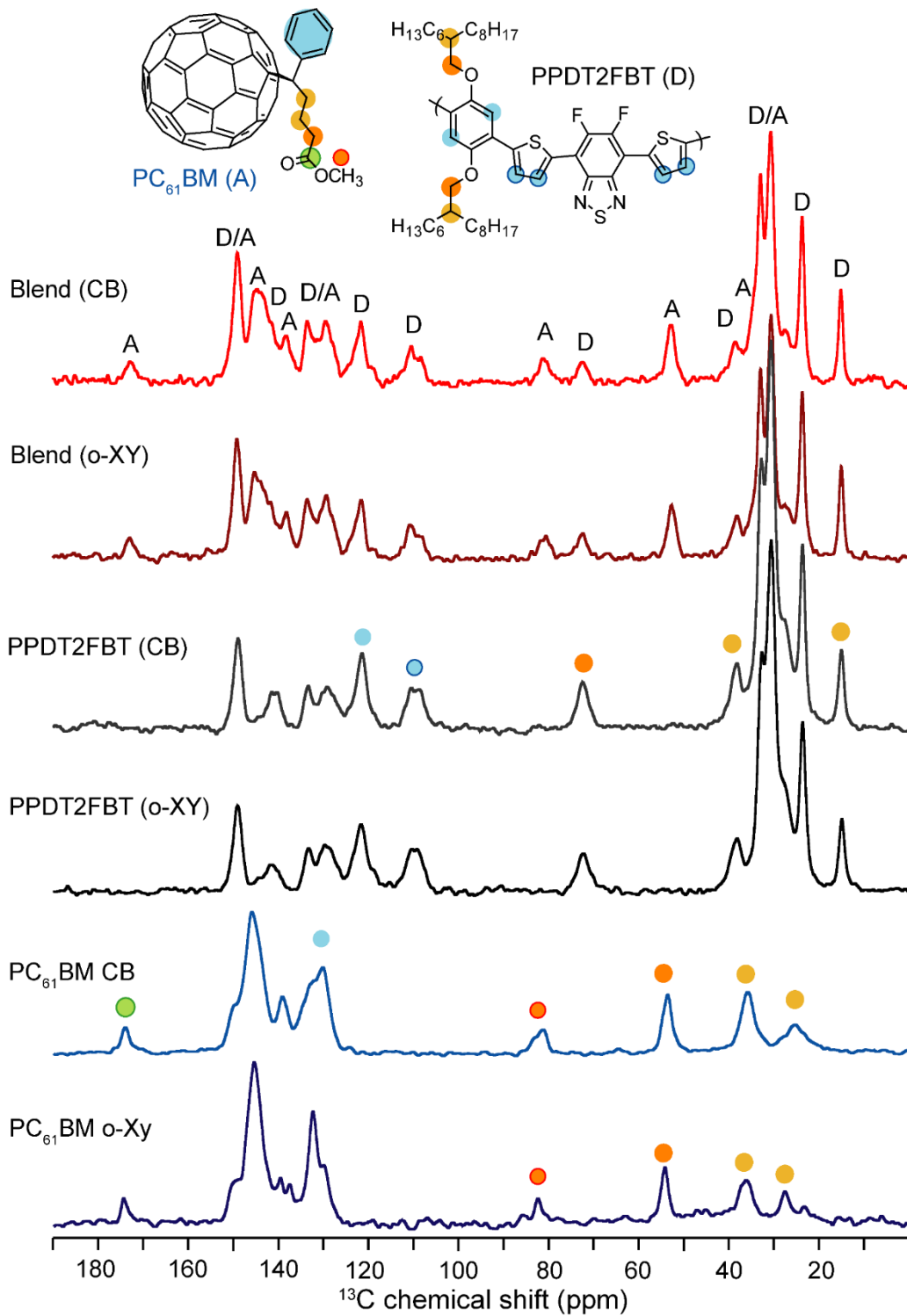


Figure S8. Solid-state 1D $^{13}\text{C}\{^1\text{H}\}$ CP-MAS NMR spectra of PPDT2FBT, PC₆₁BM, and PPDT2FBT:PC₆₁BM blends processed from chlorobenzene and *o*-xylene solvents.

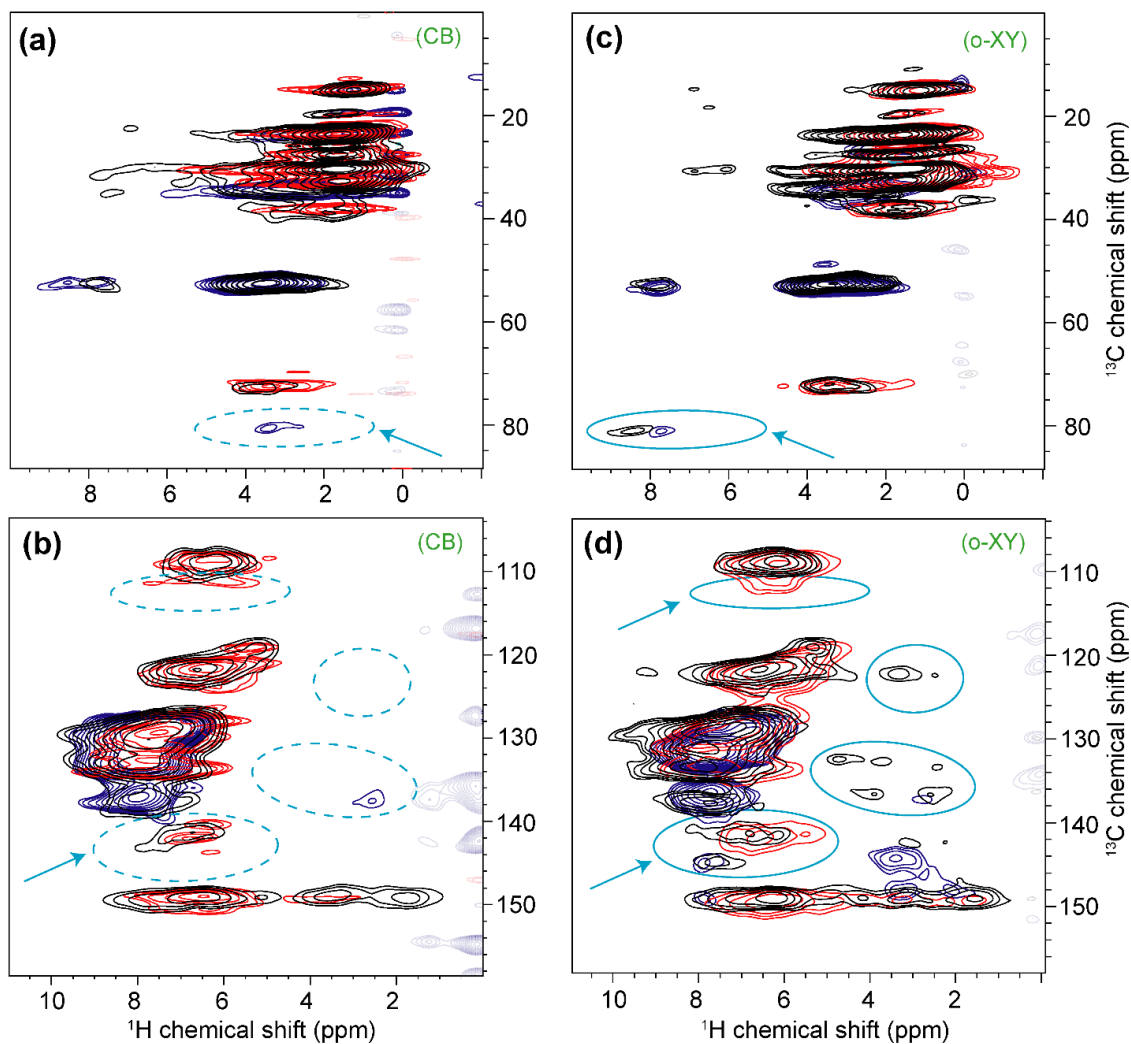


Figure S9. Solid-state 2D ^1H - ^{13}C HETCOR NMR spectra of PPDT2FBT, PC₆₁BM, and PPDT2FBT:PC₆₁BM blends processed from a,b) chlorobenzene and c,d) *o*-xylene solvents.

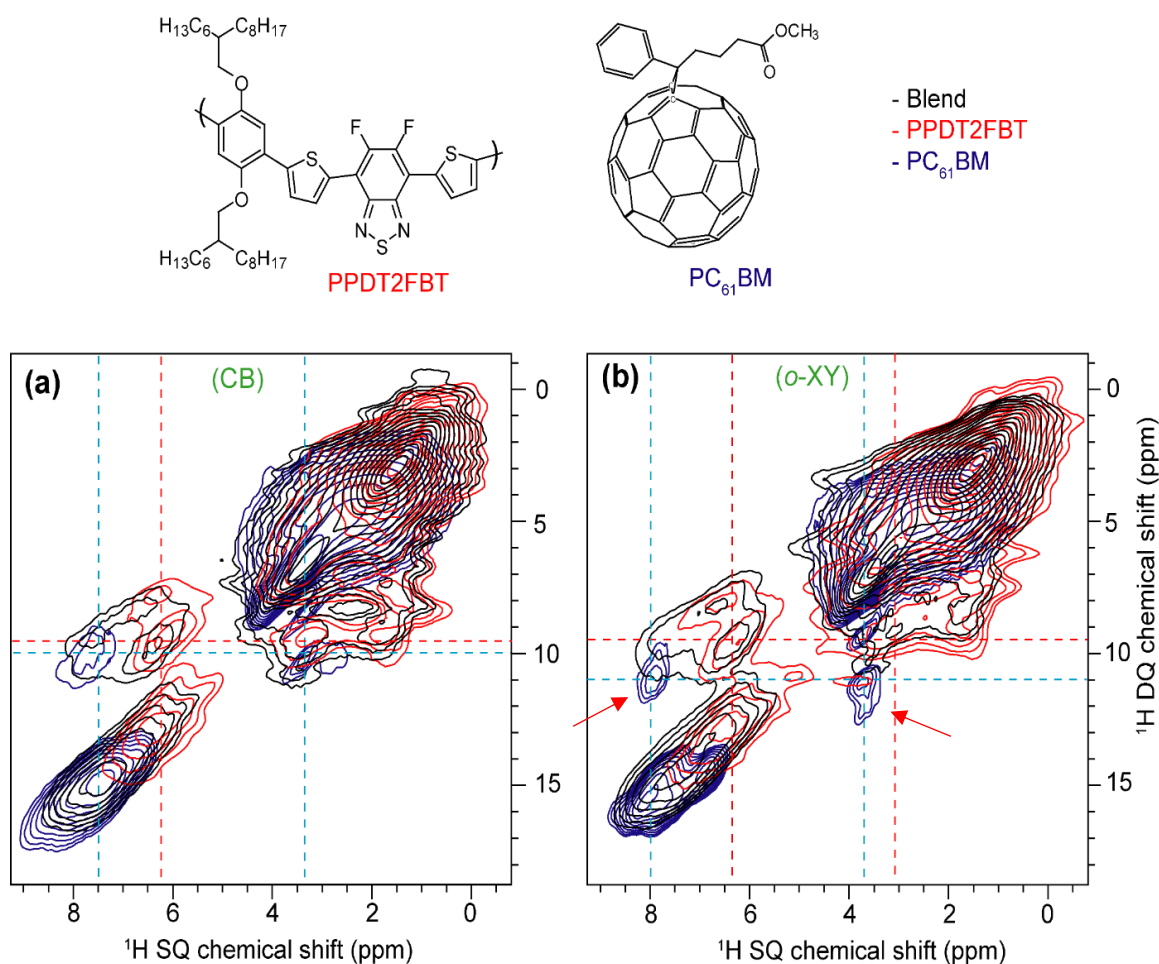


Figure S10. Solid-state 2D ¹H-¹H DQ-SQ correlation NMR spectra of PPDT2FBT, PC₆₁BM, and PPDT2FBT:PC₆₁BM blends processed from a) chlorobenzene and b) *o*-xylene solvents. Red arrows indicate the subtle differences in the aromatic ¹H DQ signals, which correspond to the changes in the local chemical environments of acceptor molecules in the BHJ blend processed from a green (*o*-XY) solvent.

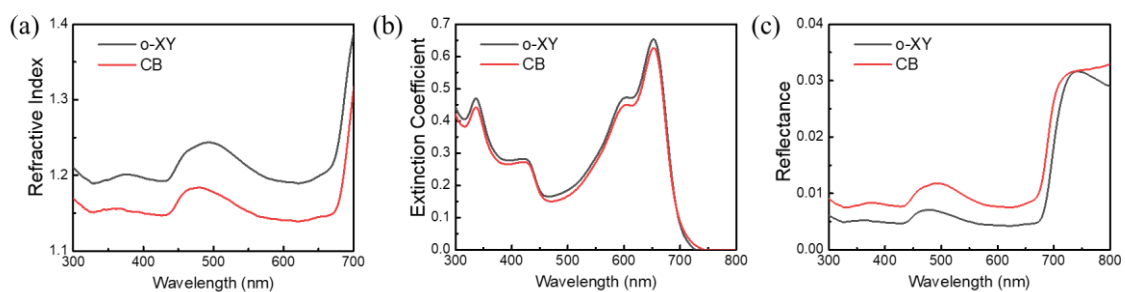
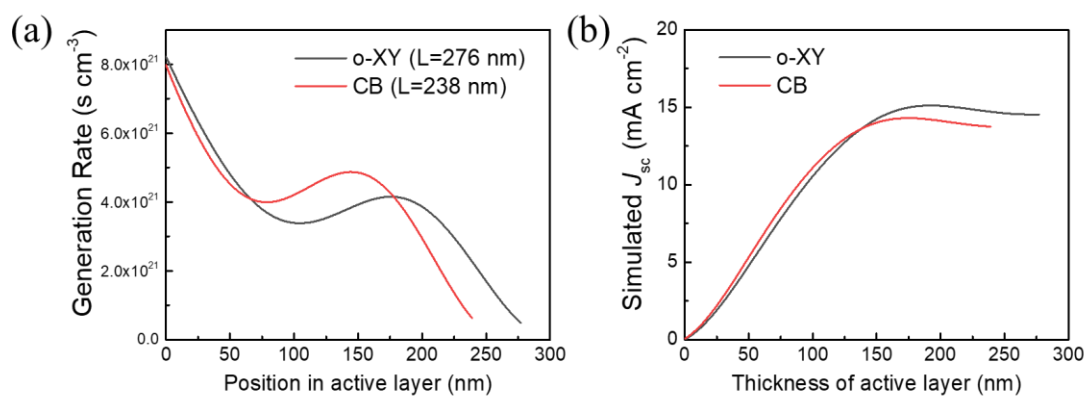


Figure S11. The optical properties of the PPDT2FBT:PC₆₁BM film prepared with CB and o-XY: **a)** refractive index, **b)** extinction coefficient and **c)** reflectance.



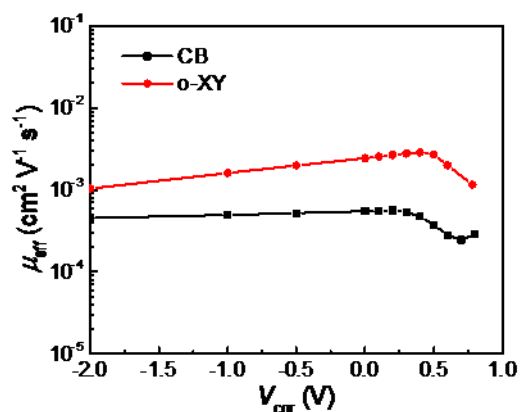


Figure S12. a) Calculated generation rates of free charge carriers and b) simulated J_{sc} in dependence of the active layer thickness of PPDT2FBT:PC₆₁BM devices processed from CB and o-XY.

Figure S13. The chemical capacitance spectroscopy of PPDT2FBT:PC₆₁BM devices processing from (a) o-XY and (b) CB under different illumination intensities.

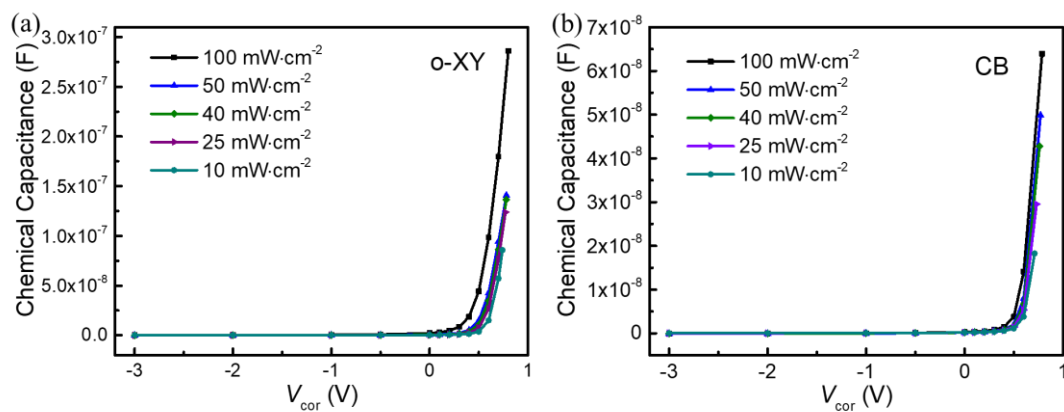


Figure S14. The effective mobility (μ_{eff}) of PPDT2FBT:PC₆₁BM devices processed from o-XY and CB under 100 mW cm⁻² illumination.

Modelling of the recombination current density, J_{rec} . The recombination current density J_{rec} can be determined as follows.

$$J_{\text{ph}} = J_{\text{L}} - J_{\text{D}}, \quad (\text{S2})$$

$$J_{\text{rec}} = J_{\text{ph,sat}} - J_{\text{ph}}, \quad (\text{S3})$$

where J_{ph} is the photocurrent density, J_{L} is the current density under illumination, J_{D} is the current density in the dark, and $J_{\text{ph,sat}}$ is the saturated photocurrent density at large reverse bias (-2 V). The calculated recombination current density $J_{\text{rec,sum}}$ includes three components, namely the contributions from bimolecular ($J_{\text{rec,bm}}$), bulk-trap- ($J_{\text{rec,bulk}}$), and surface-trap-assisted ($J_{\text{rec,surf}}$) recombination, thus yielding:

$$J_{\text{rec,sum}} = J_{\text{rec,bm}} + J_{\text{rec,bulk}} + J_{\text{rec,surf}}. \quad (\text{S4})$$

The bimolecular component $J_{\text{rec,bm}}$ can be described by the following equation:

$$J_{\text{rec,bm}} = qLk_{\text{bm}}n^2 = \frac{q^2L}{\varepsilon\varepsilon_0}\xi(\mu_n + \mu_p)n^2, \quad (\text{S5})$$

where k_{bm} is the bimolecular recombination coefficient, ζ is the Langevin prefactor, which is the ratio between the measured k_{bm} in organic solar cells and what would be expected as bimolecular recombination coefficient k_{L} from the Langevin theory ($\zeta = k_{\text{bm}}/k_{\text{L}}$), and $\mu_{\text{n,p}}$ are the electron and hole mobilities, respectively, which were replaced by the effective mobility in this study. The following expression describes the bulk trap-assisted component $J_{\text{rec,bulk}}$:

$$J_{\text{rec,bulk}} = qLk_{\text{bulk}}n = \frac{q^2L}{\varepsilon\varepsilon_0}\mu_{\text{n}}N_{\text{t,b}}n, \quad (\text{S6})$$

where $N_{\text{t,b}}$ is the density of deep traps in the bulk and k_{bulk} is the bulk-trap assisted recombination coefficient. The surface trap-assisted component $J_{\text{rec,surf}}$ can be described similarly as $J_{\text{rec,bulk}}$, with the addition of a field-dependent term:

$$J_{\text{rec,surf}} = qLk_{\text{surf}}(V_{\text{cor}})n = \frac{q^2}{\varepsilon\varepsilon_0} \frac{\mu_{\text{p}}N_{\text{t,s}}n}{\exp\left[\frac{q(V_{\text{bi}}-V_{\text{cor}})}{kT}\right]}, \quad (\text{S7})$$

where $N_{\text{t,s}}$ is the density of surface traps, V_{bi} is the built-in voltage and $k_{\text{surf}}(V_{\text{cor}})$ is the surface-trap assisted recombination coefficient. It should be noted that the mobilities in equations (S8)-(S10) were replaced by the effective mobility μ_{eff} . The experimental and calculated recombination current densities for both devices are shown in **Figure S15** under different illumination intensities.

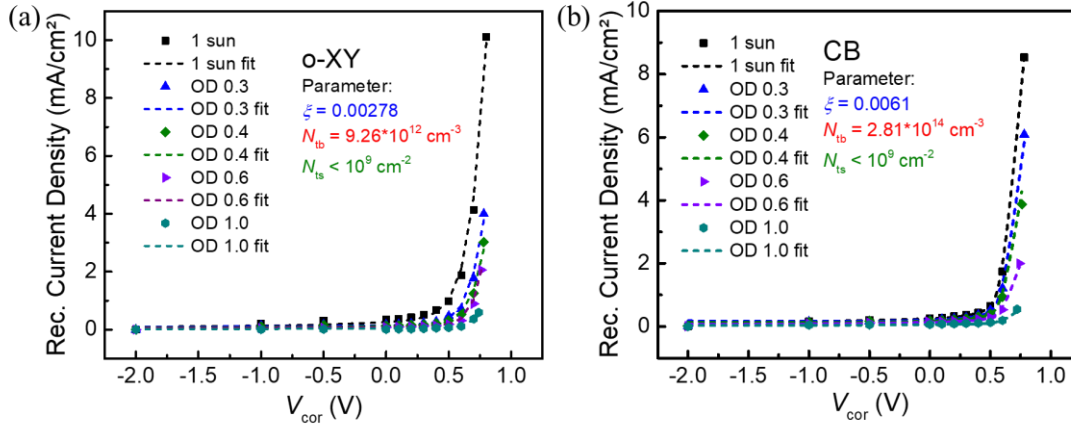


Figure S15. Measured and calculated recombination current density of PPDT2FBT:PC₆₁BM solar cells processed from a) o-XY and b) CB under different illumination intensities.

V_{oc} Modeling. The V_{oc} of the studied devices can also be calculated by employing the proposed analytical bimolecular, bulk-, and surface-trap assisted recombination model in order to assess its validity specifically under open-circuit conditions at different light intensities.^[111] The following equations can be used:

$$V_{oc} = \frac{2kT}{q} \ln \left[\frac{\sqrt{(k_{bulk} + k_{surf})^2 + 4k_{bm}PG} - k_{bulk} - k_{surf}}{2k_{bm}n_i} \right], \quad (S8)$$

$$PG = \frac{\sqrt[3]{J_{ph,sat}}}{qL}, \quad (S9)$$

where P is the geminate recombination coefficient, G is the photo-generation rate, j is a parameter adjusting the model for the non-unity of the $\log J_{\text{ph,sat}}\text{-}\log I$ -plot caused by imbalances in the electron and hole mobility, and n_i is the intrinsic charge carrier density. In this model, n_i is used as a single fitting parameter ($n_{i,\text{CB}} = 1.76 \cdot 10^9 \text{ cm}^{-3}$, $n_{i,\text{o-XY}} = 6.28 \cdot 10^9 \text{ cm}^{-3}$), while the values for k_{bm} , k_{bulk} , and k_{surf} are taken as previously determined by fitting the recombination currents at different light intensities (**Figure S15**). In comparison to previous studies, j only slightly deviates from unity and the intrinsic charge carrier densities are well within the range of what other studies have revealed for organic solar cells.^[111]

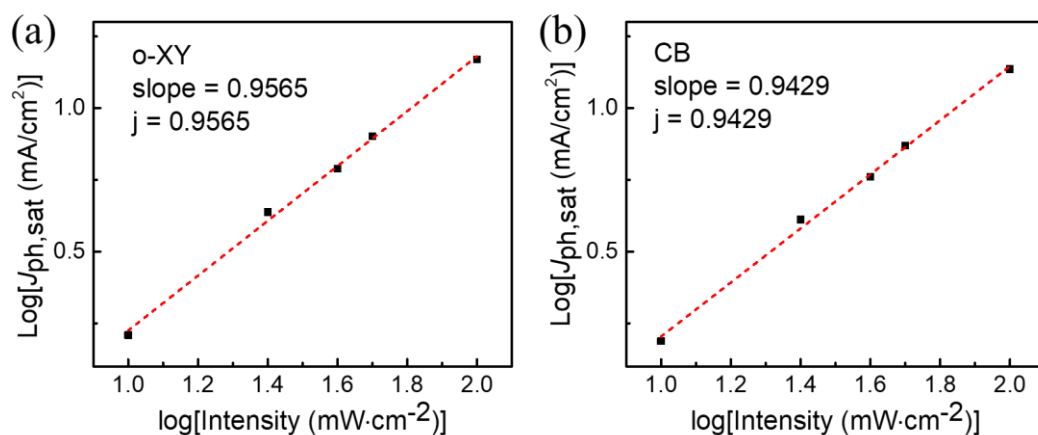


Figure S16. Relationship between saturated photocurrent density $J_{\text{ph,sat}}$ and light intensity of PPDT2FBT:PC₆₁BM devices from (a) o-XY and (b) CB. The slope of the plot is used as the empirical parameter j .

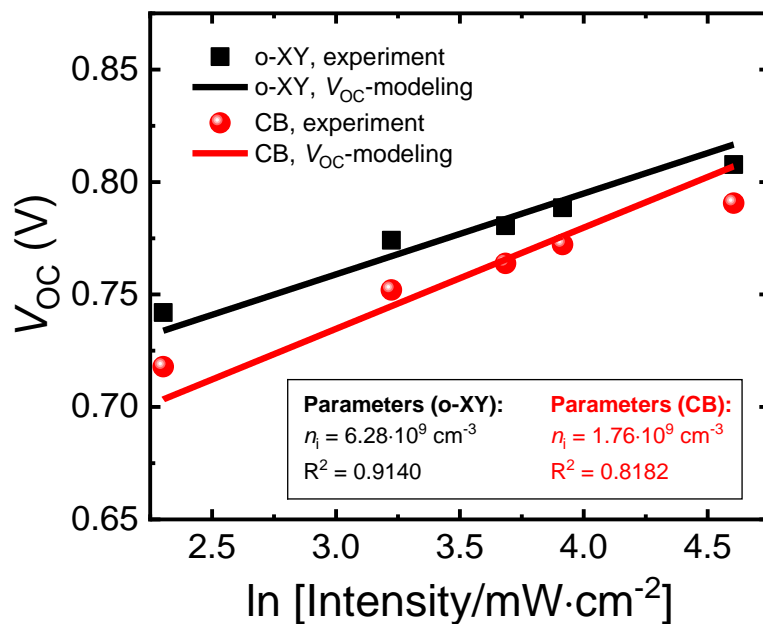


Figure S17. Experimental (symbols) and calculated (solid lines) V_{oc} vs. light intensity plots of the two investigated solar cells.

Table S2. Photovoltaic performances of PPDT2FBT:PC₆₁BM devices processed from o-XY and CB with varied additives and casting temperature under illumination of an AM 1.5G at 100 mW·cm⁻².

Solvent	Additive	Cast Temp. (°C)	J_{sc} (mA cm ⁻²)	V_{oc} (V)	FF	PCE* (%)
CB	1% DIO	25	12.5 ± 0.3	0.79 ± 0.002	0.70 ± 0.01	7.01 ± 0.1
CB	1% DIO	110	12.1 ± 0.7	0.76 ± 0.002	0.58 ± 0.02	5.43 ± 0.3
CB	1% AA	25	12.7 ± 0.5	0.79 ± 0.002	0.66 ± 0.01	6.62 ± 0.3
CB	1% AA	110	13.5 ± 0.2	0.79 ± 0.002	0.60 ± 0.02	6.27 ± 0.1
o-XY	1% DIO	25	11.8 ± 0.5	0.80 ± 0.003	0.66 ± 0.03	6.26 ± 0.3
o-XY	1% DIO	110	12.5 ± 0.6	0.79 ± 0.004	0.57 ± 0.02	5.60 ± 0.4
o-XY	1% AA	25	14.2 ± 0.2	0.80 ± 0.002	0.71 ± 0.01	8.12 ± 0.4
o-XY	1% AA	110	15.6 ± 0.2	0.80 ± 0.005	0.72 ± 0.01	9.10 ± 0.1

*Average data were obtained from at least 10 independent devices.

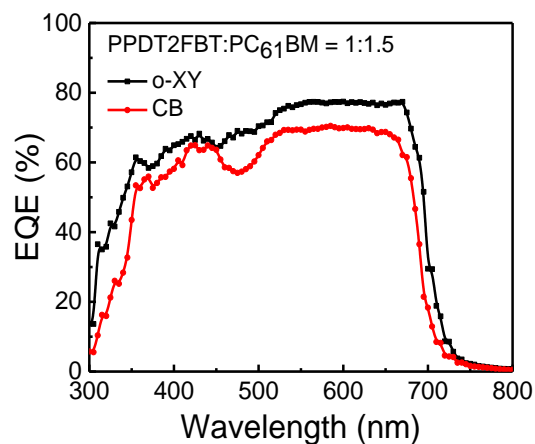


Figure S18. EQE spectra of PPDT2FBT:PC₆₁BM devices casted from o-XY and CB under illumination of an AM 1.5 G at 100 mW·cm⁻².

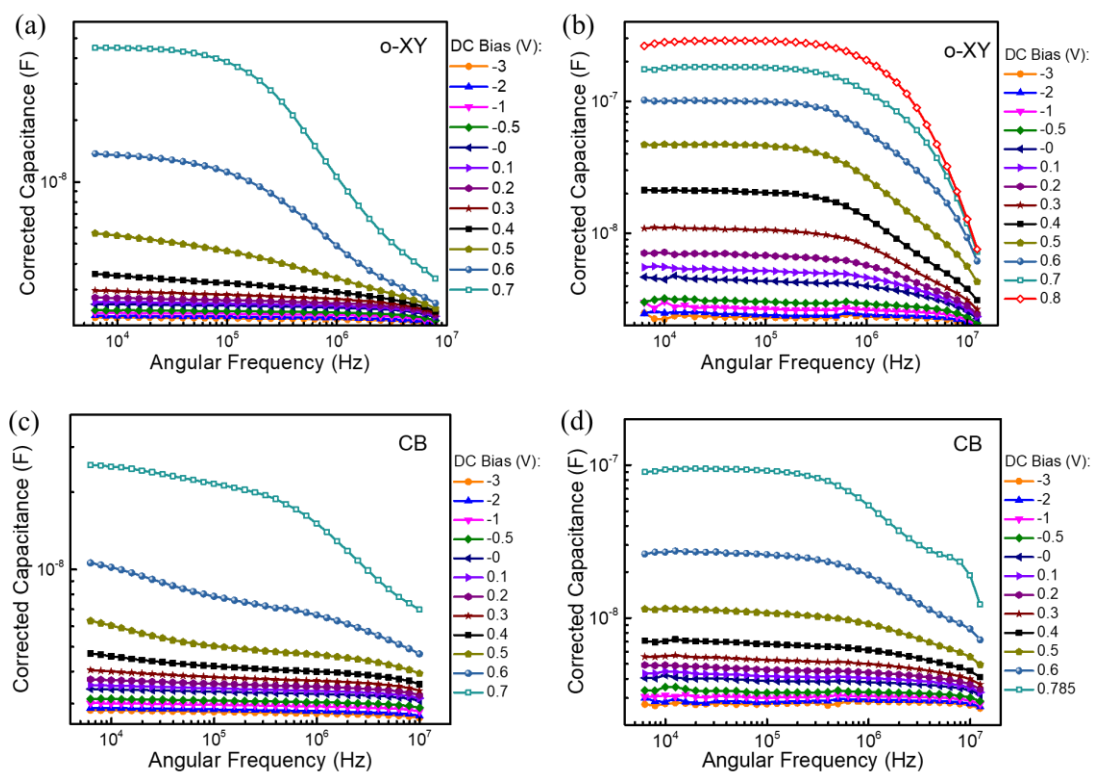


Figure S19. The corrected capacitance spectroscopy of PPDT2FBT:PC₆₁BM devices processing from o-XY a) in the dark and b) at simulated 100 mW·cm⁻² AM 1.5 G illumination. The corrected capacitance spectroscopy of PPDT2FBT:PC₆₁BM devices processing from CB c) in the dark and d) at simulated 100 mW·cm⁻² AM 1.5 G illumination.

Synthesis of 2-bromothiophene-3-carboxylic acid (1). Similar to a reported procedure,^[176] 3-thiophenecarboxylic acid (5 g, 39.0 mmol) was added to a dry 250 mL round bottom flask equipped with a stir bar. After transferring the flask to the glovebox, 100 mL of dry THF was added and placed under a constant flow of argon upon removal from the glove box. The reaction vessel was chilled to -78 °C and 2 equivalents of 2.5 M n-butyllithium in hexanes (31.2 mL, 78 mmol) was added dropwise over 30 minutes. The reaction mixture was allowed to react for 3 hours at -78 °C followed by the dropwise addition of liquid bromine (2.1 mL, 40.7 mmol) at -78 °C. The mixture was then allowed to slowly warm up to room temperature while mixing for over 16 hours. A small amount of HCl (2 mL of 1 M) was added to the reaction mixture turning the mixture into a clear solution. The solvent was removed under reduced pressure followed by the addition of ethyl acetate which was added to a separatory funnel and extracted with 1 M HCl twice. The organic layers were combined, dried over Na₂SO₄ and filtered. The organic solvent was removed under reduced pressure to produce an impure white powder which was recrystallized using a water/ethanol 4:1 mixture to produce white crystals (6.1 g, 75%). ¹H NMR (500 MHz, C₂D₆OS): δ (ppm) 13.10 (s, 1H), 7.62 (d, J = 5.7 Hz, 1H), 7.32 (d, J = 5.8 Hz, 1H). NMR chemical shifts are consistent with a previous report.^[177]

Synthesis of 2-butyloctyl 2-bromothiophene-3-carboxylate (2). Similar to reported procedures,^[176,177] 100 mL of dry dichloromethane (DCM) and 2-bromothiophene-3-carboxylic acid (1) (3 g, 14.5 mmol) were added to a dry 250 mL round bottom flask equipped with a stir bar. Then, 512 mg (4.2 mmol, 0.29 equiv.) of 4-dimethylaminopyridine (DMAP) was added followed by the addition of 1.25 equivalents of N,N'-dicyclohexylcarbodiimide (DCC) (3.75 g, 18.1 mmol). Then 1.1 equivalents of 2-butyl-1-octanol (2.97 g, 15.9 mmol) was added into the flask and the reaction mixture was left to stir overnight (16 hours) at room temperature. The solvent was removed under reduced pressure via rotary evaporation and the remaining contents were purified using silica gel column chromatography with 2:1 ratio of hexane:dichloromethane as mobile phase to afford a colorless oil (4.9 g, 89%). ¹H NMR (500 MHz, CDCl₃), δ(ppm): 7.36 (d, J = 5.8 Hz, 1H), 7.21 (d, J = 5.8 Hz, 1H), 4.20 (d, J = 5.5 Hz, 2H), 1.77-1.71 (m, 1H), 1.41-1.26 (m, 16H), 0.91-0.88 (m, 6H). ¹³C{¹H} NMR (126 MHz, CDCl₃), δ (ppm):162.59, 131.87, 129.91, 126.18, 119.83, 68.09, 37.73, 32.21, 31.76, 31.44, 30.01, 29.35, 27.10, 23.38, 23.04, 14.49, 14.46. NMR spectra are consistent with a previous report.^[178]

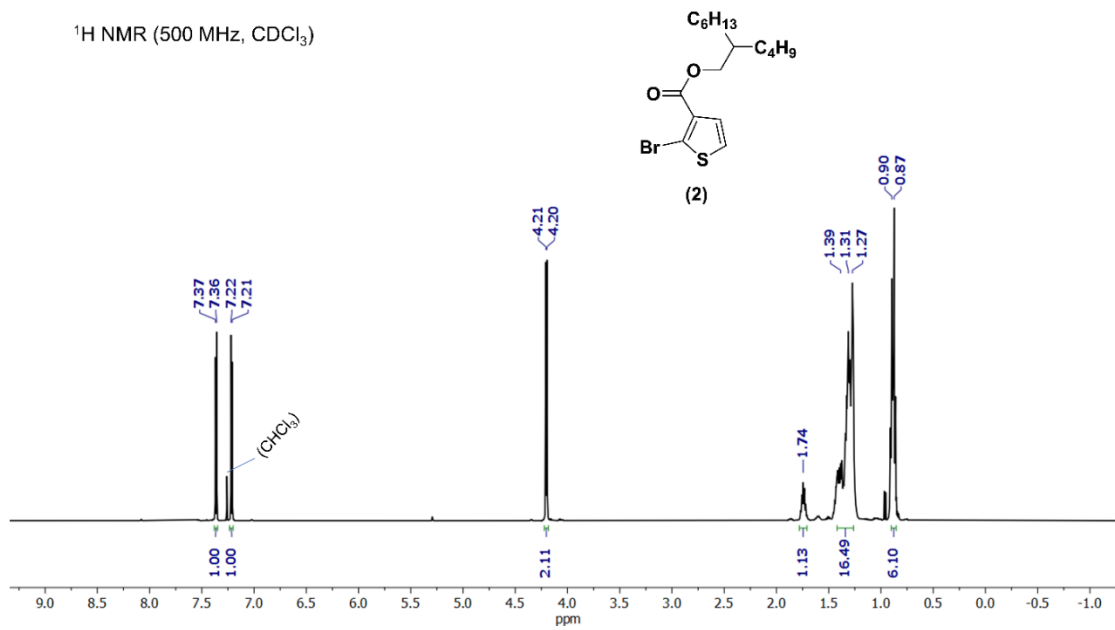


Figure S20. ^1H NMR of 2-butyl 2-bromo-3-(octylthio)acrylate (2).

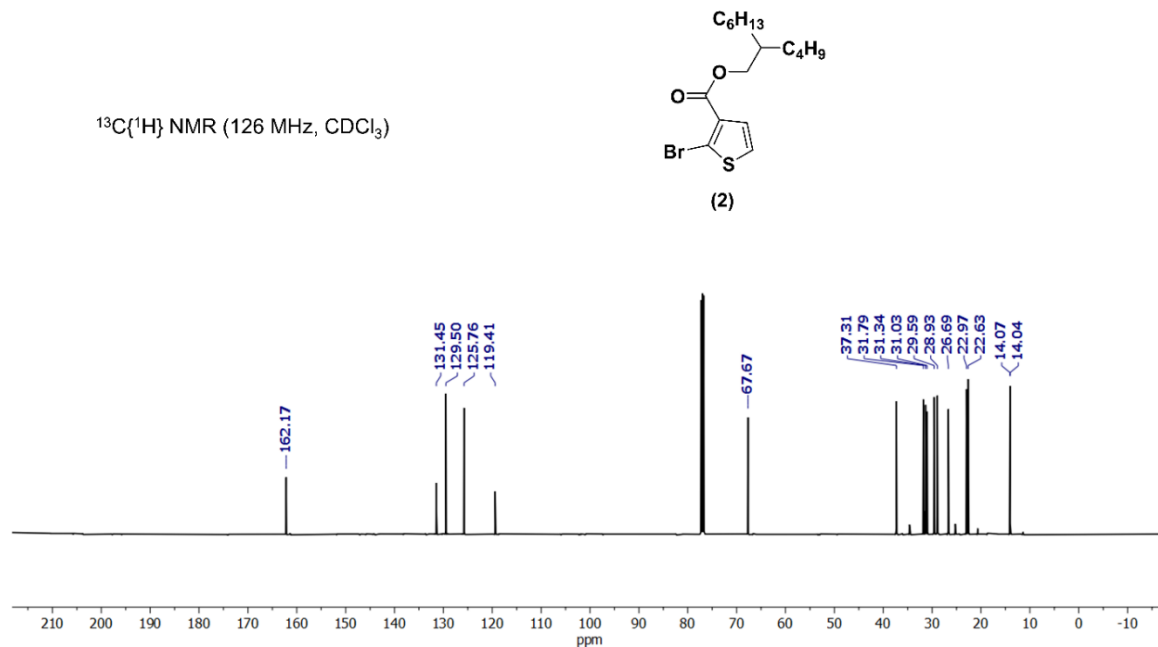


Figure S21. $^{13}\text{C}\{^1\text{H}\}$ NMR of 2-butyl 2-bromo-3-(octylcarbamoyl)thiophene (2).

Synthesis of bis(2-butyl 2-bromo-3-(octylcarbamoyl)thiophene) [2,2':5',2'':5'',2''':2''''-quaterthiophene]-3,3''''-dicarboxylate (3). A dry 150 mL round bottom flask equipped with a stir bar, 5,5'-bis(trimethylstannyl)-2,2'-bithiophene (2 g, 4.07 mmol), and compound 2 (3.51 g, 9.35 mmol) was transferred into a glove box. Then, tetrakis(triphenylphosphine)palladium(0) (235 mg, 0.20 mmol) was added to the flask followed by 30 mL of dry toluene. The reaction flask was removed from the glove box and heated to 120 °C and stirred for 18 hours. The solvent was removed under reduced pressure and the remaining mixture was purified using silica gel chromatography using hexane:DCM (5:2) as the eluent to produce an orange oil (2.51 g, 82%). ^1H NMR (300 MHz, CDCl_3), δ (ppm): 7.48 (d, $J = 4$ Hz, 2H), 7.38 (d, $J = 3$ Hz, 2H), 7.20 (d, $J = 4$ Hz, 2H), 7.16

(d, J = 3 Hz, 2H), 4.16 (d, J = 4 Hz, 4H), 1.73-1.66 (m, 2H), 1.34-1.22 (m, 32H), 0.90-0.83 (m, 12H); $^{13}\text{C}\{^1\text{H}\}$ NMR (126 MHz, CDCl_3), δ (ppm): 163.32, 142.82, 139.04, 133.25, 130.62, 130.10, 128.03, 124.03, 123.87, 67.70, 37.42, 31.91, 31.41, 31.09, 29.72, 29.03, 26.79, 23.08, 22.74, 14.18, 14.15. HR-MS (APCI) m/z for $\text{C}_{42}\text{H}_{58}\text{O}_4\text{S}_4$ theoretical (M+H): 755.3290, found (M+H): 755.3279.

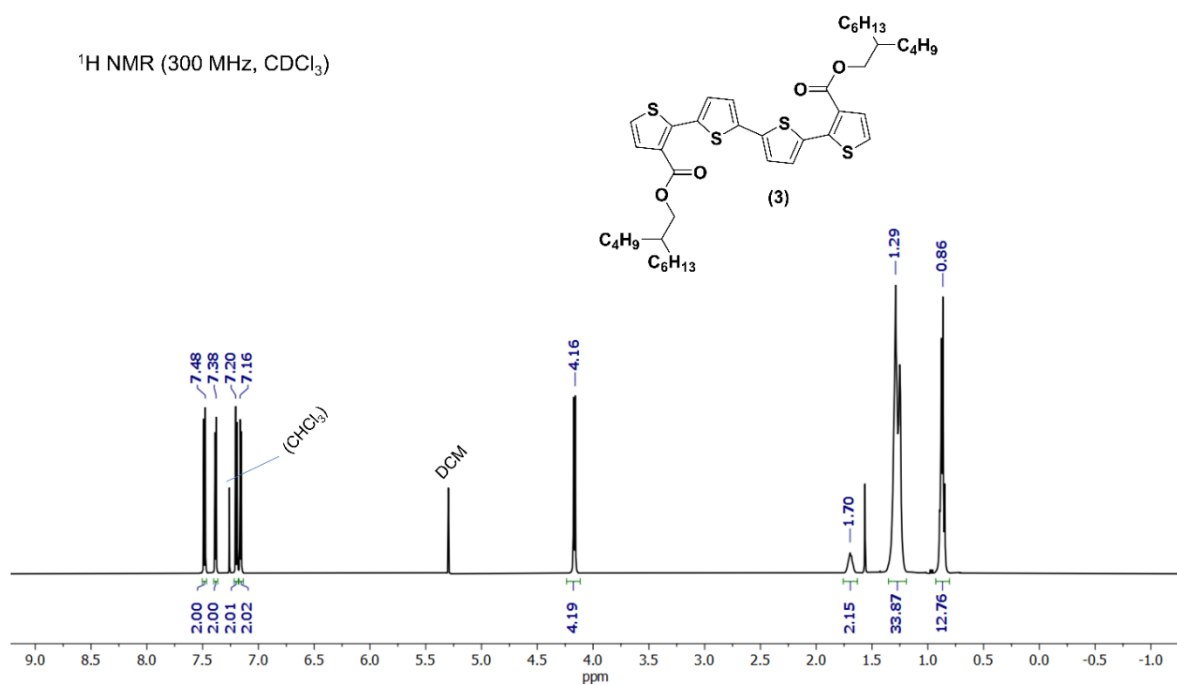


Figure S22. ^1H NMR of bis(2-butylloctyl) [2,2':5',2'':5'',2''':5'''-quaterthiophene]-3,3''-dicarboxylate (3).

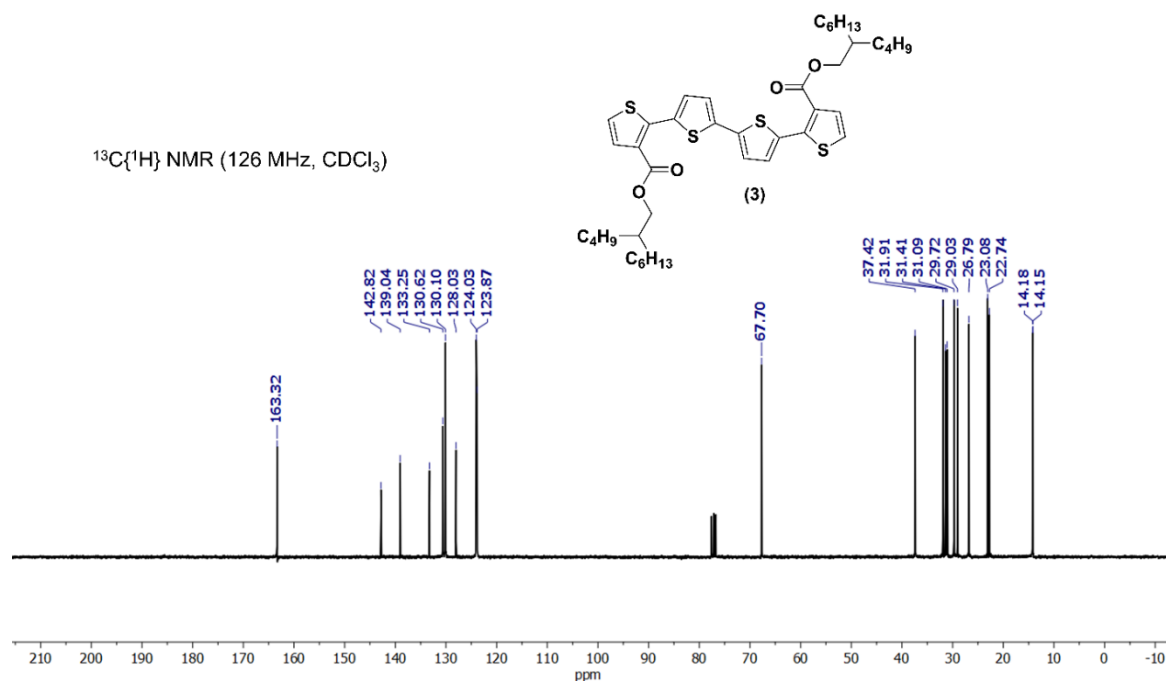


Figure S23. $^{13}\text{C}\{^1\text{H}\}$ NMR of bis(2-butyloctyl) [2,2':5',2'':5'':2'''-quaterthiophene]-3,3'''-dicarboxylate (3)

Synthesis of bis(2-butyloctyl) 5,5'''-dibromo-[2,2':5',2'':5'':2'''-quaterthiophene]-3,3'''-dicarboxylate (4). To a 150 mL round bottom flask was added a stir bar, compound 3 (2 g, 2.65 mmol) and 70 mL of DMF. Then 2.7 equivalents of NBS (1.27 g, 7.13 mmol) was added to the solution in small portions at 0 °C. The reaction was sealed, protected from light and stirred for 16 hours. Subsequently, the solvent was removed under reduced pressure followed by extraction using DCM and water. The organic layer was dried over Na_2SO_4 , filtered and concentrated under reduced pressure. The crude product was purified using silica gel chromatography using hexane:DCM (4:1) as the eluent to produce an orange solid (1.55 g,

64%). ^1H NMR (300 MHz, CDCl_3), δ (ppm): 7.42 (s, 2H), 7.33 (d, $J = 3$ Hz 2H), 7.14 (d, $J = 3$ Hz 2H), 4.16 (d, $J = 4$ Hz, 4H), 1.72-1.64 (m, 2H), 1.34-1.20 (m, 32H), 0.92-0.83 (m, 12H); $^{13}\text{C}\{^1\text{H}\}$ NMR (126 MHz, CDCl_3), δ (ppm): 162.26, 144.14, 139.48, 132.89, 132.26, 130.55, 128.33, 124.31, 110.82, 68.11, 37.44, 31.97, 31.43, 31.12, 29.75, 29.09, 26.84, 23.13, 22.80, 14.25, 14.21. HR-MS (APCI) m/z for $\text{C}_{42}\text{H}_{56}\text{Br}_2\text{O}_4\text{S}_4$ theoretical ($\text{M}+\text{H}$): 911.1501, found ($\text{M}+\text{H}$): 911.1485.

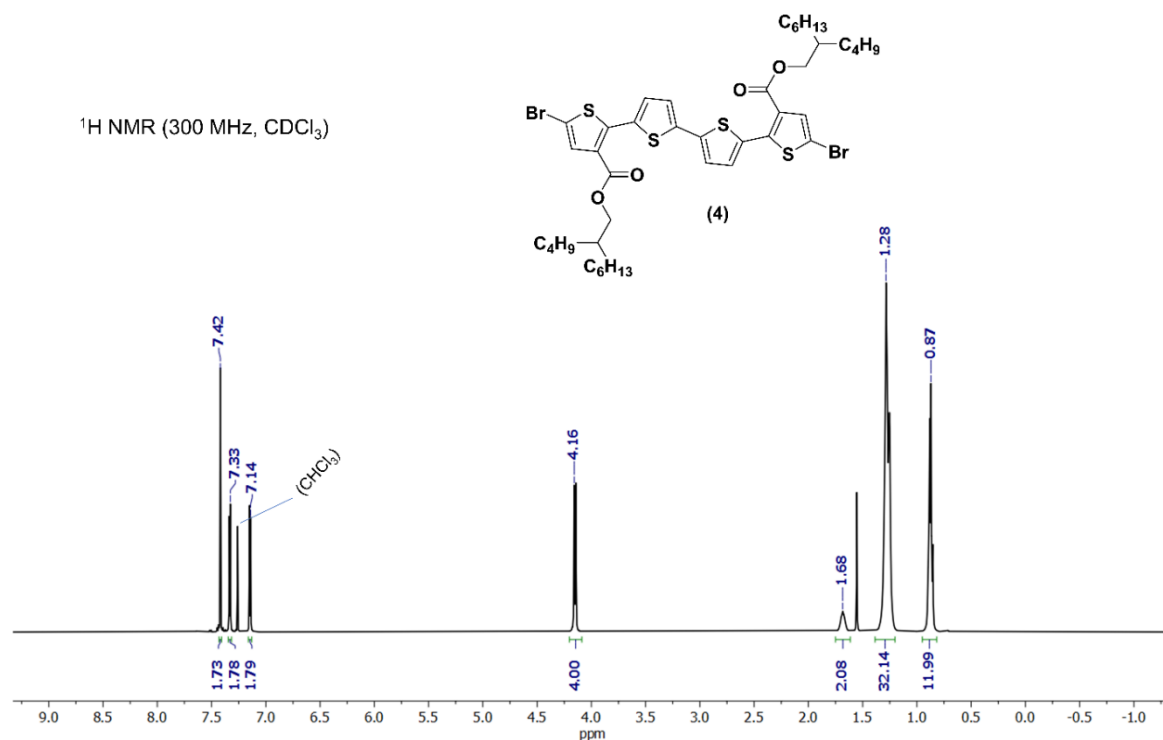


Figure S24. ^1H NMR of bis(2-butyl octyl) 5,5''-dibromo-[2,2':5',2'':5'',2''']-quaterthiophene-3,3'''-dicarboxylate (4).

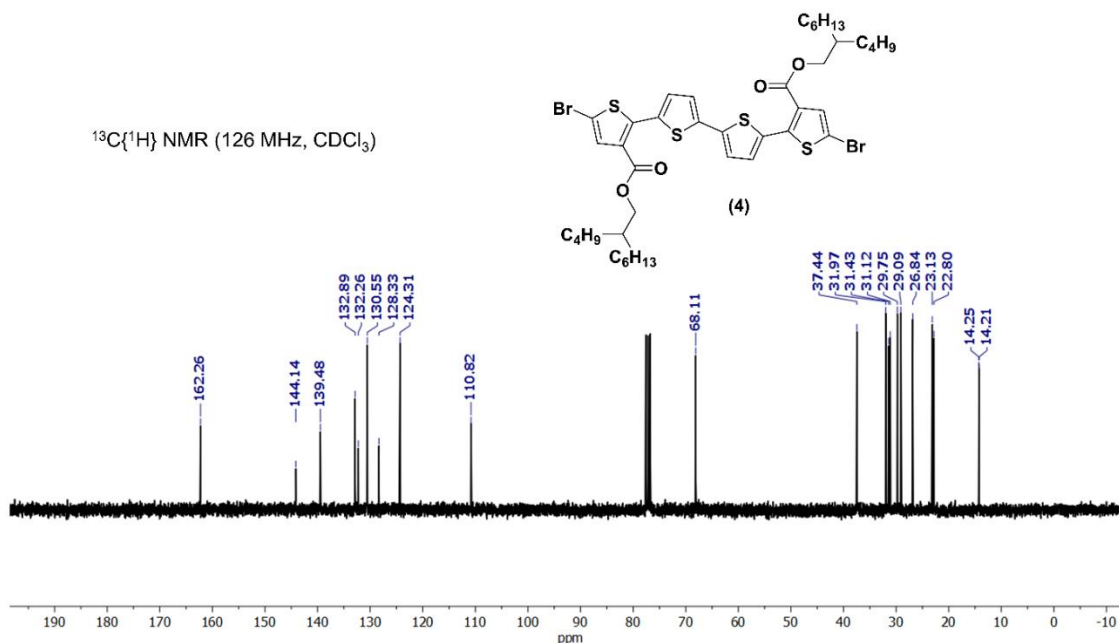


Figure S25. $^{13}\text{C}\{^1\text{H}\}$ NMR of bis(2-butyl-octyl) 5,5''-dibromo-[2,2':5',2'':5'',2'''-quaterthiophene]-3,3'''-dicarboxylate (4).

Polymerization Procedure. (4,8-Bis(4-chloro-5-(2-ethylhexyl)thiophen-2-yl)benzo[1,2-b:4,5-b']dithiophene-2,6-diyl)bis(tri-n-methylstannane) (compound 5, 248 mg, 0.255 mmol, 1 equiv.) and the complementary co-monomer, di-bromo di-ester quarterthiophene (compound 4, 233 mg, 0.255 mmol, 1 equiv.) were added to a dry 50 mL round bottom flask equipped with a magnetic stir bar. The round bottom was transferred into a glove box where toluene (10 mL), $\text{Pd}_2(\text{dba})_3 \cdot \text{CHCl}_3$ (7.9 mg, 0.03 equiv.), and $\text{P}(\text{o-tol})_3$ (9.3 mg, 0.12 equiv.) were added to the flask. The vessel was capped and removed from the glove box and put under the constant flow of argon. Next, the reaction vessel was heated to 105 °C and allowed to react for 24

hours. The polymerization was then cooled to 90 °C and exposed to air to add an excess amount of Pd scavenger diethylammonium diethyldithiocarbamate and 10 mL of chlorobenzene. The mixture was stirred for 1 hour before it was precipitated into 250 mL of methanol. The impure polymer was filtered through a cellulose extraction thimble and subjected to successive Soxhlet extractions with methanol, acetone, hexanes, and finally recovered from chloroform. The chloroform solution of the purified product was concentrated under reduced pressure and precipitated into methanol. Finally, the pure polymer powder was collected via vacuum filtration and dried under vacuum for 24 hours.

$^1\text{H NMR}$ (400 MHz, $o\text{-Cl}_2\text{C}_6\text{D}_4$)

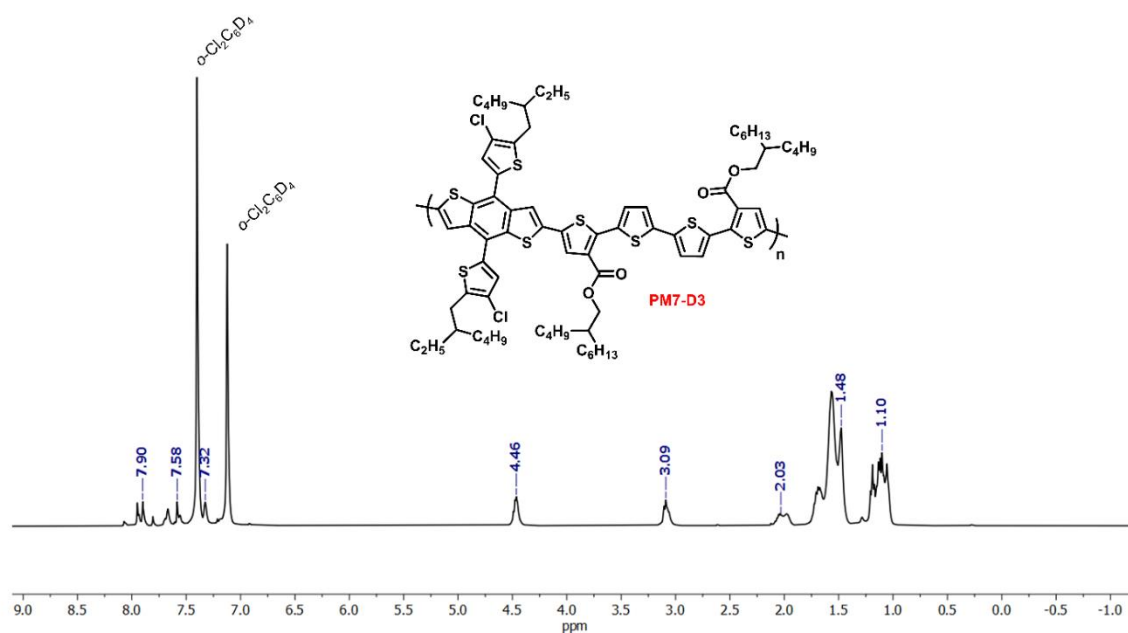


Figure S26. $^1\text{H NMR}$ spectra of PM7-D3 in o -dichlorobenzene- D_4 at 110 °C. δ (ppm): 8.08-7.78 (m, 4H), 7.71-7.53 (m, 4H), 7.32 (s, 2H), 4.46 (m, 4H), 3.09 (m, 4H), 2.03 (m, 4H), 1.78-

1.41 (m, 48H), 1.25-1.00 (m, 24H).

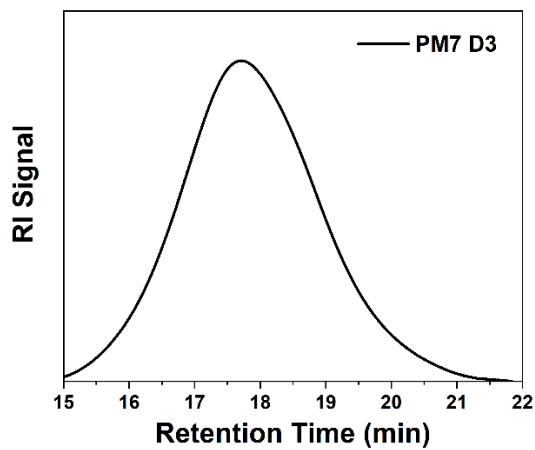


Figure S27. High temperature (140 °C) GPC trace of PM7-D3 in 1,2,4-trichlorobenzene. Mn: 64.6 kg/mol, Mw: 148.6 kg/mol, Đ: 2.30 (vs polystyrene).

Table S3: results of purity assessment using elemental analysis.

Studied Element	Theoretical %	Experimental %
C	65.25	65.49
H	6.77	6.88

S	18.33	18.20
---	-------	-------

Synthetic characterizations. ^1H NMR and ^{13}C NMR spectra for all monomers and molecular precursors were acquired on a Bruker Avance IIIHD 500 MHz or Bruker Avance IIIHD 700 MHz instruments using CDCl_3 as solvent; the residual CHCl_3 peak was used as a reference for all reported chemical shifts (^1H : $\delta = 7.26$ ppm, ^{13}C : $\delta = 77.16$ ppm). ^1H NMR for the polymer was acquired on a Bruker Avance IIIHD 400 MHz using *o*-dichlorobenzene- D_4 as the solvent at 110°C ; the residual solvent peak was used as a reference for the polymer chemical shifts (^1H : $\delta = 6.93$ ppm, and $\delta = 7.20$ ppm). Mass spectroscopy of small molecules were obtained by direct infusion atmospheric pressure chemical ionization (APCI) in positive mode using a Thermo Scientific Orbitrap ID-X Tribrid mass spectrometer. Gel permeation chromatography (GPC) was performed using a Tosoh EcoSEC high temperature GPC instrument with RI detector to determine the number average molecular weight (M_n), weight average molecular weight (M_w) and dispersity (D) for all polymers. Experiments were run using 1,2,4-trichlorobenzene (TCB) as eluent at 140°C at a flow rate of 1 mL/min on two 7.8 mm x 30 cm, 13 μm TSK-Gel GMHHR-H(S) HT2 columns in series. The instrument was calibrated using polystyrene standards (1,390-1,214,000 g/mol) and the data were analyzed using 8321GPC-WS analysis software. The GPC samples were prepared by dissolving the polymers in TCB at a 1 mg/mL concentration and stirred at 120°C for at least 3 hours before filtering through a 0.45 mm PTFE filter. Elemental analyses were conducted by Atlantic

Microlab Inc.

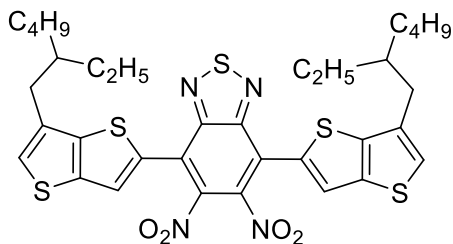


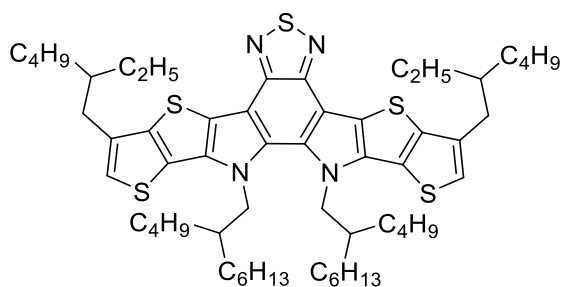
Figure S28. Chemical structure of intermediates for synthesis of Y-series NFAs.

4,7-Bis(6-(2-ethylhexyl)thino[3,2-b]thiophen-2-yl)-5,6-dinitrobenzo[c][1,2,5]thiadiazole

(01). Compound 01 was synthesized by following the literature-reported procedure.^[176]

¹H NMR (500 MHz, CDCl₃) δ 7.75 – 7.71 (m, 2H), 7.20 – 7.16 (m, 2H), 2.73 (d, *J* = 7.1 Hz, 4H), 1.85 – 1.72 (m, 2H), 1.59 – 1.55 (m, 2H), 1.42 – 1.31 (m, 14H), 0.98 – 0.88 (m, 12H).

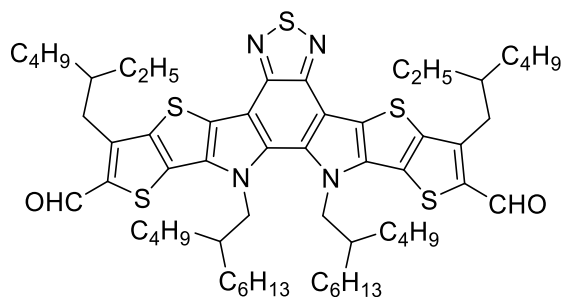
HRMS (MALDI) *m/z* [M]⁺ calcd. for C₃₄H₃₈N₄O₄S₅ 726.1491; found 726.1502.



3,9-Bis(2-ethylhexyl)-12,13-bis(2-butyl-octyl)-12,13-dihydro-[1,2,5]thiadiazolo[3,4-e]thieno [2'',3''':4',5']thieno[2',3':4,5]pyrrolo[3,2-g]thieno[2',3':4,5]thieno[3,2-b]indole

(02). Compound **01** (1.38 mmol) and triphenylphosphine (13.8 mmol) was dissolved in *o*-dichlorobenzene (10 mL) under nitrogen. After being refluxed at 180 °C overnight, *o*-dichlorobenzene was distilled out of the reaction. Then, the excess triphenylphosphine was eliminated by flash column chromatography on silica gel using chloroform as eluent. The red residue was mixed with K₂CO₃ (13.8 mmol), KI (0.55 mmol) and 2-butyloctyl bromide (12.4 mmol) in two neck-round bottom flasks. The mixture was deoxygenated with nitrogen for 15 min. Anhydrous DMF (40 mL) was added to the mixture, and the mixture was heated up to 90 °C overnight. The cooled down mixture was filtered through Celite and washed with DCM. The organic layers were combined, concentrated in vacuo, and purified with column chromatography on silica gel using DCM/hexane (1/4, v/v) as the eluent to give an orange solid product (85% yield).

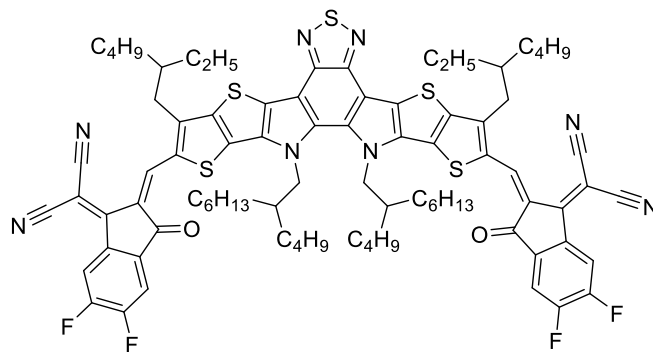
¹H NMR (400 MHz, CDCl₃) δ 7.02 (s, 2H), 4.61 (d, *J* = 7.8 Hz, 4H), 4.05 (d, *J* = 5.9 Hz, 2H), 2.78 (m, 4H), 2.10 (s, 2H), 1.98 (s, 2H), 1.48 – 1.35 (m, 20H), 1.03 – 0.85 (m, 30H), 0.75 – 0.56 (m, 20H). HRMS (MALDI) *m/z* [M]⁺ calcd. for C₅₈H₈₆N₄S₅ 998.5450; found 998.5478.



3,9-Bis(2-ethylhexyl)-12,13-bis(2-butyloctyl)-12,13-dihydro-[1,2,5]thiadiazolo[3,4-

e]thieno [2'',3'':4',5']thieno[2',3':4,5]pyrrolo[3,2-g]thieno[2',3':4,5]thieno[3,2-b]indole-2,10-dicarbaldehyde (**03**). To a solution of dichloroethane (4 mL) with DMF (9.4 mmol) at 0 °C, POCl₃ (4.7 mmol) was added slowly under nitrogen. The mixture was allowed to heat up to room temperature for 20 min. Then, the solution of compound **02** (1.2 mmol) in DCE (15 mL) was transferred to the mixture at 0 °C. After being refluxed at 85 °C overnight, 1M NaOH (20 mL) was added and stirred for 3 h. The mixture was extracted with DCM and water, and the organic layers were combined, concentrated in vacuo, and purified with column chromatography on silica gel using DCM/hexane (1/1, v/v) as the eluent to give an orange solid product (78% yield).

¹H NMR (400 MHz, CDCl₃) δ 10.11 (s, 2H), 4.60 (d, *J* = 7.9 Hz, 4H), 3.09 (d, *J* = 7.5 Hz, 4H), 2.01 (q, *J* = 6.6 Hz, 4H), 1.47 – 1.26 (m, 16H), 1.07 – 0.78 (m, 41H), 0.61 (ddt, *J* = 19.5, 14.3, 7.0 Hz, 15H). ¹³C NMR (101 MHz, CDCl₃) δ 181.97, 147.47, 146.37, 143.39, 143.37, 137.74, 136.75, 132.90, 129.51, 127.38, 112.33, 110.00, 55.22, 40.59, 40.53, 38.81, 32.91, 32.73, 31.45, 30.21, 30.17, 30.10, 30.04, 29.26, 29.25, 28.79, 27.79, 27.64, 26.12, 25.21, 25.05, 22.97, 22.68, 22.65, 22.40, 22.38, 14.06, 13.91, 13.67, 13.64, 10.85, 10.83. Anal. Calcd for C₆₀H₈₆N₄O₂S₅ (%): C, 68.27; H, 8.21; N, 5.31. Found (%): C, 68.53; H, 8.12; N, 5.33. HRMS (MALDI) *m/z* [M]⁺ calcd. for C₆₀H₈₆N₄O₂S₅ 1054.5349; found 1054.5377.



2,2'-((2Z,2'Z)-((3,9-Bis(2-ethylhexyl)-12,13-bis(2-butyloctyl)-12,13-dihydro-[1,2,5]thiadiazolo [3,4-e]thieno[2',3':4,5']thieno[2',3':4,5]pyrrolo[3,2-g]thieno[2',3':4,5]thieno[3,2-b]indole-2,10-diylium))bis(methaneylylidene))bis(5,6-difluoro-3-oxo-2,3-dihydro-1H-indene-2,1-diylidene)) dimalononitrile (PTI04). The solution of compound **03** (0.1 mmol) and 2-(5, 6-difluoro-3-oxo-2,3-dihydro-1H-inden-1-ylidene) malononitrile (0.6 mmol) in dry chloroform (8 mL) were slowly added pyridine (3.5 mmol) under nitrogen. The mixture was stirred at reflux for 2 h. After cooling to room temperature, the mixture was poured into methanol and filtered. The residue was purified with column chromatography on silica gel using chloroform/hexane (3/1, v/v) as the eluent to give a dark blue solid (86% yield).

^1H NMR (400 MHz, CDCl_3) δ 9.12 (s, 2H), 8.53 (dd, $J = 10.0, 6.4$ Hz, 2H), 7.66 (t, $J = 7.5$ Hz, 2H), 4.72 (d, $J = 8.0$ Hz, 4H), 3.15 (d, $J = 7.7$ Hz, 4H), 2.13 – 2.03 (m, 2H), 2.03 – 1.93 (m, 2H), 1.49 – 1.41 (m, 4H), 1.41 – 1.19 (m, 13H), 1.18 – 0.94 (m, 17H), 0.90 (t, $J = 7.3$ Hz, 16H), 0.83 (t, $J = 6.9$ Hz, 10H), 0.61 (p, $J = 7.1$ Hz, 12H). ^{13}C NMR (101 MHz, CDCl_3) δ 159.08, 153.43, 147.49, 145.35, 137.51, 135.71, 134.15, 134.07, 130.93, 120.08, 115.09, 114.58, 113.45, 55.62, 41.43, 39.14, 34.41, 32.65, 31.54, 30.35, 29.36, 28.77, 27.77, 25.97,

23.00, 22.76, 22.43, 14.08, 13.99, 13.72, 10.96. Anal. Calcd for C₈₄H₉₀F₄N₈O₂S₅(%): C, 68.17; H, 6.13; N, 7.57. Found (%):C, 68.25; H, 6.25; N, 7.58. HRMS (MALDI) m/z [M]⁺ calcd. for C₈₄H₉₀F₄N₈O₂S₅ 1478.5721; found 1478.5755.

Synthetic Characterization. ¹H NMR and ¹³C NMR spectra for all monomers and molecular precursors were acquired on a Bruker Avance IIIHD 500 MHz or Bruker Avance IIIHD 700 MHz instruments using CDCl₃ as solvent; the residual CHCl₃ peak was used as a reference for all reported chemical shifts (¹H: δ= 7.26 ppm, ¹³C: δ= 77.16 ppm). ¹H NMR for the polymer was acquired on a Bruker Avance IIIHD 400 MHz using *o*-dichlorobenzene-D₄ as the solvent at 110 °C; the residual solvent peak was used as a reference for the polymer chemical shifts (¹H: δ = 6.93 ppm, and δ = 7.20 ppm). Mass spectroscopy of small molecules were obtained by direct infusion atmospheric pressure chemical ionization (APCI) in positive mode using a Thermo Scientific Orbitrap ID-X Tribrid mass spectrometer. Gel permeation chromatography (GPC) was performed using a Tosoh EcoSEC high temperature GPC instrument with RI detector to determine the number average molecular weight (M_n), weight average molecular weight (M_w) and dispersity (D) for all polymers. Experiments were run using 1,2,4-trichlorobenzene (TCB) as eluent at 140 °C at a flow rate of 1 mL/min on two 7.8 mm x 30 cm, 13 μm TSK-Gel GMHHR-H(S) HT2 columns in series. The instrument was calibrated using polystyrene standards (1,390-1,214,000 g/mol) and the data were analyzed using 8321GPC-WS analysis software. The GPC samples were prepared by dissolving the polymers in TCB at a 1 mg/mL concentration and stirred at 120 °C for at least 3 hours before filtering through a 0.45 mm PTFE filter. Elemental analyses were conducted by Atlantic Microlab Inc.

Table S4 Results of purity assessment using elemental analysis.

Studied Element	Theoretical %	Experimental %
C	65.25	65.53
H	6.77	6.80
S	18.33	18.35

Synthesis of 5-bromothiophene-3-carboxylic acid (1). Similar to a reported procedure,^[176] 3-thiophenecarboxylic acid (6 g, 46.0 mmol) was added to a dry 250 mL round bottom flask equipped with a stir bar. Then, 50 mL of glacial acetic acid was added by syringe to the flask under positive argon pressure. Liquid bromine (2.2 mL, 42.7 mmol) was added dropwise for over 20 minutes to the flask at room temperature. The reaction mixture was stirred for 2 hours at room temperature. At the end of this time, the reaction mixture was poured into cold water and the precipitate was isolated by vacuum filtration as a white powder. The desired product was obtained as white crystals after recrystallization from water and 10 v% ethanol. ¹H NMR (700 MHz, CDCl₃), δ (ppm): 8.12 (d, $J = 1.5$ Hz, 1H), 7.51 (d, $J = 1.5$ Hz, 1H). ¹³C{¹H} NMR (176 MHz, CDCl₃), δ (ppm): 166.74, 135.84, 133.05, 130.38, 113.3. NMR spectra are consistent with a previous report.^[177]

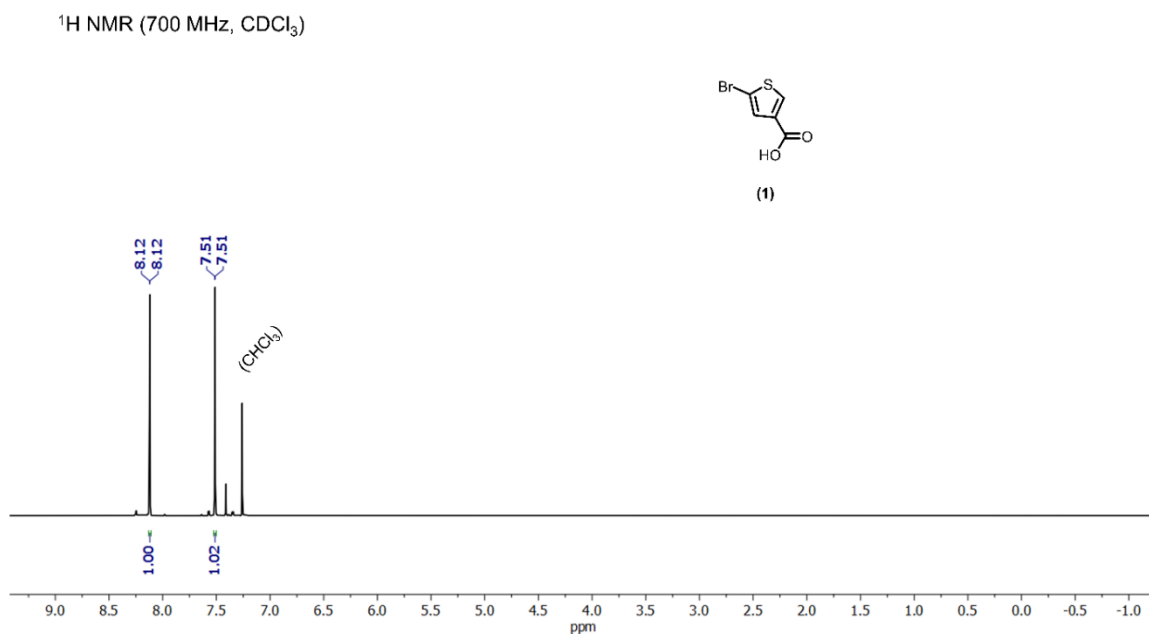


Figure S29. ^1H NMR of 5-bromothiophene-3-carboxylic acid (1).

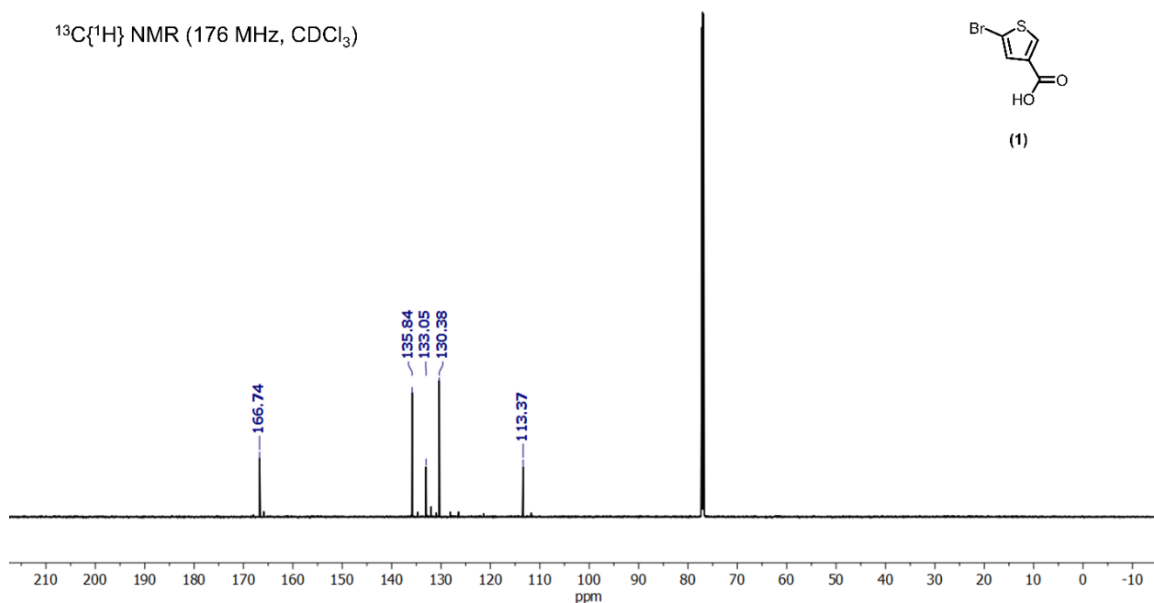


Figure S30. $^{13}\text{C}\{^1\text{H}\}$ NMR of 5-bromothiophene-3-carboxylic acid (1).

Synthesis of 2-butyloctyl 5-bromothiophene-3-carboxylate (2). Similar to reported procedures,^[176,179] 100 mL of dry dichloromethane (DCM) and 5-bromothiophene-3-carboxylic acid (1) (3 g, 14.5 mmol) were added to a pre-dried 250 mL round bottom flask equipped with a stir bar. Then, 512 mg (4.2 mmol, 0.29 equiv.) of 4-dimethylaminopyridine (DMAP) was added followed by the addition of 1.25 equivalents of N,N'-dicyclohexylcarbodiimide (DCC) (3.75 g, 18.1 mmol). Then 1.1 equivalents of 2-butyl-1-octanol (2.97 g, 15.9 mmol) was added into the flask and the reaction mixture was left to stir overnight (16 hours) at room temperature. The solvent was removed under reduced pressure

via rotary evaporation and the remaining contents were purified using silica gel column chromatography with 3.5:1.5 ratio of hexane:dichloromethane as mobile phase to afford a colorless oil (4.1 g, 75%). ^1H NMR (500 MHz, CDCl_3), δ (ppm): 7.96 (d, $J = 1.5$ Hz, 1H), 7.45 (d, $J = 1.5$ Hz, 1H), 4.16 (d, $J = 5.7$ Hz, 2H). 1.75-1.70 (m, 1H), 1.37-1.25 (m, 16 H), 0.90-0.86(m, 6H). $^{13}\text{C}\{^1\text{H}\}$ NMR (126 MHz, CDCl_3), δ (ppm): 161.73, 134.30, 133.61, 130.21, 112.84, 67.76, 37.39, 31.83, 31.40, 31.08, 29.62, 28.98, 26.73, 22.99, 22.67, 14.12, 14.07. NMR spectra are consistent with a previous report.^[177]

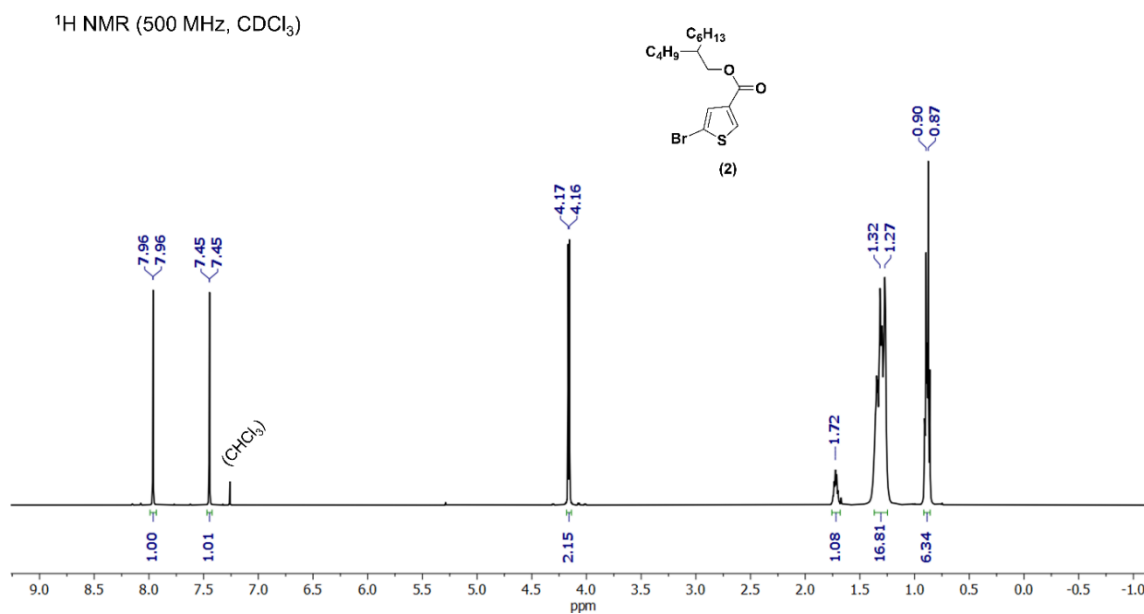


Figure S31. ^1H NMR of 2-butyl octyl 5-bromothiophene-3-carboxylate (2).

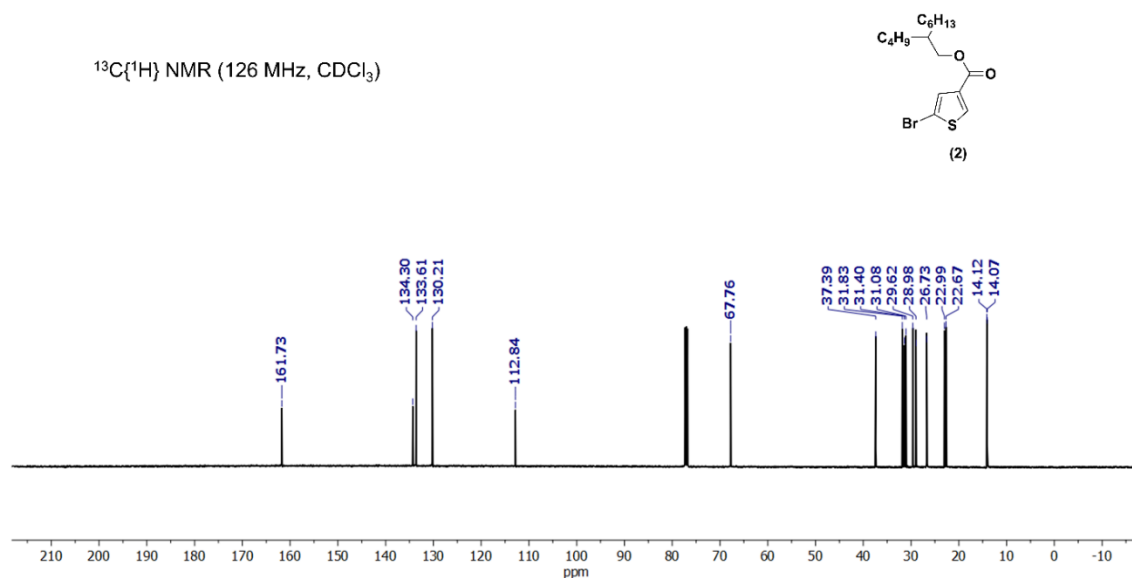


Figure S32. $^{13}\text{C}\{^1\text{H}\}$ NMR of 2-butyloctyl 5-bromothiophene-3-carboxylate (2).

Synthesis of bis(2-butyloctyl) [2,2'-bithiophene]-4,4'-dicarboxylate (3). To a dry 250 mL round bottom flask was added 30 mL of dry dimethylformamide (DMF), 2-butyloctyl 5-bromothiophene-3-carboxylate (2) (2.8 g, 7.54 mmol), and a stir bar under positive argon pressure. Then, 958 mg (3.77 mmol, 0.5 equiv.) of bis(pinacolato)diboron was added followed by addition of 3 equivalents of potassium carbonate (K_2CO_3) (3.12 g, 22.6 mmol). Next, [1,1'-bis(diphenylphosphino)ferrocene]dichloropalladium(II), 1:1 complex with dichloromethane ($\text{Pd}(\text{dppf})\text{Cl}_2 \cdot \text{CH}_2\text{Cl}_2$) (615 mg, 0.75 mmol, 0.1 equiv.) was added into the flask and the reaction mixture was left to stir overnight (16 hours) at 110 °C. The solvent was removed under reduced pressure and the remaining contents were purified using silica gel column

chromatography with 2:3 ratio of hexane:dichloromethane as mobile phase to afford a light yellow oil (2.2 g, 78%). ^1H NMR (500 MHz, CDCl_3), δ (ppm): 7.98 (d, $J = 1.3$ Hz, 2H), 7.57 (d, $J = 1.3$ Hz, 2H), 4.19 (d, $J = 5.8$ Hz, 4H), 1.78-1.73 (m, 2H), 1.42-1.26 (m, 32H), 0.92-0.86 (m, 12H). $^{13}\text{C}\{^1\text{H}\}$ NMR (126 MHz, CDCl_3), δ (ppm): 162.50, 136.95, 134.64, 131.69, 124.59, 67.78, 37.41, 31.84, 31.44, 31.12, 29.63, 28.99, 26.75, 23.00, 22.67, 14.11, 14.09. NMR spectra are consistent with a previous report.^[177]

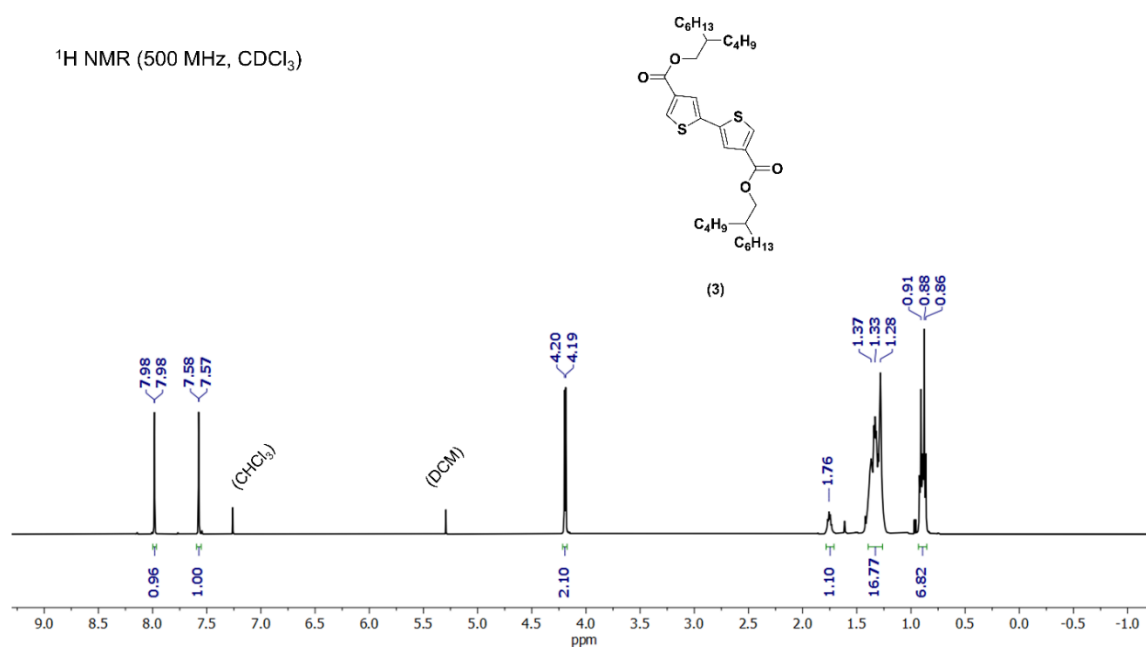


Figure S33. ^1H NMR of bis(2-butyl octyl) [2,2'-bithiophene]-4,4'-dicarboxylate (3).

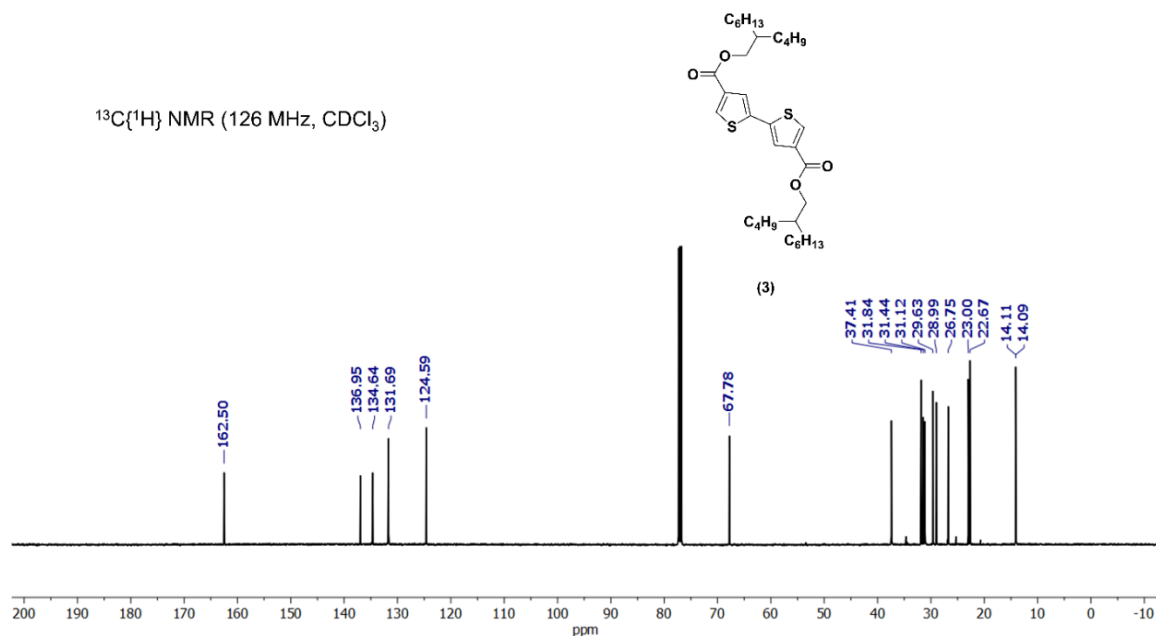


Figure S34. $^{13}\text{C}\{^1\text{H}\}$ NMR of bis(2-butyloctyl) [2,2'-bithiophene]-4,4'-dicarboxylate (3).

Synthesis of bis(2-butyloctyl) 5,5'-dibromo-[2,2'-bithiophene]-4,4'-dicarboxylate (4). To a dry 250 mL round bottom flask was added 50 mL of chloroform, bis(2-butyloctyl) [2,2'-bithiophene]-4,4'-dicarboxylate (3) (1.72 g, 2.92 mmol), and a stir bar under positive argon pressure. Subsequently, 20 mL of trifluoroacetic acid (TFA) was added to the reaction flask. N-Bromosuccinimide (NBS) (1.30 g, 7.3 mmol, 2.5 equiv.) was added over 20 minutes to the flask at room temperature. The reaction mixture was left to stir overnight (16 hours) at room temperature. After this, the reaction was quenched by adding 50 mL of distilled water. The reaction mixture was extracted with 100 mL of DCM and the extract was washed with water followed by a brine solution. The organic layer was dried over sodium sulfate and the salt was

filtered out. The solvent was removed under reduced pressure and the remaining contents were purified using silica gel column chromatography with a 2:1 ratio of hexane:dichloromethane as mobile phase to afford a light yellow oil (1.53 g, 70%). ^1H NMR (500 MHz, CDCl_3), δ (ppm): 7.34 (s, 2H), 4.20 (d, $J = 5.6$ Hz, 4H), 1.77-1.72 (m, 2H), 1.42-1.25 (m, 32H), 0.91-0.85 (m, 12H). $^{13}\text{C}\{^1\text{H}\}$ NMR (126 MHz, CDCl_3), δ (ppm): 161.60, 135.27, 132.34, 126.03, 118.91, 68.06, 37.33, 31.85, 31.39, 31.06, 29.64, 28.97, 26.74, 23.01, 22.68, 14.13, 14.10. NMR spectra are consistent with previous report.^[177]

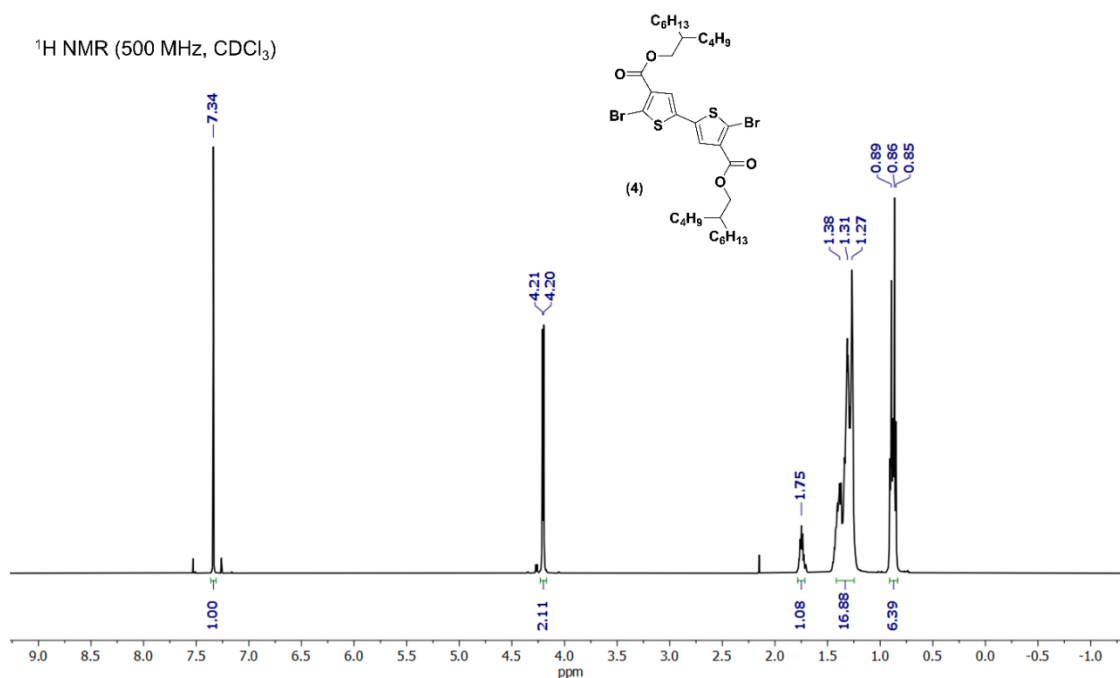


Figure S35. ^1H NMR of bis(2-butylloctyl) 5,5'-dibromo-[2,2'-bithiophene]-4,4'-

dicarboxylate (4).

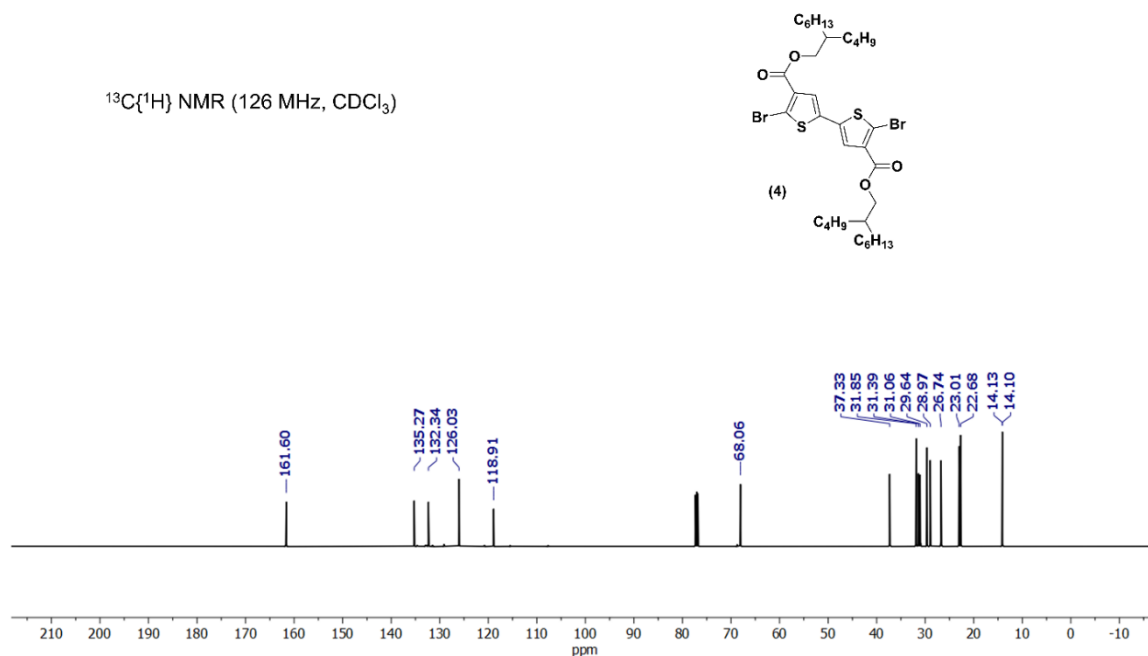


Figure S36. $^{13}\text{C}\{^1\text{H}\}$ NMR of bis(2-butylloctyl) 5,5'-dibromo-[2,2'-bithiophene]-4,4'-dicarboxylate (4).

Synthesis of bis(2-butylloctyl) [2,2':5',2'':5'',2'''-quaterthiophene]-3',4''-dicarboxylate (5). To a dry 250 mL round bottom flask was added 40 mL of DMF, bis(2-butylloctyl) 5,5'-dibromo-[2,2'-bithiophene]-4,4'-dicarboxylate (4) (1.86 g, 2.59 mmol), and a stir bar under positive argon pressure. Subsequently, 2-(tributylstannyl)thiophene (2.03 g, 5.44 mmol, 2.1 equiv.) was added using a syringe to the flask at room temperature followed by addition of tetrakis(triphenylphosphine)palladium(0) ($\text{Pd}(\text{PPh}_3)_4$) (178 mg, 0.06 equiv.). The reaction

mixture was left to stir overnight (16 hours) at 125 °C. After this, the reaction was quenched by adding 50 mL of distilled water. The reaction mixture was extracted with 100 mL of DCM and the extract was washed with water and a brine solution. The organic layer was dried over sodium sulfate and the salt was filtered out. The solvent was removed under reduced pressure and the remaining contents were purified using silica gel column chromatography with 2:1 ratio of hexane:dichloromethane as mobile phase to afford a light yellow solid (1.8 g, 92%). ^1H NMR (500 MHz, CDCl_3), δ (ppm): 7.53 (s, 2H), 7.46 (dd, $J = 3.7, 1.2$ Hz, 2H), 7.42 (dd, $J = 5.2, 1.2$ Hz, 2H), 7.08 (dd, $J = 5.1, 3.6$ Hz, 2H), 4.16 (d, $J = 5.7$ Hz, 4H), 1.71-1.66 (m, 2H), 1.32-1.24 (m, 32H), 0.91-0.86 (m, 12H). $^{13}\text{C}\{^1\text{H}\}$ NMR (126 MHz, CDCl_3), δ (ppm): 162.93, 142.16, 133.78, 133.33, 129.56, 128.70, 128.09, 127.28, 126.87, 67.91, 37.31, 31.85, 31.32, 31.00, 29.64, 28.96, 26.72, 23.01, 22.70, 14.14, 14.12. HR-MS (ESI) m/z for $\text{C}_{42}\text{H}_{58}\text{O}_4\text{S}_4$ theoretical (M+H): 755.3290, found (M+H): 755.3284.

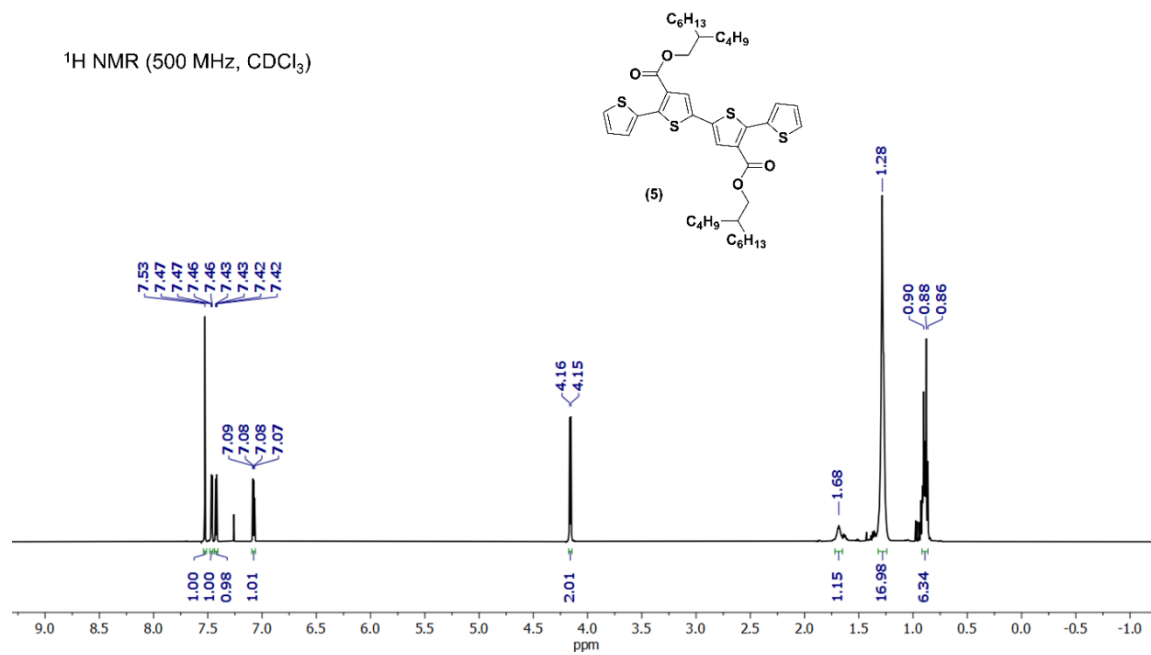


Figure S37. ¹H NMR of bis(2-butyldecyl) [2,2':5',2'':5'':2'''-quaterthiophene]-3',4''-dicarboxylate (5).

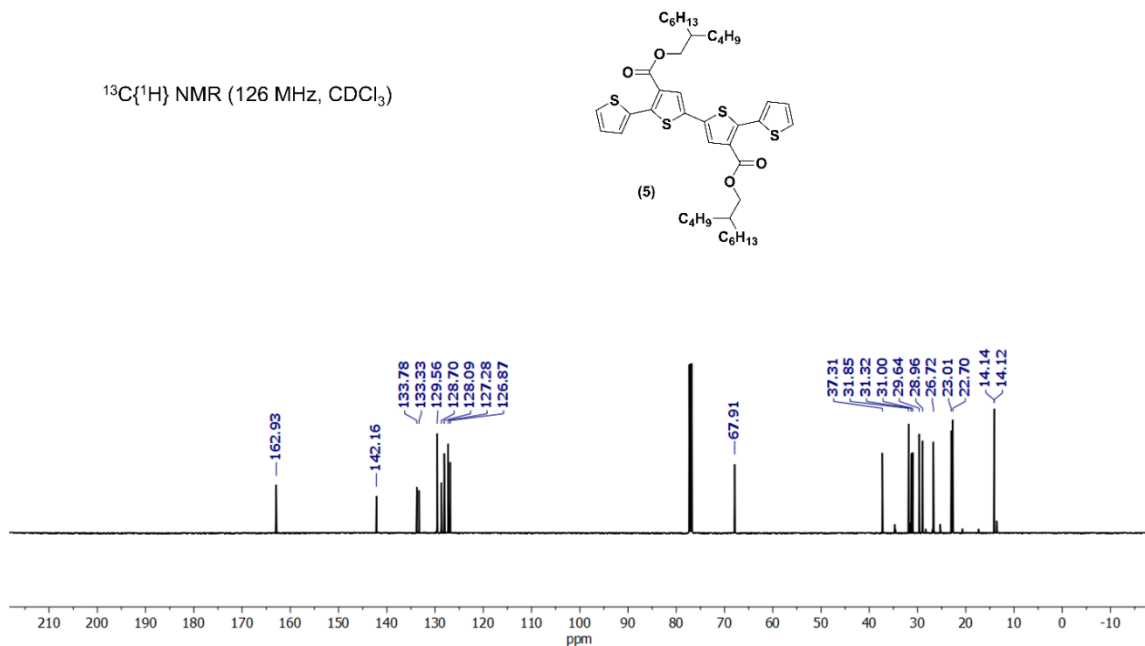


Figure S38. $^{13}\text{C}\{^1\text{H}\}$ NMR of bis(2-butyloctyl) [2,2':5',2'':5'':2'''-quaterthiophene]-3',4''-dicarboxylate (5).

Synthesis of bis(2-butyloctyl) 5,5'''-dibromo-[2,2':5',2'':5'':2'''-quaterthiophene]-3',4''-dicarboxylate (6). To a dry 250 mL round bottom flask was added 50 mL of DMF, bis(2-butyloctyl) [2,2':5',2'':5'':2'''-quaterthiophene]-3',4''-dicarboxylate (5) (865 mg, 1.15 mmol), and a stir bar under positive argon pressure. Subsequently, NBS (428 mg, 2.41 mmol, 2.1 equiv.) was added over 20 minutes to the flask at room temperature. The reaction mixture was left to stir overnight (16 hours) at room temperature. After this time, the reaction was quenched by adding 50 mL of distilled water. The reaction mixture was extracted with 100 mL of DCM and the extract was washed with water and a brine solution. The organic layer was dried over

sodium sulfate and the salts was filtered out. The solvent was removed under reduced pressure and the remaining contents were purified using silica gel column chromatography with 2:1 ratio of hexane:dichloromethane as mobile phase to afford a yellow solid (840 mg, 80%). ^1H NMR (700 MHz, CDCl_3), δ (ppm): 7.49 (s, 2H), 7.20 (d, $J = 3.9$ Hz, 2H), 7.03 (d, $J = 3.9$ Hz, 2H), 4.17 (d, $J = 5.8$ Hz, 4H), 1.73-1.68 (m, 2H), 1.32-1.25 (m, 32H), 0.91-0.86 (m, 12H). $^{13}\text{C}\{^1\text{H}\}$ NMR (176 MHz, CDCl_3) δ (ppm): 162.77, 141.33, 134.70, 133.64, 129.90, 129.59, 128.69, 126.96, 115.77, 68.12, 37.30, 31.85, 31.33, 31.01, 29.65, 28.95, 26.72, 23.01, 22.69, 14.13, 14.12. HR-MS (ESI) m/z for $\text{C}_{42}\text{H}_{56}\text{O}_4\text{S}_4\text{Br}_2$ theoretical ($\text{M}+\text{H}$): 911.1501, found ($\text{M}+\text{H}$): 911.1501.

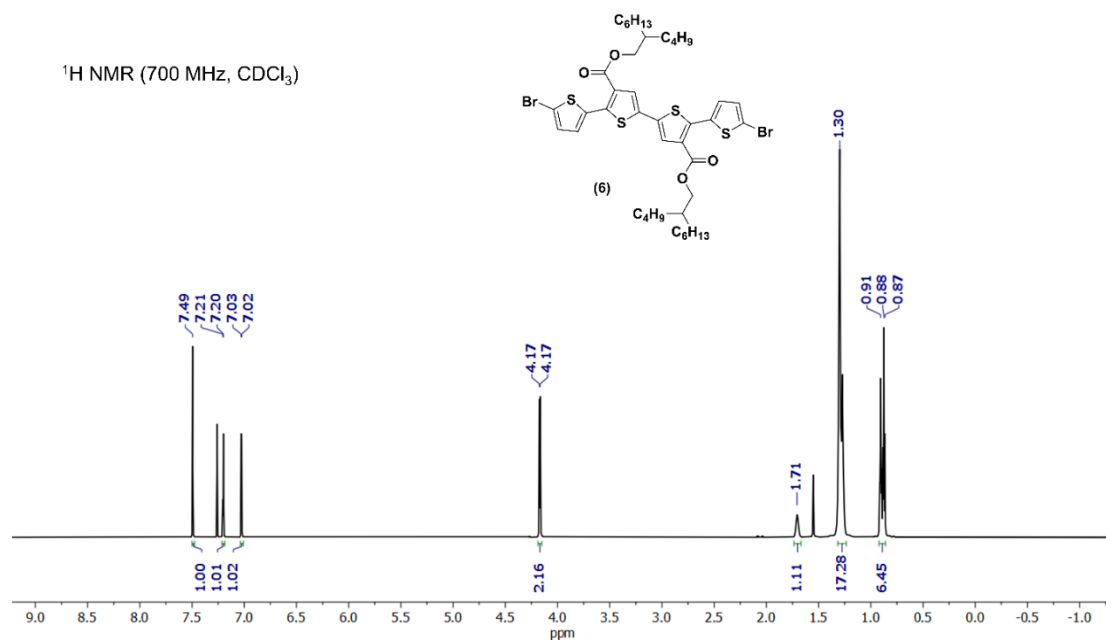


Figure S39. ^1H NMR of bis(2-butyl octyl) 5,5''-dibromo-[2,2':5',2'':5'',2'']-quaterthiophene]-

3',4''-dicarboxylate (6).

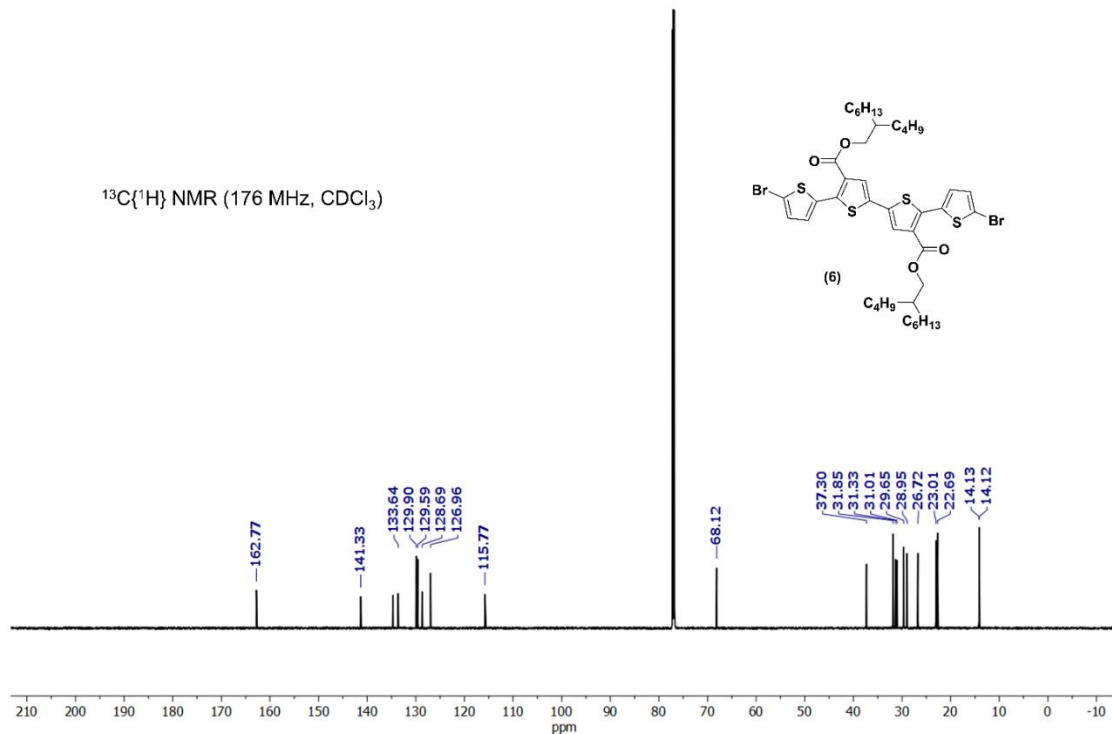


Figure S40. $^{13}\text{C}\{^1\text{H}\}$ NMR of bis(2-butyldecyl) 5,5''-dibromo-[2,2':5',2'':5'',2'''-quaterthiophene]-3',4''-dicarboxylate (6).

Polymerization Procedure. (4,8-Bis(4-chloro-5-(2-ethylhexyl)thiophen-2-yl)benzo[1,2-b:4,5-b']dithiophene-2,6-diyl)bis(tri-n-methylstannane) (compound 7, 248 mg, 0.255 mmol, 1 equiv.) and the complementary co-monomer, di-bromo di-ester quaterthiophene (compound D5, 233 mg, 0.255 mmol, 1 equiv.) were added to a dry 50 mL round bottom flask equipped with a magnetic stir bar. The round bottom was transferred into a glove box where toluene (10 mL), $\text{Pd}_2(\text{dba})_3 \cdot \text{CHCl}_3$ (7.9 mg, 0.03 equiv.), and $\text{P}(\text{o-tol})_3$ (9.3 mg, 0.12 equiv.) were added

to the flask. The vessel was capped and removed from the glove box and put under the constant flow of argon. Next, the reaction vessel was heated to 105 °C and allowed to react for 24 hours. The polymerization was then cooled to 90 °C and exposed to air to add an excess amount of Pd scavenger diethylammonium diethyldithiocarbamate and 10 mL of chlorobenzene. The mixture was stirred for 1 hour before it was precipitated into 250 mL of methanol. The impure polymer was filtered through a cellulose extraction thimble and subjected to successive Soxhlet extractions with methanol, acetone, hexanes, and finally recovered from chloroform. The chloroform solution of the purified product was concentrated under reduced pressure and precipitated into methanol. Finally, the pure polymer powder was collected via vacuum filtration and dried under vacuum for 24 hours. The full name of the polymer is poly[bis(2-butyloctyl) 5-(4,8-bis(4-chloro-5-(2-ethylhexyl)thiophen-2-yl)benzo[1,2-b:4,5-b']dithiophen-2-yl)-[2,2':5',2'':5'',2'''-quaterthiophene]-3',4''-dicarboxylate], which can be also referred to as PM7-D5.

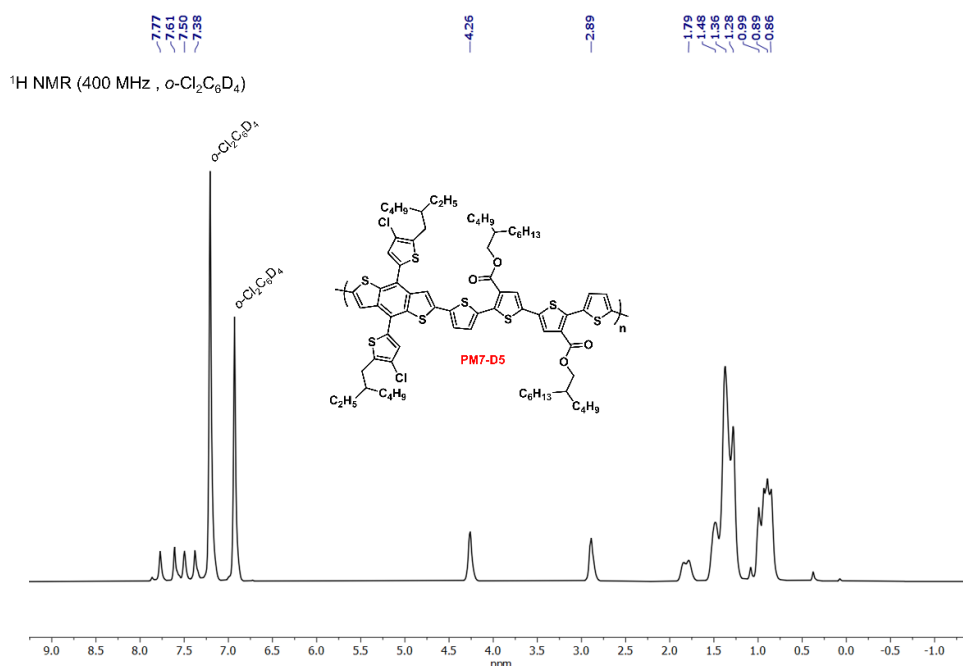


Figure S41. ^1H NMR spectra of PM7-D5 in *o*-dichlorobenzene- D_4 at $110\text{ }^\circ\text{C}$.

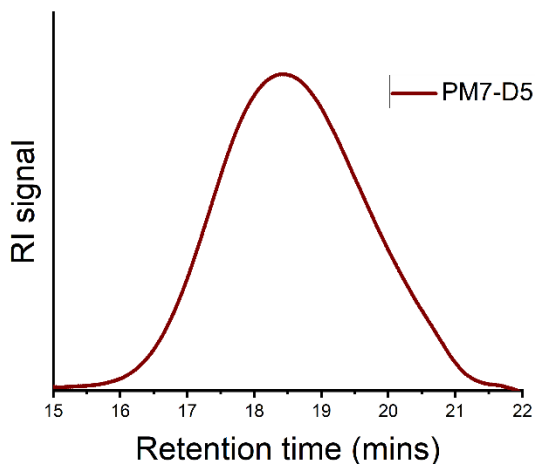


Figure S42. High temperature ($140\text{ }^\circ\text{C}$) GPC trace of PM7-D5 in 1,2,4-trichlorobenzene.

OPD Device Fabrication. All the devices on an ITO/glass substrate were fabricated in an inverted structure of indium tin oxide (ITO)/zinc oxide (ZnO)/PM7-D5:Y12/MoO_x/Ag. OPD devices were fabricated according to the following procedures. ITO substrates (purchased from Thin Film Devices, Inc.) were cleaned by detergent, then sequentially ultrasonicated in DI water, acetone, and isopropanol for 30 min. Diethyl zinc and tetrahydrofuran (THF) were mixed in a volume ratio of 1.5:1 and spin-coated on the clean ITO substrates at 4000 rpm for 30 s, followed by 15 min annealing at $150\text{ }^\circ\text{C}$ to make a thick ZnO film ($\sim 65\text{ nm}$). Solutions (total concentration of 10 mg/mL) of PM7-D5:Y12 in a 1:1.2 weight ratio were prepared in

either CB, o-XY, or 2-MeTHF, which was stirred and kept at elevated temperatures (2-MeTHF at 40 °C, CB at 60 °C, o-XY at 80 °C) overnight. Prior to hot spin casting, the stock solutions and the corresponding substrates were all heated up to a certain temperature (CB: 90 °C, o-XY: 100 °C, and 2-MeTHF: 75 °C), respectively. On the top of the ZnO layer, the hot solution was spin-coated at 650 rpm to form thick active layers (180–210 nm), of which the thickness was measured by an Ambios XP-100 stylus profilometer. All the films were thermally annealed at 110 °C for 10 minutes. After settling the films to cool to room temperature, the MoO_x/Ag (7 nm/120 nm) electrode with an active area of 0.05 cm² was then deposited on top of the active layer by thermal evaporation in a high vacuum (<10⁻⁶ torr). For wearable devices, flexible ITO/PET substrates with a surface resistivity of 100 Ω/sq (purchased from Sigma-Aldrich) were used to replace all the ITO/glass substrates. These flexible devices with wires connected to the electrodes were further encapsulated with another thin PET film on the top using a two-part fast drying epoxy. All the other steps of the fabrication of the flexible devices were the same as the regular devices.

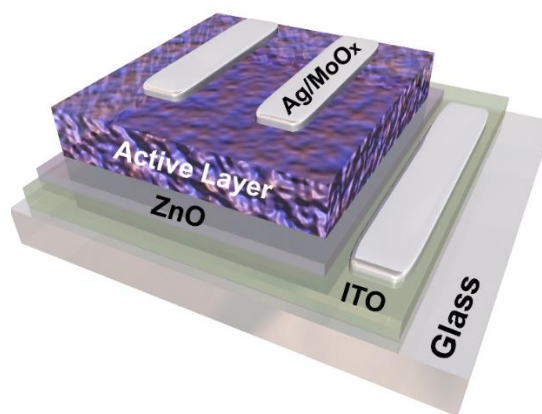


Figure S43. The device structure of designed OPDs. For wearable devices, the bottom substrate was PET instead of glass.

Differential Pulse Voltammetry (DPV) Measurements. Electrochemical differential pulse voltammetry (DPV) measurements were performed using a 2 mV step size, 80 ms step time and 50 mV pulse amplitude. The voltammetry experiments were performed in a glove box using a standard three-electrode cell on a 0.07 cm² glassy carbon button working electrode, an Ag/Ag⁺ (10 mM AgNO₃) reference electrode and a platinum flag counter electrode. Polymer films and NFA films were dropped cast from a 1 mg/mL chloroform solution onto the working electrode and allowed to air dry. Electrochemical experiments were performed using dry acetonitrile with a TBAPF₆ supporting electrolyte at a concentration of 0.5 M in an argon filled glovebox. Ferrocene/ferrocenium (−5.12 V vs vacuum) was used as an internal standard calibrated against the Ag/Ag⁺ reference electrode ($E_{1/2} = 85$ mV).

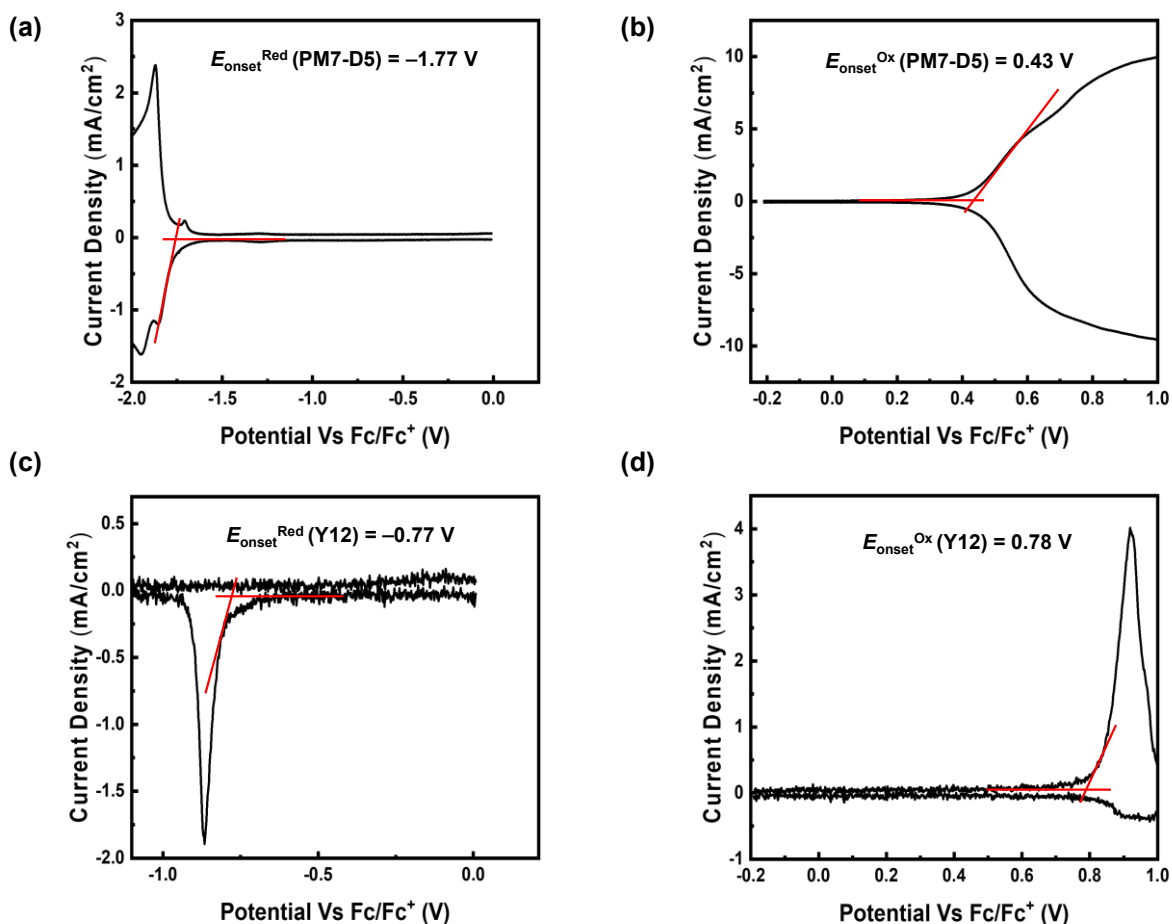


Figure S44. Differential pulse voltammograms of PM7-D5 during (a) electrochemical reduction and (b) oxidation. Differential pulse voltammograms of Y12 during (c) electrochemical reduction and (d) oxidation. The intersections of red lines indicate the extraction of onset potentials of ionization and electron affinity from DPV.

Topographic Characterization. All AFM height images were obtained using a Bruker Multimode 8 atomic force microscopy with tapping mode under nitrogen atmosphere. AFM tips with a force constant of 40 N/m and resonance frequency of c.a. 300 kHz were used in the AFM measurements. First-order image flattening was performed on the morphology

images and the measured morphology heights were offset to set the scale start point to 0 nm.

Transmission Electron Microscopy. The morphology of active layers were investigated utilizing transmission electron microscopy Jeol JEM-1400 Plus equipped with a field emission LaB and a high-sensitivity CCD camera Gatan. The analysis of active layers was performed at an accelerating voltage of 120 kV. BHJ films were spin-coated as the active layers in devices on Glass/ITO/PSS substrates. Then, carefully detached from the substrates by dissolving the PSS interlayer in DI water and then transferred on lacey carbon film TEM grids.

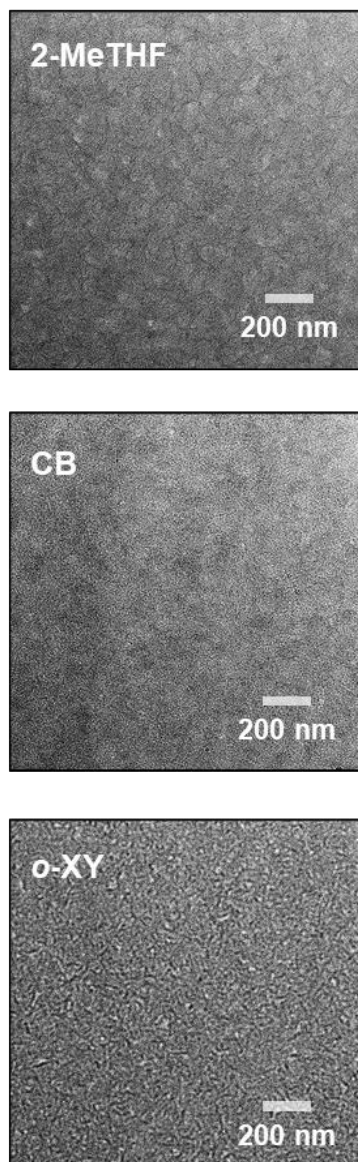


Figure S45. Enlarged TEM images of PM7-D5:Y12 blend films processed with 2-MeTHF, CB, and o-XY, respectively.

GIWAXS Characterization. Two-dimensional (2D)-GIWAXS measurements were performed at the PLS-II 3C beamline of the Pohang Accelerator Laboratory (PAL) in the Republic of Korea. 2D-GIWAXS images were collected at 11 keV ($\lambda_{\text{GIWAXS}} = 1.1271 \text{ \AA}$) with

an Eiger 4M detector (sample-to-detector distance: 209.01 mm). The incidence angle (α_i) of the X-ray beam was set between the critical angles of the thin film and substrate.

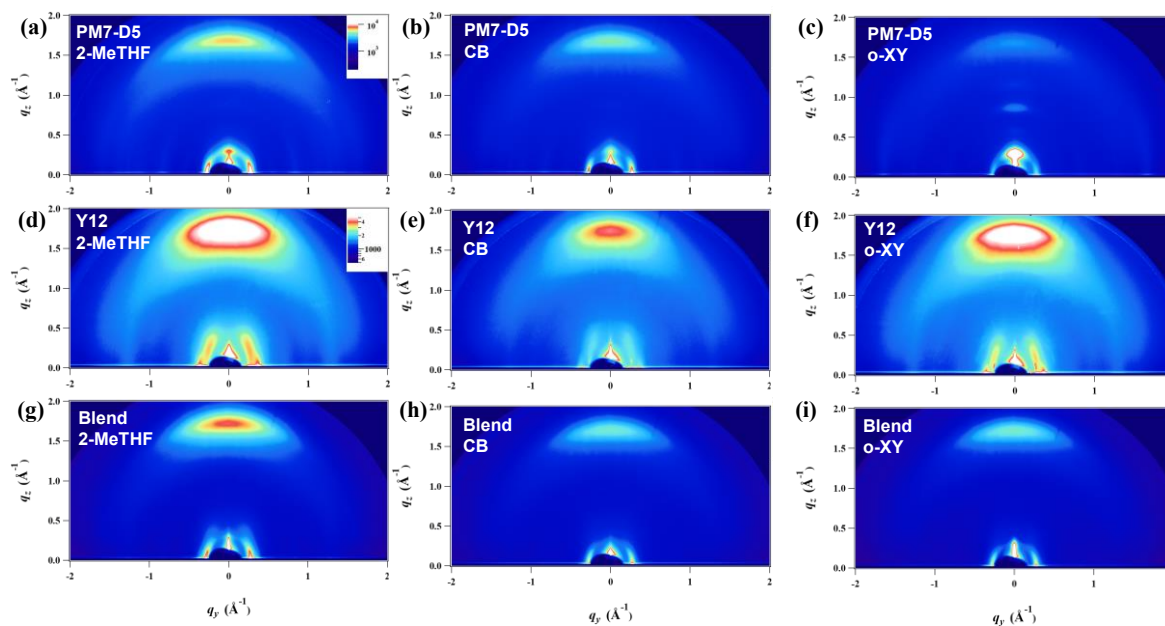


Figure S46. In-plane and out-of-plane GIWAXS images for the pristine (a-c) PM7-D5, (d-f) Y12, and (g-i) blend films processed from 2-MeTHF, CB, and o-XY, respectively.

(a)	PM7-D5 (2-MeTHF)					
q_z (\AA^{-1})	d (nm)	L_c (nm)	q_{xy} (\AA^{-1})	d (nm)	L_c (nm)	
0.31	2.01	3.97	0.29	2.16	13.22	
1.71	0.37	4.08	0.59	1.06	9.25	
			0.88	0.71	8.34	

(b)	PM7-D5 (CB)					
q_z (\AA^{-1})	d (nm)	L_c (nm)	q_{xy} (\AA^{-1})	d (nm)	L_c (nm)	
1.71	0.37	3.77	0.29	2.19	13.60	
			0.58	1.09	9.09	
			0.88	0.72	8.68	

(c)	PM7-D5 (o-XY)					
q_z (\AA^{-1})	d (nm)	L_c (nm)	q_{xy} (\AA^{-1})	d (nm)	L_c (nm)	
0.32	1.99	14.61	0.29	2.17	9.42	
0.91	0.69	7.53	1.33	0.47	7.29	
1.71	0.37	3.89	1.71	0.37	3.82	

(d)	Y12 (2-MeTHF)					
q_z (\AA^{-1})	d (nm)	L_c (nm)	q_{xy} (\AA^{-1})	d (nm)	L_c (nm)	
1.76	0.36	2.81	0.30	2.11	2.22	
			0.39	1.63	7.92	
			1.34	0.47	4.13	

(e)	Y12 (CB)					
q_z (\AA^{-1})	d (nm)	L_c (nm)	q_{xy} (\AA^{-1})	d (nm)	L_c (nm)	
1.77	0.36	2.71	0.29	2.20	24.29	
			0.39	1.61	14.70	
			1.34	0.47	3.99	

(f)	Y12 (o-XY)					
q_z (\AA^{-1})	d (nm)	L_c (nm)	q_{xy} (\AA^{-1})	d (nm)	L_c (nm)	
1.79	0.35	3.03	0.29	2.17	14.35	
			0.38	1.64	16.58	
			1.34	0.47	4.11	

(g)	Blend (2-MeTHF)					
q_z (\AA^{-1})	d (nm)	L_c (nm)	q_{xy} (\AA^{-1})	d (nm)	L_c (nm)	
1.75	0.36	3.76	0.30	2.10	10.74	
			0.88	0.71	7.20	

(h)	Blend (CB)					
q_z (\AA^{-1})	d (nm)	L_c (nm)	q_{xy} (\AA^{-1})	d (nm)	L_c (nm)	
1.73	0.36	3.44	0.30	2.12	12.29	
			0.88	0.71	10.78	

(i)	Blend (o-XY)					
q_z (\AA^{-1})	d (nm)	L_c (nm)	q_{xy} (\AA^{-1})	d (nm)	L_c (nm)	
1.75	0.36	3.91	0.29	2.14	12.61	
			0.88	0.72	8.69	

Figure S47. In-plane and out-of-plane GIWAXS profiles for the pristine (a-c) PM7-D5, (d-f) Y12, and (g-i) blend films processed from 2-MeTHF, CB, and o-XY, respectively.

Solid-state NMR Spectroscopy. For high-field ssNMR experiments, thin-film materials were prepared by dissolving PM7-D5, Y12, and their blends in CB or 2-MeTHF solvents, which were spin coated on glass substrates using the same optimized conditions used for the device fabrication. The neat and blended thin films were thermal annealed at 110 °C for 10 minutes and allowed to settle to cool to room temperature. All thin films were scratched from the glass substrates using a razor blade to collect these materials (~15 mg each) into glass vials, which were sealed with Parafilm and aluminum foil prior to shipment to the University of Lille for ssNMR studies. The neat Y12 and blend PM7-D5:Y12 materials were separately packed into 1.3 mm (outer diameter) cylindrical zirconia rotors fitted with Vespel[®] caps. All fast magic-angle spinning (MAS, 50 kHz) 1D ¹H, ¹³C, ¹⁹F, and 2D ¹H-¹³C, ¹H-¹H and ¹⁹F-¹⁹F NMR experiments were carried out on a Bruker AVANCE NEO (18.8 T, Larmor frequencies were

^1H = 800.1 MHz, ^{19}F = 752.9 MHz, ^{13}C = 201.2 MHz) spectrometer with a 1.3 mm H-X probehead. The ^1H and ^{13}C spectra were calibrated with respect to neat TMS using adamantane as an external reference (^{13}C resonance, 35.8 ppm, and the ^1H resonance, 1.85 ppm), and ^{19}F MAS spectra were calibrated to the ^{19}F chemical shift of Teflon at 132 ppm, in turn calibrated using neat CFCl_3 (^{19}F , 0 ppm) as an external reference.

For the next compounds and blends, 1D ^1H MAS NMR experiments were carried out by co-adding 32 transients with a ^1H interscan delay of 3 seconds, and ^{19}F spectra were acquired with 256 co-added transients, using an interscan delay of 10 seconds. 1D $^1\text{H} \rightarrow ^{13}\text{C}$ CP-MAS NMR spectra of neat were acquired with 2048 co-added transients and for the blend films, 4096 transients were co-added. The ^1H -detected 2D $^1\text{H} - ^{13}\text{C}$ HETCOR spectra of neat compounds were acquired with 98 t_1 increments, each with co-addition of 104 transients, and for the blend film 98 t_1 increments were acquired, each with 128 co-added transients, with 4 ms CP contact time. 2D $^{19}\text{F} - ^{19}\text{F}$ spin-diffusion NMR spectra were acquired with a three-pulse noesy like sequence. For neat Y12 and PM7-D5:Y12, 64 t_1 increments were acquired, 16 co-added transients each, using a 200 ms mixing times.

Analysis of 1D ^1H MAS NMR Spectra of Neat Compounds and Blends. Figure S48 compares 1D ^1H MAS NMR spectra of neat PM7-D5, Y12, and PM7-D5:Y12 blend, whereby the broad distribution of ^1H signals in the aliphatic region (0-4 ppm) correspond to distinct aliphatic proton sites which showed subtle differences in the line shapes. However, the aromatic regions in the range of 5-10 ppm (expanded regions shown in the inset) showed differences in the line shapes for the PM7:D5 and Y12 molecules, suggesting the different

local environments of aromatic groups. Although this comparison provides a qualitative picture of different packing interactions in donor and acceptor molecules, accurate identification the signals corresponding to distinct aliphatic and aromatic proton sites and through-space interactions between them is not feasible due to severely overlapped signal intensities.

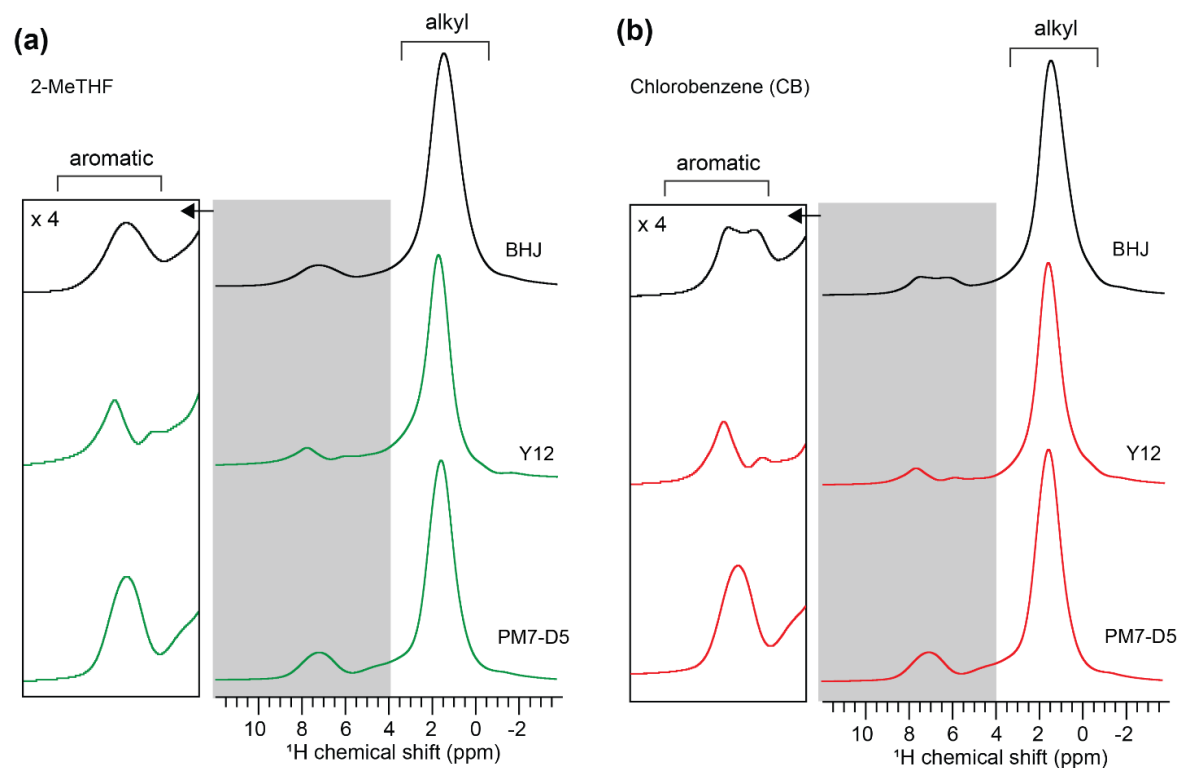


Figure S48. Solid-state 1D ^1H spectra of neat films and PM7-D5:Y12 blend films processed from CB and 2-MeTHF. All spectra were acquired at 18.8 T ($^1\text{H} = 800.1$ MHz) and at 50 kHz MAS.

Analysis of 1D $^1\text{H} \rightarrow ^{13}\text{C}$ CP-MAS NMR Spectra of Neat Compounds and Blends. In a CP-MAS experiment, simultaneous excitation of ^1H and ^{13}C nuclei is carried out to achieve

$^1\text{H} \rightarrow ^{13}\text{C}$ polarization transfer and hence ^{13}C signal intensities are enhanced. Figure S49 shows a comparison of 1D $^{13}\text{C}\{^1\text{H}\}$ CP-MAS NMR spectra between neat Y12, PM7-D5, and PM7-D5:Y12 blend: the signals corresponding to the distinct aliphatic and aromatic carbon sites can be identified. In the aliphatic region, ^{13}C signals at 10-16 ppm corresponds to terminal methyl groups, and signals at 20-35 ppm are attributed to central methylene groups in the linear and branched sidechains, and weak intensity signals at 35-42 ppm indicate -CH- moieties in branched sidechains, and in the range 50-70 ppm indicate -OCH₂- groups (PM7-D5) and -NCH₂- groups (Y12).

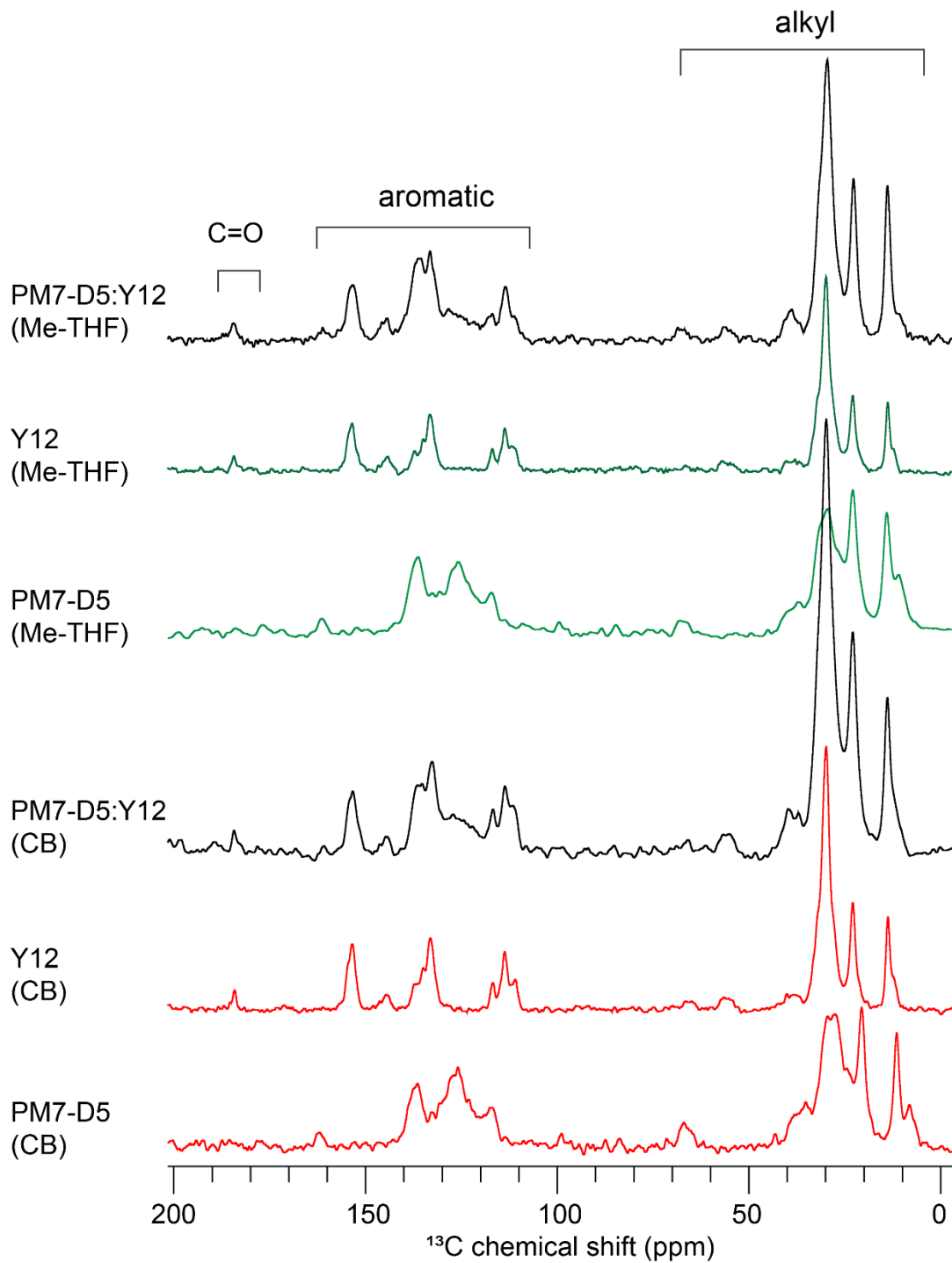


Figure S49. Solid-state 1D ^{13}C spectra of neat films and PM7-D5:Y12 blend films processed from CB and 2-MeTHF. All spectra were acquired at 18.8 T (Larmor frequencies of ^1H and

^{13}C nuclei are 800.1 MHz and 201.2 MHz, respectively).

***J-V* Curve, EQE and Impedance Measurements.** All the photoresponse and electrical measurements were conducted inside a glovebox under a nitrogen atmosphere. PPG and all-pulse oximetry experiments were performed on human subjects and were carried out with informed consent and under regular conditions. *J-V* characteristics were measured with a high-quality optical fiber to guide the light from the solar simulator equipped with a Keithley 2635A source measurement unit. Illuminated *J-V* curves were measured under AM 1.5G illumination ($100 \text{ mW}\cdot\text{cm}^{-2}$). EQE measurements were conducted with an EQE system, in which the monochromatic light intensity was calibrated using a Si photodiode. The spectral distributions of the real and imaginary components of the impedance of all devices were measured by an impedance analyzer (Solartron SI 1260A) in the dark and under illumination. To prevent the effect of the AC signal on the impedance during the measurement, a small amplitude AC signal (40 mV) was applied.

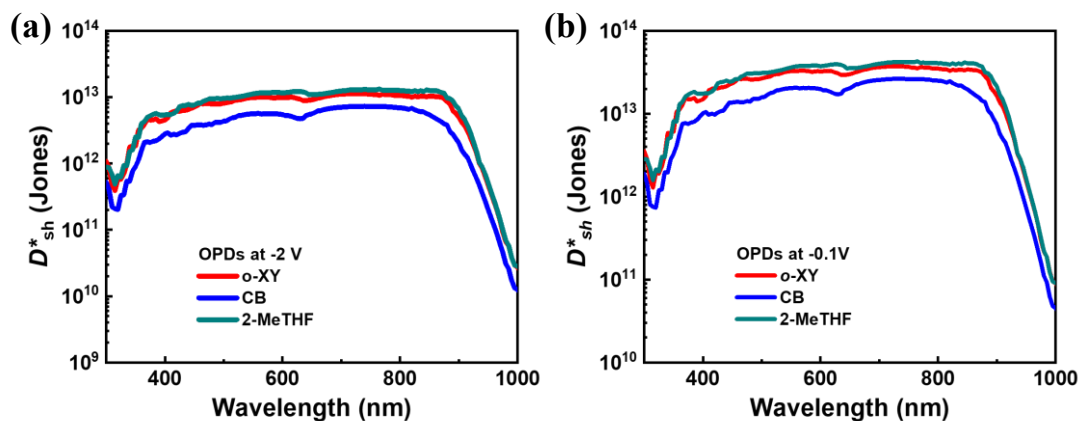


Figure S50. D_{sh}^* of OPDs cast from different solvents under an applied bias of (a) -2 V, and (b) -0.1 V.

LDR, Response Speed, and Noise Measurement. In the LDR and response speed measurements, the OPDs were illuminated by LEDs with different center peak wavelengths (850 nm or 940 nm, *Chanzon® LED*). For LDR measurement, the intensity of the LEDs was controlled by using a source measurement unit (Keithley 2602B SMU) and the light intensity was calibrated by using a commercial Si photodetector. The photo-current from OPDs was recorded by using a Keithley 4200-SCS Semiconductor Characterization System. For response speed measurement, a function generator (Stanford Research Systems DS345) was used to modulate the output light source with frequencies from 1 Hz to 200 kHz. The modulated photocurrent signal from OPDs was amplified (Stanford Research Systems SRS570) and collected by an oscilloscope (Keysight DSOX3022T). The noise measurements of the devices were carried out in the dark using a battery-powered pre-amplifier (Stanford Research Systems SRS570) coupled with an oscilloscope (Keysight DSOX3022T) operated with fast Fourier transform analysis.

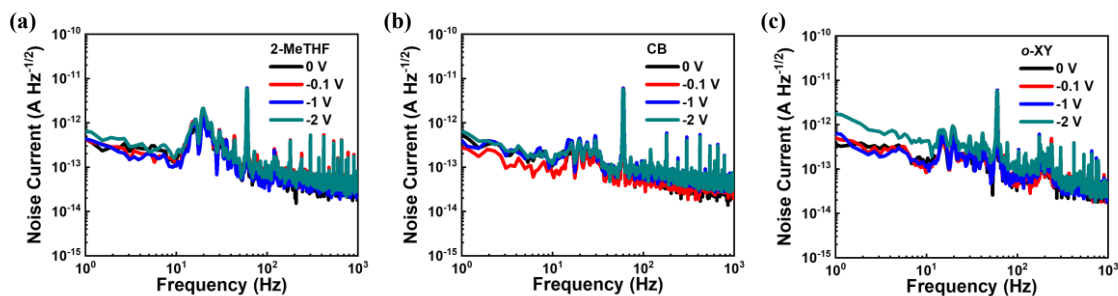


Figure S51. Noise current spectral density of the OPDs processed with different solvents: (a) 2-MeTHF, (b) CB, and (c) o-XY. These data were also collected at different reverse biases (0

V, -0.1 , -1 , and -2 V).

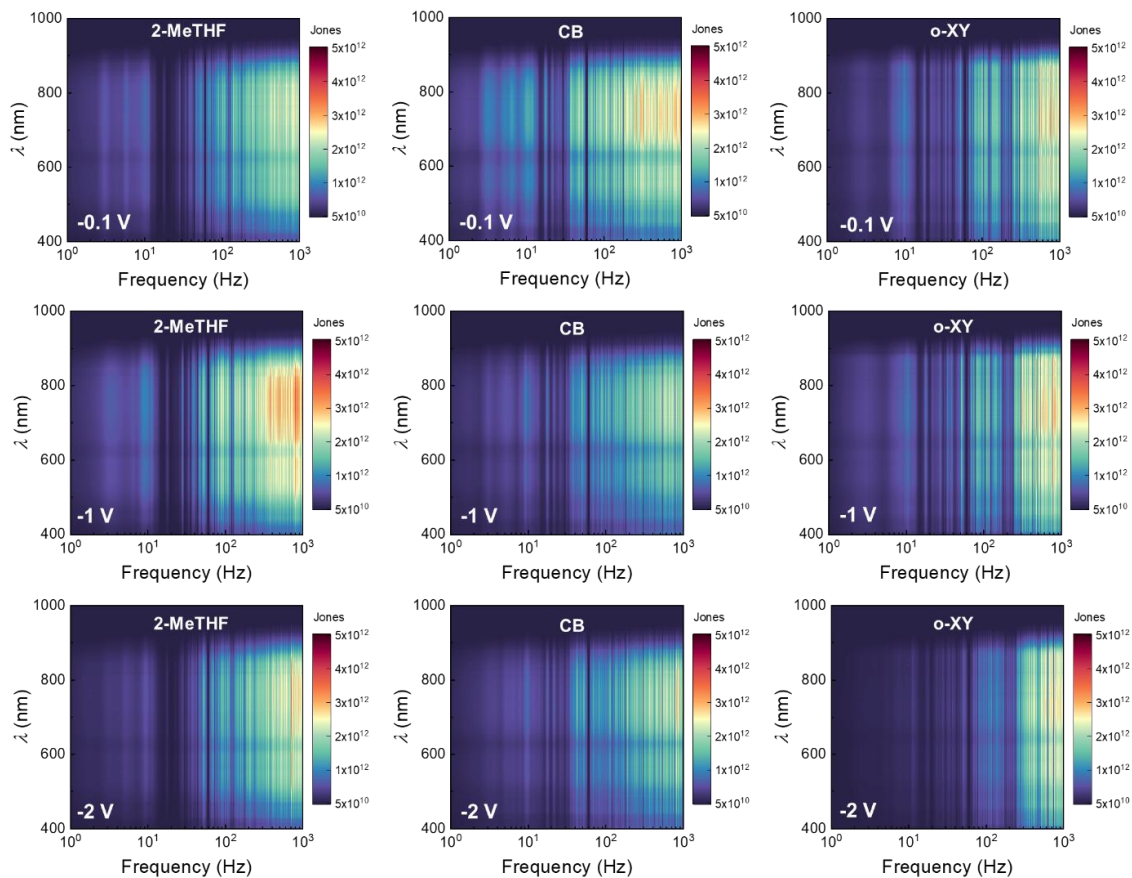


Figure S52. Specific detectivity (D^*) as a function of frequency and incident light wavelength of OPDs processed with different solvents (2-MeTHF, CB, and o-XY) and under different reverse biases (-0.1 V, -1 V, and -2 V).

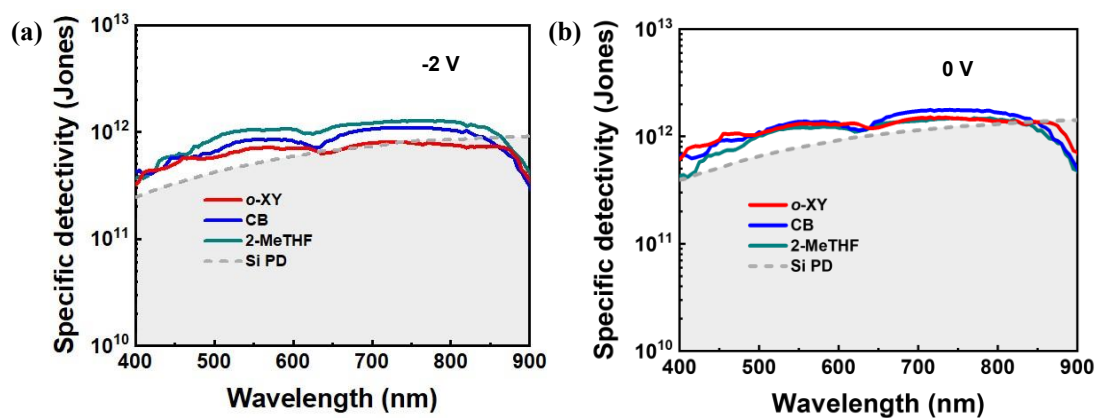


Figure S53. Specific detectivity of PM7-D5:Y12 OPDs and a commercial Si photodiode (Newport 818-UV) at the frequency of 155 Hz under (a) -2V , and (b) 0 V .

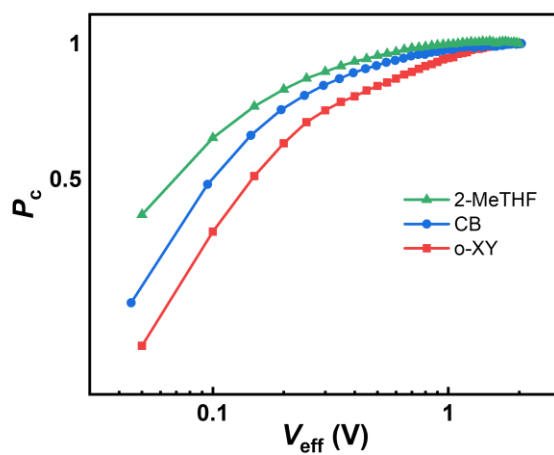


Figure S54. Voltage-dependent charge collection probability (P_c) of 2-METHF OPD under AM 1.5 G illumination at 100 mW cm^{-2} .

Calculation of Free Charge Carrier Density (n) from Impedance Measurement.

Impedance spectroscopy is used to measure the charge carrier density in the PM7-D5:Y12 active layer under different biases.^[53,63,111,124] To maintain the steady state properties of the system during the measurement under different DC bias and frequency, a small AC signal (40 mV) is applied during the measurement. The measured capacitance of the BHJ layer is corrected to minimize the effect of the series resistance (R_s) and the parasitic inductance (L') of the connecting cables, which can be described by the following Equation S1.

$$C_{\text{cor}} = -\frac{1}{\omega} \left[\frac{Z'' - \omega L'}{(Z' - R_s)^2 + (Z'' - \omega L')^2} \right] \quad (\text{s10})$$

Here, ω is the angular frequency of the AC signal, and Z' as well as Z'' are the real and imaginary components of impedance, respectively. Next, the geometrical capacitance (C_g) of the active layer was determined as the corrected capacitance measured under a large reverse bias (-1 V) in the dark, where C_{cor} is independent of the applied bias. And the charge carrier density n can be further determined using Equation (S2) with voltage-dependent impedance spectroscopy, where the changing of n is represented by the integrated frequency-dependent chemical capacitance C_{chem} .

$$n(V_{\text{cor}}) = n_{\text{sat}} + \frac{1}{qAL} \int_{V_{\text{sat}}}^{V_{\text{cor}}} C_{\text{chem}} dV_{\text{cor}}, \quad (\text{s11})$$

$$n_{\text{sat}} = \frac{1}{qAL} C_{\text{sat}}(V_0 - V_{\text{sat}}), \quad (\text{s12})$$

where A is the device area (0.05 cm^{-2}), V_{sat} is the reverse bias at which the J_{ph} saturates (-1 V), and C_{sat} is the internal capacitance at V_{sat} determined by the difference of the corrected capacitance measured under illumination and in the dark. The obtained n in 2-MeTHF device shows overall higher values ($n = 0.55\text{-}1.69 \times 10^{16} \text{ cm}^{-3}$) than these of the corresponding reference CB OPD ($n = 0.45\text{-}1.06 \times 10^{16} \text{ cm}^{-3}$) and o-XY device ($n = 0.52\text{-}1.65 \times 10^{16} \text{ cm}^{-3}$) under 100 mW cm^{-2} illumination.

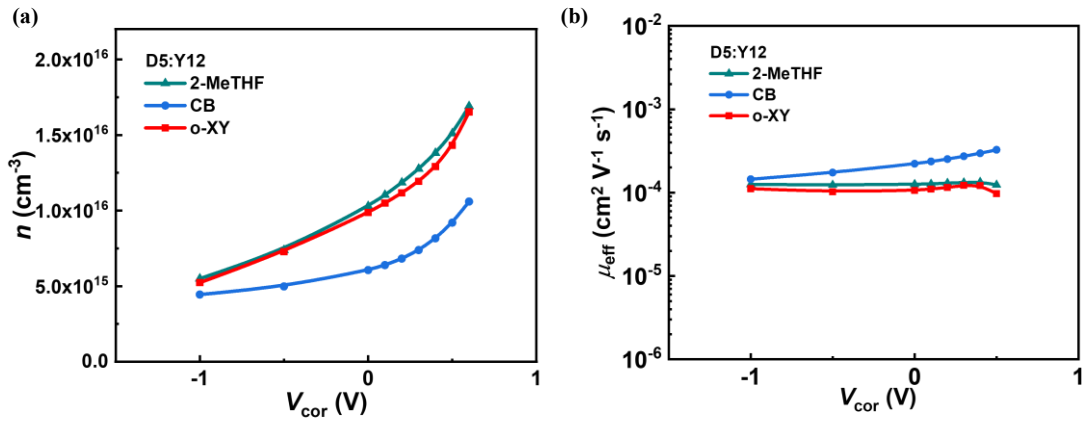


Figure S55. (a) Charge carrier density n and (b) effective mobility μ_{eff} of PM7-D5:Y12 devices under AM 1.5G illumination ($100 \text{ mW} \cdot \text{cm}^{-2}$).

PPG and Blood Oxygen Saturation Measurement. The transmission-mode PPG and blood oxygen level measurement setups were illuminated by LEDs at different wavelengths (850 nm or 940 nm, *Chanzon*® LED). The light emitted from LEDs was partially transmitted through a fingertip of a volunteer, which was eventually recorded by our wearable OPD on the volunteer's finger. Considering the fast charge transport and sufficient charge carrier

collection in the optimized devices, the OPD was directly operated under short-circuit current mode (*i.e.* without external voltage bias), and the photocurrent was amplified and converted to a voltage signal using a low noise amplifier SR570 (*Stanford Research Systems*). The output voltage signal was then displayed and extracted by using an oscilloscope (Keysight DSOX3022T) operated with fast Fourier transform analysis to get the real-time heart rate. Besides, no further calibration is required for pulse oximetry.

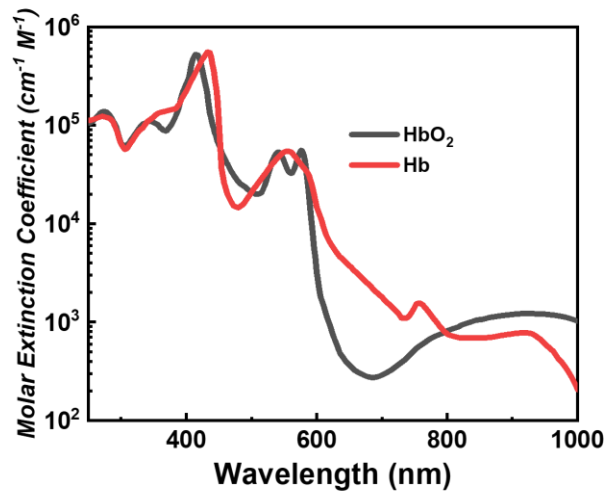


Figure S56. Molar extinction coefficients of oxygenated hemoglobin and deoxygenated hemoglobin.^[180]

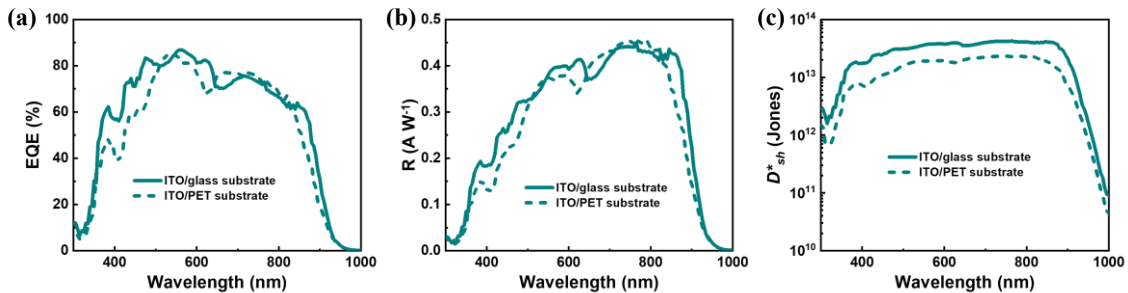


Figure S57. (a) EQE, (b) responsivity, and (c) shot-noise-limited specific detectivity (D_{sh}^*) of

PM7-D5:Y12 OPD processed with 2-MeTHF at -0.1 V with ITO/glass substrate (solid line) and flexible ITO/PET substrate (dash line).

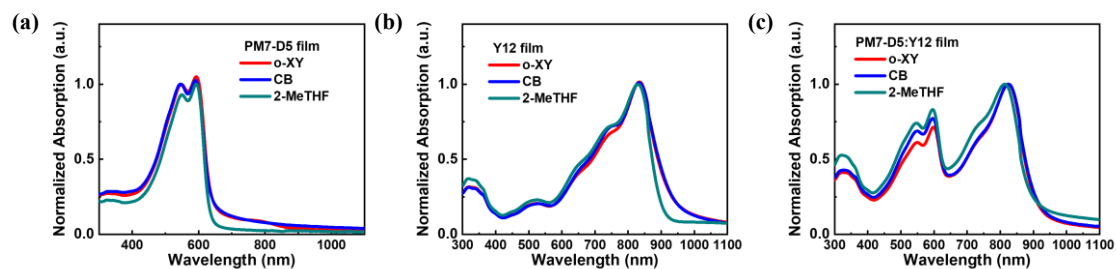


Figure S58. Normalized thin-film absorption of PM7-D5, Y12, and their BHJ blends processed with o-XY, CB and 2-MeTHF, respectively.